THE INTERACTION OF QUANTUM DOTS WITH PLASMONS SUPPORTED BY METAL WAVEGUIDES

Hettiarachchige Chamanei Sandamali Perera

Bachelor of Science (hons)

(University of Peradeniya, Sri Lanka)

Submitted in fulfilment of the requirements for the degree of

Doctor of Philosophy

Chemistry Physics and Mechanical Engineering

Science and Engineering Faculty

Queensland University of Technology

2016

Keywords

Plasmonic, Surface plasmons, Quantum Dots, waveguides, grating, refractive index sensor, plasmon excitation

Publication list

Peer reviewed Journal articles:

1. **C. S. Perera**, K. C. Vernon, H. Cheng, J. Sathian , E. A. Jaatinen, and T. J. Davis, "Highly compact refractive index sensor based on stripe waveguides for Lab-on-a-chip sensing applications", submitted to JOSA-B.
2. **C. S. Perera**, K. C. Vernon, A. M. Funston and H. Cheng "Mapping bound plasmon mode on a nanoscale stripe waveguide using Quantum dots", submitted to BJ nano.
3. **C. S. Perera,** K. C. Vernon, A. M. Funston, H. Cheng, F. Eftekhari, T. J. Davis, "Excitation of bound plasmons along nanoscale stripe waveguides: a comparison of end and grating coupling techniques", Opt. Express, **23**(8), 10188-10197 (2015).
4. **C. S. Perera**, K. C. Vernon, and A. Macleod, "Simulations of the spontaneous emission of a quantum dot near a gap plasmon waveguide", J. Appl. Phys., **116**(3), 033101 (2014)

Peer reviewed conference papers and presentations

1. **C. Perera**, and K. C. Vernon, "Optimizing the Quantum dot-plasmon interaction in a nano gap waveguide", Proc. SPIE 9163, Plasmonics: metallic Nanostructures and their optical properties XII, 91632E (2014)
2. **C. Perera**, and K. C. Vernon, "Simulation of gap plasmon coupling with a quantum dot", Proc. SPIE 8923, Micro/Nano Materials, Devices, and Systems, 89230Z (2013)

Most relevant conference presentations:

1. Australian Institute of Physics, Canberra, Australia (December 2014) Oral: **C. S. Perera**, K. C. Vernon, A. Funston, H. Cheng "Exciting bound plasmon mode in asymmetric stripe waveguides using grating"
2. SPIE, Plasmonics: metallic Nanostructures and their optical properties XII, San Diego, USA (August 2014). Poster: **C. Perera**, and K. C. Vernon, "Optimizing the Quantum dot-plasmon interaction in a nano gap waveguide",
3. SPIE, Micro/Nano Materials, Devices, and Systems, Melbourne Australia (December 2013). Oral: **C. Perera**, and K. C. Vernon, "Simulation of gap plasmon coupling with a quantum dot".

Abstract

Plasmonics is a recently emerged technology that enables the compression of electromagnetic waves into miniscule metallic structures, thus enabling the focusing and routing of light on the nanoscale. Over the last 20 years, researchers have used plasmonics to go beyond the limits of conventional optics and manipulate light on the nanolevel. Plasmonics can be used to miniaturise the size of integrated chip circuits while increasing the data transmission speed. To do this, methods for exciting, routing and controlling plasmons in the circuit must be established. Plasmonic waveguides are used to rout the plasmons inside a circuit and are a major focus of this thesis. Control of the propagating plasmon is also a major focus of this thesis and is vital in order to use plasmons in all optical circuitry. The spontaneous emission rate of an optically excited quantum emitter can be altered by placing the emitter in the vicinity of the plasmon waveguide. This will increase the available number of decay channels for emitter to emit photons into. This opens up the possibility of spontaneous emission to be captured by the plasmons on the waveguide. The above manipulation of light matter interaction can be effectively used to control the plasmon propagation on a waveguide. Numerical and experimental analysis of this QD-plasmon interaction is studied in this thesis.

Finally, using the plasmon waveguides experimentally realised in this thesis, a plasmonic sensor is designed and tested. Plasmons are highly sensitive to the surrounding dielectric environment. This unique property of plasmons can be used to fabricate ultrasensitive detectors in sensing applications. In this work, we have utilised this property to build a highly sensitive and highly compact refractive index sensor.

Table of Contents

Keywords iii
Publication list v
Abstract vii
Table of Contents ix
List of Figures xi
List of Tables xvii
List of Abbreviations xix
Statement of Original Authorship xxi
Acknowledgements xxiii
Chapter 1: Introduction 25
1.1 History: 25
1.2 Background 28
1.3 Specific aims 29
1.4 Thesis outline 30
Chapter 2: Literature Review 35
2.1 The surface plasmon 35
2.2 SPP excitation and detection techniques 38
2.3 Detection and imaging of SPP 41
2.4 Plasmonics applications 49
2.5 Plasmonic waveguides 54
2.6 Mach-Zehnder interferometer 84
2.7 Quantum dot – plasmon interaction 91
2.8 Fabrication 100
Chapter 3: Numerical analysis of gap plasmon-Quantum dot interaction..... 107
3.1 Simulation of gap plasmon coupling with a quantum dot 107
3.2 Optimizing the Quantum dot-plasmon interaction in a nano gap waveguide 117
3.3 Simulations of the spontaneous emission of a quantum dot near a gap plasmon waveguide 127
Chapter 4: Excitation of bound plasmons along nanoscale waveguides: a comparison of end and grating coupling techniques 135
Chapter 5: Mapping a bound plasmon propagating on a nanoscale stripe waveguide using quantum dots: Effect of spacer layer thickness 147
Chapter 6: Highly compact refractive index sensor based on stripe waveguides for Lab-on-a-chip sensing applications 155
Chapter 7: Conclusions 163

Bibliography 167

Appendices 173

Appendix A: Modelling f QD-plasmon interactions.....173

A1. Modelling spontaneous emission decay rate into the plasmonic mode (γ_{pl}).....173

A2. Modelling total decay rate (γ_{tot}) 177

Appendix B: Supplementary materials 179

B1. Gap waveguide fabrication.....179

B2. Excitation technique.....184

List of Figures

Figure 1.1 Evolution of microprocessor dimensions with time. Data source: Intel. 26

Figure 1.2 Lycurgus cup. Due to the plasmonic excitation of metal NPs inside the glass, the cup appears greenish in colour when viewed in reflected light and appears reddish in colour when viewed in transmitted light. 28

Figure 1.3 Schematic diagram of the plasmonic refractive index sensor design used in Chapter 6. Sample solution is confined inside the blue box shown. 32

Figure 2.1 Schematic representation of SP on a metal-dielectric interface. The SP is propagating along the *x* direction, and its electric field is evanescently decaying along *y*. 36

Figure 2.2 Dispersion of SPP on a metal surface. Light line and SP dispersion are also shown [3] 37

Figure 2.3 Light diffraction due to surface defect [3]. Diffracted light consists of photons with broad wavevector range. Some of these photons can couple with SPs on the metal. 38

Figure 2.4 (a) Kretschmann geometry and (b) two-layer Krestchmann geometry [3] used to excite SPPs on a thin metal film 39

Figure 2.5 Otto geometry [3] used to excite SPPs on a thick metal film. 39

Figure 2.6 Phase matching of light to SPPs on a metal surface using grating coupling 40

Figure 2.7 Locally excite SPPs on a metal surface using SNOM tip [3]. Light transmitted through the aperture consists of photons with broad wavevector range allowing locally exciting SPPs 41

Figure 2.8 Generic dispersion relation of an SPP at a metal/air interface. LR into the substrate occurs at the region enclosed by the light lines in air and in higher index substrate [6] 42

Figure 2.9 Schematic of the excitation of a white-light continuum of SPPs and their observation through detection of the leakage radiation with an index-matched oil-immersion lens [24] 44

Figure 2.10 Schematic representation of QD excited by propagating plasmons on the waveguide [38]. QD_{bulk} denotes the QDs spatially displaced from the waveguide, QD_{pl} denotes the QDs in the immediate vicinity of the waveguide fluoresce interacting with the plasmon mediated electric field and θ represents the polarisation angle of the incoming light. 46

Figure 2.11 (a) SEM image of a Ag NW logic gate (b) – (f) QD emission images of the logic gate in operation. I1 and I2 are input channels. O1 and O2 are output channels [34] 47

Figure 2.12 (a) Fluorescence image of BlIPP coated nanoparticle chain for 785 nm laser. (b) Fluorescence image of the same NP chain taken after 20 min exposure to laser light and (c) difference image [40] 48

Figure 2.13 (a) Typical SPR setup and (b) Reflectivity vs angle of incidence. Solid line represents the reflectivity measured at metal/dielectric interface before binding molecules and dashed line represents the reflectivity measured after binding molecules. The difference between the angular positions of the dips is often used to define sensitivity. 50

Figure 2.14 Conceptual illustration of SERS setup. Presence of a bound molecule results in strong enhancement in the local near-field intensity. 51

Figure 2.15 Schematic diagram of an electronic interconnect. L is the length and A is the cross sectional area of the interconnect..... 52

Figure 2.16 Graphical interpretation of operation speed versus critical device dimension of different chip technologies [44] 53

Figure 2.17 Essential optical components of an all-optical circuit 54

Figure 2.18 Basic plasmonic waveguide structures. a) Metal slab, b) metal stripe, c) gap waveguide, d) v-groove waveguide and e) wedge waveguide. All structures shown here are on a glass substrate (blue) with air superstrate (light blue), and metal is shown in yellow colour. 55

Figure 2.19 E_y distribution of (a) an SPP mode on a metal-dielectric interface. (b) Two bound SPP modes on a metal slab..... 57

Figure 2.20 The direction of E_z field for a structure with (a) symmetric surface charge distribution (a_b mode) and (b) asymmetric charge distribution (s_b mode). 58

Figure 2.21 Normalised phase and attenuation constants of the a_b and s_b modes supported by an asymmetric metal slab at 633 nm excitation assuming metal as silver and top and bottom dielectrics with refractive indices 1.55 and 1.5 respectively [47]. 59

Figure 2.22 Metal stripe with permittivity $\varepsilon_{r,2}$, thickness *t*, and width *w*, surrounded by upper and lower dielectric media ($\varepsilon_{r,3}$, $\varepsilon_{r,1}$). SPP modes are propagate in the +*z* direction (directed up out of the page) [59]..... 62

Figure 2.23 a) normalised phase constant and b) attenuation constant of modes supported by the symmetric metal slab with infinite width and finite width (w= 1 μm). The metal is silver and the structure surrounded by PMMA ($\varepsilon_{r,1} = \varepsilon_{r,3} = 4$), and excited using a 633 nm laser [60]. 63

Figure 2.24 Contour and 3D plots of $\mathrm{Re}\{S_z\}$ of the ss_b^0 mode for w= 1μm (a) t= 80 nm, (b) t=20 nm, (c) t=100 nm and (d) t= 40 nm. Other parameters $\lambda_0 = 633$ nm, $\varepsilon_{r,2} = -19 - j0.53$ and $\varepsilon_{r,1} = \varepsilon_{r,3} = 4$. Waveguide cross-section in (c) and (d) are located in the *x-y* plane. Figures (a) and (b) are adapted from [60] and figures (c) and (d) adapted from [61] 66

Figure 2.25 SEM image of chemically synthesised Ag NWs spincoated on ITO coated glass. Image obtained by author at QUT. 68

Figure 2.26 Plasmon propagation on a Silver NW excited via 100x oil high numerical aperture objective a) under dark filed microscope. b) without dark field. Red dots along the NW are due to scattering of propagating SPPs from the nanoparticles attached to the NW.NW excitation wavelength is 633 nm. Images obtained by author at Monash University Funston lab. 69

Figure 2.27 Schematic representation of formation of gap plasmons. (a) when the gap width is sufficiently high two interfaces contain two individual single-interface SPP waves, where the field magnitude drops exponentially away from the metal surface. (b) As the gap thickness reduces these two individual SPP modes combine into one mode called "gap plasmon mode". ε_m and ε_d denote the permittivities of metal and dielectric medium respectively..... 71

Figure 2.28 Cross-section of a 3D metal gap waveguide with structure extending into the page 71

Figure 2.29 a) schematic diagram of a 3D MHGW. Blue regions represent the silver and the light brown represents aluminium, b) cross-sectional view of the MHGW in z plane. w represents the width of the gap, h represents the height of the silver region, d is the width of the Al/Ag..... 72

Figure 2.30 Schematic diagram of an asymmetric GPW. 'w' represents the width of the gap and 'h' represents the height of the gap. 74

Figure 2.31 (a) Schematic diagram of the cross sectional view of the proposed waveguide structure (b) SEM images of the fabricated waveguides with different lengths [73]. 75

Figure 2.32 SEM images of the logic gates fabricated using GPWs. (a) OR gate, (b) NOT gate and (c) XNOR gate [75]. 76

Figure 2.33 Schematic diagram of the structure with triangular groove of finite depth h and angle θ in a metal with additional screen at x=0. The metal screen supresses the scattered bulk waves in and above the groove [80]. 78

Figure 2.34 Plasmonic waveguide-ring resonator a) SEM image, b) topographical and c) Near field optical image at wavelength 1525 nm [32] 80

Figure 2.35 Truncated wedge. Wedge angle denoted by ϕ, edge is rounded with radius of curvature r, wedge height h [81]. 81

Figure 2.36 SEM image of the plasmon waveguide consisting of nanoparticles [23]. Long axis of the nanoparticle is perpendicular to the waveguide chain axis..... 82

Figure 2.37 Schematic diagram of a M-Z interferometer using gap waveguides [89]..... 85

Figure 2.38 Schematic diagram of the proposed 4 arm waveguide coupler M-Z interferometer. *D* is the separation between input arm and outer arms, *w* is the width of the waveguide and *L* is the coupling length [89]. 86

Figure 2.39 Y splitter and M-Z interferometer using v-groove waveguides. a) SEM image, b) topographical image, c) near-field optical image (at wavelength 1600 nm) using SNOM. d)-f) as a)-c) but for M-Z interferometer [32]..... 87

Figure 2.40 Schematic diagram of the M-Z interferometer consists of two metallic nanoslits described by Bartoli et al[91]. 88

Figure 2.41 M-Z interferometer design using 3 waveguide coupling [92] L_i is the input length, L_c is the coupling length, L_o is the output length, L_s is the sample length and s is the separation distance [92]. 89

Figure 2.42 An optimally coupled QD with a metallic nanowire. Disregarding the non-radiative decay (heat), coupled optical emitter can emit spontaneously into the guided plasmons of the nanowire or to the free space with rates Γ_{pl}, Γ_{rad} respectively [16]. 92

Figure 2.43 2D schematic of a symmetric GPW. Height h = 0.05 μm, $E_{x,y,z}\left(x_{QD}, y_{QD}\right)$ is measured along the line shown in red. *w* is the width of the GPW and *d* is the distance from the QD to waveguide surface 94

Figure 2.44 Schematic diagram of (a) MDM slab, electric field inside the gap is shown in red colour and (b) MDM slot waveguides with electric field profile of the fundamental mode. Yellow sphere represents the dipole emitter (QD) [17]..... 97

Figure 2.45 (a) Schematic diagram of the experimental configuration. Incoming laser light illuminates the sample through the substrate. Photoluminescence (PL) from the top and bottom of the sample are collected and analysed. (b) Geometry of the waveguide structure, *W* represents the width and *H* represents the height of the slot. Normalised electric field of slot when incident laser light is polarised (c) normal to the gap and (d) parallel to the gap [18]..... 97

Figure 2.46 Imaging plasmon propagation along a silver NW using CdSe QDs. Excitation wavelength 532 nm. Spacer layer between the

NW and QD layer is 20 nm thick SiO_2. Image was obtained by the author at Monash University Funston lab. 98

Figure 2.47 (a) Optical image of the microfluidic channel. Area inside the circle is the centre control region which is controlled by four external electrodes, (b) schematic of the QD positioned near the NW. QD is driven along the trajectory shown by black arrow according to the flow control. Inset shows an SEM image of the AgNW [19]. 99

Figure 2.48 Operating principle of Ga milling. Impinging Ga ions sputter small amount of sample material from the surface. The sputtered section leaves the sample surface as secondary ions (i^+) or neutral atoms (n^0). 102

Figure 2.49 (a) single layer PMMA resist exposed to e beam, (b) bilayer PMMA resist exposed to e beam and (c) metal deposited on a patterned and developed bilayer sample. Note the undercut is deeper than the single layer and (d) structure survives on the substrate after acetone lift-off 105

Figure A1 Symmetric waveguide structure. 1 represents the metal region and 2 represents the dielectric region. 174

Figure B1 (a) FIB milled gaps with left most gap with low number of passes, middle to right increased number of passes in raster scan and (b) a successful 300 nm wide 250 nm deep 3 µm long slot 179

Figure B2 Attempt to make stripe waveguides using FIB milling into PMMA followed by lift-off. a) Survived 100 µm x 100 µm x 100 nm square waveguide. Polymer layer in the background is left after liftoff process probably the PMMA layer exposed to e beam while imaging using SEM. b) unsuccessful 200 nm wide 250 nm deep 10 µm long stripes. 180

Figure B3 (a) 200 nm wide, 100 nm thick, 10 µm long stripe with grating structures (grating periodicity 383 nm with groove to pitch ratio 1/2), and (b) tilted view of the same stripe waveguide. The structure was produced at Melbourne Centre for Nanofabrication, Melbourne. 181

Figure B4 (a) 1 µm wide, 5 µm long 100 nm thick Au waveguides fabricated using FIB, and (b) plasmon propagating on a FIB milled stripe when excited using highly focused laser beam of wavelength 633 nm. Structures produced by the author at QUT using CARF facilities and dark field image obtained by the author using inhouse excitation setup 182

Figure B5 30 nm height, 750 nm wide, 20 µm long stripe with gratings at both ends survived successfully after lift-off process. Image was produced by author at QUT CARF. 183

Figure B6 SEM image of a plasmonic refractive index sensor consisting of three 750 nm wide, 30 nm thick Ag stripes. Outer arms are 25 µm long and central arm is 15 µm long. 184

Figure B7 Plasmon excitation set up. A highly focused laser beam focused onto the sample using high numerical aperture objective. 185

List of Tables

Table 2-1 Summary of waveguides..... 84

List of Abbreviations

ATR	Attenuated Total Reflection
CCD	Charge Coupled Device
CPP	Channel Plasmon Polariton
CVD	Chemical Vapour Deposition
EBL	E Beam Lithography
FEM	Finite Elemental Modelling
FIB	Focused Ion Beam
GPW	Gap Plasmon Waveguide
LRSPP	Long Range Surface Plasmon Polariton
LSP	Localised Surface Plasmon
LSPR	Localised Surface Plasmon Resonance
MW	Metal Waveguide
MHWG	Metal Hetero WaveGuide
MZ	Mach-Zehnder
NP	Nano Particle
NW	Nano Wire
PL	PhotoLuminescence
PMMA	PolyMethylMethAcrylate
PSTM	Photon Scanning Tunnelling Microscope
PVD	Physical Vapour Deposition
QD	Quantum Dot
RI	Refractive Index
SEM	Scanning Electron Microscope
SNOM	Scanning Near-Field Optical Microscope

SPP	Surface Plasmon Polariton
SP	Surface Plasmon
TE	Transverse Electric
TM	Transverse Magnetic
WCP	Wedge Channel Plasmon
WP	Wedge Plasmon

Statement of Original Authorship

The work contained in this thesis has not been previously submitted to meet requirements for an award at this or any other higher education institution. To the best of my knowledge and belief, the thesis contains no material previously published or written by another person except where due reference is made.

Signature:

Date: 13 January 2016

Acknowledgements

First of all, I cannot express enough my gratitude to my principal supervisor Dr. Kristy Vernon for her exceptional support, encouragement and attention throughout the project. This project would not have been successful without her sincere and valuable guidance. She was like a second mother to me. I offer my heartfelt appreciation to her for all the learning opportunities she provided me to complete this research work.

I'm also grateful to Dr. Alison Funston, Monash University for sharing her expertise and the valuable guidance she extended to me. You made my stay in cold Melbourne into a warm wonderful experience.

I take this opportunity to express gratitude to my associate supervisors A/Prof. Esa Jaatinen and A/Prof. Eric Waclawik for their support during my candidacy.

I would also like to thank all of the members in the Plasmonic Device group (QUT) and Applied Optics Group (QUT) for their support, particularly Mr. Angus Mcleod and Ms. Dinithi Namarathne. You all made my journey very enjoyable.

I would like to acknowledge Central Analytical Research Facility (CARF) at Institute of Future Environments (IFE) QUT, for providing me with all the necessary facilities for the research and all the IFE staff for their support, especially Dr. Peter Hines, Dr. Mahnaz Shafiei and Dr. Tuquabo Tesfamichael.

I wish to extend my gratitude to all the collaborators around Australia. In particular, Mr. Wenming Tong and Ms. Patrycja Ballard of Funston group (Monash University), Dr. Fatima Eftekhari at Melbourne Centre for Nanofabrication and Dr. Elliot Cheng, Dr. kai-Yu Liu and Dr. Doug Mair at University of Queensland.

Last but not least, I would like to extend my sincere thanks to my parents for the unceasing encouragement and my loving husband for his support, attention and encouragement throughout this venture.

Chapter 1: Introduction

Electronic devices, circuits and components based on semiconductor technology are being miniaturised in order to achieve more compact devices with higher performances. However, the size of these devices now approaches a fundamental size limit and bandwidth limitations [1]. Thus, for the technology to continue to advance an alternative to electronics must be found. Optical interconnects such as fibre optics can transport huge amounts of data with considerably higher speed. However, conventional optical component size is limited to about half of the wavelength due to fundamental laws of diffraction. Recently emerged "Plasmonic" technology exploits unique optical properties enabling the focusing and guiding of light into nanoscale areas on a size scale comparable with current semiconductor technology, but providing speeds much faster than current semiconductor technology [2, 3]. The aim of this thesis is to contribute to the development of nano-scale plasmonic circuits and sensing technology.

The first two sections of this chapter outline the history and background to the aims in this thesis. The next section describes the specific research aims. Finally, the last section includes an outline of the remaining chapters of the thesis.

1.1 History:

Gordon E. Moore in his original paper (1965) stated that the number of transistors on an integrated chip (IC) will increase as an exponential function with time, due to the decreasing size of the transistor [1]. Indeed, the size of electronic components is decreasing every year according to Moore's Law. **Figure 1.1** depicts the evolution of overall size of the microprocessors over time. In 2005, Moore said that Moore's law

cannot be continued forever. If this trend were to continue, the size of electronic devices would reach a fundamental limit [4].

> "In terms of size (of transistor) you can see that we're approaching the size of atoms which is a fundamental barrier, but it will be two or three generations before we get there"
>
> - Gordon E. Moore

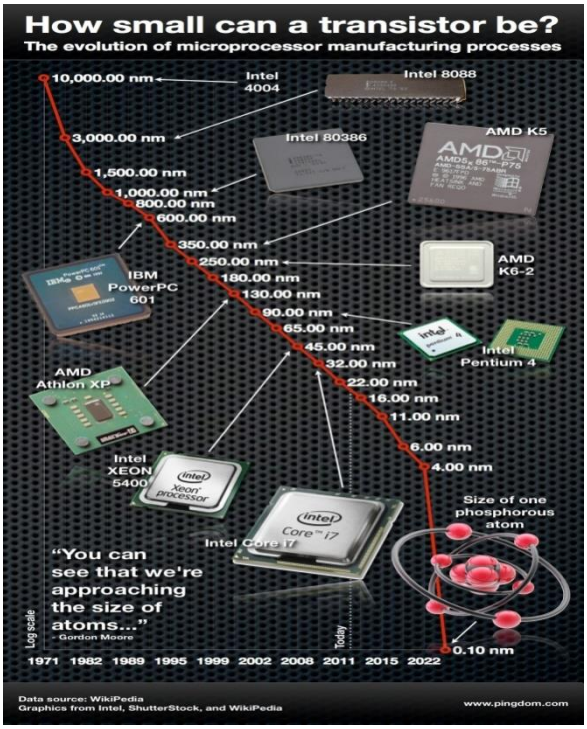

Figure 1.1 Evolution of microprocessor dimensions with time. Data source: Intel.

Alternatives to electronics are needed to overcome this problem and further advance the technology. Optical fibres are used worldwide for transmitting information. Their ability to transfer gigantic amounts of data over long distances with high data transmission rate made fibre optics span the globe and researchers started wondering whether optics is a possible solution to replace electronic circuits. But, using optics on

the nanoscale has a major drawback. Conventional optical devices are limited by diffraction [5, 6]; light in closely placed waveguides start interfering with each other when the waveguide size drops below half the wavelength of the light. Plasmonics is a promising field in manipulating light beyond the diffraction limit, on the nanoscale [6-8]. A plasmon is the coherent oscillation of light interacting with conduction electrons of a metal. Basically plasmons fall into two categories: Localised Surface Plasmons (LSPs) and Surface Plasmons (SPs). LSPs are involved with bound electron plasmas such as in nanoparticles (NPs). LSPs have been used since ancient times in manufacturing stained glasses. **Figure 1.2** shows an ancient Roman goblet named the Lycurgus cup dating from the 4th century A.D. This cup is made of glass incorporating small metallic nanoparticles [7]. Due to plasmonic excitation of the suspended NPs inside the glass, the cup scatters blue-green light (relatively shorter wavelengths of the visible spectrum) giving a green hue when viewed in reflected light. When a white-light source is placed inside the cup, the cup appears to be mostly reddish in colour as it transmits only the longer wavelength of the visible spectrum.

Though LSPs have been used since ancient times the nature of LSPs has only been understood in recent years. Scientists have discovered that when light is incident on metal NPs with size smaller than the incident wavelength, the NPs can interact with the electric field of the incident light resulting in the coherent plasmon oscillations or LSPs. Resonance frequency of this oscillation strongly depends on the size and shape of the NP as well as surrounding dielectric medium. LSP resonance (LSPR) has shown promising applications in sensing [9].

Figure 1.2 Lycurgus cup. Due to the plasmonic excitation of metal NPs inside the glass, the cup appears greenish in colour when viewed in reflected light and appears reddish in colour when viewed in transmitted light.

It wasn't until the early 1980s, that scientists started looking into plasmonics as a new technique to transmit optical signals on the nanoscale. They discovered that loosely bound electron plasma oscillations near a metal surface can combine with an incoming photon from the adjacent dielectric media under the right circumstances and propagate along the interface as a charge-density wave. So they termed this propagating plasmon category as Surface Plasmons (SPs). If these SPs can be controlled and guided along a circuit, SPs can find potential applications in nano optical circuits. Overall, plasmonics is a fairly young technology opening up novel applications not only in the development of nano-optical circuits but also in solar cells and sensing [8, 10-15].

1.2 Background

Plasmons are ideal candidates for focusing light into a nanoscale area. Plasmon waveguides have been proposed to be used in sensors and circuits to achieve more compact devices. For a plasmonic nano-optical circuit, there should be:

1. an efficient way to couple light in to the circuit
2. a method to route light around the circuit, and
3. an active control of the plasmon propagation inside the circuit.

Routing light: Metallic waveguides are a promising way to guide light in the circuit. Plasmonic waveguide structures considered in this thesis are stripe waveguides (nanoscale metallic bar on a glass substrate) and gap waveguides (nano slot in a thin metal film coated on a glass substrate).

Control: In order to use plasmons for nano-optical circuitry, there should be a way of controlling the plasmon propagation. It has been experimentally shown that placing an excited dipole emitter (or quantum dot, QD) near the waveguide grants control of the plasmon propagation [16-20]. When an optically excited dipole emitter is placed in proximity to a plasmonic waveguide, SPs on the waveguide can capture the majority of the spontaneous emission into guided plasmon modes and propagate along the waveguide. This light-matter interaction can be used to control SP propagation along a waveguide and enable Boolean operations in nano-optical circuits [21].

The overall aim of this thesis is to study plasmon waveguides experimentally and determine optimal geometrical parameters for QD-plasmon coupling. This work will enable the development of future nano-optical circuits and sensing devices. The specific aims of this thesis are as follows:

1.3 Specific aims

1. Conduct a detailed theoretical analysis on QD-gap plasmon interaction (**Chapter 3**). In particular, the effect of gap waveguide dimensions, QD-waveguide distance and symmetry and asymmetry of the waveguide on QD-plasmon interaction.
2. Experimental realisation of two excitation techniques used in exciting plasmons on a nanoscale metal stripe waveguide. In particular, excitation using gratings and excitation using scattering of light from waveguide end (end coupling) will be discussed (**Chapter 4**).

3. Imaging plasmon propagation on a stripe waveguide using QDs. In particular, QD-waveguide distance and polarisation of the excited QDs will be determined (**Chapter 5**).
4. Plasmonic refractive index sensor consisting of an evanescently coupled stripe waveguide system. Sensitivity of this design will be analysed using sucrose solutions (**Chapter 6**).

1.4 Thesis outline

This thesis begins with a background literature review (**Chapter 1**) explaining why plasmonics is a potential candidate in nano-optical circuitry and sensing. The literature review (**Chapter 2**) begins with an overview into the basic plasmon properties, plasmon excitation techniques, methods to detect and image propagating plasmons, applications of plasmonics, plasmonic waveguide structures, controlling the plasmon propagation on a waveguide using QDs and fabricating plasmon waveguides.

QD-plasmon interactions are explored in Chapter 3 of this thesis (Aim 1). **Chapter 3** of this thesis is focused on optimising the Quantum Dot (QD) plasmon interaction in a gap waveguide. We theoretically studied the effect of gap waveguide dimensions, QD-to-waveguide distance, symmetry and asymmetry of the surrounding dielectric media and sharpness of the gap edges on QD-gap plasmon interaction.

The next Chapter of the thesis is devoted to exploring methods of exciting plasmons on a waveguide (Aim 2). Surface plasmons cannot couple with light travelling in the adjacent media due to wavevector mismatch [6]. Special optical arrangements can be used to increase the wavevector of the incoming light to facilitate the coupling. **Chapter 4** of this thesis is focused on exciting a bound long range SP mode on a nanoscale stripe waveguide. We will be comparing the efficiencies of two excitation

techniques used to excite plasmons on the waveguide. The two excitation techniques used are grating coupling and edge coupling using a highly focused laser beam.

Monitoring of the plasmon propagation is explored in Chapter 5, (Aim 3). If quantum dots are placed in proximity to a waveguide, propagating plasmons can excite the QDs. These QD emissions can be used to image plasmon propagation on a waveguide. The intensity of the QD emission is proportional to the strength of the Electric field at the QD's position. In the vicinity of a metal, QD photoluminescence (PL) also depends on the distance of the QD to the metal surface. The emitter must be placed sufficiently far from the surface to reduce the QD PL quench due to ohmic losses in the metal. Optimising this distance to observe bound plasmon propagation on a nanoscale stripe waveguide is discussed in **Chapter 5**.

Finally, a working plasmonic device is developed using the plasmon waveguides and excitation techniques. Due to the plasmon's high sensitivity to the surrounding dielectric medium, plasmons can be used for sensing. This sensitivity of the plasmon to the surrounding environment is used to design a plasmonic refractive index (RI) sensor. We were able to fabricate a highly compact RI sensor with a high sensitivity using stripe waveguides (Aim 4). Our design consists of 3 stripe waveguides, with two outer arms evanescently coupling with the input arm (**Figure 1.3**).

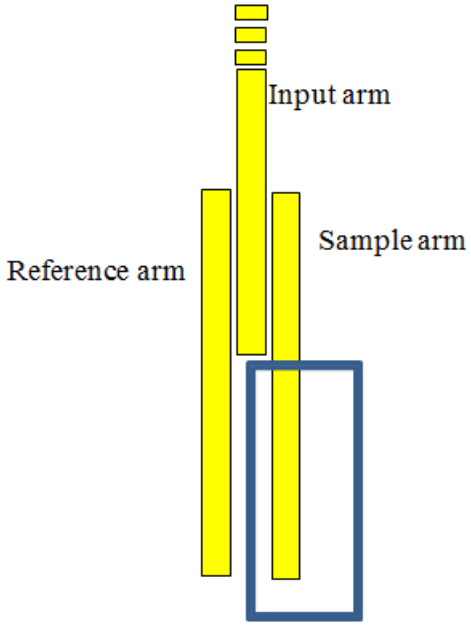

Figure 1.3 Schematic diagram of the plasmonic refractive index sensor design used in Chapter 6. Sample solution is confined inside the blue box shown.

This sensor can measure the refractive index change of a sample by measuring the output intensity in one arm. The wavenumber of the propagating wave changes when propagating in different dielectric media, resulting in a change in the output intensity at the end of the waveguide. Results and analysis are included in **Chapter 6**.

The thesis concludes with a discussion of the outcomes of the six papers presented for examination. **In particular, for the first time, bound long range plasmons on a nanoscale metal stripe waveguide were excited in the visible region and the plasmon propagation visually observed over a 50 μm distance.** The outcome of this work will be beneficial for the development of passive plasmonic devices based on stripe waveguides. As an example of the benefits of these waveguides for passive plasmonic devices, **a highly compact plasmonic RI sensor using two coupling stripes has been experimentally achieved** with a resolution of 2×10^{-4} RIU (refractive index unit) per relative intensity change in the sample arm. Finally, the

theoretical investigation into QD-gap plasmon interactions will prove beneficial in plasmon propagation control in future plasmonic circuitry.

Chapter 2: Literature Review

2.1 The surface plasmon

Surface plasmons (SPs) are collective oscillations of free electrons predominantly existing on metal dielectric interfaces (**Figure 2.1**). They are useful, primarily because plasmons enable confinement and routing of light on a nanoscale level. This cannot be achieved using conventional optics due to the diffraction limit [2, 7].

In the low frequency region (microwave and far infrared frequencies) only a negligible fraction of the impinging electromagnetic waves penetrates into the metal. With increasing frequencies towards near infrared and visible part of the electromagenetic spectrum, field penetration into the metal increases increasing dissipation. At the ultraviolet regime, electromagnetic waves are allowed to penetrate the metal. The strong frequency dependency of the optical properties of the metal can be explained using a complex dielectric function. The complex dielectric constant of free-electron like metals (ε) can be expressed as [3, 6]

$$\varepsilon(\omega) = 1 - \frac{\omega_p^2}{\omega^2} \qquad \textbf{(2.1)}$$

where ω_p is the plasma frequency of the free electron gas, and ω is the angular frequency of the incident light. At the low frequency region when the frequency range is below the plasma frequency ($\omega < \omega_p$), metals retain their metallic behaviour. At this region the real part of the dielectric constant becomes negative.

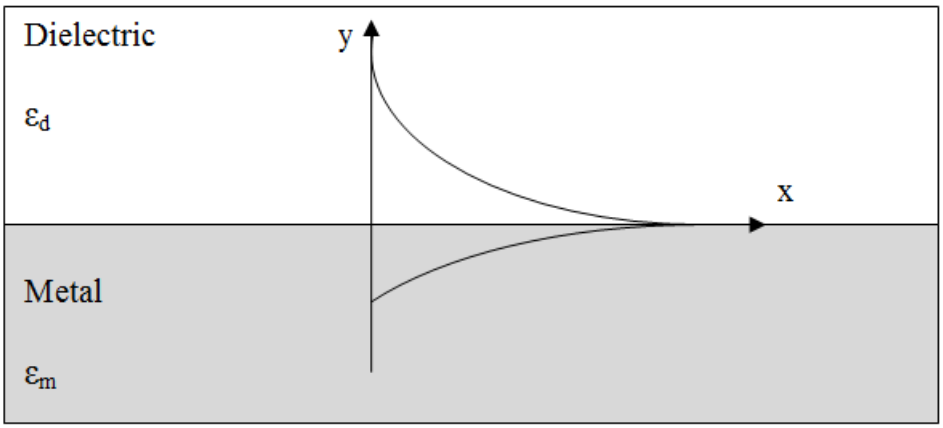

Figure 2.1 Schematic representation of SP on a metal-dielectric interface. The SP is propagating along the *x* direction, and its electric field is evanescently decaying along *y*.

SPs are transverse magnetic (TM) waves in nature with only one non-zero magnetic field component perpendicular to the surface. The behaviour of the magnetic field of the SP in the two media can be well explained using Maxwell's equations [6]:

$$\frac{\partial^2 H_{d,m}}{\partial x^2} + \frac{\partial^2 H_{d,m}}{\partial y^2} + \frac{\omega^2}{c^2}\varepsilon_{d,m} H_{d,m} = 0 \qquad \textbf{(2.2)}$$

where H is the z component of the magnetic field, c is the speed of light, ε is the permittivity and ω is the angular frequency. d, m subscripts denote the isotropic media in contact (dielectric and metal). The dispersion relationship can be derived from the above equation using conventional boundary conditions at the metal-dielectric interface. Using the above method, the wavenumber of the SP, k is

$$k = \frac{\omega}{c}\sqrt{\frac{\varepsilon_m \varepsilon_d}{\varepsilon_m + \varepsilon_d}} \qquad \textbf{(2.3)}$$

If ε_m is negative and larger in magnitude than ε_d, k is positive and real. This is known as the existence condition for the SP and is the reason why SPs can be supported by metal-dielectric interfaces.

Let's assume the SP is excited by an incoming electromagnetic wave travelling through the dielectric. The wavenumber of the electromagnetic wave, k_d travelling in the dielectric medium is given by

$$k_d = \frac{\omega}{c}\sqrt{\varepsilon_d} \qquad \textbf{(2.4)}$$

When the SP existence condition is satisfied, k is larger than k_d which leads to a mismatch between the wavenumbers of the SP and light travelling in the adjacent medium. This means that SPs cannot leak into light waves travelling in adjacent dielectric medium and SPs cannot be simply excited by shining light on a metal surface (**Figure 2.2**).

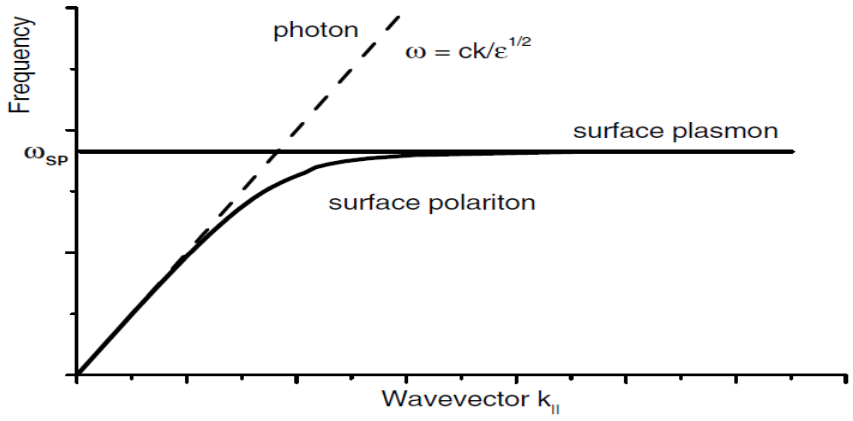

Figure 2.2 Dispersion of SPP on a metal surface. Light line and SP dispersion are also shown [3]

Wavevector mismatch between incoming photons and SPs on the metal-dielectric interface can be eliminated using special optical arrangements. These arrangements increase the incoming photon wavevector. When the wavevectors match with each other, incoming photons can couple with SPs and propagate along the interface. The

term Surface Plasmon Polariton (SPP) is used for propagating plasmons. It is a mix of excitation of SP and propagating photon.

2.2 SPP excitation and detection techniques

There are several techniques to increase the wavevector of the incoming photon to excite SPPs. Some of these include phase matching using Attenuated Total Reflection (ATR), excitation via a focused laser beam, and locally exciting SPPs using a scanning near-field microscope.

The simplest technique to excite SPPs is using a rough metal surface. If the surface is rough, SPP excitation can be achieved using light diffracting from the surface feature as the near field of such diffracted photons include all wavevectors (**Figure 2.3**). Since the roughness is irregular, efficiency of this technique is unpredictable and low.

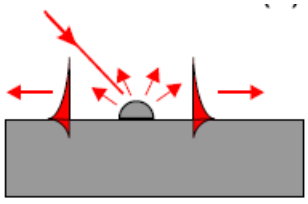

Figure 2.3 Light diffraction due to surface defect [3]. Diffracted light consists of photons with broad wavevector range. Some of these photons can couple with SPs on the metal.

The ATR technique has a much higher efficiency. There are two types of ATR techniques. One is Otto geometry and the other is Kretschmann geometry. Kretschmann geometry is used for thin metal films [**Figure 2.4 (a)**]. An incident wave travels through the prism at an angle of incidence greater than the angle of total internal reflection and illuminates the film. The photon wavevector is increased inside the glass. At a certain incident angle θ, the in-plane wavevector of the photon inside the prism matches with the SPP wavevector at the metal-air interface, at this point light will tunnel through the thin metal film and generate the SPP.

$$k_{SP} = \frac{\omega}{c}\sqrt{\varepsilon_{prism}}\sin\theta \qquad \textbf{(2.5)}$$

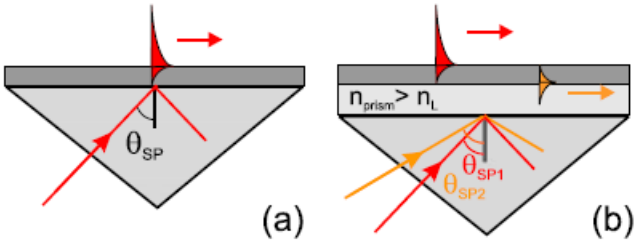

Figure 2.4 (a) Kretschmann geometry and (b) two-layer Krestchmann geometry [3] used to excite SPPs on a thin metal film

The photons can be coupled to SPPs with a very high efficiency with this technique. The efficiency of this method decreases with the increase of the metal thickness; this is because the tunnelling efficiency decreases with increasing thickness. By using a dielectric layer with refractive index less than that of the prism sandwiched between prism and metal, it is possible to excite SPPs on the inner metal interface [**Figure 2.4 (b)**]. In this two layer Kretschmann geometry inner and outer surface of the metal film can be excited at different incidence angles.

For a thick metal film, SPPs are excited using Otto configuration (**Figure 2.5**).

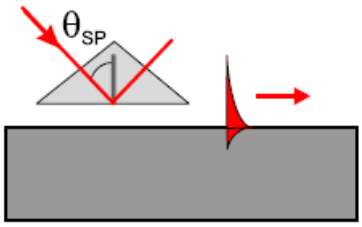

Figure 2.5 Otto geometry [3] used to excite SPPs on a thick metal film.

In the Otto excitation method, an incoming photon has an angle of incidence greater than the angle of total internal reflection at the prism-air interface. This provides an evanescent wave at the bottom of the prism and a reflected plane wave inside the prism.

The evanescent wave (also known as the tunnelling wave) can excite SPPs on the metal surface. Prism coupling techniques are efficient but due to prism configuration, it makes the system bulky. Therefore, these techniques are not overly useful in manufacturing miniaturised all-optical circuits.

An alternative method to excite SPPs is to use grating coupling. A diffracted photon from the grating with a wavevector matched to that of the SP on the metal-dielectric interface can couple into SPPs. Light shines onto a grating with a periodicity of *a* such that *k* will be matched to that of the SP (k_{sp}) (**Figure 2.6**). The mismatch between wavevectors can be eliminated by phase matching whenever the condition

$$\beta = k\sin\theta + vg \qquad \textbf{(2.6)}$$

is fulfilled, where β is the wavenumber of the plasmon, $g = 2\pi/a$ with $v = 1,2,3,\ldots$

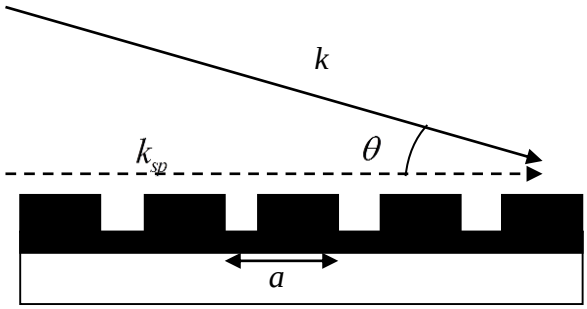

Figure 2.6 Phase matching of light to SPPs on a metal surface using grating coupling

The efficiency of the grating coupling can be increased by optimising the grating periodicity so that the majority of the diffracted light obtains the additional momentum needed to couple with the SPPs on the interface. Grating coupling is used in experimental work presented in this thesis under **Chapter 4.**

SPPs on a metal-dielectric interface can also be excited locally using a Scanning Near-Field Optical Microscope (SNOM). A SNOM tip consists of a fibre tip with subwavelength aperture. As shown in **Figure 2.7** light diffracted on the aperture has a broad range of wavevector distribution allowing phase matching excitation of SPP at subwavelength precision. Dual probe SNOM can excite SPP using one probe and detect SPP using the other probe. SNOM SPP detection will be discussed further in **Section 2.3**.

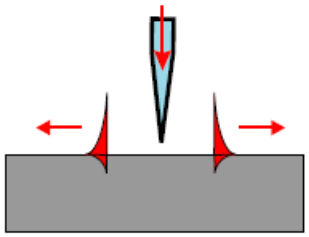

Figure 2.7 Locally excite SPPs on a metal surface using SNOM tip [3]. Light transmitted through the aperture consists of photons with broad wavevector range allowing locally exciting SPPs.

Excitation of SPPs is only part of the experimental problem. Once the SPPs are excited, methods for detecting and monitoring the SPP as it propagate need to be established.

2.3 Detection and imaging of SPP

The propagating SPs cannot outcouple directly to freely propagating light due to wavevector mismatch. The simplest way to detect SPPs is to capture the plasmon outcoupling to radiated light, which can occur when the SPP strikes a surface defect or discontinuity [3, 22, 23]. If the surface is rough, an excited SPP can radiate in to adjacent dielectric medium due to light diffracting from the surface feature. The near field of such diffracted photons consist of all wavevectors. Also, SPPs propagating on a fabricated waveguide can outcouple from the end of the waveguide due to discontinuity of the metal surface at the end. In experiments presented in this thesis

Chapter 4 and **Chapter 6** used outcoupling light from waveguide end to detect SPP propagation on a waveguide.

Other methods to detect SPP are; using Leakage radiation (LR), Photon Scanning Tunnelling Microscopy (PSTM), Scanning Near field Optical Microscopy (SNOM), Quantum Dots (QDs) and fluorescent dyes.

Leakage radiation (LR) can be explained using the dispersion curve of SPPs excited at the metal/air interface of a perfectly smooth metal (**Figure 2.8**). The wavevector of the photon travelling in air (k_0) is lower than that of an SPP on the metal/air interface ($k = n_{air}\,\omega/c$). Therefore, SPPs do not radiate into air due to wavevector mismatch. However, if the metal is supported by a higher index substrate (n_s), SPP wavevectors lying in the region $k_0 < k < k_0 n_s$ can radiatively be lost into the substrate. This is known as the Leakage radiation (LR).

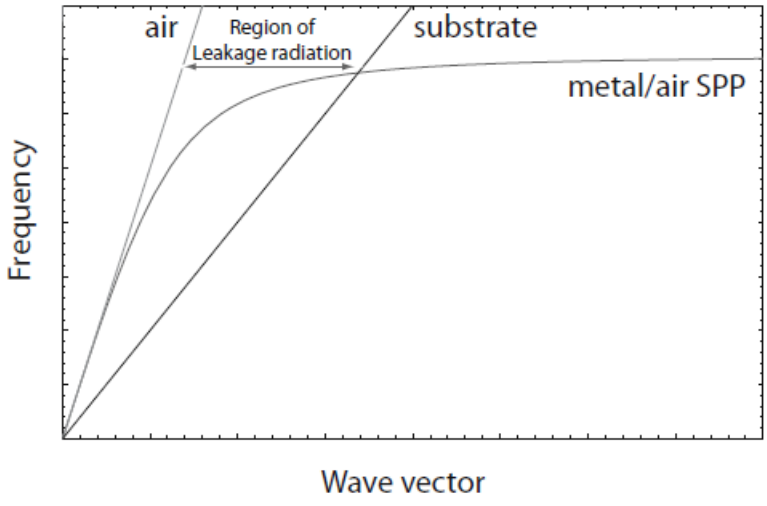

Figure 2.8 Generic dispersion relation of an SPP at a metal/air interface. LR into the substrate occurs at the region enclosed by the light lines in air and in higher index substrate [6].

Leakage radiation is another loss channel in addition to inherent absorption loss inside the metal. The leakage radiation cone in **Figure 2.8** (region of leakage radiation) can be used to image the SPP.

In prism coupling configuration as described above, the total internal reflection of the incoming photon has the in-plane momentum sufficient to excite SPP at the metal/air interface via tunnelling. SPPs with propagation constants between lines of light travelling in air and in higher index dielectric (prism) excited by this method are *leaky waves* i.e. lose energy due to leakage radiation into the prism. The observed reflected beam has a minimum at the SPP excitation angle due to destructive interference of the reflected beam with the LR.

In a variant to the prism coupling, Bouhelier and Wiederrecht developed a technique to excite SPP using a highly focused laser beam and to detect SPPs propagating along a thin metal film on glass using leakage radiation [24]. They used a high numerical aperture oil-immersion microscope objective to focus broad spectrum light on to the sample. Incoming light through the high numerical aperture objective has a large angular spread such that some angles are greater than the critical angle at glass/air. The sample is in contact with the objective via index matching oil. Incoming light can couple with the SPP via phase matching at the metal/air interface.

If the metal film is sufficiently thin (~ 50 nm) and placed on a glass substrate, the SPP modes become leaky and radiate into the glass as leakage radiation [25]. The excited SPPs radiate back into the glass substrate as leakage radiation. LR can be collected using the same objective. Since the emission angle of LR is higher than the critical angle in the glass substrate, index-matched oil is used to avoid the total internal reflection at air/glass interface (**Figure 2.9**). LR is radiated at an angle θ_{SPP} w.r.t. the

normal of the interface. At this angle, phase matching is available between LR in the glass and the SPP on the metal-air interface [26];

$$k_{SPP} = nk_0 \sin\theta_{SPP} \quad \textbf{(2.7)}$$

where k_{SP} and nk_0 refers to the wavevectors of the SPP and LR respectively.

Detected LR at a given lateral position contains useful information about the SPP as it travels at the opposite interface. At every point along the SPP propagation direction phase and strength of the LR electric field are proportional to the electromagnetic near field of the SPP on the metal-air interface.

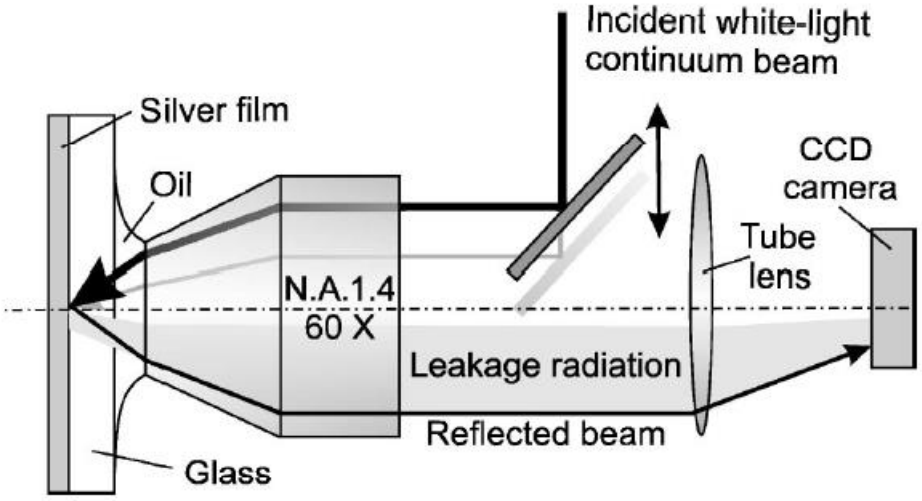

Figure 2.9 Schematic of the excitation of a white-light continuum of SPPs and their observation through detection of the leakage radiation with an index-matched oil-immersion lens **[24].**

In experiments, we use a bound SP mode propagating on a waveguide as bound modes are necessary for the strong plasmon confinement needed in miniaturised optical circuits. Therefore, LR was not used in this thesis.

One of the alternatives to LR is Photon scanning tunnelling microscopy (PSTM). PSTM is another one of the popular methods used in detecting SPs directly [27-29]. PSTM was invented by Reddick et al. in 1989[30]. PSTM operation is based on the frustrated evanescent field. Total internal reflection occurs on the surface of the sample

and a fibre tip scans over the surface. Tunnelled photons can be collected at the other end of the tip for analysis. The spatial resolution of PSTM depends mainly on the aperture size of the tip. PSTM offers detailed information on surface plasmon penetration depth by scanning the sample while varying the tip to surface distance and measuring the SP intensity locally. The same method is applied to determine the SPP propagation distance.

Another very accurate SPP detection method is Scanning Near-field Optical Microscopy (SNOM) [31, 32]. The idea of SNOM was first proposed by Edward Hutchinson Synge in 1928. SNOM is also categorised under scanning probe microscopes and operates in a similar way to the PSTM. When a sample interacts with light, it creates near field and far field light components. Far-field light is utilised in conventional optical microscopy. The evanescent field consists of a tightly localised field confined near the sample surface (near field). The confinement of this field is less than a single wavelength of light. This evanescent field contains high spatial frequency information and the amplitude of the near field is highest at the first few nanometers from the object surface. This evanescent field decays exponentially away from the surface. SNOM probe is able to utilise the evanescent field before it undergoes diffraction. The tip of the SNOM must be kept very close to the near-field zone in order to collect the evanescent field. SNOM probe is available with an aperture at the end of the tip (aperture mode) or with a sharp tip without an aperture at the end (apertureless mode). Aperture mode is more popular as it is convenient to set up and understood well. Surface plasmons can be imaged by raster scanning the probe tip over the waveguide.

SNOM is the most powerful technique to image SPP to date. However, it is expensive, and time consuming to set up. Lower resolution far field detection can be less

expensive, easier to implement and more straightforward to interpret. Use of quantum dots and fluorescent dyes homogeneously distributed in the immediate vicinity of a waveguide is a convenient way to image SPP propagation along a waveguide [19, 28, 33-36]. When a dye or QDs are placed in proximity to the waveguide surface, the plasmon generated electromagnetic field can interact with the dye molecule/QD making them fluoresce. Schematic excitation of QDs by plasmons is shown in **Figure 2.10** below. Intensity of the dye/QD luminescence is proportional to strength of the plasmon field at that point. Distance between dye molecule/QD to waveguide surface must be carefully manipulated. Fluorescence rate of a dye molecule/QD becomes a function of the metal surface to molecule/QD distance [37]. If dye molecules/QDs are located very close to the metal waveguide, non-radiative losses become dominant and quench the luminescence. If they are placed too far away from the tail of the evanescent field, plasmon mediated electromagnetic fields can't interact with dye molecules/QDs hence emitting intensity is lower.

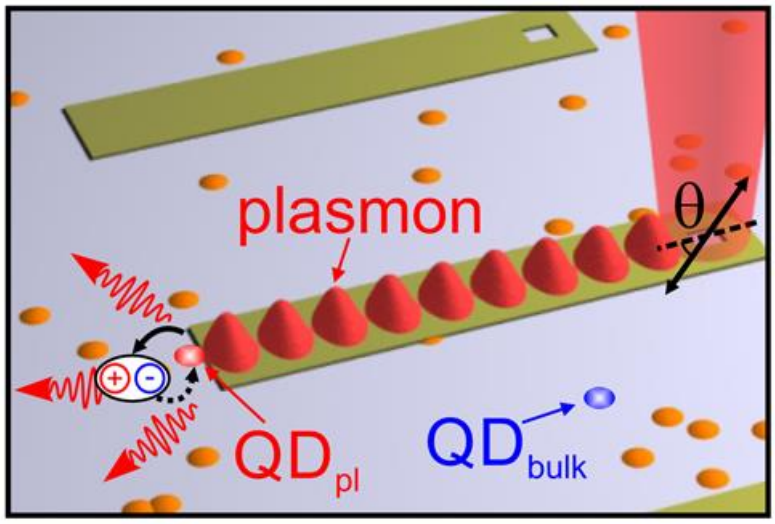

Figure 2.10 Schematic representation of QD excited by propagating plasmons on the waveguide [38]. QD_{bulk} denotes the QDs spatially displaced from the waveguide, QD_{pl} denotes the QDs in the immediate vicinity of the waveguide fluoresce interacting with the plasmon mediated electric field and θ represents the polarisation angle of the incoming light.

Kaniber et al have imaged SPP propagation on a lithographically defined gold (Au) waveguide on GaAs substrate coated with InGaAs QDs [38]. Wei et al. used QD based imaging to image plasmon propagation of interferometric logic gates developed using Silver (Ag) nanowires (NWs) [34]. QD emission images for the Ag NW logic gate are shown in **Figure 2.11** below.

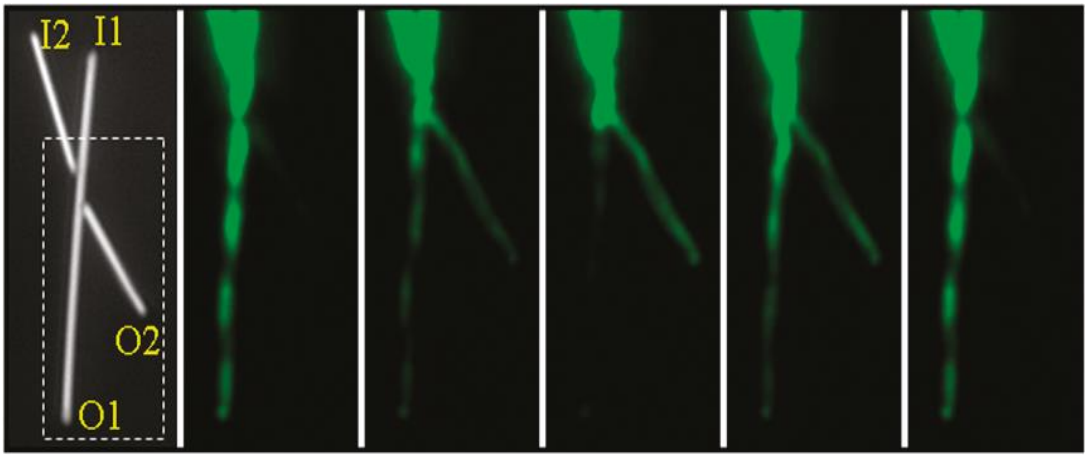

Figure 2.11 (a) SEM image of a Ag NW logic gate (b) – (f) QD emission images of the logic gate in operation. I1 and I2 are input channels. O1 and O2 are output channels [34].

Fluorescence bleaching can occur due to decomposition of dye molecule after a certain number of absorption/emission cycles. [33]. Bleaching can be minimised by using a low power excitation laser. However, it can also be used for imaging. Solis et al. used fluorescence bleaching to image SPP propagation. This novel imaging technique is named Bleached Image Plasmon Propagation (BlIPP) [39]. In simple terms, this technique is a destructive technique which allows one to image the plasmon propagation utilising the photobleaching behaviour of photoluminescent dye molecules. First, MEH-PPV dye was coated on silver nanowires (NWs). SPPs generated on the NW interact with dye molecules causing it to fluoresce. When the sample is exposed to a laser with high power for a long time (~9 min), MEH-PPV starts to photobleach due to direct laser excitation at the excitation end and along the NW due to plasmon excitation. As shown in **Figure 2.12** the intensity difference

between the initial image and the photobleached image is constructed into an image called a difference image. Plasmon propagation is most apparent in the difference image.

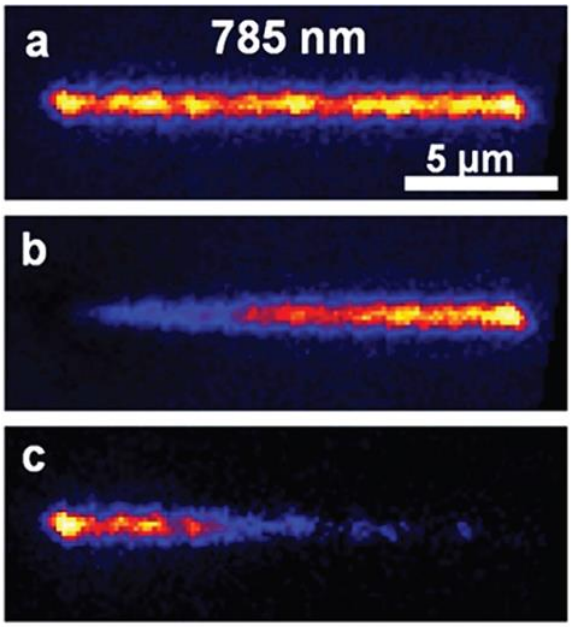

Figure 2.12 (a) Fluorescence image of BlIPP coated nanoparticle chain for 785 nm laser. (b) Fluorescence image of the same NP chain taken after 20 min exposure to laser light and (c) difference image [40].

In this section we discussed using plasmon excited QDs to image plasmon propagation. **Chapter 4** of this thesis involves using QDs to image plasmon propagation on a nanoscale stripe waveguide. The effect of QD-to-waveguide distance is studied in detail in that chapter.

If an optically excited QD is placed in close proximity to a plasmonic structure, spontaneous emission (SE) of this emitter can be greatly enhanced due to increase in Local Density of States (LDOS) or in simple words increase in number of decay channels for SE to decay into. This concept can be adopted to control the plasmon propagation and will be discussed in more detail in **Section 2.7**. The ability to control plasmon propagation is essential in many applications, including nano-optical

circuitry. Theoretical investigation of QDs interacting with plasmons supported by a metal gap waveguide is analysed in **Chapter 3** of this thesis.

2.4 Plasmonics applications

Now that we've established some of the methods for exciting and observing propagating plasmons, let's discuss plasmonic applications. Surface plasmons are collective oscillations of electrons at the metal-dielectric interface. Optical waves can couple into these electrons and the combined exciton forms either localised or propagating surface plasmons. The plasmon resonance mainly depends on the metal dielectric function, dielectric constant of the surrounding medium, size and shape of the nanostructure.

2.4.1 Sensing:

Surface plasmon resonance (SPR) reflectivity measurements can be used to sense the refractive index of the surrounding dielectric medium. Propagating surface plasmons on a chemically functionalised metal surface can be used to monitor the binding molecules to the metal surface. In a typical SPR setup, surface plasmons on a metal film evaporated on a prism are excited in Krestchmann configuration. As discussed in **Section 2.3** at a certain angle (resonant angle), the reflected light has a minimum. At the resonant angle, reflected light destructively interferes with leakage radiation of SPs. The dielectric constant of the metal/air interface changes when molecules are bound to the metal surface. Due to this modification, shift in the resonant angle occurs at the metal/dielectric interface due to binding molecules affecting the SPP propagation or the incident angle of the excitation light. Shift in the angle of the reflected light at SPR is used to measure the dielectric properties of different molecules (**Figure 2.13**).

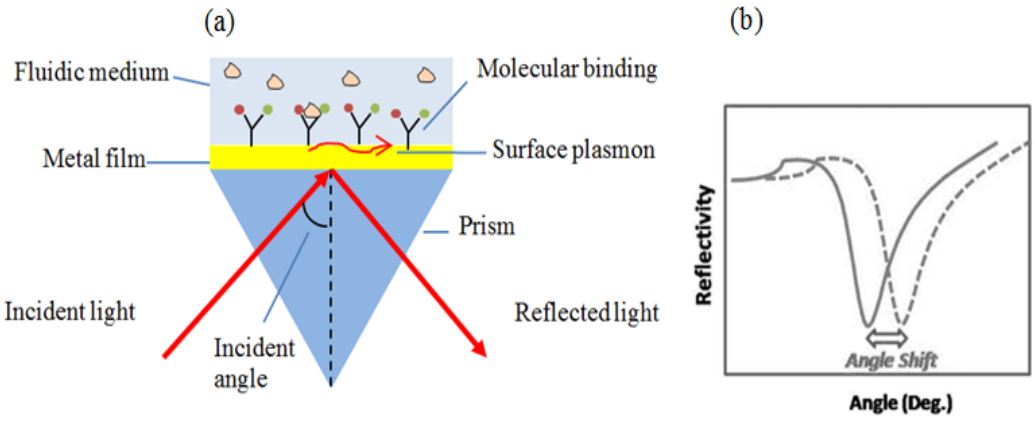

Figure 2.13 (a) Typical SPR setup and (b) Reflectivity vs angle of incidence. Solid line represents the reflectivity measured at metal/dielectric interface before binding molecules and dashed line represents the reflectivity measured after binding molecules. The difference between the angular positions of the dips is often used to define sensitivity.

SPRs of localised SPs are also highly sensitive to the surrounding dielectric media and nanoparticle based SPR sensing is widely used.

Rough metal surfaces are also useful for sensing applications. Electromagnetic (EM) fields near a metal surface increase greatly when an EM wave is incident on a rough metal surface as opposed to a smooth film. This can be explained using two phenomena. First is the concentration of the EM fields at a sharp metallic tip (surface roughness). Second is the excitation of the localised SPs at the metal surface resulting in fluorescence and second-harmonic generation (**Figure 2.14**).

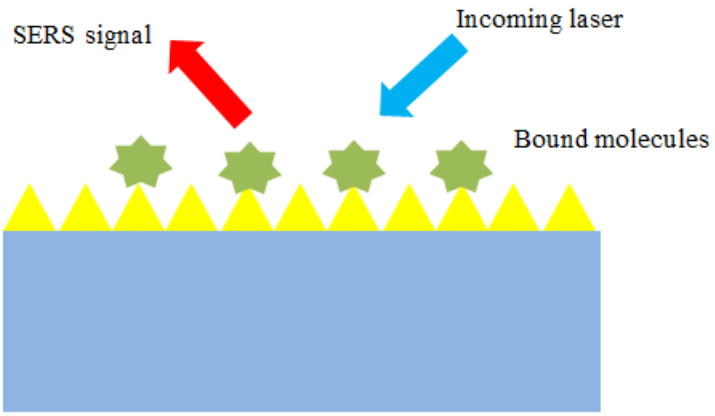

Figure 2.14 Conceptual illustration of SERS setup. Presence of a bound molecule results in strong enhancement in the local near-field intensity.

When a molecule is bound to the roughened metal substrate, plasmons enhance the local near-field resulting in a strong interaction with the molecule. The increase in Raman signal is mainly used in Surface Enhanced Raman Spectroscopy (SERS). SERS signals contain detailed information about the molecular structures bound to the metal surface and are thus useful in identification surface bound molecules.

Propagating SPs on a plasmon waveguide are also highly sensitive to the surrounding dielectric media. Slight modification to the surrounding dielectric media results in change in properties of the propagating plasmons (such as intensity, wavenumber, intensity etc). These properties can be utilised to design a refractive index sensor using plasmonic waveguides. More details about sensing applications are stated under Mach-Zehnder interferometer (**section 2.6**). **Chapter 6** of this thesis is about experimental realisation of such a refractive index sensor based on nano scale stripe waveguides.

2.4.2 Circuits:

As the data rates and component packing density increase in an electronic chip, the electrical interconnectors become increasingly limited by the RC-delay where R is the

circuit resistance and C is the circuit capacitance. A schematic of an electronic interconnect is given in **Figure 2.15**.

Figure 2.15 Schematic diagram of an electronic interconnect. L is the length and A is the cross sectional area of the interconnect

Resistance of an interconnector is proportional to its length (L) and inversely proportional to the cross-sectional area (A) is given by equation (2.8). Capacitance of an interconnector (C) is proportional to its length (L) (equation (2.9).

$$R \propto \frac{L}{A} \tag{2.8}$$

$$C \propto L \tag{2.9}$$

where L is the length of the interconnector and A is the cross-sectional area. Therefore the maximum bit rate (B_{max}) is given by;

$$B_{max} \propto \frac{1}{RC} \propto \frac{A}{L^2} \tag{2.10}$$

We can conclude that electronic components are aspect-ratio limited in speed. On the other hand, the bit rate in optical communication is fundamentally limited only by the carrier frequency with large amount of data carrying capacity. On-chip optical data communication is a promising method to address the above problem [41-43]. Therefore, optical alternatives will be a potential solution for future chips. The conventional optics are diffraction limited in size and tend to be two or three times larger than the nanoscale electronic counterparts. The obvious challenge is to overcome the mismatch

between sizes and interfacing these two technologies. Plasmonics is a promising candidate to circumvent the interfacing issue. This technology enables the manipulation of light in nanoscale areas. By integrating plasmonics into the electronic chip, it is possible to strengthen the chip performances by utilising each technology adequately. Using a photonic integrated circuit has its own benefits such as small size, faster data transmission and the reduced optical power requirement due to strong light-matter interaction. **Figure 2.16** below depicts the current operating speeds and critical dimensions of the different chip technologies.

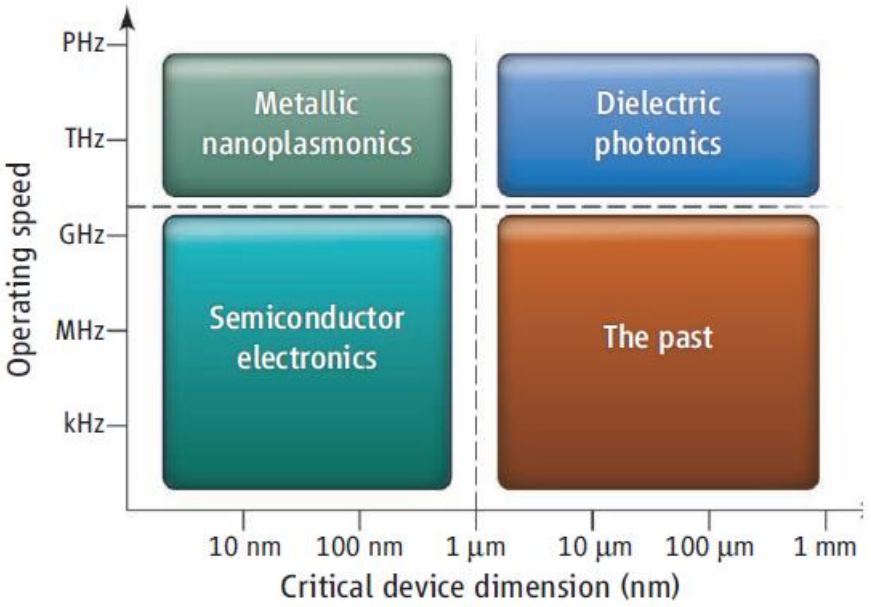

Figure 2.16 Graphical interpretation of operation speed versus critical device dimension of different chip technologies [44]

For an optical circuit to replace all electronic components, it should have three major components to handle light at the vicinity of the nanoscale [45]:

1. An effective method of coupling light in to the circuit (Excitation)
2. An effective method of guiding light around the circuit (waveguides)
3. Active components to control light propagation in the circuit like components able to handle Boolean operations

A schematic of such an optical circuit is shown in **Figure 2.17** below.

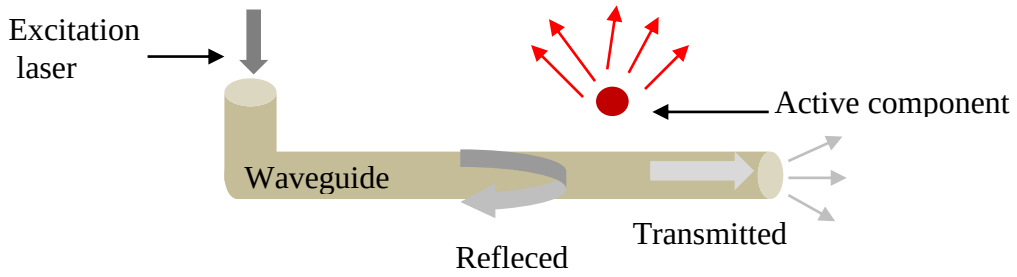

Figure 2.17 Essential optical components of an all-optical circuit

The above three points sum up the overall aim of this thesis. Experimental realisation of a plasmon waveguide for nano-optical applications is discussed in **Chapter 4**. The same chapter discusses and compares two excitation methods.

Chapter 3 theoretically investigates how to control plasmon propagation using QD-plasmon interaction. **Chapter 5** experimentally realises how to optimise the QD-plasmon interaction on a nanoscale stripe waveguide.

A variety of plasmonic waveguide structures have been investigated in the literature with the purpose of using them in on-chip interconnects. These waveguides will be discussed in **Section 2.5**.

2.5 Plasmonic waveguides

SPPs can be confined and routed using plasmonic waveguides. Basic plasmonic waveguide structures are metal slabs, metal stripes, rectangular gaps/ v-grooves cut in a thin metal film or metal wedges (**Figure 2.18**).

Figure 2.18 Basic plasmonic waveguide structures. a) Metal slab, b) metal stripe, c) gap waveguide, d) v-groove waveguide and e) wedge waveguide. All structures shown here are on a glass substrate (blue) with air superstrate (light blue), and metal is shown in yellow colour**.**

Once SPPs are generated on a metal-dielectric interface, the next step is to study the properties of these propagating plasmons in order to use them in applications. SPPs have different properties depending on the waveguide structure they are supported by. Long Range SPP (LRSPP) modes supported by a metal slab have 1D confinement. SPP with 2D confinement can be achieved using 2D plasmonic waveguides. These SPP modes will be extensively discussed in this section.

2.5.1 Metal slab.

SPPs on a flat infinite metal surface are nonradiative and have maximal intensity at the metal dielectric interface. SPP waves decay exponentially away into both the metal and the dielectric medium (**Figure 2.1**). For a metal surrounded by an ideal dielectric medium, attenuation is mainly caused by the free electron scattering in the metal. Interband transitions at the shorter wavelengths and roughness of the surface also increase the attenuation.

A thin metal film buried inside a lossless dielectric medium (Dielectric/Metal/Dielectric or DMD structure) can support single-interface SPP waves on both interfaces. When the thickness of the metal reduces, these two individual SPP waves can couple to form Long-rang SPP (LRSPP) [46]. LRSPP has less attenuation than single interface SPP, therefore can achieve a long propagation length.

The origin of LRSPP can be understood when investigating the modes of a metal slab. Take a metal slab with upper and lower dielectric layers with permittivities ε_{d_1} and ε_{d_2} respectively. ε_m denotes the permittivity of the metal. **Figure 2.19(a)** below depicts the distribution of the main transverse electric field (E_y) of a bound SPP on an infinite metal-dielectric interface. The SPP mode travels in $+z$ direction. In a symmetric thick metal slab (where $\varepsilon_{d_1} = \varepsilon_{d_2}$) there are two individual single interface modes on the upper and lower interfaces. As the thickness (t) reduces these two individual modes couple and form two types of coupled modes travelling in the $+z$ direction. These two modes are purely bound TM modes ($E_x = H_y = H_z$) with only transverse field components E_y and H_x exhibiting symmetric or asymmetric distribution along the x axis. The mode with E_y symmetrically distributed about the x axis is called the *symmetric bound mode* and is denoted by s_b. The other mode with asymmetric distribution of E_y about the x axis is called the *asymmetric bound mode* (a_b). Subscript b denotes that the mode is bound. **Figure 2.19(b)** shows the E_y distribution of a_b and s_b modes.

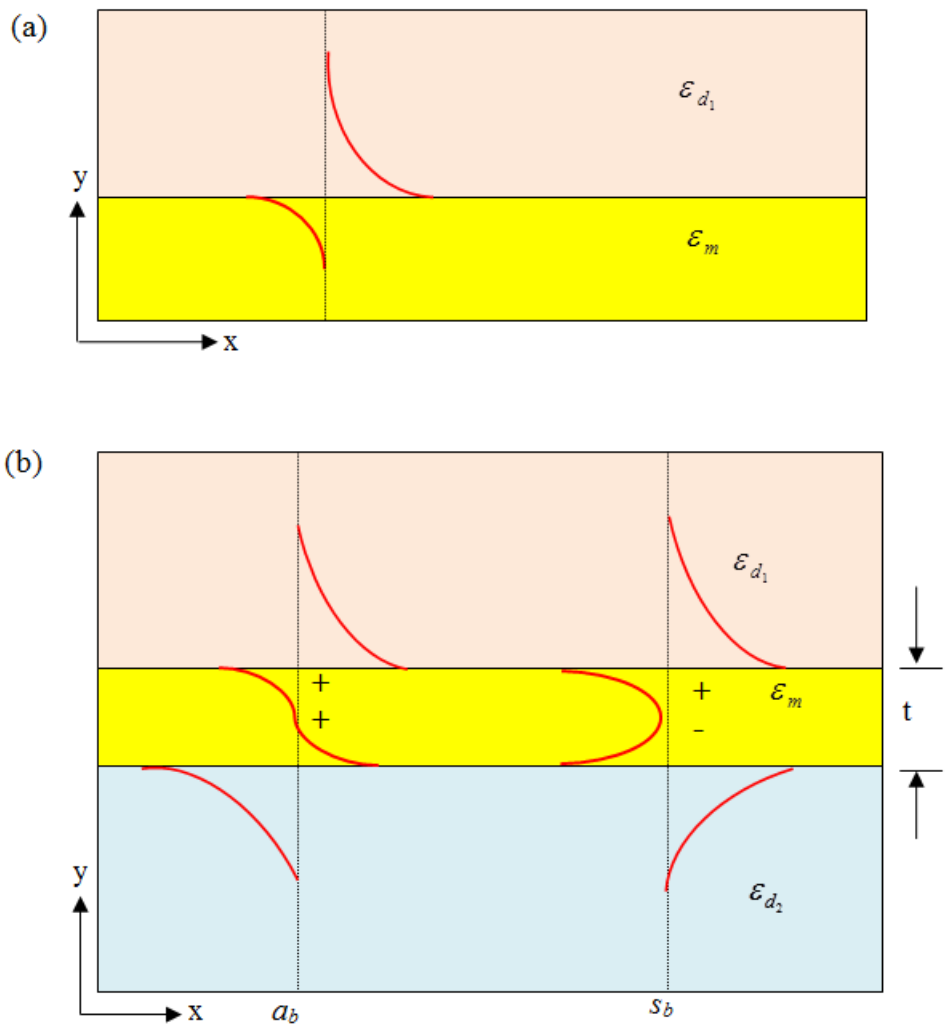

Figure 2.19 E_y distribution of (a) an SPP mode on a metal-dielectric interface. (b) Two bound SPP modes on a metal slab

+ and – terms in **Figure 2.19** describe the charge distribution of each mode inside the metal. In terms of charge distribution across the metal film, s_b has asymmetric charge distribution and a_b has symmetric charge distribution (**Figure 2.20**).

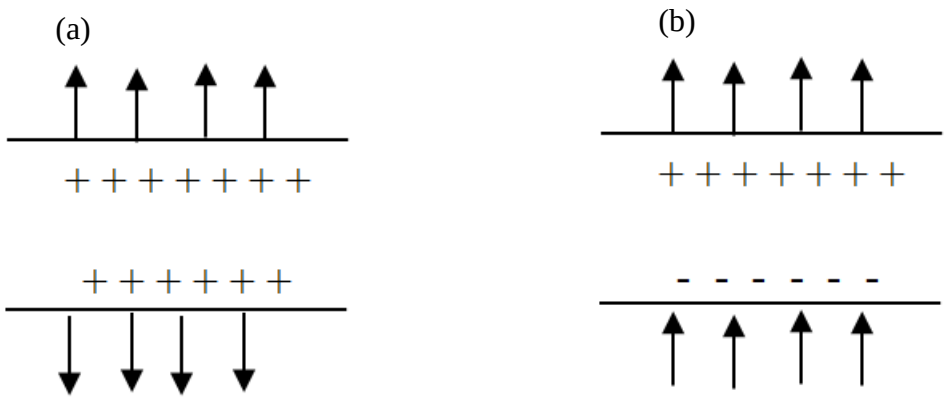

Figure 2.20 The direction of E_z field for a structure with (a) symmetric surface charge distribution (***a*****b*** mode) and (b) asymmetric charge distribution (***s*****b*** mode).

In the asymmetric structure with lossless cladding, the mode is propagating in the $+z$ direction with $e^{-\gamma z}$ where the complex propagation constant of the propagating mode γ is given by,

$$\gamma = \alpha + j\beta \tag{2.11}$$

where α and β are the attenuation and phase constants respectively. Normalised attenuation and phase constants are given by,

$$\frac{\beta}{\beta_0} = \mathrm{Re}\left[\sqrt{\frac{\varepsilon_{r,m}\varepsilon_{r,d}}{\varepsilon_{r,m}+\varepsilon_{r,d}}}\right] \tag{2.12}$$

$$\frac{\alpha}{\beta_0} = \mathrm{Im}\left[\sqrt{\frac{\varepsilon_{r,m}\varepsilon_{r,d}}{\varepsilon_{r,m}+\varepsilon_{r,d}}}\right] \tag{2.13}$$

where $\beta_0 = \omega/c$ is the phase constant of plane waves in free space with c the speed of light in vacuum.

Normalised propagation constant $\left(\gamma_{eff}\right)$ is given by,

$$\gamma_{eff} = \frac{\gamma}{\beta_0} = \frac{\alpha}{\beta_0} + j\frac{\beta}{\beta_0} = k_{eff} + jn_{eff} \tag{2.14}$$

The complex effective index of a mode is given by

$$N_{eff} = -j\gamma_{eff} = n_{eff} - jk_{eff} \tag{2.15}$$

where n_{eff} is the effective mode index and k_{eff} is the normalised attenuation.

The relative complex permittivity $\varepsilon_r = \varepsilon/\varepsilon_0$ with ε_0 as the permittivity of free space is related to refractive index terms n, k via $\varepsilon_r = (n - jk)^2$.

Figure 2.21 below depicts the normalised attenuation and phase constants of a_b and s_b modes supported by an asymmetric metal slab with dielectrics $\varepsilon_{d_1} = 1.5^2$, $\varepsilon_{d_2} = 1.55^2$ and metal as silver with $\varepsilon_m = (0.00657 - j4)^2$

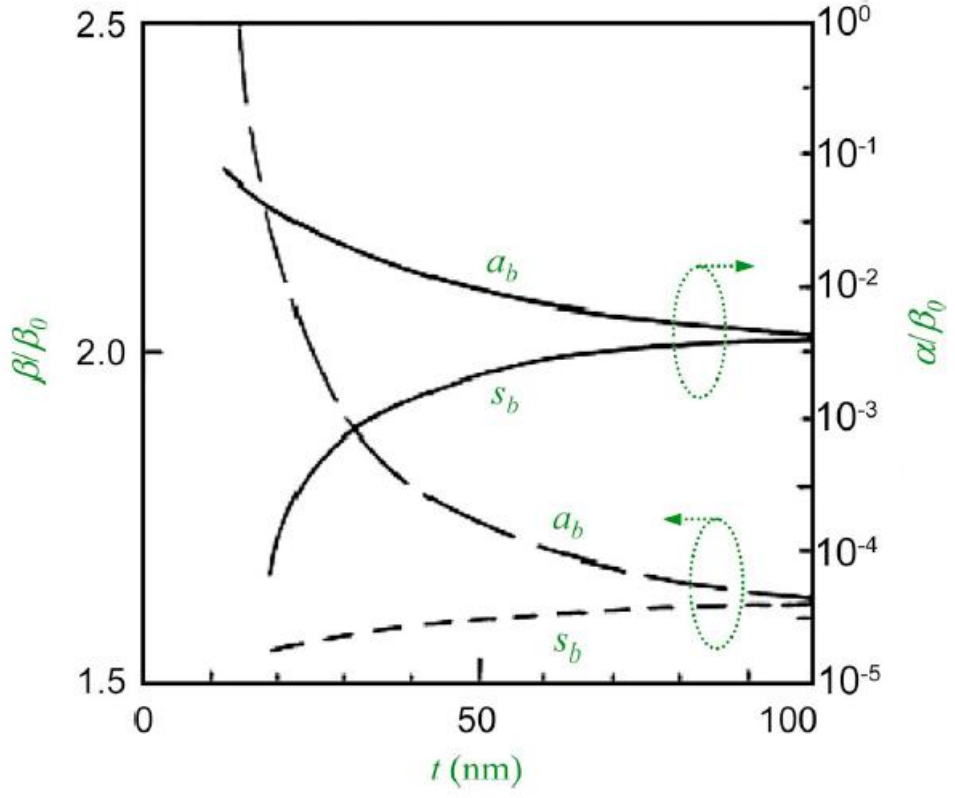

Figure 2.21 Normalised phase and attenuation constants of the a_b and s_b modes supported by an asymmetric metal slab at 633 nm excitation assuming metal as silver and top and bottom dielectrics with refractive indices 1.55 and 1.5 respectively [47].

Attenuation of the SPP fields increases when the fields penetrate more in to the metal. As the thickness of the metal film decreases, phase and attenuation of the symmetric mode decrease (**Figure 2.21**). Therefore, the symmetric SPP mode field penetrates more into the surrounding media than into the metal, increasing the propagation length. Thus the symmetric SPP mode is termed long range SPP. As thickness goes to 0, the symmetric mode slowly evolves into the vertically polarised TEM wave in the surrounding dielectric media. Attenuation and phase of the asymmetric mode increase with decreasing thickness as the SPP fields penetrate more into the metal, decreasing the propagation length [46].

If the metal slab is asymmetric (where $\varepsilon_{d_1} \neq \varepsilon_{d_2}$) when the metal thickness decreases, the s_b mode remains non-radiative only for thicknesses greater than a certain thickness *t*, named as cut-off thickness (refer **Figure 2.21**) which depends on the permittivities of the surrounding dielectrics and metal as well as the operating wavelength of the incoming light. When the thickness increases, the a_b mode becomes the single interface mode on the interface between the higher-index dielectric and metal, while the s_b evolves into a single interface mode on the lower index dielectric and metal interface. LRSPPs on a metal slab are only localised in one dimension. To effectively guide light around a circuit, waveguides with sub-wavelength confinement in two dimensions must be developed. Plasmon waveguides provide sub-wavelength confinement in two dimensions and help to guide light within the circuit. The trade-off between confinement and loss demands a prudent choice of waveguide geometry. To achieve a larger propagation length with a good subwavelength confinement various waveguides have been designed such as the Gap Plasmon Waveguide (GPW), wedge waveguide, metal nano wires, metallic stripes, and V-groove waveguides [5, 21, 48-55].

Each waveguide has its own advantages in routing light in nanoscale areas. Such advantages may include ease of fabrication, unaffected to structural imperfections, single mode operation and guiding light around sharp bends with low loss [20, 56-58].

2.5.2 Stripe waveguides

Metal slab applications are limited due to the 1D confinement of the SPP mode and infinite width. A metal stripe waveguide is more useful for many practical applications. It consists of a metal film with finite thickness and width, and a length on the micrometre scale, submerged in dielectric. Basically a metal stripe is a finite version of a metal slab. Due to these finite dimensions, lateral confinement to the mode is introduced as well as higher order modes with extrema along the width of the stripe (2D field confinement) (**Figure 2.22**). A metal film with finite width (stripe) doesn't have pure TM modes. Every mode contains all six electric and magnetic field components. For symmetric structure with $w > t$, the E_y field component dominates. E_y becomes the dominant component of transverse electric field when $w >> t$. As the thickness increases the E_x field component starts to increase in magnitude and starts to dominate if $w < t$.

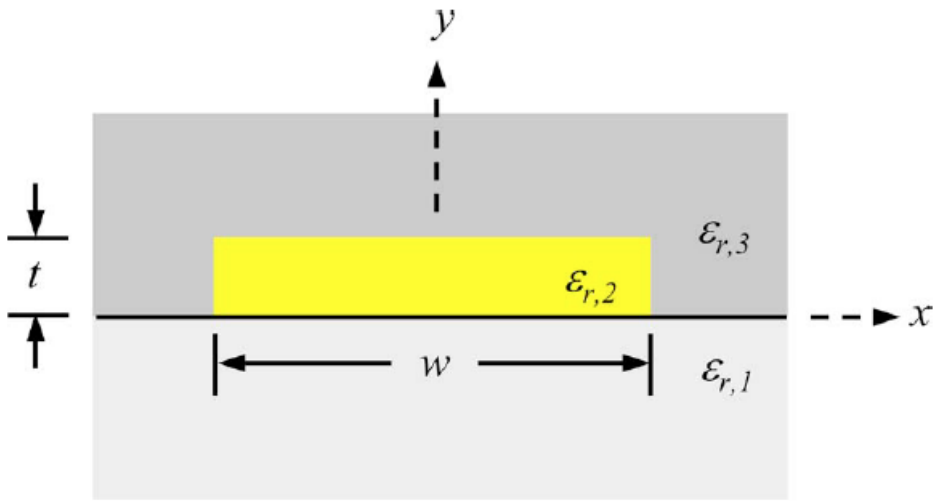

Figure 2.22 Metal stripe with permittivity $\varepsilon_{r,2}$, thickness *t*, and width *w*, surrounded by upper and lower dielectric media ($\varepsilon_{r,3}$, $\varepsilon_{r,1}$). SPP modes are propagate in the +*z* direction (directed up out of the page) [59].

For sufficiently thin metal films, upper and lower bound SPP modes couple due to field tunnelling through the metal forming four **fundamental modes** supported by the metal stripe [46, 60]. These four fundamental modes are labelled as aa_b^0, as_b^0, sa_b^0, and ss_b^0. Notations used in naming the modes are: *a* and *s* refer to asymmetric and symmetric respectively where the first letter is associated with the horizontal dimension and the second letter with the vertical dimension; b represents the mode being "purely bound" and the superscript counts the number of extrema in the horizontal distribution of E_y.

In a stripe with $w >> t$, all four modes have dispersive behaviour with respect to the film thickness hence categorised mainly into lower attenuation modes or higher attenuation modes depending on the field distribution of E_y along the *y*-axis.

Four fundamental modes in a stripe with w = 1μm are analysed in **Figure 2.23**. For very thick films the four fundamental modes are asymptotic and degenerate with an elemental corner mode [61].

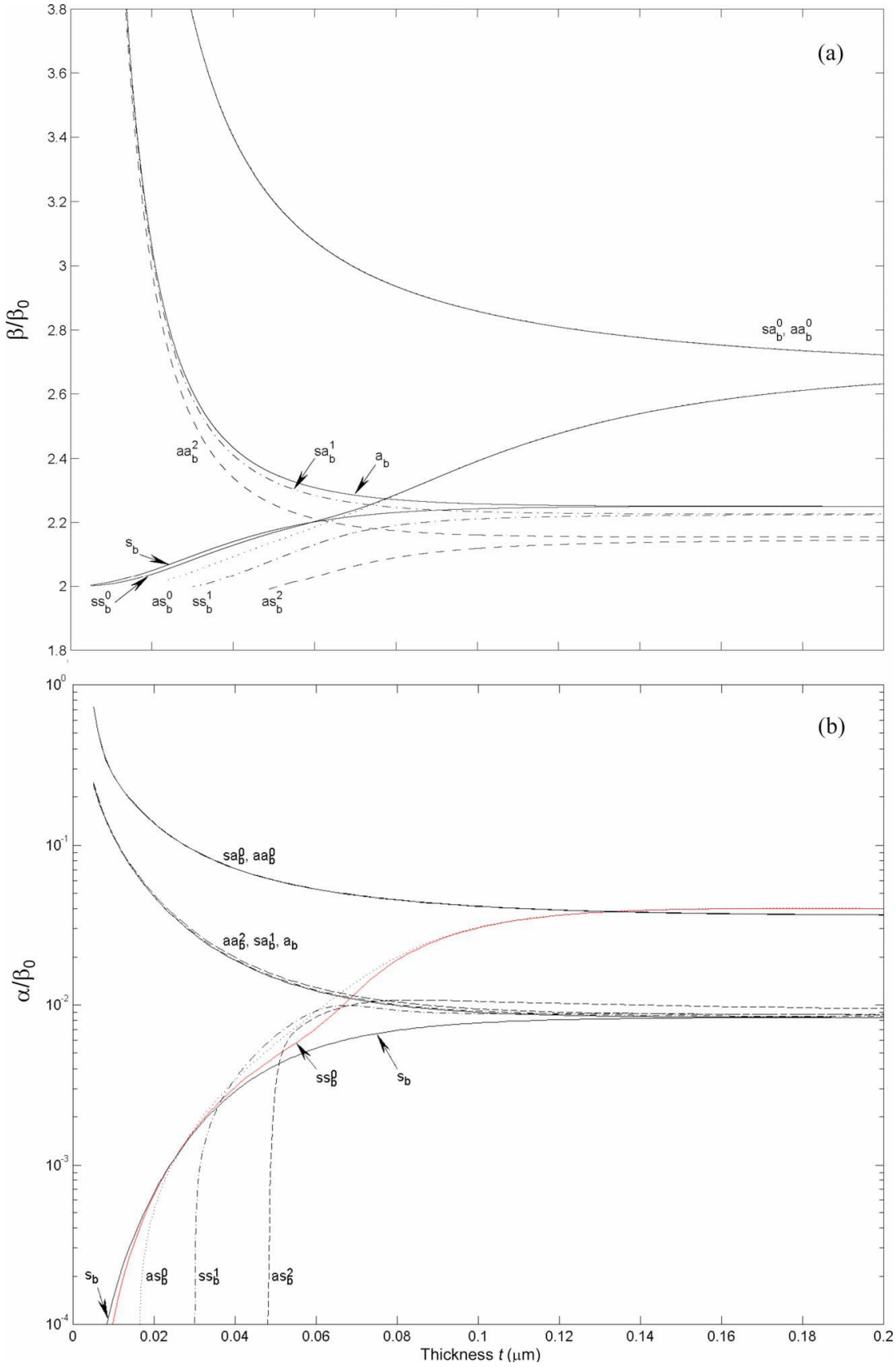

Figure 2.23 a) normalised phase constant and b) attenuation constant of modes supported by the symmetric metal slab with infinite width and finite width (w= 1 μm). The metal is silver and the structure surrounded by PMMA ($\varepsilon_{r,1} = \varepsilon_{r,3} = 4$), and excited using a 633 nm laser [60].

Power confinement factor (CF) is the ratio of mode complex power carried through a portion of a waveguide's cross-section with respect to the mode complex power carried through the entire waveguide cross-section [60].

$$cf = \frac{|\iint_{A_c} S_z ds|}{|\iint_{A_\infty} S_z ds|} \tag{2.16}$$

where A_c is the area of the waveguide core, A_∞ is the integration over the entire waveguide cross-section. S_z is the z component of the poynting vector[60]

$$S_z = \frac{1}{2}\left(E_x H_y^* - E_y H_x^*\right) \tag{2.17}$$

where $H_{x,y}^*$ is the complex conjugate of $H_{x,y}$.

As the thickness of the film gradually decreases, coupling between top and bottom edges increases. Then four modes split into pairs as the upper branch (aa_b^0, sa_b^0) and lower branch (ss_b^0, as_b^0). Upper branch modes have dominant main transverse electric field that shows asymmetry with respect to the *x* axis and its counterpart shows dominant main transverse electric filed exhibiting symmetry with respect to the *x* axis. Consider the symmetric metal stripe comprised of a nanoscale metal stripe,

($\varepsilon_{r,2} = -19 - j0.53$ at 633 nm wavelength) surrounded by a dielectric

($\varepsilon_{r,1} = \varepsilon_{r,3} = 4$). The ss_b^0 mode is one of the fundamental modes supported by this waveguide. This mode evolves into a vertically polarised TEM wave of the background (or a bulk wave in the surrounding dielectric background) as the width and the thickness goes to zero. As demonstrated in **Figure 2.24(a)** and **2.24(c)** using $\mathrm{Re}\{S_z\}$, E_y and H_x fields of the ss_b^0 mode in a thicker stripe waveguide tend to localise near the metal corner. Maxima of these localised modes also occur at the corners with

fields decaying exponentially away from the corners. For very thick and wide metal films, these four modes degenerate with isolated corner mode. As the thickness decreases, the top and bottom edge modes start coupling with each other generating a pair as upper branch (aa_b^0, sa_b^0) with dominant E_y field exhibiting asymmetry with respect to the *x* axis and lower branch (ss_b^0, as_b^0) with dominant E_y field exhibiting symmetry with respect to the *x* axis. With further decreasing of the thickness it has been observed that lower branch modes spread across the stripe cross section with Gaussian-like fields. The E_y field of the ss_b^0 has an extremum near the centre of the interface. The E_y field of the $as_b{}^0$ mode develops two extrema along the *x* axis and becomes leaky below a certain cutoff dimension (*w*, *t*) as *t* goes to zero as shown in **Figure 2.24(a)**. This mode is fundamental for larger *w* and *t* and becomes the first *long-range-higher-order* mode as *t* goes to zero[46].

This behavioural change of this mode as *w*, *t* goes to zero accompanied by reduced confinement and attenuation make this mode the fundamental LRSPP mode of the stripe. Symmetry of the structure is important for the mode to remain purely bound. The Gaussian distribution of the ss_b^0 mode enables efficient coupling via end-fire excitation [46].

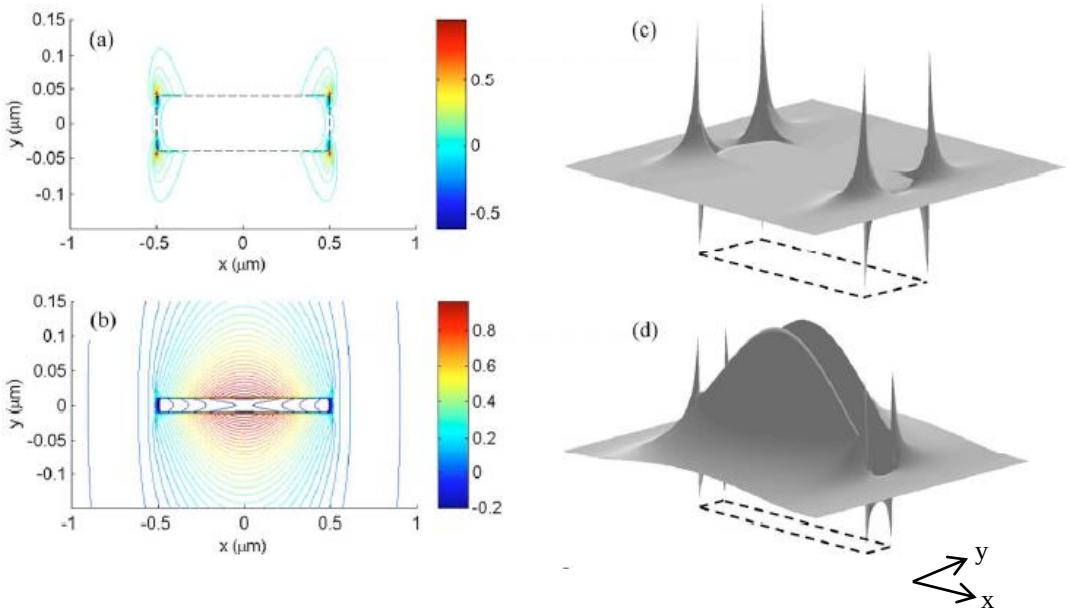

Figure 2.24 Contour and 3D plots of $\mathrm{Re}\{S_z\}$ of the ss_b^0 mode for w= 1μm (a) t= 80 nm, (b) t=20 nm, (c) t=100 nm and (d) t= 40 nm. Other parameters $\lambda_0 = 633$ nm, $\varepsilon_{r,2} = -19 - j0.53$ and $\varepsilon_{r,1} = \varepsilon_{r,3} = 4$. Waveguide cross-section in (c) and (d) are located in the *x*-*y* plane. Figures (a) and (b) are adapted from [60] and figures (c) and (d) adapted from [61]

All the other a_b-like modes (aa_b^m, sa_b^m) remain degenerate for all thicknesses and increase in attenuation as thickness goes to zero. Endfire excitation cannot efficiently excite these modes due to asymmetry in E_y along *x*.

In an asymmetric structure where the dielectric permittivities above and below the metal stripe are different, mode fields exhibit symmetric or asymmetric distributions with respect to the *x* axis. True field symmetries are observed only along the *y* axis. LRSPPs can exist on this structure but only close to cutoff. s_b - like modes are localised along the lowest dielectric/metal interface, and a_b - like modes are localised along the highest index dielectric/metal interface. LRSPP modes are localised on the lower index side with fields extending deeply into the high-index cladding [46].

Bracher et al have studied theoretically and experimentally the plasmon propagation length and polarisation of the SPP travelling on lithographically defined gold stripe

waveguides on GaAs substrate. They measured the plasmon propagation length which ranged from 10 to 40 μm depending on the waveguide width (w= 2-5 μm) under excitation wavelengths 760-920 nm [62]. They also have used proximal self-assembled quantum dots to track the plasmon propagation in an Au stripe waveguide on GaAs substrate [38].

As described earlier, due to the Gaussian distribution of the LRSPP mode in symmetric stripes, end-fire excitation is widely used in exciting LRSPP on stripes. Gratings are more popular as microscale reflectors [63, 64] but specially arranged gratings can provide better coupling to the LRSPP on stripe waveguides than end-fire excitation. Excitation of the bound LRSPP mode on a nanoscale stripe waveguide using highly focused laser beam and grating coupling will be discussed in **Chapter 4**.

Many passive nano-optical devices based on stripe waveguides have been proposed, such as four-port couplers, Y-junctions, S-bends and interferometers[32, 63, 65-67]. Experimental realisation of refractive index interferometric sensor design consisting of nanoscale stripe waveguides will be discussed in detail in **Chapter 5**. Theory of this design will be discussed in **Section 2.6**.

2.5.3 Nanowires

Fabricated metal stripes suffer losses due to scattering from rough surfaces and grain boundaries. Colloidal synthesis of nanowires (NWs) results in nanowire structures with a smooth surface and no grain boundaries. Metallic nanowires are potential candidates for plasmonic waveguiding (**Figure 2.25**) [6, 22]. Chemically synthesised Silver (Ag) NWs are unstable under ambient conditions when exposed to atmosphere. Gold NWs on the other hand are very stable. NWs can be made with high aspect ratios

and structural properties. Most plasmonic NWs have pentagonal cross section with diameter of 100 nm and length range from 10 to 20 μm [6, 22].

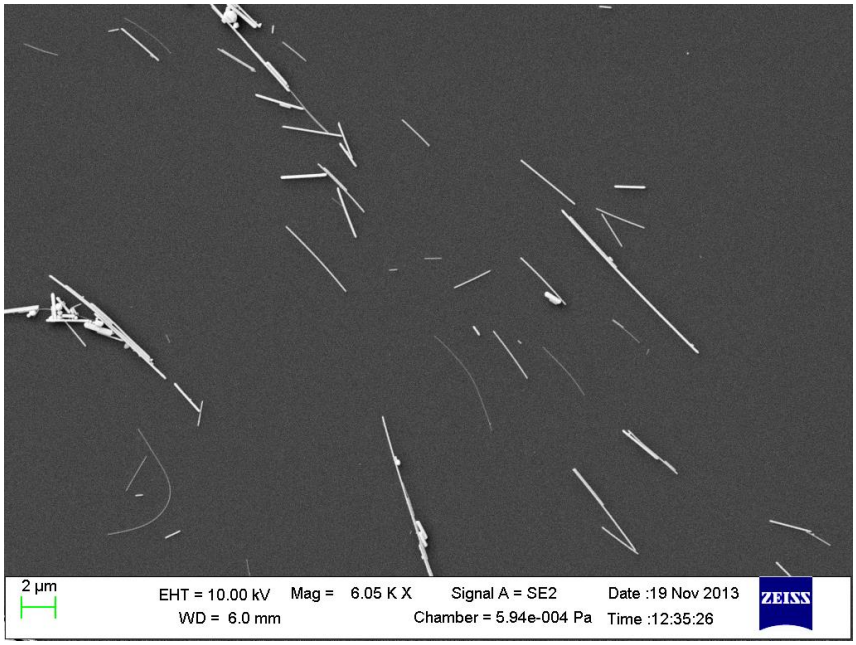

Figure 2.25 SEM image of chemically synthesised Ag NWs spincoated on ITO coated glass. Image obtained by author at QUT.

Propagation length is shorter for gold NWs compared to silver NWs. Particularly in the visible region, gold interband absorption is higher than that of silver, resulting increased optical absorption and hence decreasing the propagation length of SPPs. Propagation lengths and group velocities of gold and silver NWs have been studied by Pelton et al [68]. The group velocity is given by,

$$v_{gr} = \frac{d\omega}{dk_{SP}} \tag{2.18}$$

where v_{gr} is the group velocity, ω is the angular frequency and k_{SP} is the wavenumber of the SP propagating along the NW. Pelton et al. report that propagation lengths for 120 nm diameter gold NWs on a glass substrate covered with PMMA (refractive index similar to glass ~1.48) to preserve the symmetric environment vary from 2.4 μm to 3.6

μm for excitation wavelengths 760 to 860 nm [68]. For silver NWs this varies from 11 to 17.5 μm over the same measured frequency. These results are consistent with the previously reported values with lower wavelengths by Ditlbacher et al with 10 μm for silver NWs at wavelength 785 nm [22] and Link et al with 1.8 μm for gold NWs at wavelength 540 nm [39].

Figure 2.26 shows plasmon propagation on a chemically synthesised Ag NW excited using a highly focused laser beam (excitation wavelength 633nm).

Figure 2.26 Plasmon propagation on a Silver NW excited via 100x oil high numerical aperture objective a) under dark filed microscope. b) without dark field. Red dots along the NW are due to scattering of propagating SPPs from the nanoparticles attached to the NW.NW excitation wavelength is 633 nm. Images obtained by author at Monash University Funston lab.

The energy attenuation of propagating SPPs due to bending of the NW has recently been studied by Weng et al [69]. They have used chemically synthesised silver NWs with diameters from 550 to 800 nm and lengths from 20 to 50 μm. A tapered optical fibre was used to apply pressure at one end of the NW and natural adhesion between NW and glass substrate made it possible to hold one end and bend the other end. Bending loss decreases from 10 to 5 dB with increasing bend radius from 5 to 30 μm [69]. It is also observed that the bending loss of curved NWs increase with increasing

NW cross section. Moreover, energy loss due to dissipation is significant at longer wavelengths.

Even though NWs provide longer propagation lengths than metal stripes, the orientation of NWs is difficulty to control. The difficulty in positioning NWs can make creating optical devices from NWs difficult. However, Wei et al. have demonstrated AND, OR and NOT gates made using a chemically synthesised silver NW network [34]. They have used the fluorescence of quantum dots coated on top of the NW network to image the electric field distribution of the propagating plasmons. QD emission images of this experiment are provided in **Figure 2.11** in **Section 2.3** above. Wei et al showed that the plasmonic binary NOR gate can be realised through cascaded OR and NOT gates in four-terminal NW network [70].

2.5.4 Metal Gap Waveguides

The simplest version of a Metal/Dieletric/Metal (MDM) structure is a gap in a metal slab (**Figure 2.27**). This structure can support a number of optical modes depending on the gap dimensions. When the gap width is sufficiently high, two interfaces contain two individual single-interface SPP waves, where the field magnitude drops exponentially away from the metal surface. As the gap thickness reduces these two individual SPP modes combine into one mode called "gap plasmon mode". Similar to the super modes supported by the DMD (metal slab) structure discussed above, the gap plasmon mode consists of symmetric and anti-symmetric modes depending on the electric field E_y exhibiting symmetric or asymmetric distribution along the x axis. The symmetric mode of the gap plasmon becomes more localised as the thickness is reduced and shows no cut-off for decreasing thickness. Wavenumber of the asymmetric gap plasmon mode increases with the decreasing thickness of the gap. The

electric field distribution of a gap plasmon mode inside the gap is perpendicular to the metal surface or in *y* direction.

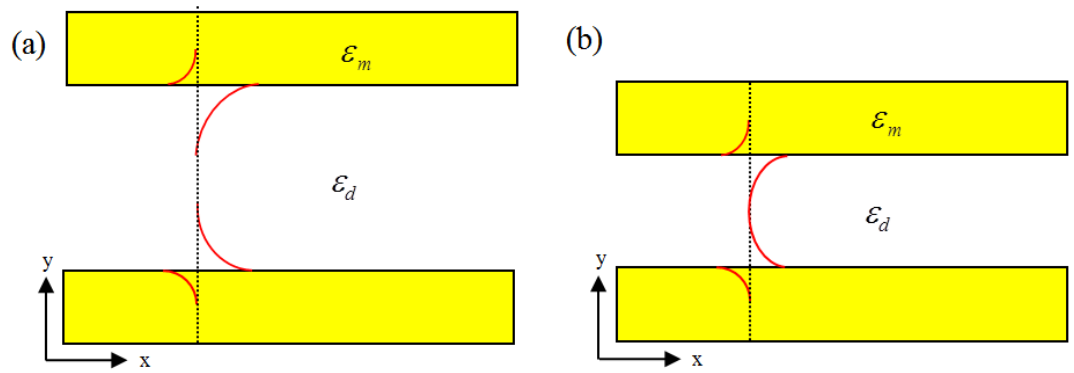

Figure 2.27 Schematic representation of formation of gap plasmons. (a) when the gap width is sufficiently high two interfaces contain two individual single-interface SPP waves, where the field magnitude drops exponentially away from the metal surface. (b) As the gap thickness reduces these two individual SPP modes combine into one mode called "gap plasmon mode". ε_m and ε_d denote the permittivities of metal and dielectric medium respectively.

Gap plasmons are utilised in different gap waveguide structures. A 3D metal gap waveguide was proposed in 2003 by Tanaka et al [21]. A cross-section of this waveguide is shown in **Figure 2.28**. The structure extends into the page.

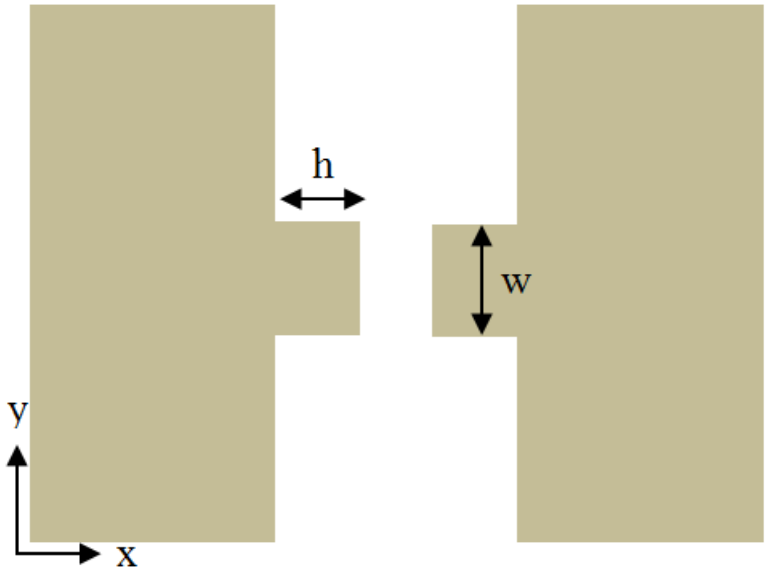

Figure 2.28 Cross-section of a 3D metal gap waveguide with structure extending into the page

Gap plasmons are formed inside the gap. Since the phase-velocity of SPPs is lower in the narrow region than in the wider region, SPPs are confined near the narrow gap region and propagate along the channel.

Wang et. al. in 2004 proposed a similar structure with a slight difference - the metal parts in the centre are composed of different metal from the rest [71]. They call this structure a Metal Hetero Gap waveguide (MHGW). The proposed 3D heterowaveguide had silver inlaid in the central part of the aluminium waveguide (**Figure 2.29**).

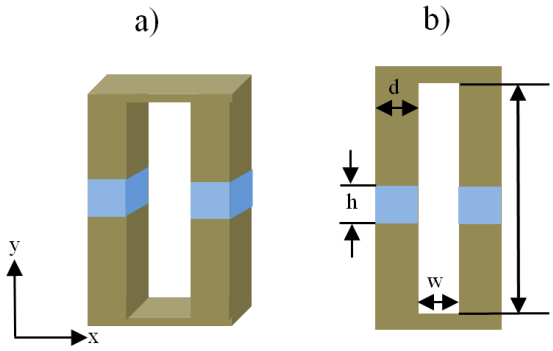

Figure 2.29 a) schematic diagram of a 3D MHGW. Blue regions represent the silver and the light brown represents aluminium, b) cross-sectional view of the MHGW in z plane. w represents the width of the gap, h represents the height of the silver region, d is the width of the Al/Ag

In these waveguides plasmons can be generated using a TM polarised light incident normal to the entrance face of the waveguide. Wang et al modelled the plasmon propagation in the MHWG using finite-difference time-domain (FDTD) method and showed that the plasmons are confined and propagate in the silver region [71].

Modal area of the plasmon mode decreased with decreasing width (*w*) of the waveguide increasing the wavenumber difference between aluminium and silver. Therefore narrowing the waveguide cross section and increasing the refractive index

of the dielectric medium in the gap can increase the plasmon confinement in this structure.

Although 3D MGW and MHWG provide strong subwavelength plasmon confinement they are bulky devices making it difficult to integrate with planar technology. As an alternative to 3D MGW and MHWG, more compact waveguides with smaller bend losses are required. This resulted in the development of Gap Plasmon Waveguides (GPWs).

GPWs consist of a gap in a thin metal film which provides a good subwavelength localisation of the guided mode (**Figure 2.30**). Phase velocities of plasmons that propagate in a nanosized metallic gap strongly depend on the gap width and height [51-53]. This means that by scaling the gap, the phase velocities can be controlled [49]. These waveguides are reasonably easy to fabricate lithographically. It has been shown that using GPWs a propagation length in the micrometer range can be achieved for visible, near IR and IR excitations [72, 73]. The guided plasmon is also fairly impervious to structural defects and can tolerate guiding around sharp bends [20, 45, 50, 56, 58]. A symmetric GPW is composed of a subwavelength gap in a thin metal film embedded in a homogeneous infinite dielectric media. It has been shown that this type of GPW always supports a bound mode in a wide frequency range [20, 52, 53, 74]. However, in most practical situations the metal film will be sitting on a glass substrate and the gap will be filled with air. This will lead to an asymmetric GPW, in which the surrounding dielectric media above and below the metal film are different.

In an asymmetric GPW depicted in **Figure 2.30** below, the modes become leaky above a cut off wavelength. In fact there is a cut off width or metal film thickness where the fundamental mode isn't bound but becomes leaky for a certain excitation wavelength. For both asymmetric and symmetric situations, as the metal film thickness

is reduced, the effective refractive index of the fundamental mode increases leading to stronger field confinement but also a decreased propagation length [52, 53, 55].

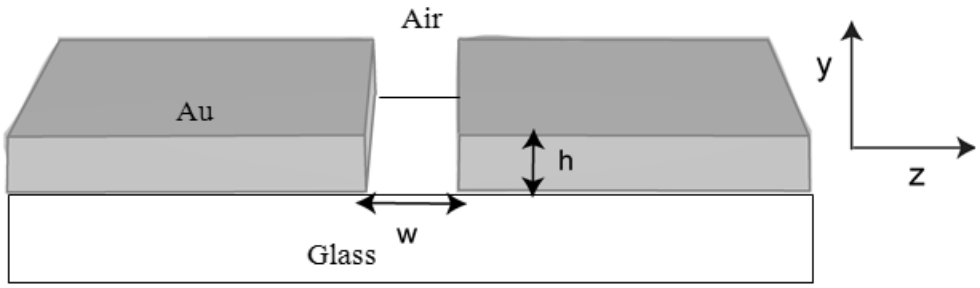

Figure 2.30 Schematic diagram of an asymmetric GPW. 'w' represents the width of the gap and 'h' represents the height of the gap.

An asymmetric GPW can be defined lithographically on a metal coated glass microscope slide using a focused ion beam lithography technique. Widely used metals for GPW fabrications are gold and silver. The characteristics of the guided plasmon in the GPW will depend on the dimensions of the slot (width *w*, height *h*) and fabrication related artefacts [58].

In a regime where dimensions of the slot are much smaller than the wavelength, it has been shown that this structure supports a fundamental bound mode and this bound mode is quasi-TEM so it can be excited by using a linearly polarised light source [52].

Gramotnev et al have used L-shaped gap surface plasmons waveguides fabricated using SiO_2 strip partially enclosed between two metal films (**Figure 2.31**) [73].

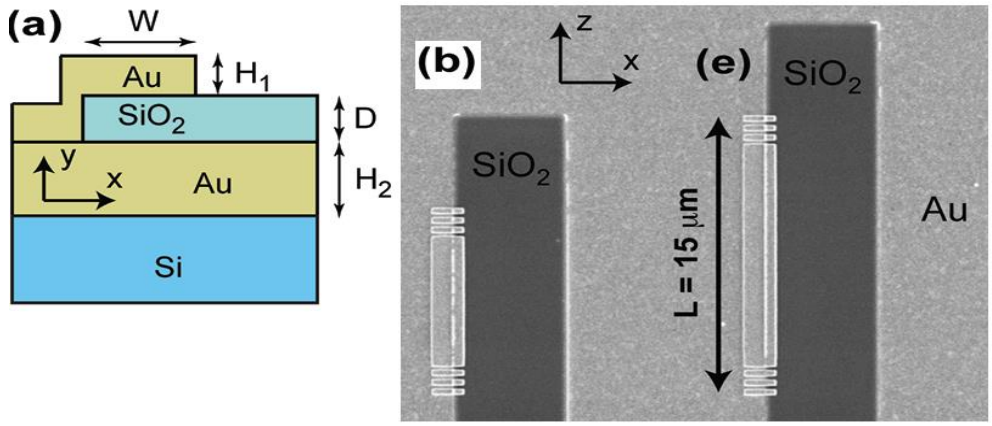

Figure 2.31 (a) Schematic diagram of the cross sectional view of the proposed waveguide structure (b) SEM images of the fabricated waveguides with different lengths [73].

The proposed L-GSPW has strong plasmon localisation in the nanogap with significant propagation length around 7μm. It was shown that this structure has high transmission through 90 degree bends with low cross talk between two neighbouring waveguides. Gong et al. have developed all optical logic gates using nanoscale plasmonic gap waveguides [75]. SEM images of the fabricated all optical logic gates using GPWs are shown in **Figure 2.32** below.

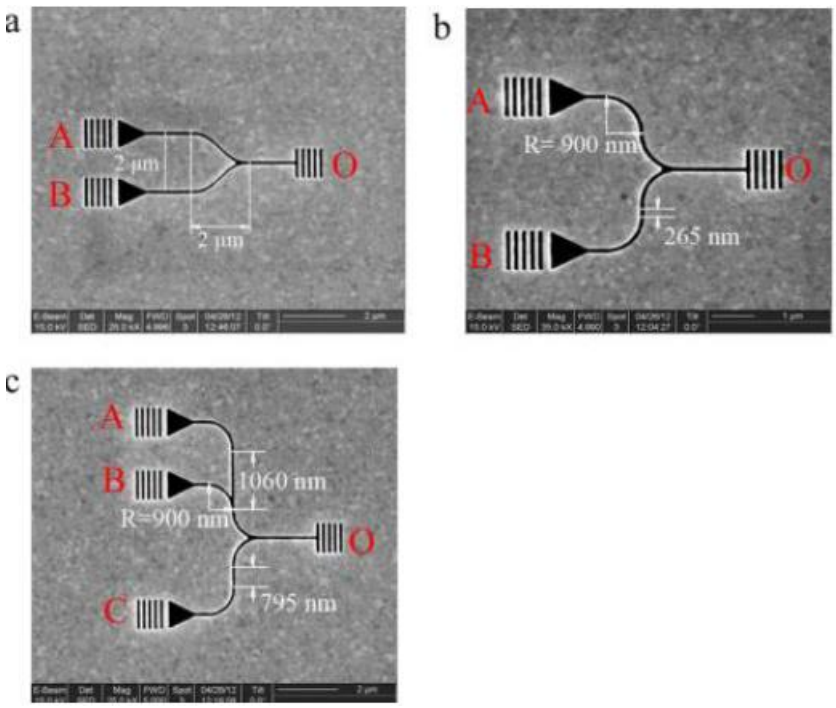

Figure 2.32 SEM images of the logic gates fabricated using GPWs. (a) OR gate, (b) NOT gate and (c) XNOR gate [75].

Gong et al. have demonstrated XNOR, XOR, NOT, and OR logic gates using GPWs. These gates are based on the interference of SPP modes in GPWs which generate quasi-TEM SPP modes strongly localised at the interface of the gap. They have used a grating structure to enhance the in-coupling (out-coupling) efficiencies at the input (output) end. Input gratings were normally illuminated by a continuous wave laser of 830 nm. The intensity contrast ratio between the output logic "1" and "0" reached 24dB which is 4 fold higher than previously reported results. The size of the devices shown in **Figure 2.32** is less than 5 μm in lateral dimensions and consists of 100 nm x 100 nm cross section gaps filled with air.

Due to ease of fabrication and ability to guide strongly localised SPP modes, GPWs are popular in plasmonic applications. In order to use GPWs in application there should be a method to control the plasmon propagation on the waveguide. Active devices can be incorporated into the application device to perform Boolean operations such as

NAND and NOR gates. Chang et al. proposed a single-photon transistor using metallic NWs. Similar to an electronic transistor, a small optical gate can be used to control the optical signal field. A small dipole quantum emitter is placed above the metallic NW and SPPs travelling along the NW can excite the emitter. Then the spontaneous emission of the excited emitter can couple with SPs on the NW and travel in the opposite direction, i.e. the photon has been reflected. Above concept can be used to control the SP propagation in an all optical device with GPWs. Therefore, we studied QD-gap plasmon interaction in **Chapter 3.**

2.5.5 Grooves and wedges

GPWs are easy to fabricate but have lower transmission of the SPP through 90 degree bends. It has been experimentally demonstrated that V-groove waveguides have better transmission in sharp bends than other waveguide structures [31, 32]. V grooves are made from a V shaped channel cut into a metal film (or a dielectric wedge in a metal film). Maradudin et al. in 1972 obtained the dispersion relationship for electrostatic modes confined in a dielectric wedge whose boundary is formed by the intersection of two semi-infinite planes making an angle between them [76]. Maradudin et al. in 1990 theoretically suggested that the channel of finite width cut into otherwise planer metal (or a polar dielectric medium) in contact with vacuum can support electrostatic modes guided along the channel [77]. They presented the exact dispersion relationship for these modes using Green's theorem but they neglected the retardation. They used the term channel polariton (CP) to describe the channel guided electromagnetic modes. In 2002 Maradudin et al. took retardation into account [78] but only considered a real negative dielectric function with no absorption.

Later in 2002, Maradudin et al. improved their theoretical work by taking into account the retardation of the guided modes in the channel and termed the propagating SPP modes as Channel Plasmon Polaritons (CPPs). In 2004, Pile et. al demonstrated the existence of similar CPPs near the tip of a dielectric wedge (or triangular groove filled with dielectric media) in a metal [79] and termed these electromagnetic waves as Wedge Channel Plasmons (WCPs). Channel plasmon polariton (CPP) is another term used for WCP. Pile et al. have extensively analysed a groove with infinite depth (where depth is sufficient to assume edge effects are negligible) using finite-difference time-domain (FDTD) method. Existence of non-dissipating periodically changing EM field confined near the apex of the groove is numerical evidence of CPPs generated by end-fire excitation. It is shown that the CPPs are generated only at smaller groove angles. Decreasing groove angle readily increases the wavevector of the fundamental CPP mode while increasing the field localisation beyond the diffraction limit. Later in the same year Gramotnev et al. theoretically showed that a multimode subwavelength V groove waveguide can convert into a single mode subwavelength waveguide by adjusting the groove depth [80] (**Figure 2.33**).

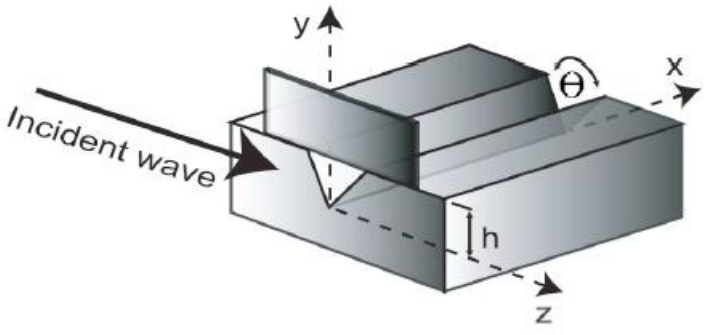

Figure 2.33 Schematic diagram of the structure with triangular groove of finite depth h and angle θ in a metal with additional screen at x=0. The metal screen supresses the scattered bulk waves in and above the groove [80].

Gramotnev et al. observed periodic modulation of the field distribution at a groove apex of a silver-vacuum V-groove of 30° angle when excited using 0.633 μm light (end-fire excitation). The penetration depth of the second CPP along *y* axis of the groove was around 800 nm while the fundamental mode had a penetration depth around 300 nm. Then groove depth was adjusted to 300 nm, closer to the fundamental mode penetration depth. This eliminated the second mode due to insufficient penetration depth and only the fundamental mode can be readily guided along the groove. Increasing groove angle also helps to decrease the number of CPP modes. Gramotnev et al. emphasised the fact that no CPP can exist at a groove angle larger than the critical angle and strong localisation of CPP can only be achieved with smaller angle grooves. In 2008, Moreno and colleagues numerically showed that CPP modes supported by finite height grooves exhibit cutoff at different wavelengths. Using the dispersion curves of SPPs on a flat metal surface, WPP(∞) mode of an infinitely deep metal wedge and CPP modes in a finite metal V-groove, they showed that close to the cutoff CPP modes approach and cross the WPP(∞) line. Hence they conclude that close to the cutoff CPP modes are hybrids of WPP supported by the metal corners at the top of the groove and CPP modes supported by the tip of the groove.

Bozhevolnyi et al reported the first experimental observation and characterisation of CPPs in 2005 [31]. Focused ion beam milled 460 μm long 1μm deep grooves in a 1.9 μm thick gold layer with 16˚ and 25˚ angles were excited by launching 1425 – 1620 nm light using a tapered-lensed polarisation maintaining single mode fibre and observed using an uncoated fibre tip of a scanning near field optical microscopy (SNOM). Propagation length derived from the SNOM images varied between 90 and 250 μm. This variation depends on the wavelength of the input light and poor reproducibility of the fibre coupling arrangement that was adjusted using far-field

observations. Bozhevolnyi et al. have demonstrated S-bends, Y- splitters, ring resonators and a Mach-Zhender interferometer using CPPs in a 25˚ angle, 1.1-1.3 μm deep FIB milled grooves in a gold layer of thickness 1.8 μm. Structures were excited using end-fire coupling with 1425-1620 nm radiation [32] (**Figure 2.34**).

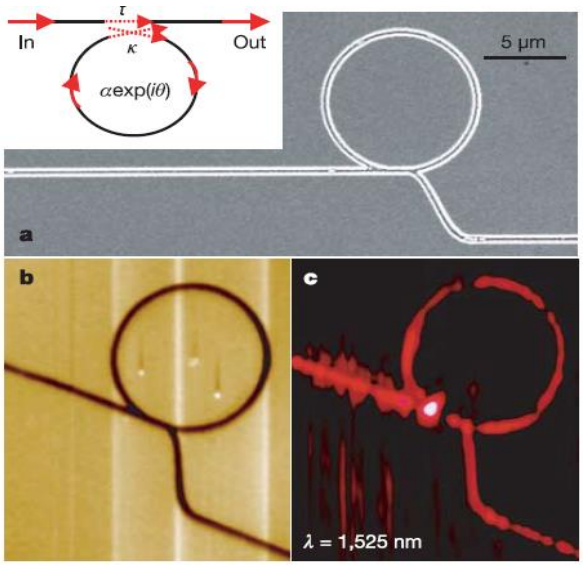

Figure 2.34 Plasmonic waveguide-ring resonator a) SEM image, b) topographical and c) Near field optical image at wavelength 1525 nm [32]

CPPs in V-grooves have been proven to have strong localisation with relatively low dissipation, near-zero losses at sharp bends, low sensitivity to structural imperfections and broad band transmission [32]. V grooves are compact and compatible with planar technology. The main drawback is the fabrication of V grooves under FIB is extremely complicated.

Wedge plasmon waveguides consist of a wedge surrounded by vacuum with an infinitely long edge extending in the z direction. Moreno et al. studied the modes supported by a metallic wedge waveguide [81]. SPP modes in wedge waveguides are

termed as Wedge Plasmon Polaritons (WPPs). Moreno et al. studied truncated wedges (y = h) and nontrucated wedges ($h \to \infty$) (**Figure 2.35**).

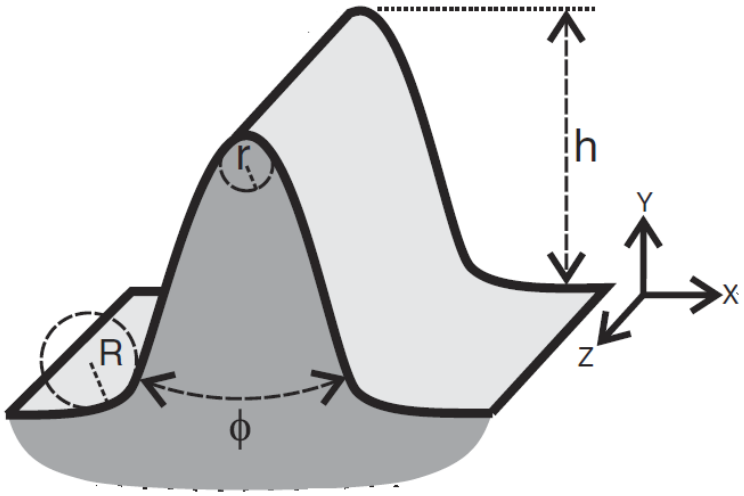

Figure 2.35 Truncated wedge. Wedge angle denoted by ϕ, edge is rounded with radius of curvature r, wedge height h [81].

Moreno et al. realised that the wedge plasmon waveguide structures provide good subwavelength confinement. Wedge plasmon polaritons (WPPs) have the same propagation lengths as CPP but have stronger localisation. SPPs travelling along a flat surface can be coupled into the WPP by using gradual modification of the surface profile.

2.5.6 Particle chain

Even though CPPS and WPPs provide significant propagation lengths with near zero losses for transmission through 90 degree sharp bends, fabricating these waveguides is extremely difficult. Scientists working on plasmonic waveguides were looking into other possible alternatives to use as plasmonic waveguides which are relatively easier to fabricate with good propagation length and low bending losses. It is found that closely spaced metallic nanoparticles can act as a plasmon waveguide [82]. Three

dimensional confinements of the electrons in metal nanoparticles lead to well-defined surface plasmon resonance frequencies. It is well known that light at SPR frequencies interacts strongly with the nanoparticle's electron cloud. For nanoparticles with diameter less than the wavelength, plasmon excitation produces an oscillating electric dipole field in a resonantly enhanced localised electromagnetic near field close to the particle surface [83]. One dimensional particle arrays exhibit coupled modes due to near-field interactions between adjacent nanoparticles. When distance from the centre of one particle to the centre of the adjacent particle is less than the incident light wavelength, neighbouring particles couple via dipolar interactions. Nanoparticle chains can lead to the coherent propagation of electromagnetic energy along the array. Maier et al. demonstrated experimentally that energy transport is indeed possible in metal nanorods with dimensions 90 nm x 30 nm x 30 nm and 50 nm surface-to-surface spacing between adjacent nanorods [23]. The long axis of the nanoparticle is perpendicular to the waveguide chain axis allowing increased near field coupling area (**Figure 2.36**). Structures were made using electron beam lithography and found the decay length of 6dB per 195 ± 28 nm which is in excellent agreement with the theoretical predictions of 6 dB per 200 nm [82].

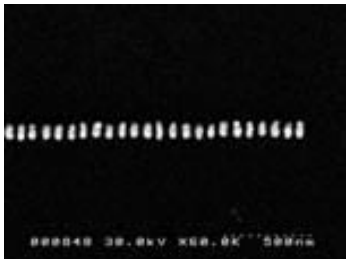

Figure 2.36 SEM image of the plasmon waveguide consisting of nanoparticles [23]. Long axis of the nanoparticle is perpendicular to the waveguide chain axis.

Relatively poor propagation length (~500 nm) in nanorod chains discouraged the further exploration of NP waveguides. Alternatively, chemically synthesised metal NPs were deposited into EBL made trenches. Following liftoff, this method created tightly packed metal NP waveguides with interparticle distance 1-5 nm [40, 84]. Decreased interparticle distance results in the formation of subradiant plasmon modes. These modes are collective oscillations with different phase for each NP reducing the coupling into propagating light, hence termed as dark modes [85, 86]. Solis et al. experimentally demonstrated dark-mode plasmons propagating around 2.6 μm on lithographically made nanoparticle stripe waveguide excited with 950 nm laser [40]. However, such propagation lengths are still low as compared to other plasmon waveguides.

Summary of the above section is given in the **Table 2.1** below.

Waveguide	Properties
Metal slab	• A thin metal film buried inside a lossless dielectric medium • When the thickness of the metal reduces, two individual SPP waves on each interface can couple to form Long-rang SPP • LRSPPs on a metal slab are only localised in one dimension is a disadvantage
Metal stripe	• consists of a metal film with finite thickness and width, and a length • Long propagation lengths can be achieved • Easy to fabricate • Fabricated metal stripes suffer losses due to scattering from rough surfaces and grain boundaries
Metal nanowires	• Colloidal synthesis of nanowires (NWs) results in nanowire structures with a smooth surface and no grain boundaries • NWs provide longer propagation lengths than metal stripes, • the orientation of NWs is difficulty to control.

Gap waveguides	• GPWs are easy to fabricate • Moderate propagation lengths • have lower transmission of the SPP through 90 degree bends
V grooves	• V shaped channel cut into a metal film • have strong localisation with relatively low dissipation, • near-zero losses at sharp bends, • low sensitivity to structural imperfections and broad band transmission • Compact and compatible with planar technology. • Fabrication of V grooves under FIB is extremely complicated.
Wedge	• wedge surrounded by vacuum with an infinitely long edge extending in the z direction • WPPs have the same propagation lengths as CPP but have stronger localisation. • Fabrication is extremely difficult
Particle chain	• Relatively poor propagation length (~500 nm) in of NP waveguides • Particle chains with interparticle distance 1-5 nm form dark modes

Table 2-1 Summary of waveguides

In the above section we discussed plasmonic waveguides, modes supported by each waveguides and possible applications of these waveguides such as Y splitters, ring resonators, logic gates etc. Another useful plasmonic application in the sensing area is called the Mach-Zehnder interferometer. This interferometer can be fabricated using different plasmonic waveguides.

2.6 Mach-Zehnder interferometer

Plasmonic Mach-Zehnder interferometer is a passive nano-optical component that can be employed in sensing applications and is created using several plasmon waveguides. In physics the MZ interferometer is a device used to determine the relative phase shift

variations between two collimated beams derived by splitting light from a single source [87]. Wang et al. proposed a plasmonic MZ interferometer consisting of splitting and recombining gap waveguides [88] with 30 nm wide, 500 nm long Ag gap waveguides separated by 250 nm (**Figure 2.37**). The structure transports ~20% of the incident energy to the output waveguide and suffers from reflection of the SPP from the end of each waveguide.

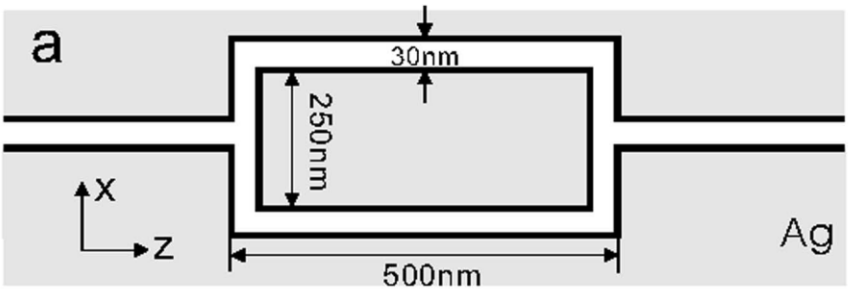

Figure 2.37 Schematic diagram of a M-Z interferometer using gap waveguides [89].

To overcome the reflection, Wang et al. suggested an M-Z interferometer design using waveguide couplers. The phenomena of optical tunnelling which occurs in closely placed waveguides was used in the new design. In this configuration light field in one waveguide can evanescently couple into the other waveguide if the waveguide separation is sufficiently small.

The suggested 4 arm M-Z interferometer design is shown in **Figure 2.38**. The complex electric field (E_j) in each waveguide can be written as [88, 89]

$$E_j = \left(\sqrt{2}/2\right) A_0 \cos\left(\sqrt{2}Cz\right) e^{i\beta z} \quad \text{for (j = 1, 3)} \tag{2.19}$$

$$E_2 = iA_0 \sin\left(\sqrt{2}Cz\right) e^{i\beta z} \tag{2.20}$$

j=2 indicates the central input and output waveguides and j = 1, 3 represents the interferometric arms. β and C are the propagation constant and the coupling coefficient respectively.

Coupling length defined by,

$$L_c = \left(\pi/2\sqrt{2}\,C\right) + \left(m\pi/\sqrt{2}\,C\right), \quad \text{m} = 0, 1, 2, \ldots \tag{2.21}$$

L_c determines the distance over which the light energy can couple completely from one waveguide into the adjacent waveguide [89]. When the light is coupled into the leading arm, it can be transported to the end arm via coupling into adjacent outer arms situated with proper separating distance from the leading arm.

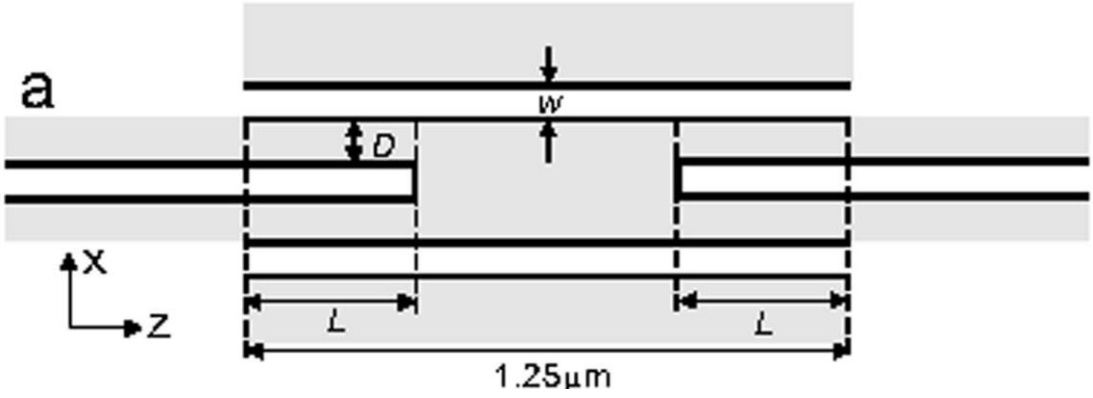

Figure 2.38 Schematic diagram of the proposed 4 arm waveguide coupler M-Z interferometer. *D* is the separation between input arm and outer arms, *w* is the width of the waveguide and *L* is the coupling length [89].

MZ interferometers can also be built using Y-splitters. Boltasseva et al. have optically characterized the Y-branch waveguides consisting of 15 nm thick 8 µm wide LRSPP stripe waveguides excited using 1475-1610 nm wavelength radiation. A Y splitter with splitting length of 10 mm between arms induced a loss around 3 dB and a Y splitter

with splitting length of 5 mm induced an additional 0.5 dB from each arm. Y-splitters can be used to fabricate a M-Z interferometer [67].

Bozhevolnyi et al. have investigated a M-Z interferometer composed of two consecutive Y-splitters using V-grooves with angles close to 25 degrees and depths of 1.1 to 1.3 μm in a thick gold layer deposited on a fused silica substrate[32]. Fabricated structures were excited using end-fire excitation (tunable laser of wavelength 1425-1620 nm). Structures performed well over the whole wavelength range with very low losses and exhibiting single-mode properties (**Figure 2.39**).

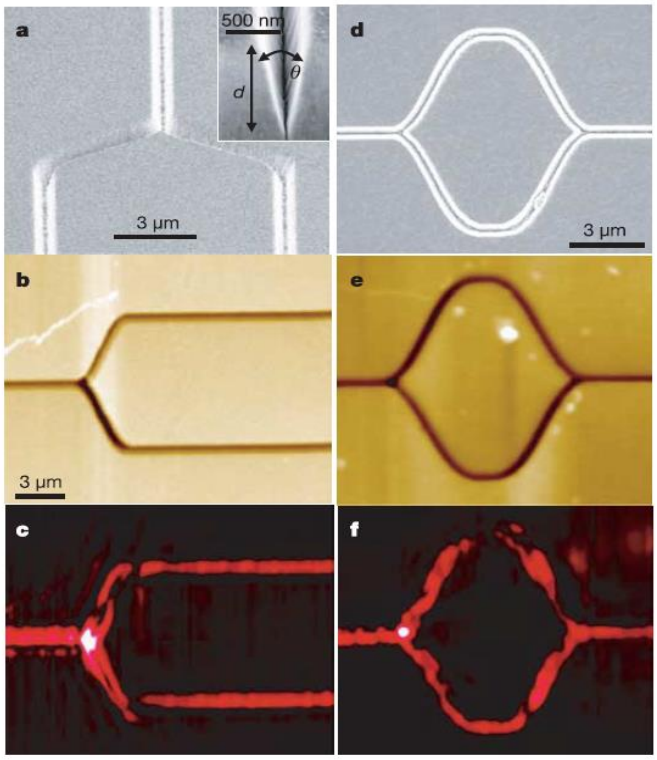

Figure 2.39 Y splitter and M-Z interferometer using v-groove waveguides. a) SEM image, b) topographical image, c) near-field optical image (at wavelength 1600 nm) using SNOM. d)-f) as a)-c) but for M-Z interferometer [32].

Transmission T of the Y splitter (T_Y) and M-Z interferometer (T_{MZ}) are obtained in the following ranges $0.82 < T_Y < 1$ and $0.4 < T_{MZ} < 0.49$ respectively using output-to-input ratios of maxima of the corresponding signal distribution.

The Y splitter showed next to zero insertion loss even though the curvature of radius used in the structure was ~1.5λ.

Pezze et al theoretically showed that the M-Z interferometer can be used to estimate the phase shifts with high sensitivity [90]. Bartoli et al. have theoretically and experimentally characterised Vertical Plasmonic M-Z interferometer (VPMZI) [91]. The structure consists of two nanoslits in a 300 nm Ag (or Au) film on a glass substrate (**Figure 2.40**).

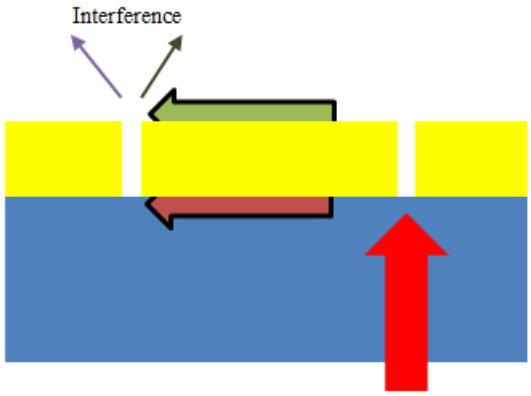

Figure 2.40 Schematic diagram of the M-Z interferometer consists of two metallic nanoslits described by Bartoli et al[91].

Both top (covered with a liquid therefore liquid/metal interface) and bottom surface (metal/ glass interface) can support SPP modes. When the rightmost slit is excited, the SPP is generated on the top and bottom surface. The SPPs travel and interfere with each other at the left slit. Sensing arm of this interferometer is the top surface and reference arm is the bottom surface. FDTD modelling showed the sensitivity of this interferometer is ~4718 nm/RIU (refractive index unit) at 860 nm wavelength and phase change sensitivity is ~72(2π)/RIU when the substrate is gold (RI 1.51) and top dielectric layer is water (RI 1.33). The most important design requirement for this interferometer to achieve higher sensitivities is to match the effective refractive index

at the top and bottom interfaces. This can be achieved by using a substrate whose refractive index is closer to the liquid layer on top. FDTD modelling shows that sensitivity can be increased to $\sim 10^4$ RI/nm using above approach [91].

Vernon et al. proposed a compact interferometer design using three LRSPP stripe waveguide coupling to measure the change in refractive index of a sample using the change in the output intensity due to phase changes occurring at the sample arm [92]. The proposed design is shown in **Figure 2.41** below.

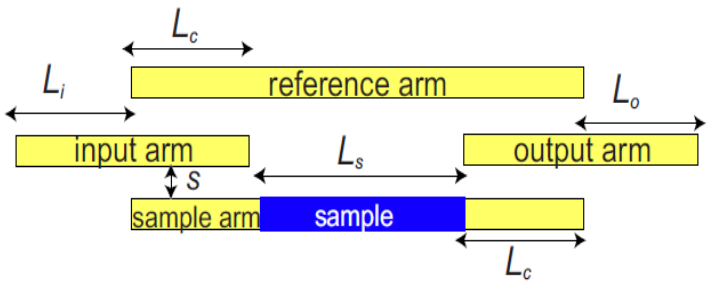

Figure 2.41 M-Z interferometer design using 3 waveguide coupling [92] L_i is the input length, L_c is the coupling length, L_o is the output length, L_s is the sample length and s is the separation distance [92].

The input arm can be excited using endfire excitation and plasmons propagate until the evanescent field starts to interact with the adjacent interferometric arms (reference and sample arms). Sample and reference arms are separated with a sufficient distance eliminating coupling with each other. Structural parameters were chosen such that isolated stripes support a single bound mode (ss_b^0). For a 750 nm wide 30 nm thick Au waveguide on glass substrate plasmons can propagate at least 50 μm when excited using 633 nm laser light. In simulations, a separation distance of 100 nm resulted in a coupling length of 13 μm.

For a sample length of L_s the resultant phase shift is given by

$$\Phi_s = \left(k_{ref} - k_{sample}\right)L_s = \frac{2\pi}{\lambda}\left(n_{ref} - n_{sample}\right)L_s \quad (2.22)$$

where, k_{ref} and n_{ref} are the wavenumber of the plasmon along the reference arm and effective refractive index on the reference arm respectively, k_{sample} and n_{sample} refer to the wavenumber of the plasmon along the sample arm and effective refractive index on the sample arm respectively. Excitation wavelength is denoted by λ and L_s for this system should meet the following condition

$$L_s < d - 2L_c - L_i - L_o \quad (2.23)$$

where L_c is the coupling length, L_i is the length of the input arm before it starts to interact with outer arms, L_o is the length of the output arm where plasmons propagate after interacting with outer arms. $L_i = L_o = 5\,\mu\text{m}$.

The output waveguide's SPP electric field (E) can be written as

$$E = a_o e^{ik(z - L_i - 2L_c - L_s)} \quad (2.24)$$

where k is the wavenumber of the ss_b^0 mode. Intensity of the output end can be written as

$$I = \frac{\alpha^2}{2}\left(1 + \cos\phi_s\right)\left(1 - \cos 2\gamma L_o\right) = I_o\left(1 + \cos\phi_s\right) \quad (2.25)$$

A small change in sample refractive index is then introduced to the model to determine the sensitivity. This change causes a small phase shift δ in ϕ_s.

$$I/I_o = \cos\left(\phi_s - \delta\right) - \cos\left(\phi_s\right) = \cos\left(\phi_s\right)\cos\left(\delta\right) + \sin\left(\phi_s\right)\sin\left(\delta\right) - \cos\left(\phi_s\right) \quad (2.26)$$

If the initial phase change is $\phi_s = \pi/2$ and δ is small, then

$$I/I_o = \sin\left(\delta\right) \approx \delta \quad (2.27)$$

Under the given conditions, fractional change in the intensity is approximately equal to the change in phase due to the small change in sample refractive index. Sensitivity

of the device is $\sim 2\times10^{-4}$ for a 1.5% change in output intensity. This interferometer is planar and more compact (2.5 μm wide) than the other M-Z interferometers and SPR refractive index sensors proposed. A similar design to this interferometer will be experimentally realised as a refractive index sensor in **Chapter 6** of this thesis.

2.7 Quantum dot – plasmon interaction

Now that various passive plasmon waveguides have been proposed and designed, a method for actively controlling their propagation will be discussed. Quantum Dot (QD) – plasmon interactions can be used for actively controlling the propagation of plasmons in a plasmonic waveguide which is essential in nanophotonic circuitry. Spontaneous emission of a quantum dot mainly depends on the transition strength of the upper and lower energy levels and local density of states (LDOS) [93]. An excited quantum emitter in free space can decay radiatively into free space. The spontaneous emission (SE) rate can be manipulated by altering the density of states in the photonic environment around the quantum emitter. SE rate can be increased by increasing the number of available electromagnetic modes the emitter can emit photons into.

An excited chemically synthesized QD which is placed in close proximity to a plasmon waveguide, results in a LDOS increase due to addition of non-radiative decay and plasmonic excitation. [16, 94]. The main three decay channels available for a QD placed in proximity to a waveguide are,

1. Direct optical emission into free space
2. Damped non-radiative decay due to the ohmic losses in the conductor
3. Spontaneous emission into the guided plasmons in the plasmon waveguide

These decay paths are shown schematically in **Figure 2.42**. Non-radiative decay occurs due to ohmic losses in the metal waveguide and these ohmic losses become

significant when the separation between the QD and the plasmonic waveguide is very small [95]. Non-radiative losses can be rectified by placing the emitter optimally i.e. sufficiently far from the waveguide. The third emission method, generation of plasmons, is the most important in controlling the interaction between plasmons and the QD.

Plasmons propagate at a greatly reduced speed because of involvement in the motion of charge-density waves [96] and the subwavelength confinement is achieved by a dramatic concentration of optical fields [7]. The high confinement and the slow velocity of plasmons cause the plasmonic waveguide to capture a large amount of the QD spontaneous emission into guided plasmon modes [95, 96]. For an optical emitter/QD placed in the vicinity of an evanescent surface plasmon mode tail, the spontaneous emission rate in to the guided SPs is proportional to $(\lambda/d)^3$ where d is the distance from the plasmonic waveguide [96].

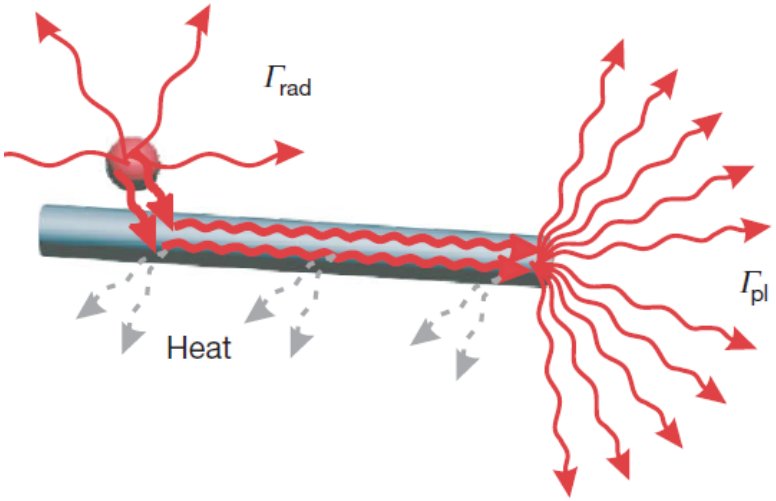

Figure 2.42 An optimally coupled QD with a metallic nanowire. Disregarding the non-radiative decay (heat), coupled optical emitter can emit spontaneously into the guided plasmons of the nanowire or to the free space with rates Γ_{pl}, Γ_{rad} respectively [16].

There is much theoretical work on how an individual QD couples with a plasmon supported by various metal waveguide structures mainly based on approximating the QD as a dipole emitter [16-18]. Chang *et al* showed that using a quasi-static approximation, spontaneous emission of a QD placed in proximity to a nanowire can be almost entirely directed into a propagating plasmon mode [95]. However, in their analytical method, the wave property of the plasmonic mode has not been taken into account.

SE of a dipole emitter in the vicinity of a metal slab/slot waveguides preferentially couple into guided plasmon modes in the waveguide due to the tight confinement of the plasmon mode in the gap region. Jun *et al* studied the different SE decay rates of a QD coupled to a gap waveguide using Finite Differential Time Domain (FDTD) method, another technique to model spontaneous emission of a dipole emitter placed close to a plasmonic waveguide [17]. However, in this model, they have used simplified assumptions for the calculation of local density of states of the plasmonic mode.

Chen *et al* have developed a model treating all decay channels of a dipole emitter in the vicinity of a plasmon waveguide (including radiative and non-radiative decay channels) meticulously using Finite Element Method (FEM) [97]. Resistive heating of the metallic waveguide is the only non-radiative decay channel included in this model. In their work, they especially focused on calculating the fraction of SE energy emitted into the plasmonic mode of the waveguide. The realistic description of this model helps to understand the physics and fundamental limitations.

In our work we used the FEM method used by *Chen et al*. to model SE of a quantum emitter placed in close proximity to a plasmonic gap waveguide [97]. We studied the effect on the SE of the symmetry of the dielectric environment and gap dimensions.

To make the problem more realistic, we studied the effect of sharpness of the gap edge on SE decay rate into a guided plasmon mode in the waveguide.

The fundamental mode of the GPW has a dominant Electric field in *y* direction. Therefore the QDs were chosen such that QD emission axis along the *y*-direction. First, using a 2D model we calculated the SE decay rate into the guided plasmon mode of the waveguide. After that, we used a 3D model to find the total decay rate of the QD emission. This is done by modelling the dipole emitter as a linear current source and by calculating the total power emitted from the current source. For more information refer **Appendix A**.

Figure 2.43 shows the cross-sectional view of a QD placed near an edge of a symmetric GPW. The QD is represented by the blue line.

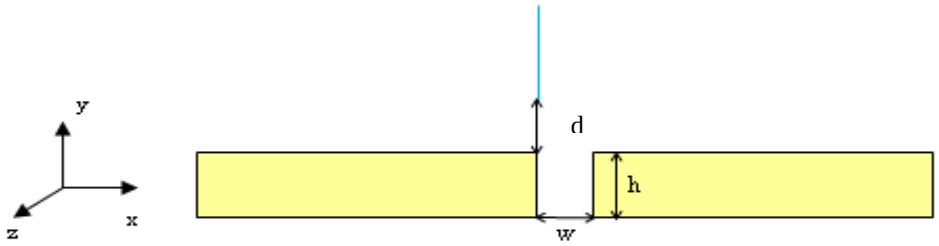

Figure 2.43 2D schematic of a symmetric GPW. Height h = 0.05 µm, $E_{x,y,z}\left(x_{QD}, y_{QD}\right)$ is measured along the line shown in red. *w* is the width of the GPW and *d* is the distance from the QD to waveguide surface

The normalised decay rate of spontaneous emission of a QD into a plasmon mode ($\hat{\gamma}_{pl}$) can be determined using Green's Dyadic for the E-field for the plasmon mode:

$$\hat{\gamma}_{pl}\left(x_{QD}, y_{QD}\right) = \frac{3\pi\varepsilon_0 \left| E_y\left(x_{QD}, y_{QD}\right)\right|^2}{k_0^2 \int (E \times H^*) \cdot \hat{z} dA} \tag{2.28}$$

where ε_0 is the permittivity of free space, k_0 is the wave number in free space, $\hat{z}$ is the

unit vector in the z-direction and the dominant E-field component for the plasmon mode of the system is E_y (**Figure 2.43).**

Determining $\hat{\gamma}_{pl}$ is imperative in optimising the QD-waveguide coupling. The spontaneous emission β factor defines the probability of the rate of spontaneous emission of the QD into the guided plasmon mode with [94]

$$\beta = \hat{\gamma}_{pl} / \hat{\gamma}_{tot} \tag{2.29}$$

where, $\hat{\gamma}_{tot}$ represents the sum of all three decay channels. Both decay rates are normalised with respect to the SE decay rate of the QD in vacuum (γ_0). A β factor of 1 means the QD decays totally into a plasmon mode [96]. The β factor has been defined analytically for a QD-metallic nanowire system, and numerically for QD-metallic stripe waveguide and GPW systems [94, 97].

To find $\hat{\gamma}_{tot}$ near the metal gap waveguide, we constructed a 3D model to accommodate the radiative decay mode and used mode matching boundary conditions to ensure the absorption of the plane waves. The QD was assumed to be a current source at near proximity to the waveguide.

$$\hat{\gamma}_{tot} = \frac{0.5\int_v \mathrm{Re}\left(\vec{J}^* \cdot \vec{E}_y\right) dV}{0.5\int_v \mathrm{Re}\left(\vec{J}^* \cdot \vec{E}_{0y}\right) dV} \tag{2.30}$$

where, $\vec{J}$ is the current source, $\vec{E}_{oy}$ is the *y* component of the electric field of the QD in vacuum. For a 1 nm current source with 1 A current, equation 2.30 reduces to

$$\hat{\gamma}_{tot} = \int \mathrm{Re}\left(E_y\right) dl \Big/ \int \mathrm{Re}\left(E_{0y}\right) dl \tag{2.31}$$

with *dl* representing the line integration over the length of the emitter. For the derivation of equation and model used, refer **Appendix** A. For results and analysis refer to **Chapter 3**.

QD-Plasmon coupling has been experimentally achieved for metallic nanowires by Akimov et al [16]. A schematic diagram of their sample is shown in **Figure 2.42**. CdSe QDs were placed in close proximity to silver NWs using a PMMA spacer layer of thickness ~30 nm. Ohmic losses can be neglected at this spacer layer thickness. They have shown that, when the QDs near NWs are optically excited, SE from QDs couple directly to guided plasmon modes of the NWs. These plasmons propagate along the NW and outcouple into the far field from the end of the NW. It is realised experimentally that the SE of a QD increasing 2.5 folds when it is the vicinity of a NW and their observation of SE coupling into plasmons on the NW opened up the possibility of using quantum optical techniques to achieve control of plasmon propagation.

In 2008, Brongersma et al. theoretically investigated the SE of a QD in a metal/dielectric/metal slab and gap waveguides (refer **Figure 2.44**) [17]. It is found that in both structures, spontaneous emission of the QD is greatly enhanced due to tightly confined plasmonic modes and that the majority of SE couples into plasmons supported by the structures.

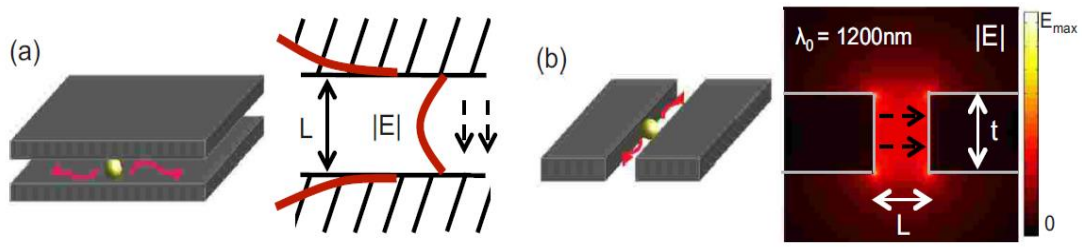

Figure 2.44 Schematic diagram of (a) MDM slab, electric field inside the gap is shown in red colour and (b) MDM slot waveguides with electric field profile of the fundamental mode. Yellow sphere represents the dipole emitter (QD) [17].

In 2010, the same group experimentally realised SE of a quantum emitter placed in proximity to a gap waveguide (**Figure 2.45**) [18].

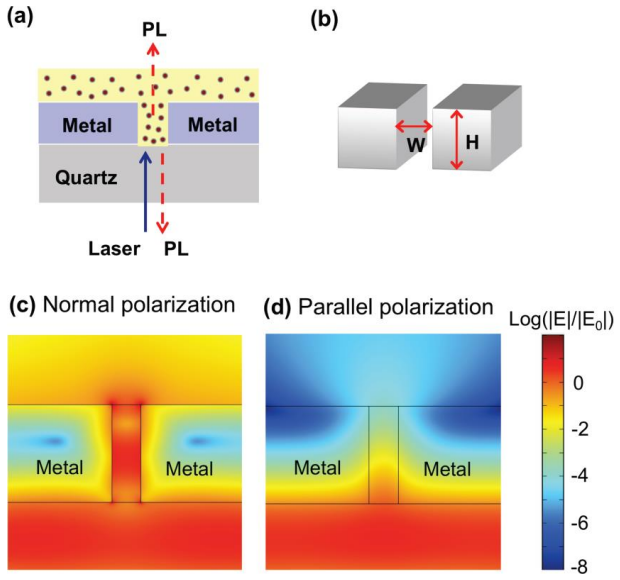

Figure 2.45 (a) Schematic diagram of the experimental configuration. Incoming laser light illuminates the sample through the substrate. Photoluminescence (PL) from the top and bottom of the sample are collected and analysed. (b) Geometry of the waveguide structure, *W* represents the width and *H* represents the height of the slot. Normalised electric field of slot when incident laser light is polarised (c) normal to the gap and (d) parallel to the gap [18].

It is observed that for a laser polarised parallel to the slot (TM polarised laser), the QD life time decreases and the QD photoluminescence becomes polarised normal to the gap with decreasing gap width. Gap plasmons are mainly TM polarised hence can only be excited using a TM polarised light. Most of the PL comes from the slit which is evidence that the SE of the QDs and the gap plasmons were interacting. To prove this, they used a laser polarised normal to the slot (TE polarised laser) and observed that the QD PL weakly depends on gap properties and that the PL spot is broad (unlike in the TM polarised laser case where the PL spot is confined in the gap region).

As discussed in **Section 2.3**, QDs can also be used to image the plasmon propagation on a waveguide. When the plasmonic waveguides are covered with a continuous QD film they can be used to track the plasmon propagation. When the waveguide structure is excited using a laser with wavelength less than the QD emission wavelength, a bright luminescence is observed around the waveguide edges that decays rapidly along the waveguide. **Figure 2.46** below shows the CCD images depicting plasmon propagation on an Ag NW imaged using CdSe QDs excited using a 532 nm laser. QD emission is centred on 612 nm. This luminescence can be interpreted due to QD emission arising from locally excited QDs. QDs are excited by the propagating SPPs close to the substrate.

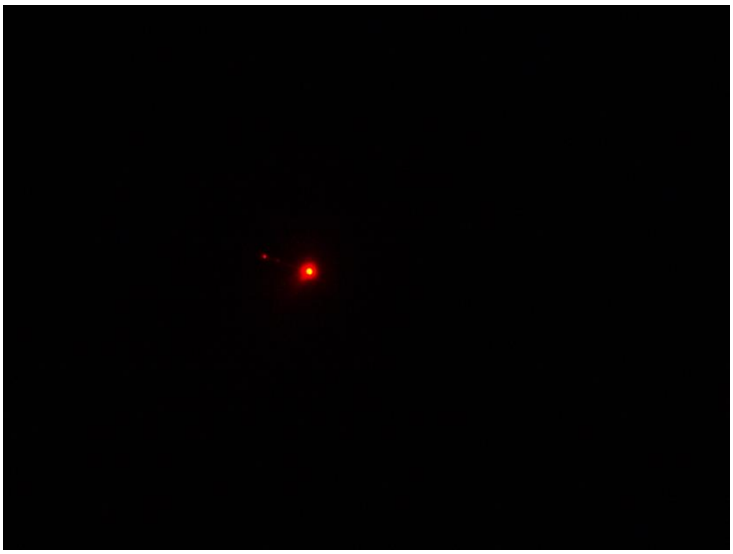

Figure 2.46 Imaging plasmon propagation along a silver NW using CdSe QDs. Excitation wavelength 532 nm. Spacer layer between the NW and QD layer is 20 nm thick SiO_2. Image was obtained by the author at Monash University Funston lab.

Gruber et al. have lithographically positioned 1-3 QDs along a plasmonic stripe waveguide with nanoscale resolution [36]. Measurements have used bottom-up fabrication techniques utilising multi step E beam lithography (EBL) to localise the QDs in the vicinity of the waveguide surface with nanoprecision. First EBL lithography was used to make a hole to deposit QDs. Highly diluted CdSeTe/ZnS QDs

were spincoated on the fabricated mask and QDs were confined into the holes after liftoff. Then a 20 nm SiO_2 spacer layer was deposited to prevent direct quenching. Then another EBL process was carried out to pattern stripe waveguides aligned with the QD filled holes. Metal stripes were fabricated after metal evaporation and liftoff process. Structures were excited using circularly polarised light of wavelength 488 nm. It is confirmed that, for a QD placed near the vicinity of the waveguide, the local plasmon field mainly controls the coupling efficiency.

Ropp et al. demonstrated the use of QDs as imaging probes and controlling the spontaneous emission at the single emitter level with nanolevel accuracy [19]. A single QD is carefully placed adjacent to a silver NW to probe the LDOS of the NW as shown in **Figure 2.47**. The QD position is controlled by activating the flow in a microfluidic device using the viscous drag to move the QD. They were able to image the LDOS of an Ag NW with a spatial accuracy of 12 nm using a single QD.

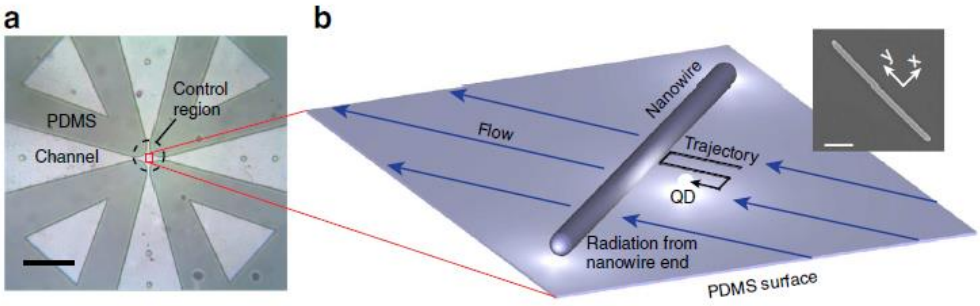

Figure 2.47 (a) Optical image of the microfluidic channel. Area inside the circle is the centre control region which is controlled by four external electrodes, (b) schematic of the QD positioned near the NW. QD is driven along the trajectory shown by black arrow according to the flow control. Inset shows an SEM image of the AgNW [19].

So far we have discussed SPs, excitation/detection of SPP, SPP modes supported by plasmonic waveguides, potential applications of plasmonic waveguides and methods to control plasmon propagation on a waveguide. We have only briefly discussed the

fabrication methods used to fabricate these devices. **Section 2.8** goes into more detail on the various fabrication techniques.

2.8 Fabrication

Plasmonic waveguides can be chemically synthesised (Eg; NWs) or fabricated lithographically (e beam lithography, Focused ion beam, Photolithography etc). The main waveguides considered in this thesis are gap waveguides and stripe waveguides. These waveguides can be fabricated using several lithographical techniques. The first step is to obtain a homogenous metal film on a substrate. It is one of the most important steps in the fabrication process. There are several physical and chemical deposition/ growth techniques available but the most common method is to deposit metal using one of the physical vapour deposition (PVD) techniques. In PVD, desired materials are vaporized under high vacuum and then condensed on to various substrates. Popular PVD techniques are Cathodic arc deposition, electron beam (e-beam) evaporation, thermal evaporation, pulsed laser deposition, and sputter deposition. In this thesis we used thermal deposition and e beam evaporation.

In the thermal deposition technique, a small amount of the source material is placed inside a small basket made out of a highly resistive heating element. Heating basket materials depend on the evaporating material. Then a high current is applied to the basket and source material is evaporated. The vacuum allows vapour particles to travel directly to the target object (substrate) positioned directly underneath the basket and condensed back to solid state. The vacuum in this technique is not as high as e beam evaporation or sputtering. Therefore this offers relatively fast deposition. A homogeneous and relatively smooth film can be obtained using this method. It is hard to obtain thicker films using thermal deposition due to the limitation in source material in the heating basket. Purity of the deposited film depends on the quality of the vacuum

inside the chamber. Therefore, sputtering and e beam evaporation which utilise high vacuum provide films with high purity.

In e-beam evaporation, source materials are contained inside crucibles. The material of which crucible is composed depends on the source material. The crucible is placed on a water (or glycerol) cooled stage [98]. In this technique, a tungsten filament in high vacuum is given a very high current and an emitted e beam bombards the target material (anode). The electron beam transforms the target material into the gaseous phase. Vaporised target material atoms then deposit on the substrate positioned directly above the target crucible. In this method, the deposition rate can be precisely controlled to be as low as 0.1 A°/s. Due to high vacuum, purity of the deposited films are higher than thermal evaporation [98].

In the sputter deposition technique, a noble gas such as Ar is injected into the target material chamber. The gas is then converted into plasma localising near the target material using magnets. The plasma discharge bombards the target material and ejects atoms from the target material. This phenomena is driven by momentum exchange between incoming ions and atoms in the material due to collision, and happens only when the kinetic energy of the bombarding ions are much higher than 1 eV. Advantages of sputtering are that even materials with high melting points can be easily sputtered and sputtering can be done using reactive ions such as O_2 and N_2. Sputtering is not suitable for waveguide fabrications using lift-off. This is due to the diffuse transport of the ejected atoms, which doesn't accurately cover step-like patterns on substrate [98].

Once the metal has been deposited, the next step is to mill out waveguide structures. Focused Ion beam (FIB) is a scientific instrument widely used as a nanofabrication technique. Most FIBs utilise a liquid metal ion source like gallium (Ga). The latest

FIBs are modified to use Helium (He) and Neon (Ne) gas as these ions are smaller than Ga ions hence can be used to fabricate structures with higher spatial resolution.

In a FIB using Ga ions, the Ga source is placed in contact with a tungsten needle. When the tungsten needle is heated supplying a current, Ga wets the tungsten needle and flows to the tip of the needle forming a Tylor cone. High electric field at the tip causes Ga to ionise and results in field emission of the atoms. The ion beam is then directed towards the sample using electrostatic lenses [99].

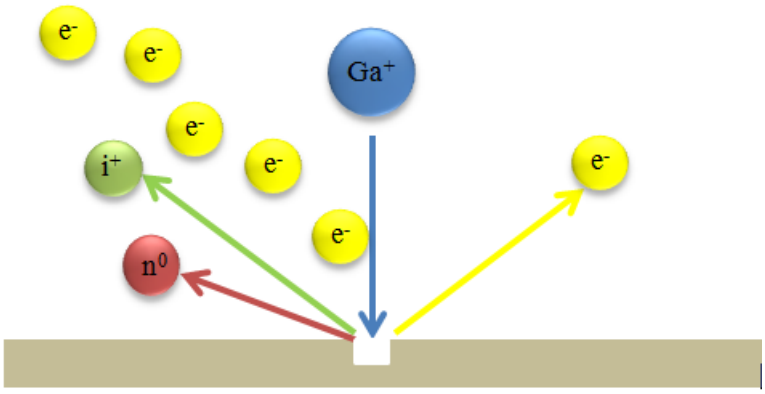

Figure 2.48 Operating principle of Ga milling. Impinging Ga ions sputter small amount of sample material from the surface. The sputtered section leaves the sample surface as secondary ions (i^+) or neutral atoms (n^0).

As the diagram shows the Ga^+ ion beam hits the sample surface and sputters a small amount of sample material (**Figure 2.48**). The sputtered material leaves the sample surface either as a secondary ion (i^+) or neutral atoms (n^0). The ion beam also produces secondary electrons (e^-). The signal from sputtered ions or secondary electrons is collected to build an image. Due to the capability of sputtering in FIB, it is used in micro and nano milling processes. Depending on the structure size, and required smoothness in the edges, FIB parameters like dwell time, number of passes in raster scan, and milling current can be adjusted to achieve a smooth edged milling with high spatial resolution on the nanolevel. FIB is also very useful to measure the depth of a

film. This is achieved using the clean cross section process. A strip of Platinum (or Tungsten if the surface is flat) can be deposited prior cross section cutting, to obtain a good contrast to the sample as well as a protective layer to the sample surface. Then by using cleaning cross-section option a cross-section cut can be milled into the sample and by measuring the depth of the cut, sample thickness can be determined.

Electron beam lithography (EBL) is another useful technique in fabrication and can provide structures with very high spatial resolution (feature size around 20 nm) than Ga-assisted FIB [100, 101]. In this technique, first an electron beam resist (like PMMA polymer) is spin coated on the substrate. Desired shapes are then patterned on the sample by carefully exposing the electron beam to the selected area. The electron beam can alter the chemical environment of the PMMA resulting in a solubility change in the exposed areas [102]. This enables the selective removal of exposed and non-exposed areas at different stages of the fabrication process. The main advantage of EBL is the ability to fabricate custom patterns with high resolution (resolution typically varies from 10 – 100 nm) [103]. The patterned PMMA mask is then developed in MIBK: IPA 1:3 solution (developer) for 30 seconds. This removes the exposed area. Desired thickness of metal is deposited onto the developed sample. Structures will be left on the substrate removing the unnecessary PMMA in an acetone bath. This step is called the lift-off procedure. Strong adhesion between the deposited metal and substrate surface is required in order for structures to survive the lift off process.

Polymethyl methacrylate (PMMA) is a widely used e beam resist. Standard PMMA solutions are available in 495K and 950K molecular weight resins in either chlorobenzene or anisole. The most popular PMMA products are 2-6% 495K PMMA in anisole (or chlorobenzene), 8-9% 495K PMMA in anisole (or chlorobenzene), 2-6% 950K PMMA in anisole (or chlorobenzene) and 8-11% 950K PMMA in anisole

(or chlorobenzene). Spincoated PMMA thickness mainly depends on the spin speed, molecular weight and the weight percentage of solid in solvent. Spin speed versus thickness curves are available for each commercially available PMMA solution. Customised PMMA solutions can easily be calibrated by varying the spin speed and measuring the film thickness.

It is advised to use a bilayer PMMA as electron beam resist [104]. In bi-layer PMMA, first the lower molecular weight (MW) PMMA is spincoated and cured at 180 °C for 10 mins. Then the higher MW PMMA is spincoated and cured at 180 °C for another 10 mins. In a bilayer process the more sensitive 495K PMMA layer is at the bottom and when exposed to electron beam, the bottom layer undercut is higher than the cut in the 950K PMMA layer (**refer Figure 2.49**). In a typical EBL process, the next step is to deposit metal on the sample after developing. Then the sample is placed in an acetone bath to liftoff the PMMA layer. E beam evaporation or thermal deposition is suitable as these methods provide less side wall coverage. For a successful lift-off, PMMA thickness should be at least three times higher than the metal thickness.

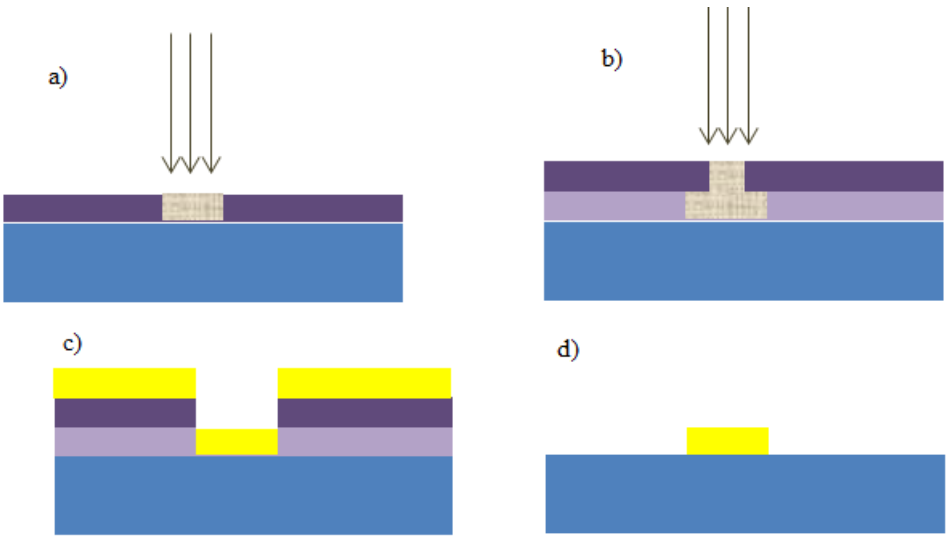

Figure 2.49 (a) single layer PMMA resist exposed to e beam, (b) bilayer PMMA resist exposed to e beam and (c) metal deposited on a patterned and developed bilayer sample. Note the undercut is deeper than the single layer and (d) structure survives on the substrate after acetone lift-off

Photolithography is a similar technique to e beam lithography. But instead of an electron beam, photolithography uses a UV beam to pattern on a photo sensitive polymer layer (photo resist). The basic procedure in UV lithography involves cleaning the wafer and preparing it to spin coat the photo resist. Then the sample is patterned by exposure to UV light [105]. The exposure of light causes a chemical change that allows the exposed photo resist to be removed using a specific developer solution. Positive photo resist, when exposed, becomes soluble in the developer and with negative photoresist, unexposed areas are soluble in the developer. Developed photoresist is normally baked for a few minutes ("hard-bake") to solidify the remaining photoresist. After that, liquid or plasma etching takes place removing the uppermost layer of the substrate which is not covered by the photoresist. Basically patterned and developed photoresist acts as a mask aiding the etching occurring on the substrate. Finally photoresist is removed using a resist stripper solution. This lithography is commonly used in fabricating micron wide structures.

This thesis includes experimental fabrication of nanoscale gap waveguides and stripe waveguides. FIB is used for the fabrication of gap waveguide and FIB and EBL are used to fabricate nanoscale stripe waveguides. Due to the nanoscale nature of the waveguides, UV lithography couldn't be used fabricate the desired structures. Detailed fabrication processes for individual waveguide structures produced in this thesis will be explained thoroughly in Chapters 4-6 and the **Supplementary section**.

This concludes the background literature and experimental and theoretical techniques used in the author's published papers used in this examination. **The overall aim of this thesis is to optimise plasmonic waveguides for nano-optical applications**. **Chapters 3** will describe the theoretical approach to understand the quantum dot - gap

plasmon interaction, and methods for controlling the propagation of plasmons along plasmonic gap waveguides. **Chapter 4** is based on optimising nanoscale stripe waveguides to support long range bound SPP mode and comparing the efficiencies of two excitation techniques to generate the desired LRSPP mode. **Chapter 5** is based on experimentally studying the QD-LRSPP interaction, mainly the effect of the spacer layer in coupling strength and Chapter 6 deals with the design of a plasmonic refractive index sensor based on stripe waveguides.

Chapter 3: Numerical analysis of gap plasmon-Quantum dot interaction

3.1 Simulation of gap plasmon coupling with a quantum dot

The authors listed below have certified* that:

1. they meet the criteria for authorship in that they have participated in the conception, execution, or interpretation, of at least that part of the publication in their field of expertise;
2. they take public responsibility for their part of the publication, except for the responsible author who accepts overall responsibility for the publication;
3. there are no other authors of the publication according to these criteria;
4. potential conflicts of interest have been disclosed to (a) granting bodies, (b) the editor or publisher of journals or other publications, and (c) the head of the responsible academic unit, and
5. they agree to the use of the publication in the student's thesis and its publication on the QUT ePrints database consistent with any limitations set by publisher requirements.

In the case of this chapter:

Simulation of a gap plasmon coupling with a quantum dot

Chamanei S. Perera and K. C. Vernon, Proc. SPIE 8923, Micro/Nano Materials, Devices, and Systems, 89230Z, (2013).

Contributor	Statement of contribution*
Chamanei Perera	wrote the manuscript, conducted numerical and data analysis
Signature	
Date	
Kristy Vernon	Originally suggested the idea, aided in simulations, data analysis, interpretation of results and paper writing

Principal Supervisor Confirmation

I have sighted email or other correspondence from all Co-authors confirming their certifying authorship.

Kristy Vernon		17 July 2015
Name	Signature	Date

Simulation of the gap plasmon coupling with a quantum dot

C. Perera and K. C. Vernon

Applied Optics and Nanotechnology Group, Science and Engineering Faculty, Queensland University of Technology, Australia.

ABSTRACT

Active control of plasmon propagation via coupling to Quantum Dots (QDs) is a hot topic in nano-photonic research. When a QD is excited it acts like a dipole emitter. If this excited QD is placed near a metallic waveguide structure, it can decay either radiatively into bulk electromagnetic radiation, non-radiatively into heating of the metal or, of interest to this project, into a plasmon mode (γ_{pl}). By altering the position of the QD it is possible to optimise the decay into the plasmon mode.

In this paper we present a system with a QD placed within the vicinity of a single mode Gap Plasmon Waveguide (GPW). First, we constructed a 2D finite element modelling simulation to find γ_{pl} using COMSOL MULTIPHYSICS for symmetric GPW structures with varying width (w) of the gap and distance of the QD to the waveguide surface (d). We then constructed a 3D model to calculate total rate of spontaneous emission of a QD (γ_{tot}) and determine spontaneous emission β factor, which is the ratio between γ_{pl} and all possible decay channels. It is shown that the decrease in width of the gap results in much larger β factor. As the gap width decreases, fraction of modal power in the metal increases slowing down the plasmon mode resulting in an enhancement in coupling efficiency. The optimized β factor for a square metallic slot waveguide is estimated up to 80%.

Keywords: Gap plasmon waveguide, quantum dots, spontaneous emission.

1. INTRODUCTION

A plasmon is a coherent oscillation of light interacting with the conduction electrons of a metal. Surface Plasmon Polaritons (SPPs) are a particular type of plasmon which propagates at a metal-dielectric interface[1]. SPPs can exist at the interface where the dielectric permittivities of the two isotropic media in contact are opposite to each other[2]. Although conductive materials support plasmons, coinage metals such as gold and silver are mostly associated with plasmonics since their plasmon resonances lie closer to the visible region of the EM spectrum enabling standard optical excitation and detection methods[2].

Different subwavelength metallic structures like v-groove, stripe, gap and nanowires are extensively studied despite the intrinsic losses of metals [3-6]. These nanostructures can be used to create nano-scale optical devices for photonics and sensing applications [7]. The plasmons enable dramatic concentration of EM field at the interface and slow motion of charge-density waves, enabling the study of light matter interaction at single emitter single photon level[7].

Micro/Nano Materials, Devices, and Systems, edited by James Friend, H. Hoe Tan, Proc. of SPIE
Vol. 8923, 89230Z · © 2013 SPIE · CCC code: 0277-786X/13/$18 · doi: 10.1117/12.2033300

Plasmons can be used in nano-circuitry. QDs enable the control of plasmon propagation, and could be implemented to perform Boolean operations[8, 9]. It is well known that emission properties of a quantum emitter can be manipulated by modifying the photonic environment[10]. According to the theory, if an excited QD is placed in close proximity to a metallic surface, there are three decay channels[11].

1. Direct optical emission into free space
2. Damped non-radiative decay due to ohmic losses in conductor
3. Spontaneous emission into guided plasmons in the plasmon waveguide.

Non-radiative losses become significant when the separation between the QD and plasmon waveguide is very close[11]. This can be rectified by placing the QD in an optimal position[11]. Fraction of spontaneous emission rate of the excited QD decay into plasmon mode is called spontaneous emission β factor[12]. This paper aims to model spontaneous emission of a QD placed in proximity to a gap plasmon waveguide and optimise the β factor.

2. METHOD

Gap plasmon waveguide, QD and their interactions were modelled in COMSOL MULTIPHYSICS using finite elemental method described by Chen *et al*[12]. The GPW was single mode and the plasmon experienced low losses in order to use Dyadic Green's function for plasmon field. Spontaneous β factor is defined as the normalised rate of spontaneous emission of a QD (γ_{tot}) into a fundamental plasmon (γ_{pl}). These values are normalised to the decay rate of a QD in vacuum (γ_0).

$$\beta = \gamma_{pl} / \gamma_{tot} \quad \text{(i)}$$

γ_{pl} can be found using electric dyadic Green's function. Numerical analysis of this is shown by Chen *et al*.

$$\gamma_{pl}(x_{QD},y_{QD}) = 3\pi\varepsilon_0 |E_y(x_{QD},y_{QD})|^2 / \{k_0^2 \int_A (\boldsymbol{E} \times \boldsymbol{H}^*).\hat{\mathbf{z}}\, dA\} \quad \text{(ii)}$$

where, k_0 is the wavenumber in vacuum, $\hat{z}$ is the unit vector in z-direction (Figure 1), and A is the transverse plane of the waveguide. The QD is modelled as a short line current oriented along y (Fig. 1). In order to determine the main electric field component of the QD (E_y) and to find the integration over the transverse plane to the waveguide (x-y plane), 2D finite elemental modelling simulation is used in this paper. In the 2D structure, it is assumed that the waveguide is infinitely long.

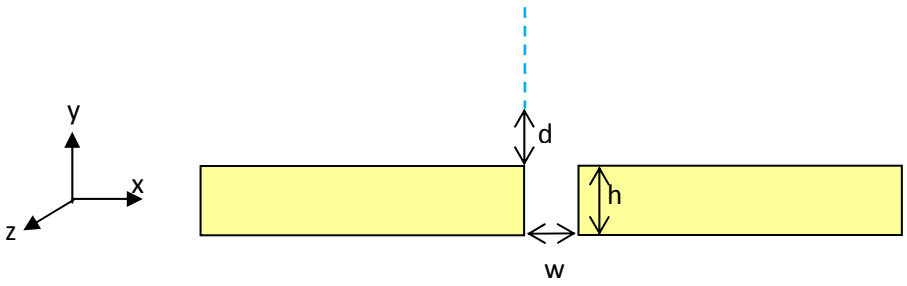

Fig. 1: 2D schematic of a symmetric GPW. w=h= 50 nm, d=5 nm unless stated otherwise. $E_{x,y,z}(x_{QD}, y_{QD})$ is measured along the dash line.

To calculate β, we have to determine γ_{tot}. We implement a 3D model in order to accommodate radiation and non-radiative modes. Total decay rate of the QD is determined using total power dissipation of the current source coupled to the waveguide[12]. Then it is normalised by the total power dissipation by the same source in vacuum[12].

$$\gamma_{tot} = \{ 0.5 \int_v \mathrm{Re}(\mathbf{J}^* . \mathbf{E}_y)\, dV \} / \{0.5 \int_v \mathrm{Re}(\mathbf{J}^* . \mathbf{E}_{0y})\, dV\} \quad \text{(iii)}$$

where $\mathbf{E}_{0y}$ is the main electric field component of QD in vacuum and $\boldsymbol{J}$ is the current source. In our model we used 1A line current with 1 nm length. Size of the line current was chosen sufficiently small to avoid higher order modes[12, 13]. This simplifies Eq. (iii) to

$$\gamma_{tot} = \{ \int_v \mathrm{Re}(\mathbf{E}_y)\, dI \} / \{0.5 \int_v \mathrm{Re}(\mathbf{E}_{0y})\, dI\} \quad \text{(iv)}$$

with dI representing the line integration over the current source. The length of the waveguide is taken so that plasmons propagated will not reflect off the ends of the waveguide and interfere with the QD. To minimise the non-radiative losses and optimise the QD-plasmon coupling, position of the QD was varied by varying the distance between the QD and the waveguide surface.

3. RESULTS

3.1 The spontaneous emission of a QD into a plasmon mode (γ_{pl})

The normalised rate of spontaneous emission of a QD into the fundamental mode of a symmetric gap plasmon waveguide was calculated. We considered a QD emission wavelength of 633 nm and the refractive indices of the waveguide $n_1 = 0.197+3.09i$ [14] representing gold and dielectric $n_2 = 1$ representing air. Height (h) of the waveguide kept at 50 nm throughout the paper. Figure 2 shows the schematic of the QD positioned above the centre of the gap edge. Distance to the QD from waveguide surface kept 5 nm unless stated otherwise.

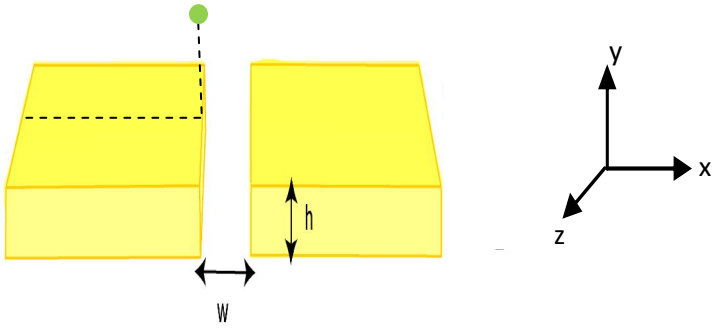

FIG. 2: Schematic diagram of the gap plasmon waveguide. QD placed half way along the edge of the gap, 5nm above the waveguide

The field of the fundamental mode is shown in Fig. 3. Field is more concentrated on the edges for larger width. Since the QD is positioned 5 nm on top of the edge of the waveguide, coupling to plasmon mode should be stronger than the QD sitting 5 nm on top of the centre with increasing width.

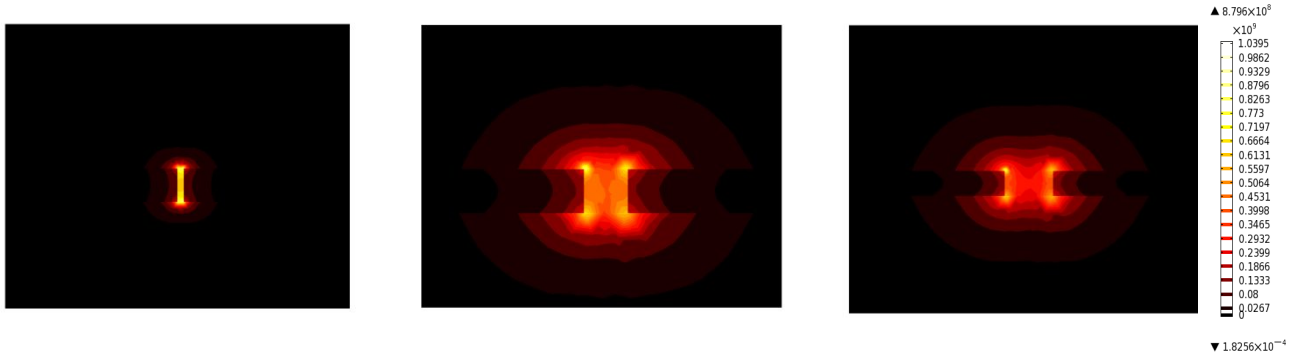

(a) (b) (c)

FIG. 3: Contour plots of the E_y component of the electric field distribution. (a) w= 10 nm, (b) w= 50 nm, and (c) w= 100 nm.

Wavenumber and the propagation length of the guided mode of the waveguide for various gap widths are studied in figure 4 below.

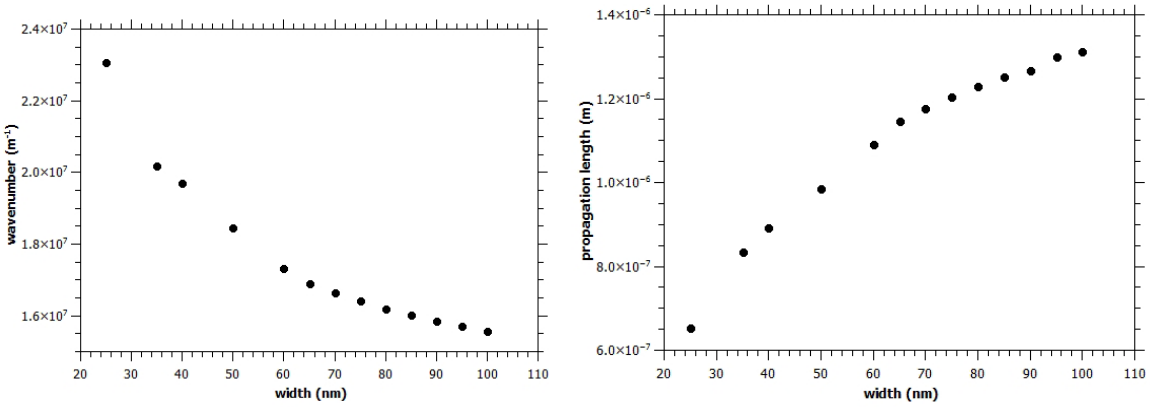

(a) (b)

FIG. 4: a) Wavenumber of the fundamental mode of the GPW versus width. b) Plot of the propagation length versus width

As the width of the slot increase the wavenumber decreased and the propagation distance increased, refer Fig. 4 (a) and (b). Propagation length decreased with decreasing slot dimensions due to the fact that the fraction of modal power in the metal increases hence slowing down the plasmonic mode. This will enhance the coupling efficiency of the quantum dot by increasing the Local Density of States (LDOS).

Large wavenumbers mean smaller group velocities which also lead to larger LDOS. This should lead to a higher γ_{pl} for smaller width which is shown in Fig. 5.

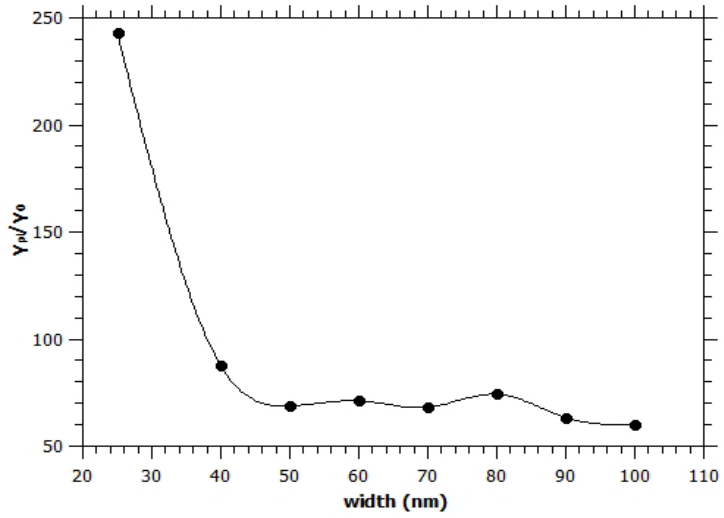

FIG. 5: Plot of the γ_{pl}/γ_0 versus width.

3.2 Spontaneous emission β factor

In order to determine the likelihood of an excited QD decaying into a plasmon, the spontaneous emission β factor must be calculated. Total rate of spontaneous emission can be computed with aid of a 3D model using Eq. (iv). β can be found using γ_{pl} and γ_{tot}.

Calculated β factor with varying width of the slot is shown in figure 6.

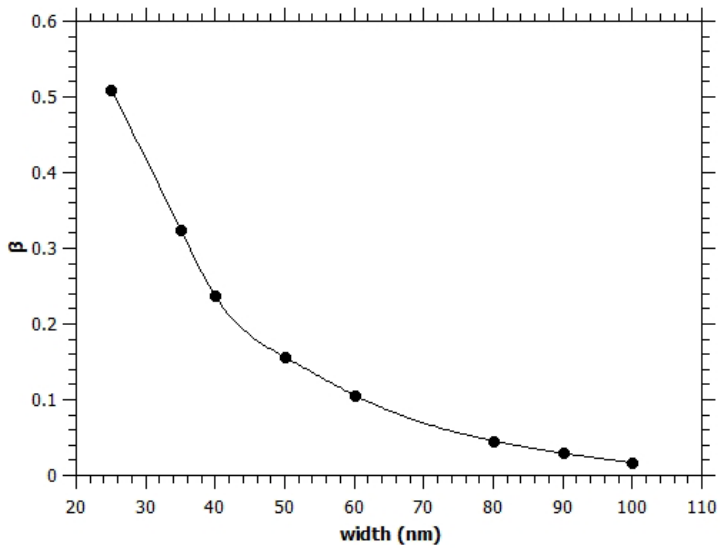

FIG. 6: Plot of the β versus width.

β factor is higher for smaller slot width, i.e strong coupling between the QD and fundamental plasmon according to figure 5. This supports the idea of higher γ_{pl} at lower values of width. Therefore it is shown that, widening the gap results in lowering the QD- plasmon coupling.

As the final step, the position dependence of QD to the waveguide surface on coupling to fundamental plasmon is determined. As can be seen from figure 7, the excited QD preferentially couple to fundamental plasmon when the QD is placed 10 nm above the waveguide edge. When the QD is positioned less than 10 nm away from the waveguide, the non-radiative decay of spontaneous emission in to ohmic losses of the waveguide is significant. This will decrease the coupling of spontaneous emission of QD in to guided plasmon mode of the waveguide hence lowering the β factor. At very large distances QD is positioned far from the evanescent surface plasmon mode tail. Therefore, spontaneous emission of QD coupling in to plasmon mode is lower at larger distances.

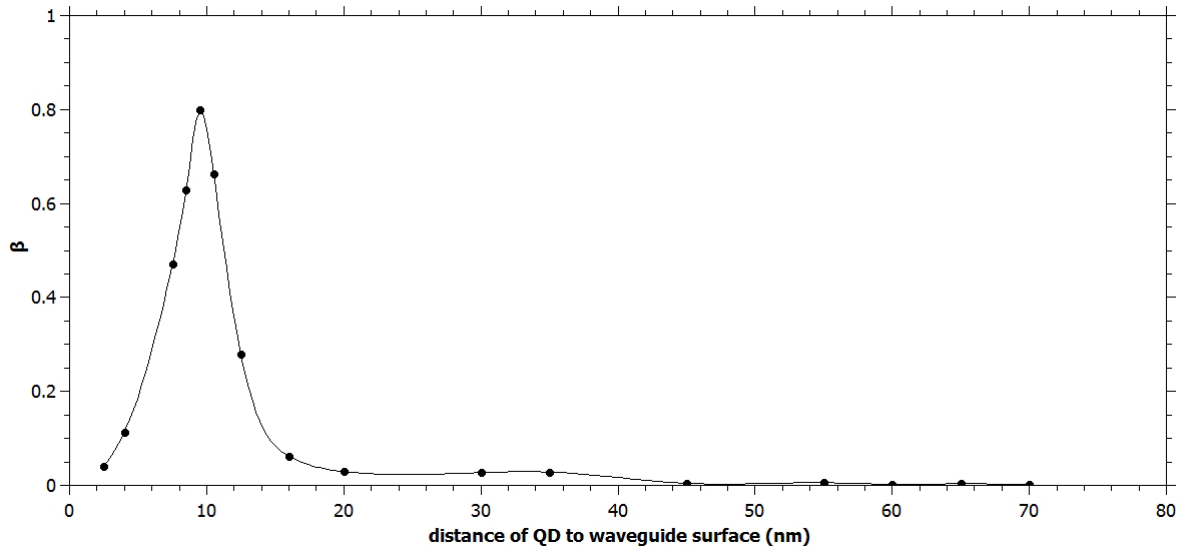

FIG. 7: Plot of the β versus distance of QD to waveguide surface; QD placed on the edge of the waveguide. w = h = 50 nm for the GPW.

4. CONCLUSIONS

The spontaneous emission of a QD into a plasmon mode (γ_{pl}) and spontaneous emission β factor have been determined for a symmetric gap plasmon waveguide with varying gap width.

When the gap width is high, fraction of modal power inside the metal is lower resulting in lower coupling between excited QD and fundamental plasmon.

It is clear that when the gap width is higher, field is more concentrated on the edges. If the QD is positioned directly above the edge, the rate of excited QD coupling to plasmon is more efficient than placing QD above the middle of the gap.

The conciliation between γ_{pl} and γ_{tot} is essential in designing a QD-plasmon coupling based circuit. We have shown that, in optimally placed QD, decay rate in to plasmon is significantly enhanced, far exceeding radiative decay and non-radiative rates. By varying distance between QD and waveguide surface a β factor of 0.8 or coupling efficiency of 80% can be achieved.

It is shown that β factor is higher for small waveguide width. Trade-off between gap dimensions and the emitter-waveguide surface distance can increase the beta factor. It is expected to numerically analyse effect of gap dimension further.

ACKNOWLEDGEMENT

C. Perera would like to acknowledge Angus Mcleod and Martin Kurth for their useful discussions about COMSOL modelling and the support from the QUT High Performance Computer Facility including HPC team. Authors would also like to acknowledge the support of Australian Research Council, through grant DP110101454.

References:

1. Maier, S.A., [Plasmonics: Funadamentals and applications], Springer, New York, 1-233 (2007).
2. Zayats, A.V. and Smolyaninov, II, "Near-field photonics: surface plasmon polaritons and localized surface plasmons", Journal of Optics a-Pure and Applied Optics, 5(4), 16-50 (2003).
3. Bozhevolnyi, S.I., "Effective-index modeling of channel plasmon polaritons", Optics Express Online, 14(20), 9467-9476 (2006).
4. Berini, P., "Plasmon-polariton waves guided by thin lossy metal films of finite width: Bound modes of asymmetric structures", Physical Review B, 63(12), 125417 (2001).
5. Veronis, G. and S. Fan, "Subwavelength plasmonic waveguide structures based on slots in thin metal films - art. no. 612308", Integrated Optics: Devices, Materials, and Technologies X, 6123, 12308-12308 (2006).
6. Barbic, M., et al., "Single crystal silver nanowires prepared by the metal amplification method", Journal of Applied Physics, 91(11), 9341-9345 (2002).
7. Atwater, H.A., "The promise of plasmonics", Scientific American, 296(4), 56-63 (2007).
8. Vernon, K.C., [Plasmonic Circuits: Manipulating light on the nanoscale in Nanotechnology in Australia], Pan Stanford: Singapore, 1-40 (2011).
9. Chang, D.E., et al., "Strong coupling of single emitters to surface plasmons", Physical Review B, 76(3), 035420-1 - 035420-26 (2007).
10. Purcell, E., Spontaneous emission probabilities at radio frequencies, in Confined Electrons and Photons], Springer, 839-839 (1995).
11. Akimov, A.V., et al., "Generation of single optical plasmons in metallic nanowires coupled to quantum dots", Nature, 450(7168), 402-406 (2007).
12. Chen, Y., et al., "Finite-element modeling of spontaneous emission of a quantum emitter at nanoscale proximity to plasmonic waveguides", Physical Review B, 81(12), 125431 (2010).
13. Martín-Cano, D., et al., "Resonance energy transfer and superradiance mediated by plasmonic nanowaveguides", Nano letters, 10(8), 3129-3134 (2010).
14. Palik, E.D., [Handbook of Optical Constants of solids, Volume I, II, and III: Subject Index and Contributor index], Elsevier Science and Tech, Maryland, 286-295 (1985).

3.2 Optimizing the Quantum dot-plasmon interaction in a nano gap waveguide

The authors listed below have certified* that:

6. they meet the criteria for authorship in that they have participated in the conception, execution, or interpretation, of at least that part of the publication in their field of expertise;
7. they take public responsibility for their part of the publication, except for the responsible author who accepts overall responsibility for the publication;
8. there are no other authors of the publication according to these criteria;
9. potential conflicts of interest have been disclosed to (a) granting bodies, (b) the editor or publisher of journals or other publications, and (c) the head of the responsible academic unit, and
10. they agree to the use of the publication in the student's thesis and its publication on the QUT ePrints database consistent with any limitations set by publisher requirements.

In the case of this chapter:

Optimizing the Quantum dot-plasmon interaction in a nano gap waveguide

- Chamanei S. Perera and K. C. Vernon, Proc. SPIE 9163, Plasmonics: metallic Nanostructures and their optical properties XII, 91632E, (2013).

Contributor	Statement of contribution*
Chamanei Perera	wrote the manuscript, conducted numerical and data analysis
Signature	
Date	
Kristy Vernon	Originally suggested the idea, aided in simulations, data analysis, interpretation of results and paper writing

Principal Supervisor Confirmation

I have sighted email or other correspondence from all Co-authors confirming their certifying authorship.

Kristy Vernon		17 July 2015
Name	Signature	Date

Optimizing the Quantum dot – plasmon interaction in a nano gap waveguide.

Chamanei S. Perera and Kristy C. Vernon

Plasmonic Device Group, Queensland University of Technology, Brisbane, QLD 4001

ABSTRACT

Spontaneous emission (SE) of a Quantum emitter depends mainly on the transmission strength between the upper and lower energy levels as well as the Local Density of States (LDOS)[1] . When a QD is placed in near a plasmon waveguide, LDOS of the QD is increased due to addition of the non-radiative decay and a plasmonic decay channel to free space emission[2-4]. The slow velocity and dramatic concentration of the electric field of the plasmon can capture majority of the SE into guided plasmon mode (Γ_{pl}).

This paper focused on studying the effect of waveguide height on the efficiency of coupling QD decay into plasmon mode using a numerical model based on finite elemental method (FEM). Symmetric gap waveguide considered in this paper support single mode and QD as a dipole emitter. 2D simulation models are done to find normalized Γ_{pl} and 3D models are used to find probability of SE decaying into plasmon mode (β) including all three decay channels. It is found out that changing gap height can increase QD-plasmon coupling, by up to a factor of 5 and optimally placed QD up to a factor of 8. To make the paper more realistic we briefly studied the effect of sharpness of the waveguide edge on SE emission into guided plasmon mode. Preliminary nano gap waveguide fabrication and testing are already underway. Authors expect to compare the theoretical results with experimental outcomes in the future.

Key words: Plasmonics, Quantum dots, Spontaneous emission

INTRODUCTION:

Surface plasmons can exist when the dielectric permittivities of the two isotropic media in contact have opposite signs. Due to the dramatic concentration of EM field at the interface, and slow motion of charge-density waves enable plasmons to interact with incoming light. Plasmons when coupled to photons can propagate along the metal-dielectric interface.

Plasmon waveguides provide sub-wavelength confinement in two dimensions and help to guide light in nanoscale. Trade-off between confinement and loss demands a prudent choice of waveguide geometry. Nano gap waveguides consist of a gap in a thin metal film which provides a good subwavelength localisation of the guided mode. Phase

Corresponding author: cp.hettiarachchige@qut.edu.au

Plasmonics: Metallic Nanostructures and Their Optical Properties XII, edited by Allan D. Boardman, Proc. of SPIE Vol. 9163, 91632E · © 2014 SPIE
CCC code: 0277-786X/14/$18 · doi: 10.1117/12.2060939

velocities of plasmons that propagate in a nanosized metallic gap strongly depend on the gap dimensions[5]. This means that by scaling the gap, the phase velocities can be controlled.

Spontaneous emission of a QD mainly depends on the strength of the upper and lower energy levels of the transition and the photonic environment[1]. It is possible to tailor the available number of states which emitting photon can occupy by changing the photonic environment. Similar example is keeping a QD near a plasmonic waveguide instead in a free space. It increases the number of decay channels for the excited QD [2, 4, 6, 7]. In addition to decaying in to free space, some of the spontaneous emission will be decayed non-radiatively in to heat losses of the metal. Majority of the SE will be captured by the plasmons on the metal surface and propagate as SPPs.

In this paper, we have focused on controlling plasmon propagation on a nano gap waveguide using a QD in near vicinity. Our aim is to study the effects of the symmetry of the gap waveguide, and the height of the gap on spontaneous emission coupling to surface plasmons and last not least optimise the SE-plasmon coupling by varying the distance between QD and waveguide surface.

METHOD:

The spontaneous emission of a QD into a plasmon mode (Γ_{pl}) can be determined using Green's Dyadic for the E-field for the plasmon mode;

$$\hat{\Gamma}_{pl}\left(x_{QD}, y_{QD}\right) = \frac{3\pi c \varepsilon_0 \mid E_y\left(x_{QD}, y_{QD}\right)\mid^2}{k_0^2 \int_A \left(\vec{E} \times \vec{H}^*\right)\hat{z} dA} \qquad \text{(i)}$$

where ε_0 is the permittivity of vacuum, k_0 is the wavenumber in vacuum, $\hat{z}$ is the unit vector in z direction and *A* is the transverse plane of the waveguide with the well-defined field components. $\hat{\Gamma}_{pl}$ represents the normalised Γ_{pl} with respect to vacuum (Γ_0). Mathematical analysis of determining $\hat{\Gamma}_{pl}$ is shown by *Cheng et al*.[2].

Probability of QD excited a single plasmon mode is given by spontaneous emission β factor

$$\beta = \frac{\hat{\Gamma}_{pl}}{\hat{\Gamma}_{tot}} \qquad \text{(ii)}$$

$\hat{\Gamma}_{tot}$ is the sum of all three decay modes.

Determining $\hat{\Gamma}_{pl}$ is imperative in optimising the QD-waveguide coupling. The spontaneous emission β factor defines the possibility of rate of spontaneous emission of QD into the guided plasmon mode[2]. β factor of 1 means the QD decays totally into a plasmon mode[2].

Nano gap waveguide considered in this model is less than (or equal) 100 nm cross section ensuring a single bound plasmon mode and length is sufficiently long enough to assume propagating SPPs do not reflect and couple back to QD. QD is considered as a dipole of 1 nm line current of 1 A. Size of the QD should be less than 2 nm to avoid higher order multiple modes[2].

Symmetric waveguide consisted of gold with refractive index n_1= 0.2567+6.8191i surrounding dielectric medium of SiO_2 with n_2= 1.53[8] (refer figure 1). Gap width kept constant at 50 nm. Gap height varied from 10 nm to 100 nm. Emission wavelength of the QD was chosen to be 1 μm.

2D finite elemental modelling technique was used to model the fundamental plasmon mode fields and determine $\hat{\Gamma}_{pl}$. Using COMSOL multiphysics it was shown that fundamental mode has a strong E_y component with maximal field along the waveguide edges (refer Figure 2). QD emission components parallel in y direction can be easily coupled to fundamental plasmon mode of the waveguide. So, QDs were placed 5 nm top of the waveguide edge (unless stated otherwise) to maximise the QD-plasmon interaction (refer figure 1 and 2).

A 3D model was used to accommodate SE's radiative decay channel and non-radiative decay into resistive heat of the metal.

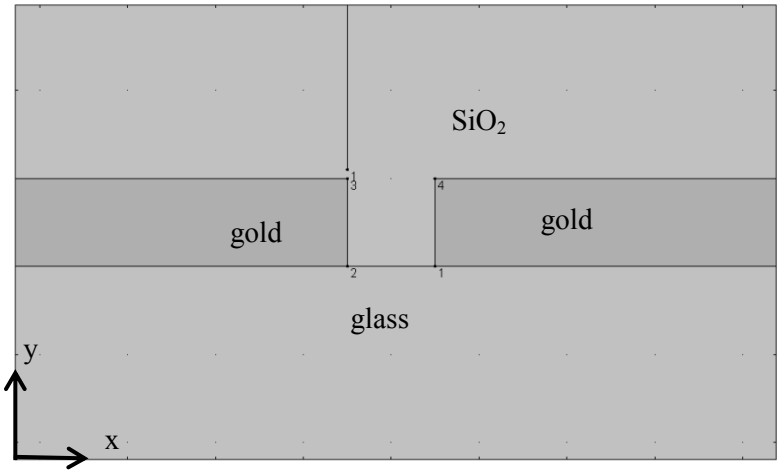

Figure 1: Schematic diagram of a symmetric waveguide. E_y measured along the line.

RESULTS:

According to Eq. 1, $\hat{\Gamma}_{pl}$ depends on the field strength in the position of the QD. Symmetric waveguides have higher field concentration at the metal/ SiO_2 interface corners (refer Figure 2).

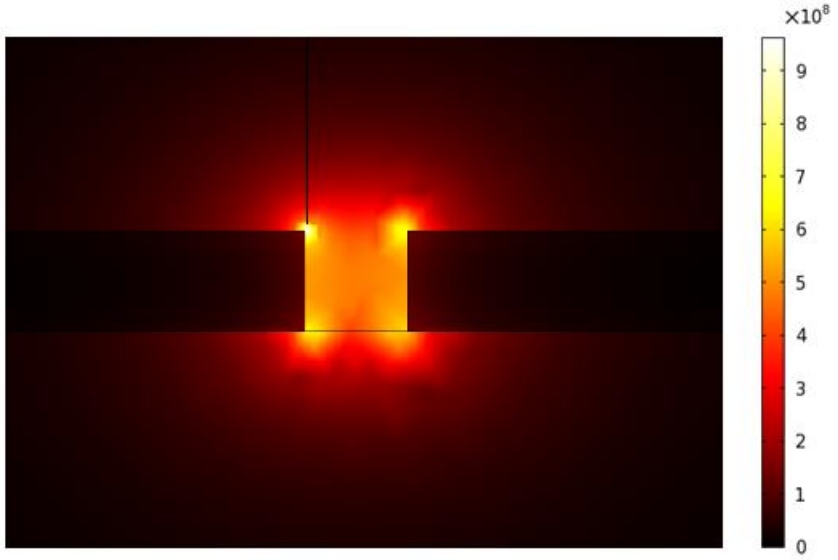

Figure 2: Field plots of the $|E_y|$ for symmetric gap waveguide. Intensity of the field is measured along the line indicated. Waveguide has 50 nm x 50 nm cross section.

Wavenumber and propagation length of the fundamental mode of the two waveguides provide insight into the QD-plasmon coupling. Wavenumber and plasmon propagation length is shown in Figure 3 below. Propagation length defines as the distance plasmon has travelled when its electric field amplitude drops factor of e. Higher wavenumber represents slower group velocity. When the group velocity is lower, plasmon can capture more photons from the spontaneous emission leading to higher LDOS. Slow group velocity plasmons have low propagation length. According to the Figure 3, wavenumber decreases with increasing gap height. When the gap height is increased, plasmons tend to localise in the gap area and are freer to propagate with higher group velocity.

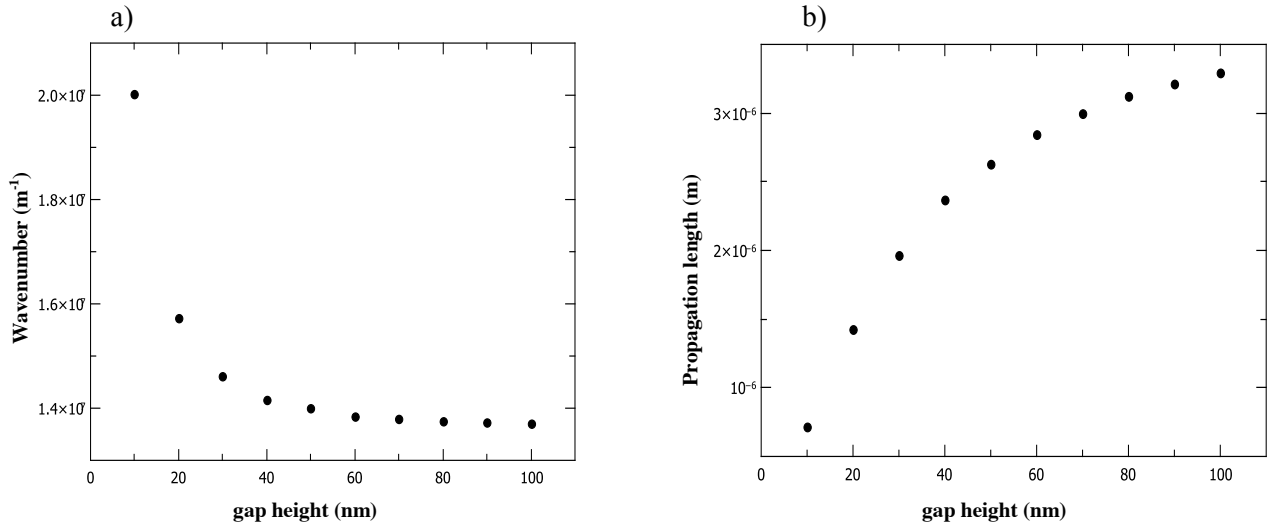

Figure 3: (a) Wavenumber of the fundamental mode vs. gap height, (b) propagation length vs gap height.

Normalised Γ_{pl} for symmetric gap waveguides are shown in Figure 4 (a) below. As expected from previous deductions, normalised rate of SE coupling into plasmon mode is decreased with increasing gap height. Following the trend of $\hat{\Gamma}_{pl}$, probability of plasmon coupling to SE of the QD decreases with increasing gap height as evidenced in Figure 4 (b). At lower gap height, low group velocity of plasmons captures majority of the SE in to guided plasmon mode.

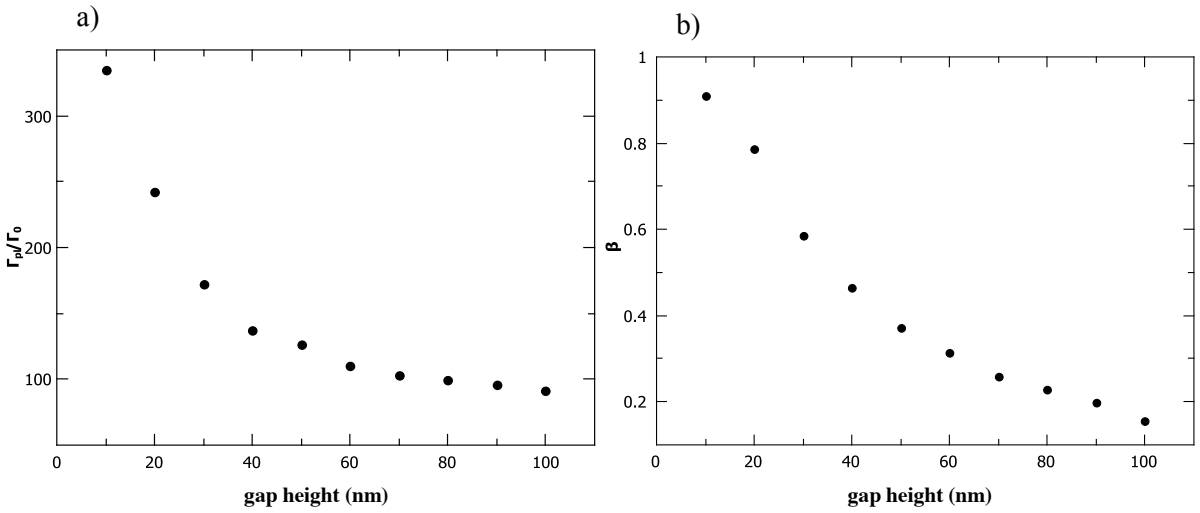

Figure 4: (a) Normalised Γ_{pl} vs gap height (b) β vs gap height.

Until this point, distance between QD and waveguide surface (d_s) was kept fixed at 5 nm. Non-radiative decay channel is significant when the distance between QD and metal surface is low. In this section we fixed the gap cross section at 50

nm x 50 nm and varied d_s from 2.5 nm to 70 nm to observe the effect of d_s in β. As shown in Figure 5, when d_s is lower than 10 nm, non-radiative decay channel is significant reducing β. When d_s is much higher than 10 nm, as the field strength low. In the system, coupling efficiency has increased by a factor of 3 by optimally placing the QD.

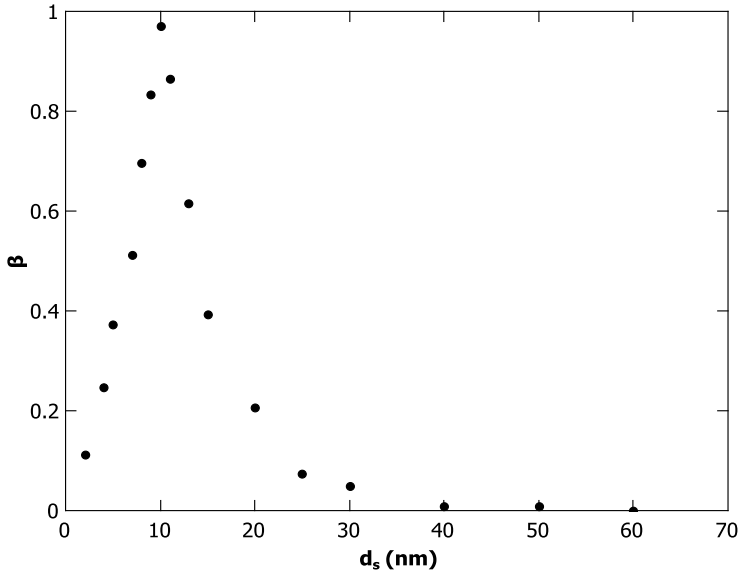

Figure 5: Dependence of β on distance between QD and waveguide surface.

In reality, it is harder to fabricate gap waveguides with 90° sharp edges. We introduced roundness with radius r_s less than or equal to height of the gap to each edge (inset of figure 6) and calculated normalised rate of SE coupling into plasmon mode. As depicted in figure 6, rate drops by factor of 2 at 5 nm edge roundness. The mode exhibits a strong concentration at the edges but strength of the electric field around the edge is slightly weakened at round edges. We could conclude that sharpness has a significant effect on the QD- gap plasmon coupling. Even though it is hard to control the detailed shape of the sharp edge in the fabrication process, it is better to make the edges sharp as possible for higher QD emission in to plasmon mode decay rate.

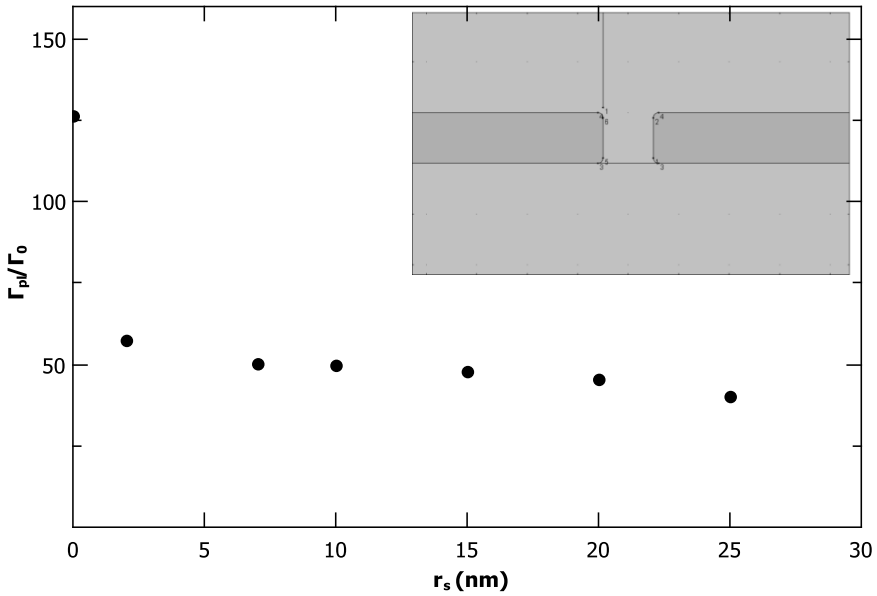

Figure 6: Normalised Γ_{pl} vs edge roundness. Inset provides a schematic diagram of the 2D waveguide with rounded edges.

DISCUSSION:

In conclusion, optimally placed quantum dot can enhance the QD – plasmon interaction. Furthermore, smaller gap heights increase the number of local density of states hence increase the probability of capturing spontaneous emission in to guided plasmon mode in waveguide. Maintaining the symmetry of the waveguide can increase the optimal coupling efficiency up to 97%. Finally, sharpness of the edge has a significant impact of plasmon mode field strength. In fabricating process, Even though it is hard to control the detailed shape of the sharp edge, it is better to make the edges sharp as possible for higher QD emission in to plasmon mode decay rate. Authors expect outcome of this paper would be useful in active control of plasmon propagation in plasmonic waveguides.

ACKNOWLEDGEMENT:

C. Perera would like to acknowledge Angus Mcleod and Martin Kurth for their useful discussions about COMSOL modelling and the support from the QUT High Performance Computer Facility including HPC team. Authors would also like to acknowledge the support of Australian Research Council, through grant DP110101454.

REFERENCES:

1. Purcell, E., Spontaneous emission probabilities at radio frequencies, in Confined Electrons and Photons], Springer US, 839-839 (1995).
2. Chen, Y., et al., "Finite-element modeling of spontaneous emission of a quantum emitter at nanoscale proximity to plasmonic waveguides", Physical Review B, 81(12), 125431 (2010).
3. Jun, Y.C., et al., "Nonresonant enhancement of spontaneous emission in metal-dielectric-metal plasmon waveguide structures", Physical Review B, 78(15), (2008).
4. Vernon, K.C., et al., "Simulations of the effect of waveguide cross-section on quantum dot–plasmon coupling", Journal of Applied Physics, 110, 074315 (2011).
5. Jun, Y.C., R. Pala, and M.L. Brongersma, "Strong Modification of Quantum Dot Spontaneous Emission via Gap Plasmon Coupling in Metal Nanoslits", Journal of Physical Chemistry C, 114(16), 7269-7273 (2010).
6. Akimov, A.V., et al., "Generation of single optical plasmons in metallic nanowires coupled to quantum dots", Nature, 450(7168), 402-406 (2007).
7. Perera, C.S., K.C. Vernon, and A. Mcleod, "Simulations of the spontaneous emission of a quantum dot near a gap plasmon waveguide", Journal of Applied Physics, 115(5), 054314 (2014).
8. Palik, E.D., [Handbook of Optical Constants of Solids: Index], Access Online via Elsevier, (1998).

3.3 Simulations of the spontaneous emission of a quantum dot near a gap plasmon waveguide

The authors listed below have certified* that:

11. they meet the criteria for authorship in that they have participated in the conception, execution, or interpretation, of at least that part of the publication in their field of expertise;
12. they take public responsibility for their part of the publication, except for the responsible author who accepts overall responsibility for the publication;
13. there are no other authors of the publication according to these criteria;
14. potential conflicts of interest have been disclosed to (a) granting bodies, (b) the editor or publisher of journals or other publications, and (c) the head of the responsible academic unit, and
15. they agree to the use of the publication in the student's thesis and its publication on the QUT ePrints database consistent with any limitations set by publisher requirements.

In the case of this chapter:

Simulations of spontaneous emission of a quantum dot near a gap plasmon waveguide

Chamanei S. Perera, K. C. Vernon and Angus McLeod, Journal of Applied Physics **115**, 054314

(2014)

_____

Contributor	Statement of contribution*
Chamanei Perera Signature Date	wrote the manuscript, conducted numerical and data analysis
Kristy Vernon	Originally suggested the idea, aided in simulations, data analysis, interpretation of results and paper writing
Angus McLeod	Aided in simulations

Principal Supervisor Confirmation

I have sighted email or other correspondence from all Co-authors confirming their certifying authorship.

Kristy Vernon		17 July 2015
Name	Signature	Date

3.3 Simulations of the spontaneous emission of a quantum dot near a gap plasmon waveguide

The authors listed below have certified* that:

11. they meet the criteria for authorship in that they have participated in the conception, execution, or interpretation, of at least that part of the publication in their field of expertise;
12. they take public responsibility for their part of the publication, except for the responsible author who accepts overall responsibility for the publication;
13. there are no other authors of the publication according to these criteria;
14. potential conflicts of interest have been disclosed to (a) granting bodies, (b) the editor or publisher of journals or other publications, and (c) the head of the responsible academic unit, and
15. they agree to the use of the publication in the student's thesis and its publication on the QUT ePrints database consistent with any limitations set by publisher requirements.

In the case of this chapter:

Simulations of spontaneous emission of a quantum dot near a gap plasmon waveguide

Chamanei S. Perera, K. C. Vernon and Angus McLeod, Journal of Applied Physics **115**, 054314

(2014)

_____

Contributor	Statement of contribution*
Chamanei Perera	wrote the manuscript, conducted numerical and data analysis
Signature	
Date	
Kristy Vernon	Originally suggested the idea, aided in simulations, data analysis, interpretation of results and paper writing
Angus McLeod	Aided in simulations

Principal Supervisor Confirmation

I have sighted email or other correspondence from all Co-authors confirming their certifying authorship.

Kristy Vernon		17 July 2015
Name	Signature	Date

Simulations of the spontaneous emission of a quantum dot near a gap plasmon waveguide

Chamanei S. Perera,[a] Kristy C. Vernon, and Angus Mcleod
Plasmonic Device Group, Queensland University of Technology, GPO box 2434, Brisbane, Queensland

(Received 7 November 2013; accepted 24 January 2014; published online 7 February 2014)

In this paper, we modeled a quantum dot at near proximity to a gap plasmon waveguide to study the quantum dot-plasmon interactions. Assuming that the waveguide is single mode, this paper is concerned about the dependence of spontaneous emission rate of the quantum dot on waveguide dimensions such as width and height. We compare coupling efficiency of a gap waveguide with symmetric configuration and asymmetric configuration illustrating that symmetric waveguide has a better coupling efficiency to the quantum dot. We also demonstrate that optimally placed quantum dot near a symmetric waveguide with 50 nm × 50 nm cross section can capture 80% of the spontaneous emission into a guided plasmon mode. © *2014 AIP Publishing LLC*.
[http://dx.doi.org/10.1063/1.4864259]

I. INTRODUCTION

Spontaneous emission rate of an excited quantum dot (QD) depends on transition strength between two states and Local Density of States (LDOS).[1] Interaction between emitter and the field can be enhanced by enhancing the number of available density of states into which photons can be emitted. This can be done by altering the density of the electromagnetic modes of the environment. Surface plasmon is an excitation of charge density waves with a tight electromagnetic field confinement.[2] By placing a QD in near vicinity of a subwavelength structure that supports SPs, it is possible to manipulate the photonic environment of the QD resulting in increasing the spontaneous emission.

Surface plasmons have potential applications in near field imaging, sensing, solar cells, and waveguiding.[3,4] Plasmonic waveguides are used in plasmonics circuitry to achieve miniaturization.[2] A subwavelength waveguide with metal-dielectric-metal configuration supports highly confined gap modes.[5]

There are three possible decay channels for an excited QD when it is placed at proximity to a gap waveguide. First, radiative decay of spontaneous emission into free space.[6] Second, non-radiative decay due to lossy metal.[6] Third is the most important decay channel which is decay into a guided plasmonic mode of the waveguide.[7] Experimentally, Jun *et al*. have shown QD-plasmon coupling for QD films on gap plasmon waveguides.[8] In their experiment, they used a pump laser polarized parallel to the gap, and the resultant collected QD emission (centered at 610 nm) was polarized normal to the slit. When they decreased the slit width, the life time of the QD decreased and the QD emission became more polarized normal to the gap. Gap modes are polarized normal to the gap so the fact that they got strongly normally polarized light from the gap is a clear example that QD emission is coupled to the gap mode.[8] Similar results have been shown by Gruber *et al*. for nanowires.[9]

Jun *et al*. have theoretically studied the spontaneous emission of a QD near a metal gap plasmon waveguide using Fermi's golden rule and FDTD simulations.[10] Their theoretical analysis is based on simplifying assumptions for the LDOS and quantum efficiency of the quantum emitter.[11] In this paper, we extend this model further by using the Green's dyadic function and finite element modeling simulations.[12] To the author's knowledge, this work presents the first model of the QD-GPW coupling that takes in to account all decay channels. In this paper, we investigate how to increase the coupling efficiency between the QD and GPW by altering gap dimensions, symmetry of the waveguide and distance between emitter and waveguide surface.

This paper focused on studying the effect of waveguide dimensions on the efficiency of coupling QD decay into plasmon mode. The numerical model we used was based on the finite elemental method (FEM) described in Chen *et al*.[12] Gap Plasmon waveguide (GPW) considered has dimensions less than 100 nm in width and height ensuring it supports single mode.[13] Like Jun *et al*.,[8,10] we found that the polarization of the QD emission significantly affected the QD-plasmon coupling.

II. THEORY

Electric field dyadic Green's function for one guided plasmon was constructed using electric field.[12] In calculating projecting LDOS for the plasmonics mode, it is assumed that the dipole emitter is oriented along y axis [refer Figure 1]. Probability of QD exciting a single plasmon mode is given by spontaneous emission β factor[12]

$$\beta = \frac{\hat{\gamma}_{pl}}{\hat{\gamma}_{tot}}, \tag{1}$$

where $\hat{\gamma}_{pl}$ represents the QD emitter decay into plasmon channel and $\hat{\gamma}_{tot}$ is the sum of all decay channels. $\hat{\gamma}_{pl}$ and $\hat{\gamma}_{tot}$ are normalized with respect to the decay rate of a QD in vacuum (γ_0).

[a]Author to whom correspondence should be addressed. Electronic mail: cp.hettiarachchige@qut.edu.au.

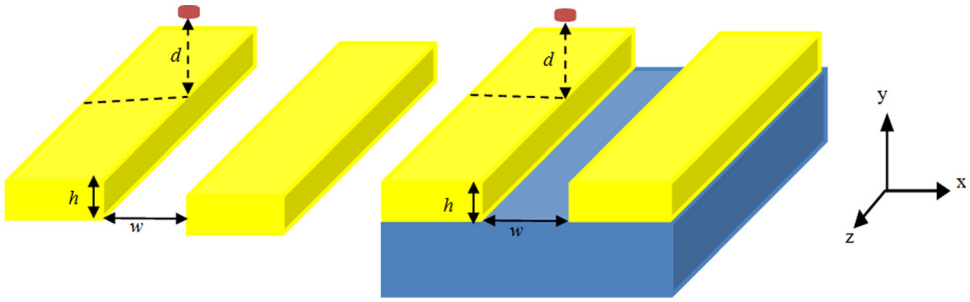

FIG. 1. Schematic diagram of a QD sitting on top of the edge of the symmetric GPW and asymmetric waveguide.

Numerical analysis for determining $\hat{\gamma}_{pl}$ is shown explicitly elsewhere.[12] Normalized by the spontaneous emission decay rate in the vacuum, the emission enhancement due to plasmonics excitation is given in

$$\hat{\gamma}_{pl}(x_{QD}, y_{QD}) = \frac{3\pi c\varepsilon_0 |E_y(x_{QD}, y_{QD})|^2}{k_0^2 \int_A (\vec{E} \times \vec{H}^*).\hat{z}\, dA}, \qquad (2)$$

where ε_0 is the permittivity of vacuum, k^0 is the wavenumber in vacuum, $\hat{z}$ is the unit vector in z direction, and A is the transverse plane of the waveguide with the well-defined field components. In Jun *et al.*, they show the importance of positioning the Quantum dots in regions of highly localized field.[8] In particular, they show that by changing the polarization of the input beam they can excite different GPW modes. Depending on the polarization and the GPW mode excited, different QDs will couple to the GPW. In our work, we look at QD coupling to the fundamental mode of the GPW. The fundamental mode of the GPW [Figures 2 and 3] has a strong E_y component with maximal field along the waveguide edges. By placing QDs along the waveguide edges, we can obtain strong QD-plasmon coupling. We choose the QD's emission axis along the y-direction. For other emission axes, it was found that the QD-plasmon coupling was significantly less.

When the QD is placed on top of the waveguide edge, components of the QD emission parallel to y direction can strongly couple to the plasmon modes of the GPW. QD is placed such that QD-plasmon coupling is maximum. According to the field plots [refer Figures 2 and 3], maximum intensity of electric field was at the edge of the waveguide. So the QD was placed 5 nm (unless stated otherwise) above the waveguide edge [refer Figure 1]. Integration in Eq. (2) takes over the entire x-y plane. A 2D finite elemental modeling is used to determine the fundamental plasmon mode fields. Waveguide was considered to be infinitely long so that plasmon reflected from the end of the waveguide will not couple back to the QD.

Numerical method was constructed using dyadic Green's function for guided plasmon mode since field components tend to concentrate more on the metallic edges and decay at the borders for larger domains.[12] Radiation mode field components do not vanish even in larger modeling domain.[12] Therefore, it is necessary to build a 3D model to accommodate radiation mode decay in calculating β factor. According to Eq. (1), total decay rate of the QD near metallic waveguide should be calculated in order to calculate β factor. Assuming quantum emitter as a current source at near proximity to the waveguide, total decay rate can be found from the total power dissipation of the current source coupled to the metallic waveguide.[12] It should be normalized with the total power dissipation of the same current source when it is in vacuum. It is important to construct the

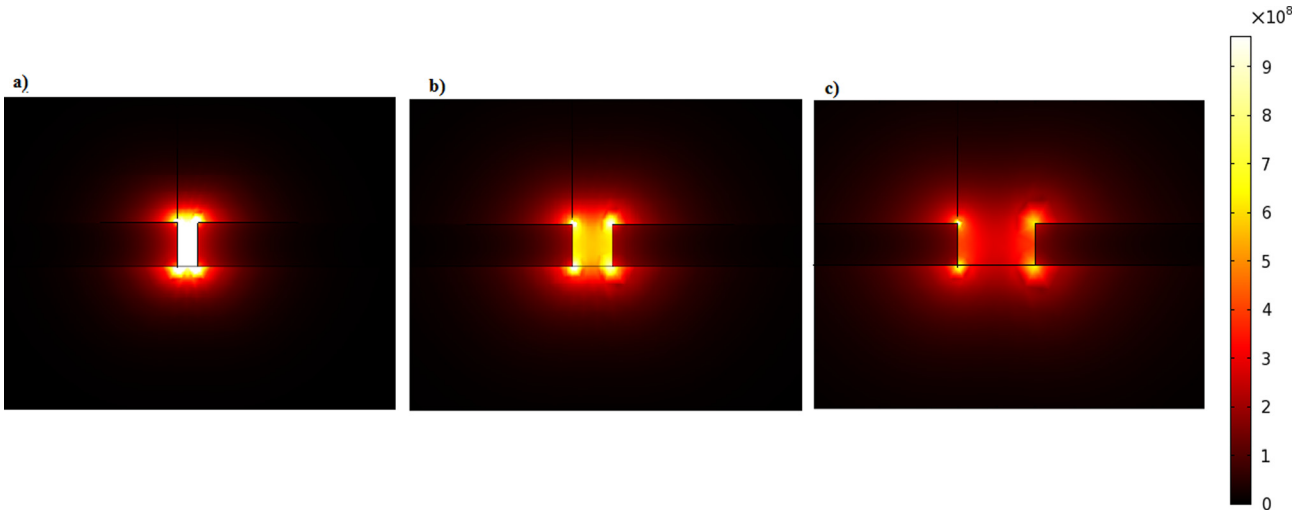

FIG. 2. Field plots of the |E| norm for symmetric GPW for (a) w = 25 nm, (b) w = 50 nm, and (c) w = 100 nm.

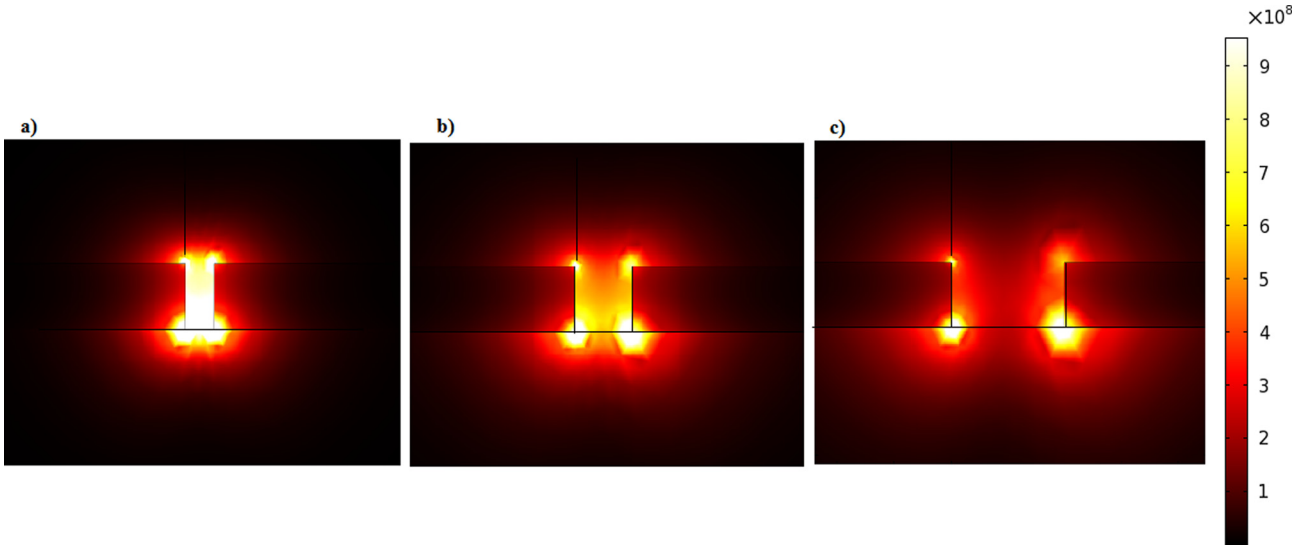

FIG. 3. Field plots of the |El norm for asymmetric GPW for (a) w= 25 nm, (b) w= 50 nm and (c) w= 100 nm.

computational domain properly. We have used scattering boundaries ensuring the absorption of plane waves

$$\hat{\gamma}_{tot} = \frac{0.5\int_v \mathrm{Re}\left(\vec{J}^* \cdot \vec{E}\right) dV}{0.5\int_v \mathrm{Re}\left(\vec{J}^* \cdot \vec{E}_0\right) dV}, \tag{3}$$

where $\vec{J}$ is the current source, $\vec{E}_0$ is the main electric field of the QD in vacuum. V is defined by the volume enclosed by the scattering boundaries. In our model, QD is considered as a 1 A line current source. The dipole moment (μ) of a line current source with finite subwavelength size (l) and current I_0 is given by[14]

$$\mu = \frac{jI_0 l}{\omega}. \tag{4}$$

Size of the current source should be restricted in order to avoid higher order multipole moments.[12] It is found that variation of total power dissipation depending on the size of the emitter is negligible when the emitter is less than 2 nm.[12] In our model, QD is modeled as a 1 nm line of current source carrying 1 A. Length of the plasmonic waveguide should be long enough to assume that reflected plasmons at the end of the waveguide don't couple back to QD. It is found that a waveguide with a length four times higher than the propagation length is sufficient.[15] Therefore, waveguide was constructed with length 10 μm.

III. RESULTS

Using the 2D finite element modeling simulations of the gap waveguide, normalized spontaneous emission of a QD into a plasmon mode ($\hat{\gamma}_{pl}$) was determined. QD was chosen with an emission wavelength of 633 nm. There were two waveguide configurations considered. Symmetric waveguide consisted of gold with refractive index $n_1 = 0.197 + 3.09i$ surrounding dielectric medium of air with $n_2 = 1$.[16] Asymmetric waveguide structure consisted of gold (n_1) on a glass substrate ($n_3 = 1.5$) with upper dielectric medium as air (n_2). QD is positioned 5 nm on top of the gap edge. Gap height (h) or width (w) was varied from 25 nm to 100 nm by keeping one parameter fixed at 50 nm. Schematic of the two waveguide configurations is shown in Figure 1.

According to Eq. (2), $\hat{\gamma}_{pl}$ depends on the strength of the field at the position of the QD. Fundamental mode fields are more concentrated on the edges for larger width and larger heights. So it was chosen to place QD on top of the edge of the waveguide. Field plots of the norm |E| are shown in Figures 3 and 4.

Field of the fundamental mode is more concentrated on the edge of the symmetric waveguide for larger dimensions [refer Figure 2]. Fundamental field is more concentrated on the edges at metal/glass interface for asymmetric waveguides [refer Figure 3]. Since the QD is placed 5 nm above the edge of the waveguide, coupling between QD and plasmon mode in symmetric waveguide should be higher than that of asymmetric waveguide.

Wavenumber and propagation length of the fundamental mode for gap widths and heights for symmetric and asymmetric waveguides are shown in Figure 4.

As the gap dimensions increase, the wavenumber decreased. Larger wavenumber implies smaller group velocity which leads to larger local density of optical states (LDOS). Larger LDOS increases the coupling efficiency to the Quantum Dot in the near vicinity. Such geometric slowing down of the plasmon mode will decrease its propagation length as can be seen in Figures 4(c) and 4(d).

Normalized spontaneous emission of a QD in to a plasmon mode of the GPW is shown in Figure 5. Normalized $\hat{\gamma}_{pl}$ is higher at smaller gap dimensions for both symmetric and asymmetric waveguides. This is in agreement with the prediction made following wavenumber behavior. Coupling to plasmon mode is higher in symmetric structure than the asymmetric structure with same gap dimensions. Enhancement in SE for thinner films is due to both group velocity and mode area reduction. As seen from the field plots of the fundamental

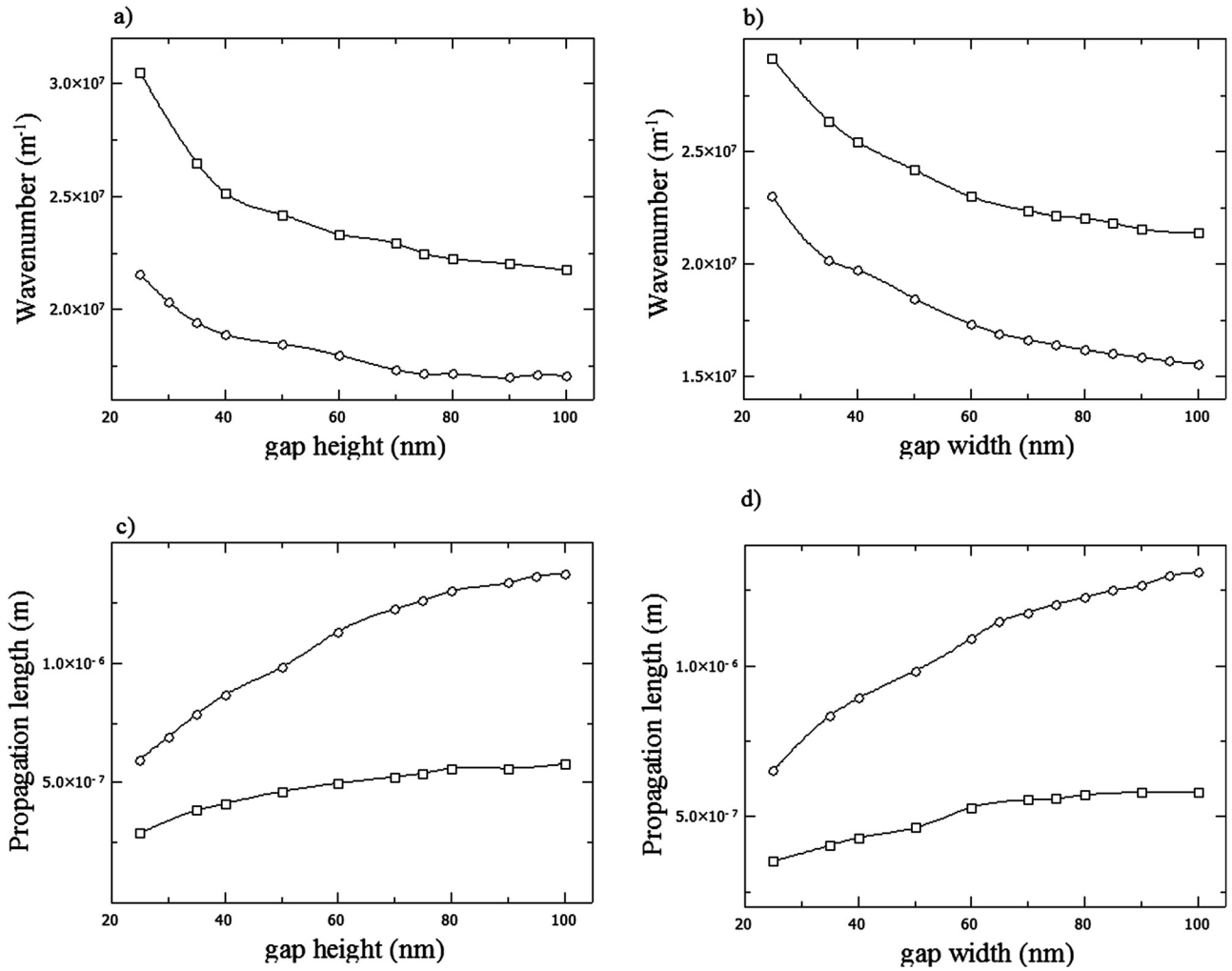

FIG. 4. Wavenumber of the fundamental mode of the GPW for (a) gap height, (b) gap width. Plots of (c) propagation length vs gap height, (d) propagation length vs gap width. Ellipse curve corresponds to symmetric GPW, square curve corresponds to asymmetric GPW.

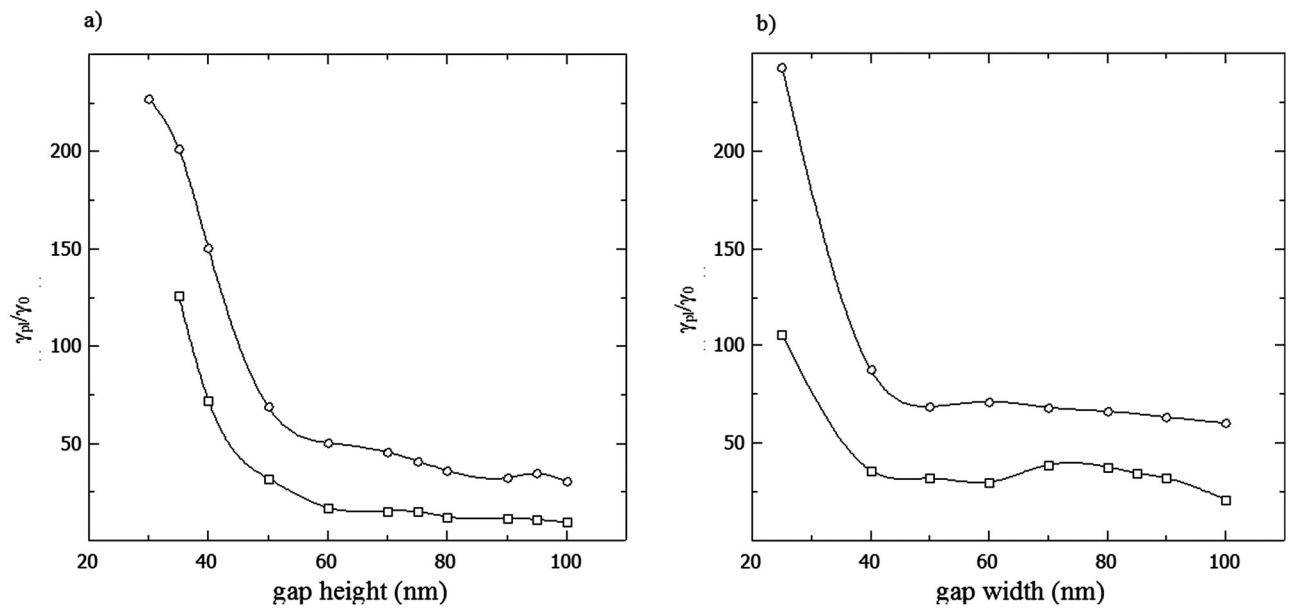

FIG. 5. γ_{pl}/γ_0 for (a) gap height and (b) gap width. Ellipse curve corresponds to symmetric GPW and square curve corresponds to asymmetric GPW.

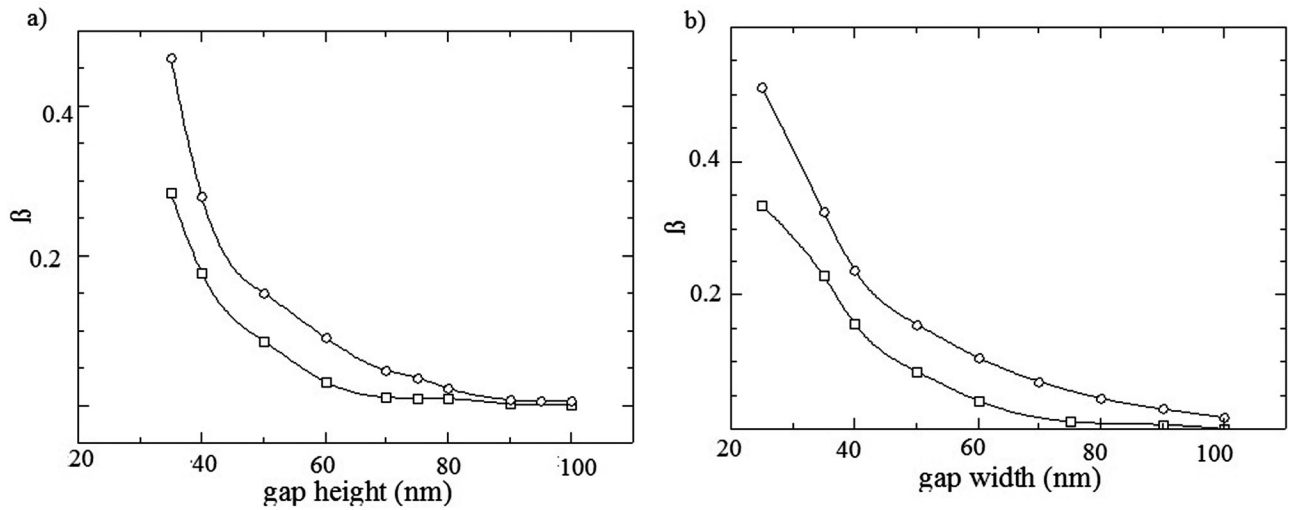

FIG. 6. Variation of spontaneous emission β factor with (a) gap height and (b) gap width. QD is placed 5 nm on top of the waveguide edge. Ellipse curve corresponds to symmetric GPW and square curve corresponds to asymmetric GPW.

mode, field is more localized on the edges of the symmetric waveguide but field is more concentrated on the bottom edges (at metal/glass interface) than air/metal edges on top for asymmetric structures. Therefore, field strength is higher for QD at symmetric waveguide structure leading to higher coupling efficiency all the time.

Jun *et al*. have shown theoretically that decreasing width at constant height of a planar MDM waveguide with a QD placed in the middle of the slit resulted in decrease of $\hat{\gamma}_{pl}$ which is in agreement with our results.[10]

To determine the probability of an excited QD in near vicinity of waveguide decaying into plasmon mode, spontaneous emission β factor must be determined. According to the equation (ii) β can be found using normalized $\hat{\gamma}_{pl}$ and $\hat{\gamma}_{tot}$. Dependence of β values with gap height and width for symmetric and asymmetric GPWs is shown in Figure 6.

Spontaneous emission β factor is higher for smaller waveguide dimensions. As explained in the normalized spontaneous emission in to plasmon mode, coupling between QD and plasmon is higher in the symmetric waveguide structure. With QD placed 5 nm on top of the symmetric waveguide edge, 45% of the excited state of the QD decay into plasmon mode.

It is said that by optimizing the position of the QD with respect to the waveguide surface, β factor can be increased by decreasing the non-radiative decay.[7] β factor is computed by varying the distance of QD from waveguide surface, Figure 7.

According to Figure 7, 80% of the excited QD can couple in to the fundamental plasmon mode in a symmetric GPW when the QD is positioned around 10 nm on top of the waveguide edge. For an asymmetric structure, this drops down to around 40%. β factor is smaller when the distance between the QD and the waveguide surface is smaller. This is mainly due to the fact that non-radiative decay of excited QD is significant when the QD is very close to the waveguide. When the distance is large, the coupling efficiency becomes low as the field strength is low. Since QD is positioned far away from the evanescent surface plasmon mode tail, β factor is lower at larger QD to waveguide distances.

IV. DISCUSSION

In conclusion, we have studied how to optimize QD-gap plasmon coupling for a single mode GPW. We observe symmetric GPW has a higher efficiency in catching spontaneous emission into guided plasmon mode than asymmetric GPW with same dimensions. With a QD placed 5 nm on top of the waveguide, increasing the width and the height of the GPW tends to decrease the coupling efficiency as fraction of modal

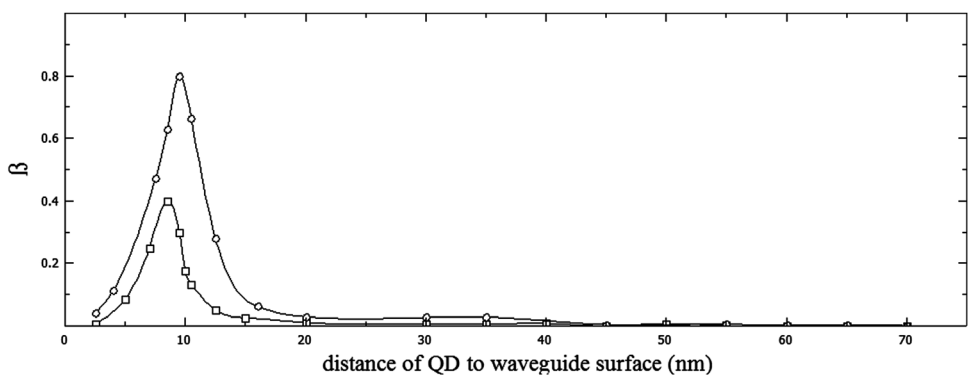

FIG. 7. Dependence of β factor with the distance of QD to waveguide surface. Ellipse curve corresponds to symmetric GPW and square curve corresponds to asymmetric GPW. Gap width and height is kept at 50 nm.

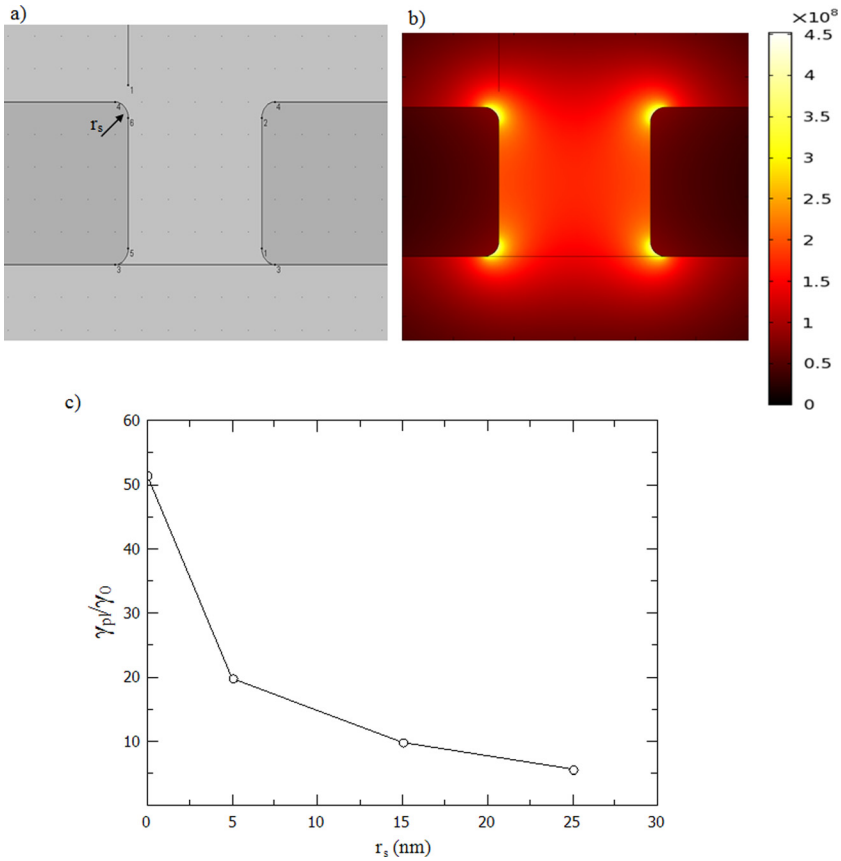

FIG. 8. (a) Schematic of a symmetric GPW with top corners of the two semi-infinite metal films are rounded with radius $0 \leq r_s \leq h/2$. (b) Field plot of |E| norm of the fundamental mode of the symmetric GPW for $r_s = 15$ nm. (c) $\hat{\gamma}_{pl}$ vs r_s for fundamental mode of the GPW with ellipse curve corresponds to symmetric GPW and square curve corresponds to asymmetric GPW.

power inside the metal is lower. There is a tradeoff between $\hat{\gamma}_{pl}$ and $\hat{\gamma}_{tot}$. Distance between QD and waveguide surface was varied to compromise $\hat{\gamma}_{pl}$ and $\hat{\gamma}_{tot}$. It is shown that for an optimally placed QD, 80% of the total spontaneous emission of the QD can be decay into guided plasmon mode of a symmetric waveguide. For an asymmetric waveguide, this coupling efficiency is around 45%. We expect this outcome would be useful for active control of plasmon propagation in plasmonics waveguides.

It should be noted that in the process of fabrication of GPW, it is hard to control the edge sharpness precisely. As shown in the Appendix, increasing the roundness of the waveguide edges will decrease the QD emission decay rate in to plasmon mode. This is due in part to the fact that arbitrary sharp edges create over estimated light intensity and thus the QD-plasmon coupling.[5,17] To quantitatively describe the behavior of the QD-plasmon coupling the edge sharpness should be compared to experimentally fabricated samples. The models in this paper provide an understanding of the QD-plasmon interaction for various waveguide widths and heights, and edge sharpness should be discussed in future work.

ACKNOWLEDGMENTS

C. P. would like to acknowledge Martin Kurth for his valuable discussions about COMSOL simulations. Authors would also like to acknowledge the support of Australian Research Council, through grant DP11010145, Eric Waclawik for his support through Asian office of aerospace research and development grant 322120-0272/53 and support from the QUT High Performance Computer facility including the HPC team.

APPENDIX: EFFECT OF THE GAP EDGE SHARPNESS

In simulations included, we modelled 2D symmetric GPW with gap dimensions $w = h = 50$ nm and QD distance to waveguide surface at 5 nm with corners of the two semi-infinite metal film regions rounded with radius $r_s \leq h/2$ as shown in Figure 8(a). The mode exhibits a strong concentration at the edges [Figure 8(b)]. When the edge is rounded the strength of the electric field around the edge is slightly weakened. The change in $\hat{\gamma}_{pl}$ value with the curvature of the edge is depicted in Figure 8(c). We can conclude that sharpness has an effect on the QD- gap plasmon coupling. Even though it is hard to control the detailed shape of the sharp edge in the fabrication process, it is better to make the edges as sharp as possible for higher QD emission in to plasmon mode decay rate.

[1]E. M. Purcell, H. C. Torrey, and R. V. Pound, "Resonance absorption by nuclear magnetic moments in a solid," Phys. Rev. **69**(1–2), 37–38 (1946).
[2]H. A. Atwater, "The promise of plasmonics," Sci. Am. **296**(4), 56–63 (2007).
[3]A. V. Zayats and I. I. Smolyaninov, "Near-field photonics: Surface plasmon polaritons and localized surface plasmons," J. Opt. A **5**(4), 16–50 (2003).
[4]H. A. Atwater and A. Polman, "Plasmonics for improved photovoltaic devices," Nature Mater. **9**(3), 205–213 (2010).
[5]G. Veronis and S. H. Fan, "Modes of subwavelength plasmonic slot waveguides," J. Lightwave Technol. **25**(9), 2511–2521 (2007).
[6]R. R. Chance, A. Prock, and R. Sibley, in *Advances in Chemical Physics*, edited by I. Prigogine and S. A. Rice (Wiley, USA, 1978), pp. 1–65.

[7]D. E. Chang, A. S. Sørensen, P. R. Hemmer, and M. D. Lukin, "Strong coupling of single emitters to surface plasmons," Phys. Rev. B **76**(3), 035420-1–035420-26 (2007).
[8]Y. C. Jun, R. Pala, and M. L. Brongersma, "Strong modification of quantum dot spontaneous emission via gap plasmon coupling in metal nanoslits," J. Phys. Chem. C **114**(16), 7269–7273 (2010).
[9]C. Gruber, A. Trügler, A. Hohenau, U. Hohenester, and J. R. Krenn, "Spectral modifications and polarization dependent coupling in tailored assemblies of quantum dots and plasmonic nanowires," Nano Lett. **13**(9), 4257–4262 (2013).
[10]Y. C. Jun, R. D. Kekatpure, J. S. White, and M. L. Brongersma, "Nonresonant enhancement of spontaneous emission in metal-dielectric-metal plasmon waveguide structures," Phys. Rev. B **78**(15), 1–4 (2008).
[11]H. Mertens, J. S. Biteen, H. A. Atwater, and A. Polman, "Polarization-selective plasmon-enhanced silicon quantum-dot luminescence," Nano Lett. **6**(11), 2622–2625 (2006).
[12]Y. Chen, T. R. Nielsen, N. Gregersen, P. Lodahl, and J. Mørk, "Finite-element modeling of spontaneous emission of a quantum emitter at nanoscale proximity to plasmonic waveguides," Phys. Rev. B **81**(12), 125431 (2010).
[13]G. Veronis and S. H. Fan, in *Nanoguides and Circuits*, edited by S. Bozhevolnyi (Pan Stanford, Singapore, 2009), pp 159–187.
[14]J. D. Jackson and R. F. Fox, *Classical Electrodynamics* (Wiley, New York, 1975).
[15]K. C. Vernon, D. E. Gomez, T. J. Davis, and N. Tischler, "Simulations of the effect of waveguide cross-section on quantum dot–plasmon coupling," J. Appl. Phys. **110**, 074315 (2011).
[16]E. D. Palik, *Handbook of Optical Constants of solids, Volume I, II, and III: Subject Index and Contributor Index* (Elsevier Science and Tech, Maryland, 1985), pp. 286–295.
[17]G. Seniutinas, L. Rosa, G. Gervinskas, E. Brasselet, and S. Juodkazis, "3D nano-structures for laser nano-manipulation," Beilstein J. Nanotechnol. **4**(1), 534–541 (2013).

Chapter 4: Excitation of bound plasmons along nanoscale waveguides: a comparison of end and grating coupling techniques

The authors listed below have certified* that:

16. they meet the criteria for authorship in that they have participated in the conception, execution, or interpretation, of at least that part of the publication in their field of expertise;
17. they take public responsibility for their part of the publication, except for the responsible author who accepts overall responsibility for the publication;
18. there are no other authors of the publication according to these criteria;
19. potential conflicts of interest have been disclosed to (a) granting bodies, (b) the editor or publisher of journals or other publications, and (c) the head of the responsible academic unit, and
20. they agree to the use of the publication in the student's thesis and its publication on the QUT ePrints database consistent with any limitations set by publisher requirements.

In the case of this chapter:

Excitation of bound plasmons along nanoscale waveguides: a comparison between end and grating coupling techniques

Chamanei S. Perera, K. C. Vernon, A. M. Funston, H. Cheng, F. Eftekhari, and T. J. Davis, Optics Express **23** (8), 10188-10197 (2015)

Contributor	Statement of contribution*
C. S. Perera Signature Date	wrote the manuscript, conducted experiment and analysis
K.C. Vernon	Originally suggested the idea, aided in simulations, data analysis, interpretation of results and paper writing
Alison Funston	Aided in experiment
H. Cheng	Aided in experiment
F. Eftekhari	Aided in experiment
T. J. Davis	Aided in interpretation of results

Principal Supervisor Confirmation

I have sighted email or other correspondence from all Co-authors confirming their certifying authorship.

Kristy Vernon		17 July 2015
Name	Signature	Date

Excitation of bound plasmons along nanoscale stripe waveguides: a comparison of end and grating coupling techniques

C. S. Perera,[1,2,*] K. C. Vernon,[1,2] A. M. Funston,[3] H. Cheng,[4] F. Eftekhari,[5] and T. J. Davis[5,6]

[1]*Plasmonic Device Group, Queensland University of Technology, Brisbane 4001, QLD, Australia*
[2]*Institute for Future Environments, Queensland University of Technology, Brisbane 4001, QLD, Australia*
[3]*School of Chemistry, Monash University, Clayton 3800, VIC, Australia*
[4]*Australian National Fabrication Facility QLD Node, AIBN, University of Queensland, St. Lucia 4072, QLD, Australia*
[5]*Melbourne Centre for Nanofabrication, Clayton 3169, VIC, Australia*
[6]*CSIRO Manufacturing Flagship, Clayton 3169, VIC, Australia*
[*]*cp.hettiarachchige@qut.edu.au*

Abstract: In this paper we excite bound long range stripe plasmon modes with a highly focused laser beam. We demonstrate highly confined plasmons propagating along a 50 μm long silver stripe 750 nm wide and 30 nm thick. Two excitation techniques were studied: focusing the laser spot onto the waveguide end and focusing the laser spot onto a silver grating. By comparing the intensity of the out-coupling photons at the end of the stripe for both grating and end excitation we are able to show that gratings provide an increase of a factor of two in the output intensity and thus out-coupling of plasmons excited by this technique are easier to detect. Authors expect that the outcome of this paper will prove beneficial for the development of passive nano-optical devices based on stripe waveguides, by providing insight into the different excitation techniques available and the advantages of each technique.

OCIS codes: (050.2770) Gratings;(240.0240) Optics at surfaces;(240.6680) Surface plasmons.

References and links

1. S. Lal, S. Link, and N. J. Halas, "Nano-optics from sensing to waveguiding," Nat. Photonics **1**(11), 641–648 (2007).
2. H. A. Atwater and A. Polman, "Plasmonics for improved photovoltaic devices," Nat. Mater. **9**(3), 205–213 (2010).
3. R. Charbonneau, C. Scales, I. Breukelaar, S. Fafard, N. Lahoud, G. Mattiussi, and P. Berini, "Passive integrated optics elements based on long-range surface plasmon polaritons," J. Lightwave Technol. **24**(1), 477–494 (2006).
4. P. Berini, "Long-range surface plasmon polaritons," Adv. Opt. Photonics **1**(3), 484–588 (2009).
5. A. Boltasseva, T. Nikolajsen, K. Leosson, K. Kjaer, M. S. Larsen, and S. I. Bozhevolnyi, "Integrated optical components utilizing long-range surface plasmon polaritons," J. Lightwave Technol. **23**(1), 413–422 (2005).
6. I. Breukelaar, P. Berini, and P. Berini, "Long-range surface plasmon polariton mode cutoff and radiation in slab waveguides," J. Opt. Soc. Am. A **23**(8), 1971–1977 (2006).
7. G. Bracher, K. Schraml, C. Jakubeit, M. Kaniber, and J. Finley, "Direct measurement of plasmon propagation lengths on lithographically defined metallic waveguides on GaAs," J. Appl. Phys. **110**(12), 123106 (2011).
8. I. Salakhutdinov, J. S. Thakur, and K. Leosson, "Characterization of long-range surface plasmon-polariton in stripe waveguides using scanning near-field optical microscopy," J. Appl. Phys. **102**(12), 123110 (2007).
9. H. Ditlbacher, J. R. Krenn, G. Schider, A. Leitner, and F. R. Aussenegg, "Two-dimensional optics with surface plasmon polaritons," Appl. Phys. Lett. **81**(10), 1762–1764 (2002).
10. K. Vernon, D. Gómez, and T. Davis, "A compact interferometric sensor design using three waveguide coupling," J. Appl. Phys. **106**(10), 104306 (2009).
11. P. Berini, "Plasmon-polariton waves guided by thin lossy metal films of finite width: Bound modes of asymmetric structures," Phys. Rev. B **63**(12), 125417 (2001).
12. B. Wang and G. P. Wang, "Simulations of nanoscale interferometer and array focusing by metal heterowaveguides," Opt. Express **13**(26), 10558–10563 (2005).

#231460 - $15.00 USD Received 29 Dec 2014; revised 5 Mar 2015; accepted 18 Mar 2015; published 13 Apr 2015

13. R. Buckley and P. Berini, "Figures of merit for 2D surface plasmon waveguides and application to metal stripes," Opt. Express **15**(19), 12174–12182 (2007).
14. J. Krenn, B. Lamprecht, H. Ditlbacher, G. Schider, M. Salerno, A. Leitner, and F. Aussenegg, "Non–diffraction-limited light transport by gold nanowires," Europhys. Lett. **60**(5), 663–669 (2002).
15. B. Lamprecht, J. R. Krenn, G. Schider, H. Ditlbacher, M. Salerno, N. Felidj, A. Leitner, F. R. Aussenegg, and J. C. Weeber, "Surface plasmon propagation in microscale metal stripes," Appl. Phys. Lett. **79**(1), 51–53 (2001).
16. R. Zia, M. D. Selker, and M. L. Brongersma, "Leaky and bound modes of surface plasmon waveguides," Phys. Rev. B **71**(16), 165431 (2005).
17. C. Chen and P. Berini, "Grating couplers for broadside input and output coupling of long-range surface plasmons," Opt. Express **18**(8), 8006–8018 (2010).
18. E. D. Palik, *Handbook of Optical Constants of Solids* (Elsevier Science and Tech, 1985).
19. G. Ghosh, "Dispersion-equation coefficients for the refractive index and birefringence of calcite and quartz crystals," Opt. Commun. **163**(1-3), 95–102 (1999).
20. A. Giannattasio, I. R. Hooper, and W. L. Barnes, "Dependence on surface profile in grating-assisted coupling of light to surface plasmon-polaritons," Opt. Commun. **261**(2), 291–295 (2006).
21. S. A. Maier, *Plasmonics: Fundamentals and Applications* (Springer, 2007).

1. Introduction

The use of plasmon waveguides for the development of sensitive nanoscale sensors and passive optical devices is a hot topic in photonics research [1–3]. A common plasmon waveguide design is the metal slab waveguide, which supports two surface plasmon polariton (SPP) modes on the upper and lower interface. These modes can couple together, forming symmetric and asymmetric modes depending on the orientation of the main E-field component [4, 5]. The symmetric mode attenuation dramatically decreases with reducing metal thickness resulting in Long Range Surface Plasmon Polaritons (LRSPPs). A metal slab with different upper and lower dielectric media can also support LRSPPs but has a mode cut-off thickness, below which the LRSPP is no longer bound and guided [4, 6].

Metal stripe waveguides are based on metal slab waveguides but have a finite width. They are one of the simplest waveguide structures that allow nanoscale confinement of the light in two dimensions. Commonly, they consist of a metallic rectangular bar surrounded by a dielectric medium, and theoretically can also support LRSPPs which propagate micron distances at or near visible excitation. Many stripe waveguide experiments are carried out in the IR or near IR ranges and these have proven the existence of the LRSPP [5, 7–9]. Whilst a number of theoretical papers based on stripe waveguide excitation in the visible predict the existence of bound LRSPP plasmon modes, there has been no experimental confirmation of this [10–13]. Several experiments have been reported in the visible for the detection of leaky plasmon modes supported by stripe waveguides [11, 14–16]. These waveguides often sit on a substrate and are exposed to air. The plasmon mode supported by the waveguide leaks into the air region and its presence is detected via near field scanning optical microscopy techniques [14]. However such waveguides do not provide the same level of field confinement in two dimensions due to the leaky nature of their modes.

Stripe waveguides are popular as a plasmon waveguide due to the long propagation lengths achieved and the simplicity of the geometry compared to other waveguides [3, 13]. However, nanoscale confinement and guided propagation of bound plasmons by these waveguides has been difficult to achieve in the visible. In this paper we investigate bound plasmon modes supported by stripe waveguides under visible excitation. Two excitation techniques are discussed – excitation of the waveguide end and excitation of a grating at the waveguide input. We define end excitation as exciting the end of a stripe waveguide by focusing a laser beam onto the stripe edge through a high NA objective. For the grating coupling, gratings were fabricated in front of the stripe waveguide and the laser beam focused through the high NA objective onto the middle of the grating. The position of the focused beam onto the grating was optimised for maximal output intensity at the stripe end.

This type of end coupling has been reported before for near IR excitation, and is also known as broadside excitation [7]. Grating excitation for stripe waveguides has not been

#231460 - $15.00 USD Received 29 Dec 2014; revised 5 Mar 2015; accepted 18 Mar 2015; published 13 Apr 2015

reported before but has been studied theoretically by Berini et al for metal slabs [17]. Authors believe this work is the first attempt to excite bound LRSPP in the visible region.

2. Theory

Silver LRSPP waveguides were designed for 640 nm excitation. The waveguides were supported by an ITO-coated glass substrate and modelled with a covering layer of SiO_2. See Fig. 1(a) for a schematic of the waveguide design.

The width of the Ag waveguides was chosen as 750 nm, and the thickness of the waveguide was varied so that only one long range mode was supported. Using COMSOL Multiphysics the modes supported by the waveguide for various waveguide thickness was calculated, along with the propagation lengths. The permittivity of silver was taken as −16.4 + 1.13i [18], ITO as 3.42 + 0.22i from Sopra database, glass 2.3 and SiO_2 as 2.4 [19]. The thickness of the ITO was set to 15 nm. The wavenumber of the long range guided modeand propagation length are shown in Fig. 2. Plasmon propagation length (L_p) is taken as the distance the plasmon travels before its intensity drops by a factor of e.

As can be seen from Fig. 2(a), the long range guided mode's wavenumber increases with increasing thickness of the metal film. This indicates that the mode becomes more localised as the metal film thickness increases, resulting in more of the plasmon being confined inside the metal. This localisation results in a decrease in the propagation distance of the mode as the film thickness increases, due to the inherent losses of the metal, Fig. 2(b). Such behaviour is typical of long range modes in asymmetric stripe structures, of low asymmetry [6]. As the metal film thickness increases the mode becomes more localised to one of the stripe edges resulting in higher confinement (larger wavenumber) and thus smaller propagation length.

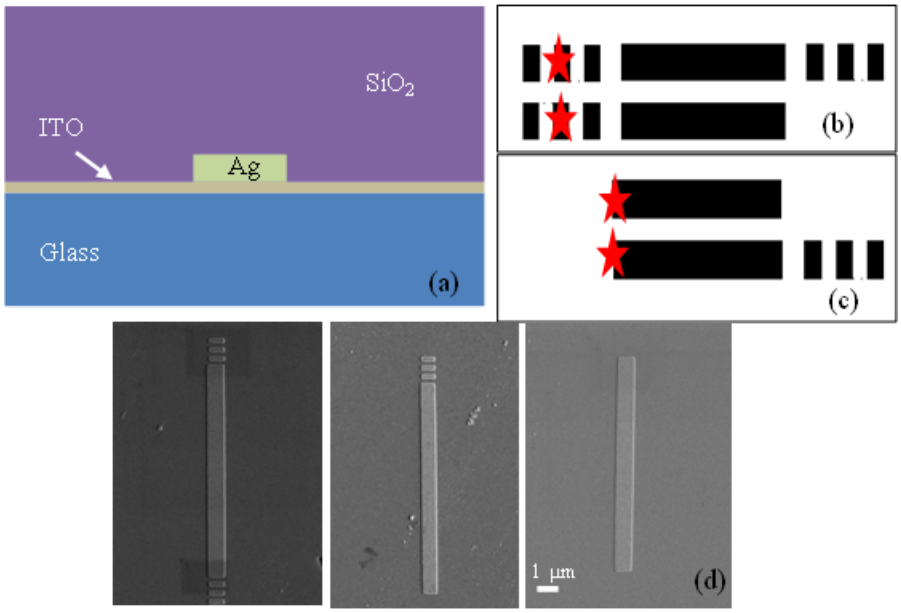

Fig. 1. Schematic of the coupling arrangements of the structures (not to scale): (a) Front-on schematic of sample (b) grating coupling (c) end coupling. Here star represents the laser spot. (d) SEM images of the three structures (width 750 nm, length 10 μm and thickness 30 nm).

#231460 - $15.00 USD Received 29 Dec 2014; revised 5 Mar 2015; accepted 18 Mar 2015; published 13 Apr 2015

20 Apr 2015 | Vol. 23, No. 8 | DOI:10.1364/OE.23.010188 | OPTICS EXPRESS 10190

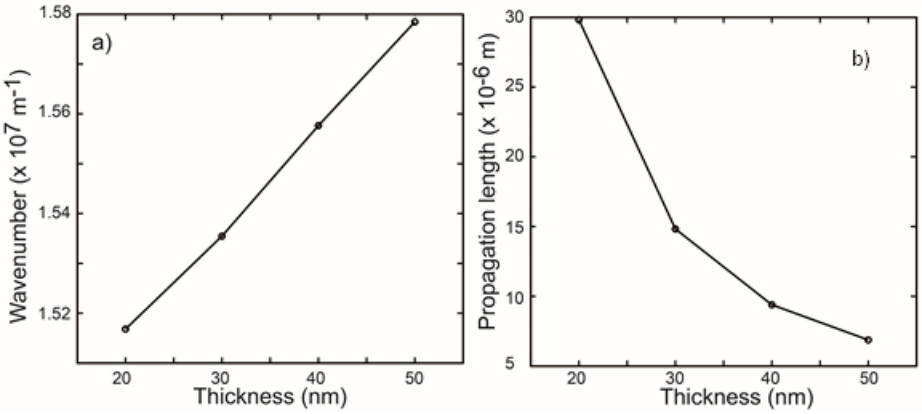

Fig. 2. (a) Wavenumber, (b) Propagation length of the LRSPP mode and their dependence on thickness.

It was found that if the stripe thickness was decreased below 20 nm, the long range mode would be cut-off and no longer bound. Also, if the thickness was above 40 nm, two long range modes existed. To ensure only one long range mode, a thickness of 30 nm was selected. For this thickness, the plasmon has a 15 micron propagation distance. The field profile of this long range plasmon mode is shown in Fig. 3.

In this paper, we test different excitation methods for exciting the LRSPP mode. Several waveguide geometries were fabricated, one without gratings, one with an input grating, one with an output grating, and one with input and output gratings. The schematic of the various ready-to excite waveguides are shown in Figs. 1(b) and 1(c).

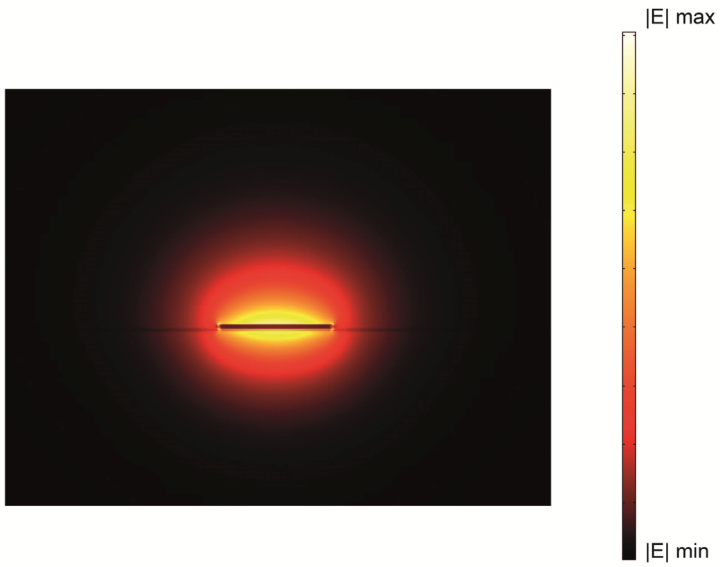

Fig. 3. |E| field plot of the LRSPP mode in a 30 nm thick, 750 nm wide waveguide on ITO coated glass.

The grating periodicity and height were selected to achieve high efficiency and to preferentially excite the LRSPP mode. Grating causes the incident LRSPP to be partially reflected in opposite direction to plasmon propagating direction. This perturbation can be reduced by strengthening the grating structure such that partial reflections of adjacent bumps

#231460 - $15.00 USD Received 29 Dec 2014; revised 5 Mar 2015; accepted 18 Mar 2015; published 13 Apr 2015

20 Apr 2015 | Vol. 23, No. 8 | DOI:10.1364/OE.23.010188 | OPTICS EXPRESS 10191

cancel out [17]. It has been proven theoretically, and experimentally in the case of square gratings, that light-SPP coupling is maximised when the groove-to-pitch ratio is equal to ½ for SPs supported by metal films [20]. Since the long range mode of the stripe waveguide has a similar field profile to the SP [17] we use the same grating formula to calculate the grating period and a groove-to-pitch ratio of ½. Using the grating equation, the wavenumber of the plasmon (β) excited by the grating is [21]

$$\beta = k\sin\theta + \frac{2\pi m}{a} \tag{1}$$

where k is the incident beam wavenumber, θ is its angle of incidence, a is the grating periodicity and m is the grating order. In our experiment the laser beam was focused at near-normal incidence on the substrate using high numerical aperture objective. Thus Eq. (1) can be approximated as

$$\beta = \frac{2\pi m}{a} \tag{2}$$

And for the 1st grating order this gives

$$\beta = \frac{2\pi}{a} \tag{3}$$

The grating period for our system is 416 nm.

There are some disadvantages with grating excitation, as discussed by Berini et al in the case of metal slabs [17]. Grating excitation not only produces the desired LRSPP mode but also other radiation modes which can affect the power of the out-coupled light from the waveguide. The total power propagating along the waveguide ($-x$ direction) at x can be written as [17]

$$P_x(x) = P_{S0}e^{2\alpha(x-x_0)} + P_{rad}(x) \tag{4}$$

where P_{S0} is the power carried by the LRSPP at $x = x_0$ (x_0 is the location of the left edge of the grating), α is the field attenuation constant of the LRSPP and $P_{rad}(x)$ is the power carried by all the other modes. Similar issues can be encountered with end excitation. The stripe edge basically operates as a surface defect [21] allowing the generation of multiple plasmon modes when the highly focused laser beam strikes the waveguide edge. However, all other modes supported by these carefully designed stripe waveguides have very low propagation lengths (< 2 μm).Both end and grating excitation techniques will be studied in this paper.

3. Method

3.1 Fabrication

Plasmonic waveguides were patterned on a 300 nm bilayer PMMA resist(950k A4 / 495 k A4 PMMA resist from Microchem GmbH) using electron beam lithography (JEOL-7800 FE-SEM with Raith Quantum Elphy) with a beam current of ~75 pA and 20 kV acceleration voltage under optimal dose of 280 μC/ cm^2. Patterned PMMA layer was then developed for 30 seconds in MIBK:IPA 1:3 solution. 30 nm Ag was evaporated on the developed sample using the PVD 75 e-beam evaporator under a slow rate of 0.27 °A/s. Scanning electron microscope image shows the 750 nm wide stripes survived successfully after lift- off in acetone bath. A 200 nm SiO_2 layer was then evaporated (with a rate of 0.5°A/s) on top of the waveguides to ensure waveguiding in the desired mode. We fabricated stripes with gratings on both ends, grating one end and no grating for different stripe lengths (5 μm, 10 μm, 20 μm,

#231460 - $15.00 USD Received 29 Dec 2014; revised 5 Mar 2015; accepted 18 Mar 2015; published 13 Apr 2015

30 µm, 40 µm, 50 µm) Refer Fig. 1(b). SEM image of three waveguides (one with grating at both ends, one with grating at one end and one with no grating) with 10 µm width are shown in Fig. 1(c). The grating periodicity was 416 nm with a groove to pitch ratio of ½.

3.2 Experimental setup

For optical characterisation and excitation of the fabricated waveguides we used an inverted microscope. Light from a linearly polarised 640 nm diode laser was focused onto the sample via a 100x oil immersion objective with NA = 1.4. Polarisation of the excitation light was varied using λ/2 plate. Plasmon out-coupling into free space photons at the distal tip of the waveguide was observed using a CCD camera (Fig. 4). To verify the plasmon nature of the guided mode, polarisation dependence of the out-coupling light was studied.

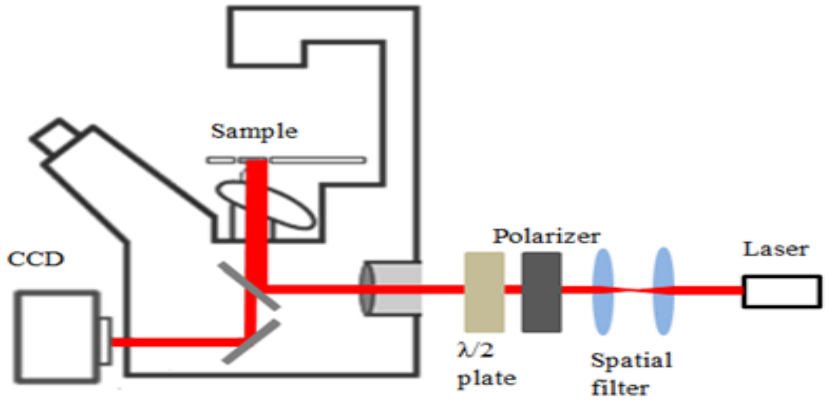

Fig. 4. Schematic diagram of the experimental set up. Objective with N/A 1.4.

4. Optical characterisation

4.1 Polarisation dependence

Figure 5 shows the experimentally measured polarisation dependency of the light out-coupled from a 20 µm long stripe excited via Fig. 5(a) and 5(b) grating excitation and Fig. 5(c) and 5(d) end excitation. The polar plots show that out-coupling is maximized when the electric field of the exciting photons are TM polarised. Calculated Degrees of Polarisation (DoP) for out-coupling intensities for plots in Fig. 5(a)-5(d) are 78%, 80%, 86% and 88% respectively.

DoP is defined as [7]

$$DoP = \frac{I_{max} - I_{min}}{I_{max} + I_{min}} \tag{5}$$

where I_{max} and I_{min} are maximum and minimum intensities of the output light at the end of the stripe waveguide.

DoP analysis shows that outcoupling light from end excitation (86-88%) is significantly TM in nature, and supports the presence of a plasmon mode [7].The end excitation DoP is also more polarised than that of grating coupling (78-80%), which is in line with the theoretical research that has shown that gratings also produced radiation modes which are not TM polarised [17].

Figure 5(d) shows CCD images of out-coupling photons from the waveguide end for 20 µm stripes with Figs. 5(d)(i) grating both sides, 5(d)(ii) excitation grating only, 5(d)(iii) no grating and 5(d)(iv) grating in the output only. It is obvious that out-coupling intensity drops when there is no grating involved in the excitation of the LRSPP.

#231460 - $15.00 USD Received 29 Dec 2014; revised 5 Mar 2015; accepted 18 Mar 2015; published 13 Apr 2015

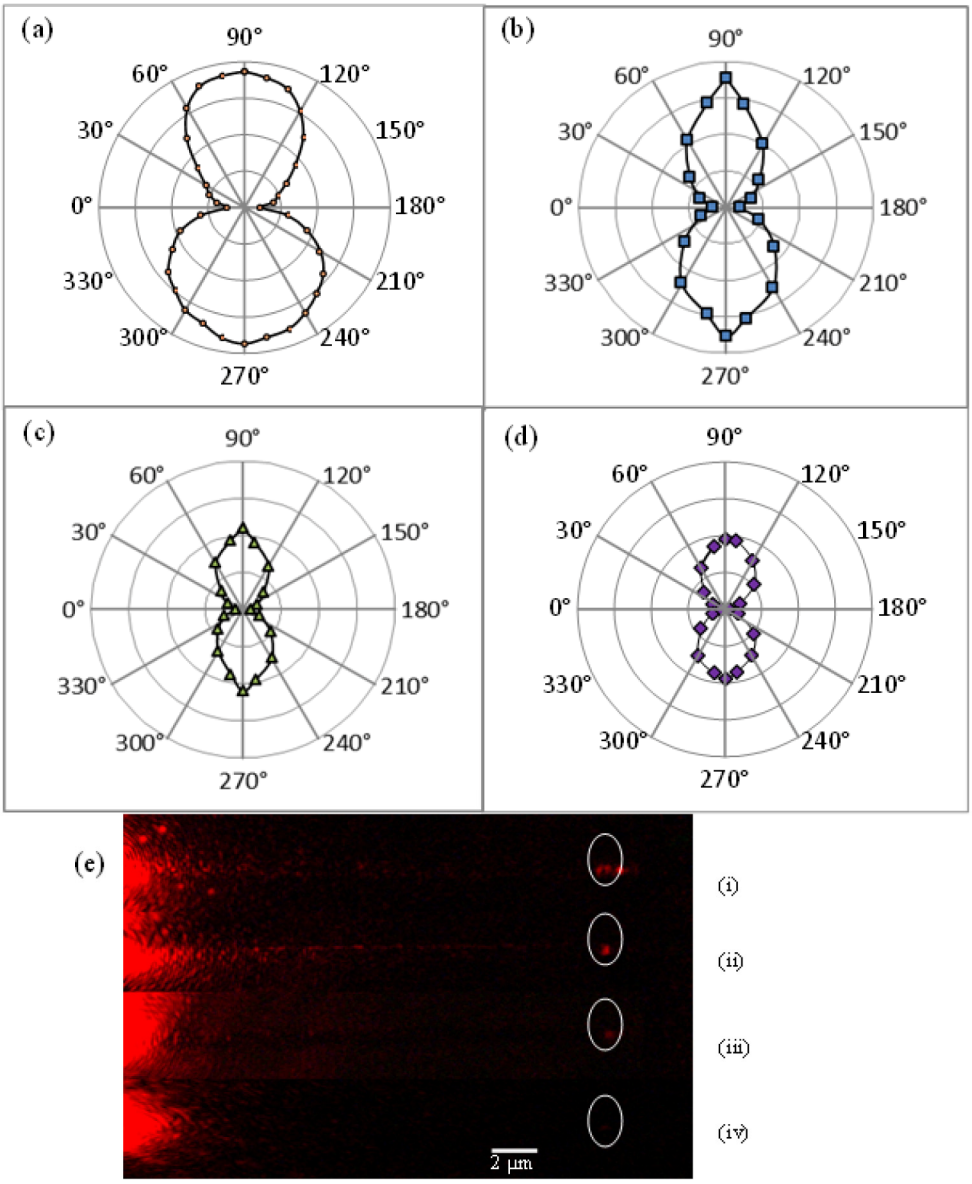

Fig. 5. Polar plots of out-coupling from (a) grating coupled stripe with grating on both side, (b) grating coupled stripe with grating on one end and (c) end coupled stripe without grating (d)end coupled stripe with grating on one end. Radial scale goes from 0 to 70 with 17.5 increments. (e) Series of CCD images of light scattering from the waveguide end 20 μm long stripe (i) grating coupled stripe with grating (ii) grating coupled stripe with grating one side (iii)end coupled stripe without grating (iv) end coupled stripe with one grating.

4.2 Propagation length

4.2.1 End coupling

To further verify that the stripes support a plasmon guided mode, the propagation length of the guided mode was investigated. Figure 6(a) shows the CCD images of the out-coupling intensity of end-coupled stripes for stripes lengths of 5 μm, 10 μm, 20 μm, 30 μm, 40 μm, while, Fig. 6(b) shows the out-coupling intensity dependence on stripe length for end

#231460 - $15.00 USD Received 29 Dec 2014; revised 5 Mar 2015; accepted 18 Mar 2015; published 13 Apr 2015

excitation. The two curves show how the presence of an out-coupling grating affects the out-coupled intensity. It is clear that the presence of an out-coupling grating does not significantly impact the output intensity.

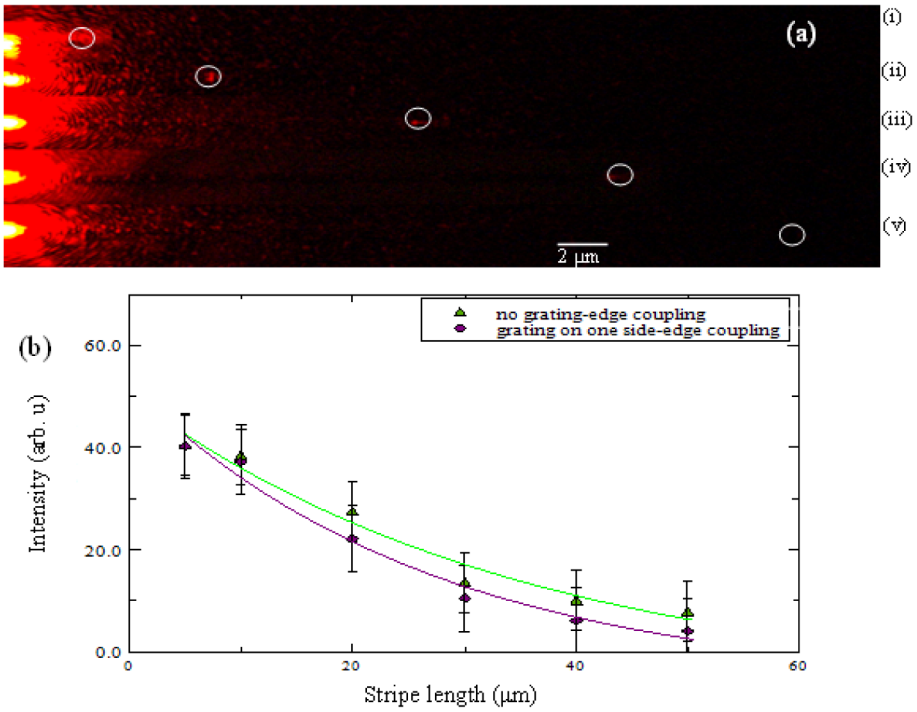

Fig. 6. (a) Series of images obtained using CCD camera. Stripes with no grating for lengths of (i)5 μm, (ii) 10 μm, (iii) 20 μm, (iv) 30 μm and (v) 40 μm. (b) Out-coupling intensity vs stripe length with exponential fit for end coupled stripes.

The out-coupling intensity for each stripe plotted in Fig. 6(b) can be used to determine the propagation length of the guided mode.

We define the propagation length L_p, as the length the plasmon travels before its initial intensity (I_0) drops by a value of e

$$L_p = \frac{I_0}{e} \tag{6}$$

By fitting an exponential to the curves in Fig. 6(b), the initial intensity I_0 is extrapolated, and the propagation length L_p determined. The propagation length is 18 ± 6 μm for stripes with gratings at in the detection channel and 20 ± 6 μm for stripe without grating which compares well with the theoretical predictions of 15 microns.

4.2.2 Grating excitation

A similar analysis has been conducted for plasmons excited via grating excitation. Figure 7(a) shows the CCD images of the out-coupling intensity of grating coupled stripes with grating both ends for stripes lengths of 5 μm, 10 μm, 20 μm, 30 μm, 40 μm, 50 μm. Figure 7(b) shows the averaged out-coupling intensity drop with the increase of stripe length for stripes excited by grating coupling. The two curves show how the presence of an output grating affects the out-coupling intensity, and once again the output grating does not have a significant affect.

#231460 - $15.00 USD Received 29 Dec 2014; revised 5 Mar 2015; accepted 18 Mar 2015; published 13 Apr 2015

However, upon comparison of Fig. 6(b) and Fig. 7(b), the intensity obtained via grating excitation is approximately double that obtained via end excitation.

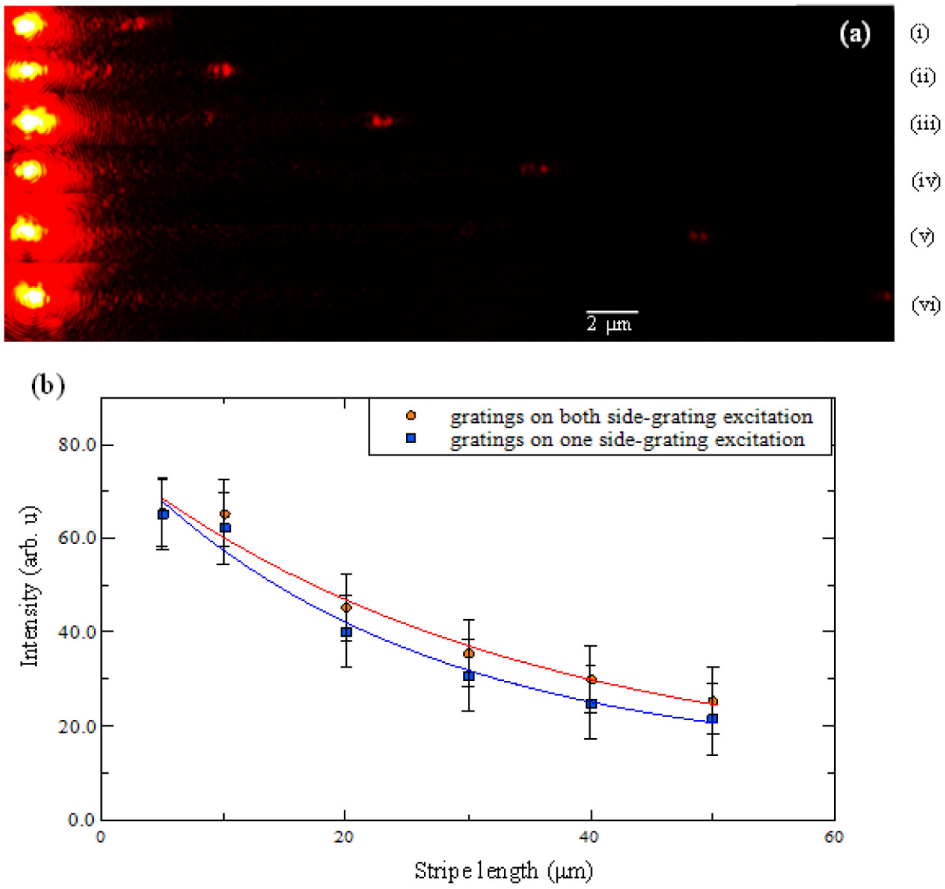

Fig. 7. (a) Series of images obtained using CCD camera. Stripes with grating either side for lengths of (i) 5 μm, (ii) 10 μm, (iii) - (vi) 50 μm with 10 μm step increment. (b) Out-coupling intensity vs stripe length with exponential fit for grating coupled stripes.

Propagation length for stripes with grating one end is 41 ± 8 μm and for stripe with grating both ends is 53 ± 7 μm. These propagation lengths are approximately two to three times that of the theoretical value of 15 μm. This discrepancy can be due to slight variation of refractive indices and thicknesses of the materials used in fabrication, but since this wasn't an issue for the end excitation, this variation in propagation length is most likely due to strong spatial transients caused by the strong involvement of radiation modes [17].

The use of grating in excitation of LRSPP on a stripe waveguide has clearly doubled the out-coupling intensity thus making the LRSPP waveguiding easier to detect visually. However, it is clear that grating excitation has resulted in the presence of other modes. From Eq. (4) it can be deduced that the effects of these radiation modes will decrease for LRSPPs that have longer propagation lengths. Thus it would seem that grating excitation would prove useful for stripes fabricated in the telecom regime where propagation lengths are much larger [17].

The grating excitation has provided almost double the output intensity at the distal end compared to that observed for end excitation. Berini et al reports the efficiency of grating coupling to be around 20% for stripe waveguides, finding that the grating excitation efficiency is higher than the efficiencies of other out-of-plane in coupling techniques to date

#231460 - $15.00 USD Received 29 Dec 2014; revised 5 Mar 2015; accepted 18 Mar 2015; published 13 Apr 2015

20 Apr 2015 | Vol. 23, No. 8 | DOI:10.1364/OE.23.010188 | OPTICS EXPRESS 10196

[17]. Thus, our findings of greater output intensity at the distal end for grating excitation vs end excitation are consistent with Berini's results. Grating excitation is designed to not only help direct light towards the waveguide but to generate only the desired plasmon mode. End coupling is similar to exciting plasmons using surface defects. It will scatter light in all directions and generate all possible modes in the stripe waveguide [21]. Since our stripe is multimodal and supports 4 bound stripe modes, it is expected that the edge excitation efficiency for our desired mode will be less than that of the grating.

In summary, we have reported optical characterization of bound LRSPPs in the visible regime. Despite their propagation length of 15 microns, we have shown that experimentally it is possible to visually detect the plasmon propagating up to 50 μm. Due to the bound nature of these LRSPPs, these plasmons have higher localisation in two dimensions than their leaky counterparts [11, 16].

We have also demonstrated that bound LRSPPs can be excited via both gratings and end excitation techniques. Polar plots depict that out-coupling LRSPP can be detected when the waveguide is excited with TM polarised photons, confirming the plasmonic nature of these modes. The grating excitation technique provides higher output intensities and easier detection than the end excitation, however, the presence of radiation modes in the grating excitation results in a lower DoP.

The advantage of end excitation is that the presence of other modes is minimal as can be seen from the DoP and the propagation length analysis. If it is important to produce single mode waveguides, end excitation is a superior technique to grating excitation. We alsodemonstrated, for end excitation, that it is possible to easily detect plasmon propagation visually up to 20 μm in the visible range.

Authors expect these findings will be beneficial for future LRSPP applications, enabling the informed decision about the best excitation technique for the particular stripe set-up.

Acknowledgments

This work was performed in parts at the Queensland node of the Australian National Fabrication Facility (ANFF), a company established under the National Collaborative Research Infrastructure Strategy to provide nano and micro-fabrication facilities for Australia's researchers and Melbourne Centre for nanofabrication (MCN) in the Victorian Node of the ANFF. CP acknowledges valuable support from the UQ AIBN, UQ CMM, and QUT CARF team. CP and KV acknowledge the Australian Research Council (ARC) grant DP110101454 and the Asian Office of Aerospace Research and Development grant FA2386-14-1-4056. AMF acknowledges the Australian Research Council (ARC) fellowship FT110100545.

#231460 - $15.00 USD Received 29 Dec 2014; revised 5 Mar 2015; accepted 18 Mar 2015; published 13 Apr 2015

Chapter 5: Mapping a bound plasmon propagating on a nanoscale stripe waveguide using quantum dots: Effect of spacer layer thickness

The authors listed below have certified* that:

21. they meet the criteria for authorship in that they have participated in the conception, execution, or interpretation, of at least that part of the publication in their field of expertise;
22. they take public responsibility for their part of the publication, except for the responsible author who accepts overall responsibility for the publication;
23. there are no other authors of the publication according to these criteria;
24. potential conflicts of interest have been disclosed to (a) granting bodies, (b) the editor or publisher of journals or other publications, and (c) the head of the responsible academic unit, and
25. they agree to the use of the publication in the student's thesis and its publication on the QUT ePrints database consistent with any limitations set by publisher requirements.

In the case of this chapter:

Mapping bound plasmon propagating on a nanoscale stripe waveguide using quantum dots: Effect of spacer layer thickness

Chamanei S. Perera, K. C. Vernon, A. M. Funston, and H. Cheng, submitted to BJ nano

Contributor	Statement of contribution*
C. S. Perera Signature Date	wrote the manuscript, conducted experiment and analysis
K.C. Vernon	Originally suggested the idea, aided in simulations, data analysis, interpretation of results and paper writing
Alison Funston	Aided in experiment
H. Cheng	Aided in experiment

Principal Supervisor Confirmation

I have sighted email or other correspondence from all Co-authors confirming their certifying authorship.

Kristy Vernon		17 July 2015
Name	Signature	Date

BEILSTEIN JOURNAL OF NANOTECHNOLOGY

Mapping bound plasmon propagation on a nanoscale stripe waveguide using quantum dots: influence of spacer layer thickness

Chamanei S. Perera[1], Alison M. Funston[2], Han-Hao Cheng[3] and Kristy C. Vernon[*1]

Full Research Paper

Open Access

Address:
[1]Queensland University of Technology, Brisbane 4001, QLD, Australia, [2]School of Chemistry, Monash University, Clayton 3800, VIC, Australia and [3]Australian National Fabrication Facility-QLD Node, AIBN, University of Queensland, St. Lucia 4072, QLD, Australia

Email:
Kristy C. Vernon[*] - k.vernon@qut.edu.au

* Corresponding author

Keywords:
photoluminescence; plasmonics; quantum dot; spacer layer; stripe waveguide

Beilstein J. Nanotechnol. **2015,** *6,* 2046–2051.
doi:10.3762/bjnano.6.208

Received: 21 July 2015
Accepted: 24 September 2015
Published: 19 October 2015

Associate Editor: A. J. Meixner

Abstract

In this paper we image the highly confined long range plasmons of a nanoscale metal stripe waveguide using quantum emitters. Plasmons were excited using a highly focused 633 nm laser beam and a specially designed grating structure to provide stronger incoupling to the desired mode. A homogeneous thin layer of quantum dots was used to image the near field intensity of the propagating plasmons on the waveguide. We observed that the photoluminescence is quenched when the QD to metal surface distance is less than 10 nm. The optimised spacer layer thickness for the stripe waveguides was found to be around 20 nm. Authors believe that the findings of this paper prove beneficial for the development of plasmonic devices utilising stripe waveguides.

Introduction

Plasmons are a coherent oscillation of electrons in a metal [1]. Loosely bound electrons can combine with incoming photons and propagate along the metal/dielectric interface. These charge density waves create a strong near-field [1]. There is increasing demand for high speed data communication as well as miniaturised devices, and plasmonics is a possible solution that can provide both the high speed and miniaturisation [2,3]. Plasmonics enables the squeezing of optical waves into miniscule structures and manipulating these waves to achieve all-optical circuits. Metal waveguides are a popular method to route light in nanoscale all-optical circuitry. Of all the waveguides, stripe waveguides are popular due to their ease of fabrication as well as the ability to support plasmon modes having relatively high propagation lengths [4,5]. These special modes are called long range surface plasmon polaritons (LRSPPs). LRSPPs have been shown to have large propagation lengths in the visible light range, greater than 10 μm [6].

When quantum dots (QDs) are placed in the vicinity of propagating plasmons, QDs can be locally excited by the plasmon if

the plasmon frequency lies within the absorption spectral range of the QDs [1,7]. Photoluminescence of the QD occurs due to excitation of the QD by the incident field of the propagating SPP on the stripe.

Intensity of the QD photoluminescence (PL) arising from the propagating plasmons is proportional to the intensity of the local electric field at the given position [7,8]. Therefore, QDs can be used to map the propagating plasmons on a waveguide [9,10]. It is well known that QD PL can be quenched via non-radiative transition of energy from QD to the metal if the QDs are placed too close to the metal surface [7,11]. Therefore, optimisation of the distance between the QD and metal surface is vital to enhance the PL intensity.

In this paper we present the mapping of the above bound plasmon mode using quantum dot photoluminescence. For a plasmonic stripe waveguide, we demonstrate that QD to waveguide surface distance is a critical factor on the QD PL [11]. We use degree of polarisation (DoP) measurements to prove that QD PL in the vicinity of the metal waveguide is arising from the local excitation of QDs by the propagating plasmon. Our experimental findings are supported by finite element modelling using COMSOL Multiphysics. Authors believe that findings of this work will prove beneficial in studying light matter interaction in nanoscale devices and all-optical circuitry.

Theory

COMSOL Multiphysics was used to run simulations on silver stripe waveguides supported on an indium tin oxide (ITO)-coated glass substrate with poly(methyl methacrylate) (PMMA) cladding. The width of the waveguide was chosen to be 750 nm to visualise easily under an optical microscope. Silver stripe waveguides were designed to be excited using a 633 nm laser. Permittivities of the materials used in modelling were, Silver as $-16.4 + 1.13i$ [12], ITO as $3.42 + 0.22i$ from Sopra database, glass 2.3, and SiO_2 as 2.4 [13]. The thickness of the ITO was 15 nm. Geometrical parameters of the stripe waveguide were theoretically determined to ensure the waveguide was single mode (ss_b^0). This required the thickness of the waveguide to be around 30 nm. The propagation length of this mode within a waveguide of these parameters has been previously reported experimentally to be 18 ± 6 μm [6]. The electric field profile of this mode is shown in Figure 1 below.

The grating periodicity (a) was calculated to provide stronger incoupling to the desired mode using [14]:

$$\beta = k \sin\theta + \frac{2\pi m}{a}, \quad (1)$$

where β is the wavenumber of the plasmon mode, k is the wavenumber of the incident light, θ is the angle of incidence and m is the order of the grating. For a 1st order grating at normal incidence of light θ = 0 and m = 1. The calculated grating periodicity was 416 nm. The groove-to-pitch ratio was chosen as 1/2 [7].

Experimental

We fabricated stripes 30 nm thick, 750 nm wide with grating using electron beam lithography (EBL). Bilayer PMMA (950k A4 and 495k A4 PMMA from Microchem GmbH) was patterned using EBL and then developed for 30 seconds in MIBK:IPA developer solution. A silver film with 30 nm thick-

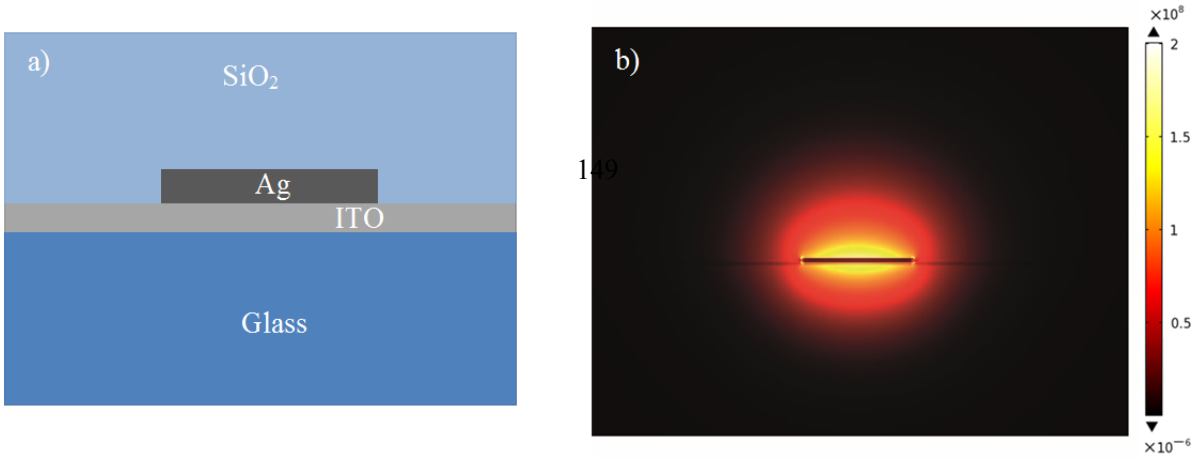

Figure 1: (a) The schematic diagram of the stripe waveguide covered with SiO_2 on an ITO-coated glass substrate, and (b) The magnitude of the electric field of the bound LRSPP mode supported by a 750 nm wide, 30 nm thick silver stripe waveguide on an ITO coated glass substrate at an excitation wavelength of 633 nm.

ness was evaporated onto the resist using PVD 75 electron beam evaporator under 0.1 Å/s. Lift-off of the resist was achieved in an acetone bath. Stripes with length 20 µm were fabricated (Figure 2). When using bilayer PMMA in EBL, the substrate must be relatively conductive. We used ITO-coated glass substrate as a conductive substrate. The presence of the ITO layer affects the plasmonic mode propagation, and thus the ITO layer is included in the FEM simulation. The ITO layer affects the propagation length and loss of the wavenumber of the guided mode and any cut-off thicknesses for particular modes. For more information see [6].

Fabricated structures were then optically tested for plasmon propagation. The sample was mounted on an inverted microscope stage. A laser beam was focused onto the input grating through the high numerical aperture (NA 1.3) 100× oil objective in contact with the backside of the sample through index matching oil (Figure 3). The outcoupled light from the opposite end of the waveguide was observed. CCD image of the outcoupling at the stripe end is shown in Figure 6b.

Finally, the samples were covered with SiO_2 spacer layers of thicknesses 5, 10, 15, 20, 25, 30, 40, and 50 nm using a PVD 75 electron beam evaporator. Quantum dots with an emission wavelength of 655 nm were obtained from invitrogen (Cat. No: Q21321MP). These carboxyl QDs are made from CdSe nanocrystals shelled with a ZnS layer. The core–shell material is further coated with a polymer layer to allow for better dispersion of the QDs in aqueous solution. These QDs have a narrow symmetric emission band with a maximum at 655 nm and are about 10 nm in size. Above QDs were diluted 50× in deionised water and spin coated onto the SiO_2 surface. Under these conditions the QD layer is highly dense. A schematic diagram of the sample cross-section is depicted in Figure 4 (image is not to scale).

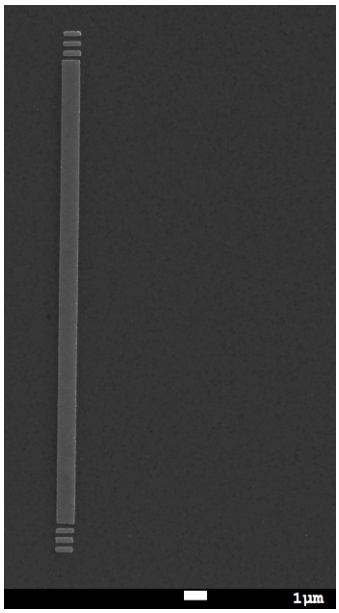

Figure 2: SEM image of 20 µm stripe with grating periodicity of 408 nm.

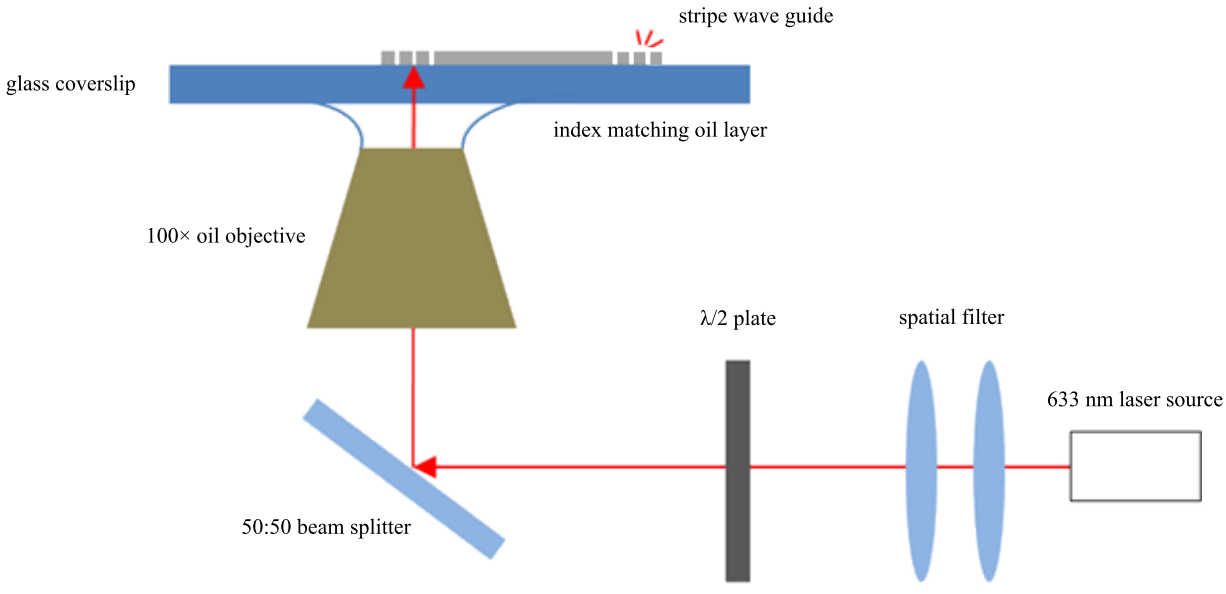

Figure 3: Conceptual representation of the excitation setup. The stripe waveguide is excited using the input gratings and light outcoupling is observed at the opposite end.

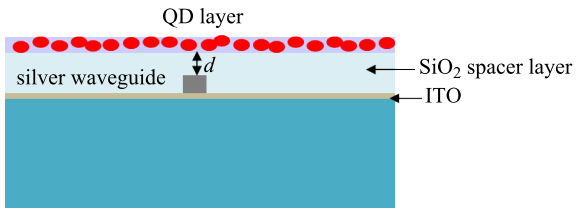

Figure 4: Schematic diagram of the cross section of the sample. Silver stripe waveguide on ITO-coated glass slide. Structures are covered with SiO_2 spacer layer with thickness *d*. QDs were spin coated on top of SiO_2.

The above experimental arrangement was modified to include a filter setup (632.8 nm excitor/649 nm single-edge dichroic beam splitter/655 nm single band bandpass filter) in the microscope for the QD emission line of 655 nm. Plasmon excited QD PL was observed at 655 nm following excitation of the stripe waveguide at 633 nm. Incident intensity of the laser was 2.52 mW/mm^2.

Results and Discussion

The polarisation dependence of the outcoupled light from the stripe waveguides (LRSPP mode) in the absence of a QD layer was investigated by varying the polarisation of the incoming excitation light (refer Figure 5). For each angle outcoupling intensity in the captured CCD image was analysed. Measured intensity values were normalised w.r.t. the incident laser intensity at the waveguide input.

Degree of Polarisation, DoP = $(I_{max} - I_{min})/(I_{max} + I_{min})$, analysis [10] shows that the outcoupled light is 78.9% TM polarised, which is in good agreement with other works and indicates the presence of plasmons [10]. This verifies that the far-field outcoupling observed at the end of the waveguides is a direct result of the propagating plasmons on the stripe.

CCD images of the plasmon outcoupling without QD and with QD are shown in Figure 6. When the LRSPP mode on the stripe waveguide was excited, the excited plasmon propagated along the stripe and scattered into the far field at the end of the waveguide or at a surface defect as shown in Figure 6a. When the waveguides were coated with a homogeneous QD layer (with a spacer layer of thickness 20 nm), we observed the bright luminescence around the waveguide rapidly decaying along the waveguide length (Figure 6b). If the frequency of the plasmons propagating on the stripe lies within the broad absorption band of the QDs, QDs in the immediate vicinity of the waveguide can be excited via propagating plasmons resulting in PL around the waveguide. We interpret the brighter QD PL along the waveguide edges is arising due to scattering of the propagating plasmons due to surface defects present along the edges. Intensity of the QD PL should be propotional to the intensity of the local field at the position of the QD. Therefore, the QDs placed in the evanescent tail of propagating plasmons provide a convenient method to probe plasmon propagation.

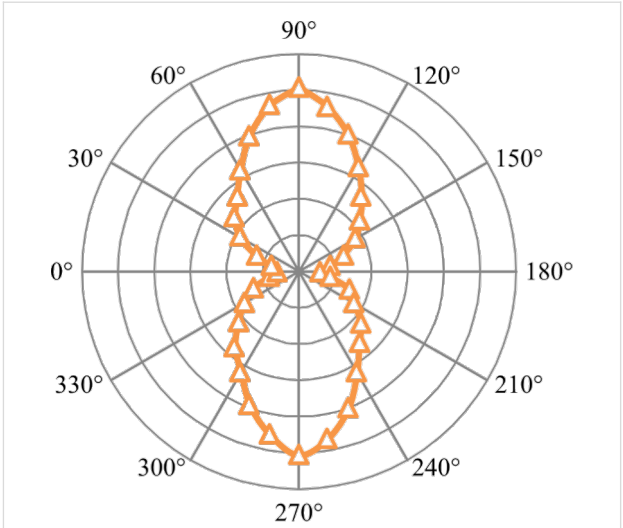

Figure 5: Polar plot for plasmons on 20 µm long stripe waveguide excited via grating coupling. Radial scale goes from 0 to 1.

Photoluminescence from the QDs where there with no waveguides in the vicinity (bulk QDs) was analysed for polarisation dependancy of the excitation laser (refer Figure 7, curve represented by the squares). DoP analysis showed that bulk QDs show a very little degree of polarisation (~8% TM polarised).

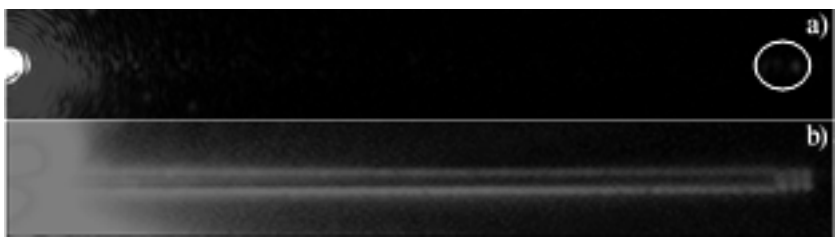

Figure 6: 20 µm stripes a) plasmon outcoupling when excited via grating coupling, b) QD coupling. Spacer layer 20 nm.

These QDs are slightly elongated in the direction of its crystal axis. The light emission of these QDs is preferentially polarised along the crystal axis [15]. The random orientation of this crystal axis in QDs in the film may result in nearly unpolarised behaviour in bulk QDs [16,17]. Then the stripe waveguides were excited using 633 nm laser light. The polarisation of this laser beam was varied and the QD PL near the waveguide surface was observed (refer Figure 7, curve represented by the circles).

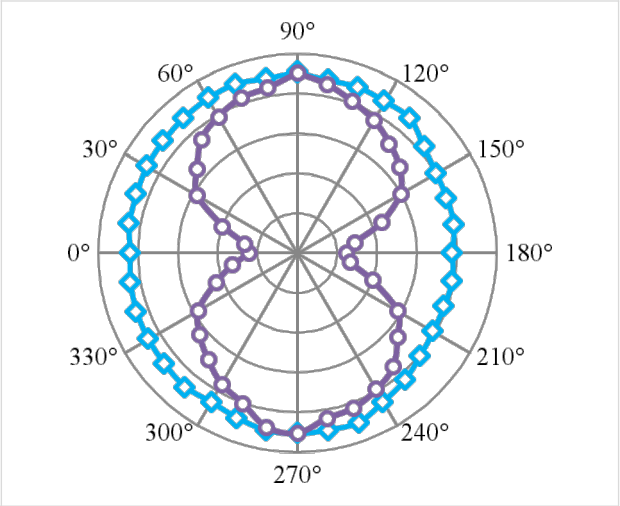

Figure 7: Polar plot for plasmon excited (circles) and b) bulk QDs (squares). The radial scale goes from 0 to 1.

As observed earlier, plasmons on the supported waveguides were 78.9% TM polarised. DoP analysis showed that the QD PL near the stripe waveguide showed 57.5% TM polarisation. In simple terms, the QD PL has an increased PL intensity when excited using a TM polarised laser. This increase in the DoP is an evidence that plasmons are causing the near-waveguide luminescence and QDs near the waveguide are excited by the propagating surface plasmons on the waveguide.

PL of the QDs can be quenched due to non-radiative decay into ohmic losses in the metal if placed too close to the metal surface of the waveguide [11]. This can be eliminated by inserting a dielectric spacer layer between QDs and the waveguide. In this experiment we used SiO_2 as the dielectric spacer layer. The SiO_2 layer acts as a spacer layer as well as helps to keep the excited LRSPP mode bound. The PL of QDs at the 20 µm long stripe end was measured as a function of spacer layer thickness (Figure 8). Intensities are normalised with respect to the incident light intensity. For each spacer layer, outcoupling intensity from five different stripes were obtained and averaged values are used in the graph below.

We observed that a spacer layer with a thickness of ca. 20 nm gives the highest outcoupling intensity. This is expected from theoretical calculations of single QD coupling to stripe waveguides [11]. When the QD to waveguide surface distance is less than 10 nm, non-radiative decay into metallic losses is prominent. Hence, the outcoupling intensity at the end is decreased and our observation is consistent with previously reported values [10,18]. After 30 nm, the distance between QD and waveguide surface increases and the QD is positioned far from the evanescent surface plasmon mode tail. Therefore, QD coupling in to plasmon-mediated free charge carriers is lower at larger distances.

Conclusion

We demonstrated that the QD PL can be used to image LRSPP propagating on a stripe waveguide. The optimised PL can be

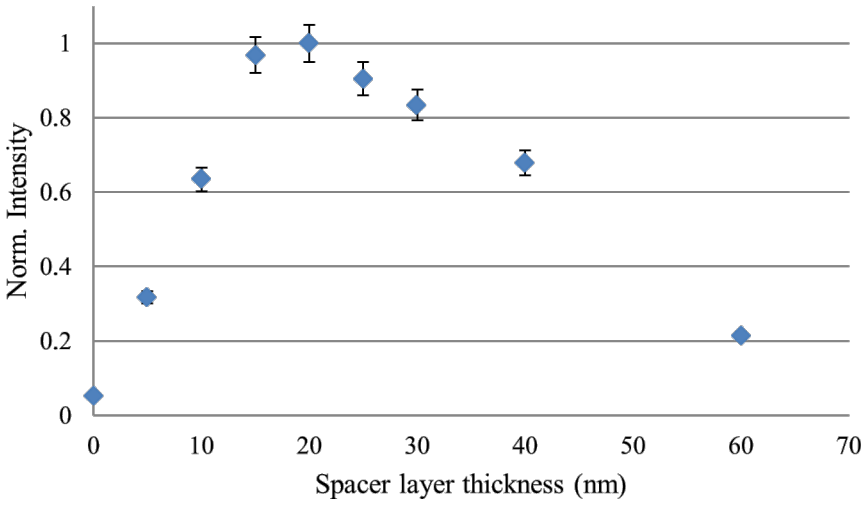

Figure 8: Normalised intensity at the outcoupling end of 20 µm stripe against spacer layer thickness.

obtained at a spacer layer thickness of approx. 18 nm. QD photoluminescence is quenched due to ohmic losses when the spacer layer thickness is less than 10 nm. Polar plots proved that the QDs in proximity to the waveguide surface were excited by the evanescent filed of the propagating plasmons.

Acknowledgements

This work was performed in parts at the Queensland node of the Australian National Fabrication Facility (ANFF), a company established under the National Collaborative Research Infrastructure Strategy to provide nano and micro-fabrication facilities for Australia's researchers. CP acknowledges valuable support from the UQ AIBN, UQ CMM, and QUT CARF team. CP and KV acknowledge the Australian Research Council (ARC) grant DP110101454 and the Asian Office of Aerospace Research and Development grant FA2386-14-1-4056. AMF acknowledges the Australian Research Council (ARC) fellowship FT110100545.

References

1. Maier, S. A. *Plasmonics: Fundamentals and Applications;* Springer, 2007. doi:10.1007/0-387-37825-1
2. Atwater, H. A. *Sci. Am.* **2007,** *296,* 56–62. doi:10.1038/scientificamerican0407-56
3. Bozhevolnyi, S. *Plasmonic nano-guides and circuits;* Pan Stanford: Singapore, 2008; p 441.
4. Berini, P. *Opt. Lett.* **1999,** *24,* 1011–1013. doi:10.1364/OL.24.001011
5. Berini, P. *Adv. Opt. Photonics* **2009,** *1,* 484–588. doi:10.1364/AOP.1.000484
6. Perera, C. S.; Vernon, K. C.; Funston, A. M.; Cheng, H.; Eftekhari, F.; Davis, T. J. *Opt. Express* **2015,** *23,* 10188–10197. doi:10.1364/OE.23.010188
7. Ditlbacher, H.; Krenn, J. R.; Felidj, N.; Lamprecht, B.; Schider, G.; Salerno, M.; Leitner, A.; Aussenegg, F. R. *Appl. Phys. Lett.* **2002,** *80,* 404–406. doi:10.1063/1.1435410
8. Wei, H.; Li, Z.; Tian, X.; Wang, Z.; Cong, F.; Liu, N.; Zhang, S.; Nordlander, P.; Halas, N. J.; Xu, H. *Nano Lett.* **2010,** *11,* 471–475. doi:10.1021/nl103228b
9. Ropp, C.; Cummins, Z.; Nah, S.; Fourkas, J. T.; Shapiro, B.; Waks, E. *Nat. Commun.* **2013,** *4,* 1447. doi:10.1038/ncomms2477
10. Bracher, G.; Schraml, K.; Blauth, M.; Wierzbowski, J.; López, N. C.; Bichler, M.; Müller, K.; Finley, J. J.; Kaniber, M. *J. Appl. Phys.* **2014,** *116,* 033101. doi:10.1063/1.4889859
11. Vernon, K. C.; Gomez, D. E.; Davis, T. J.; Tischler, N. *J. Appl. Phys.* **2011,** *110,* 074315. doi:10.1063/1.3650900
12. Palik, E. D. *Handbook of Optical Constants of Solids;* Elsevier Science and Tech, 1985; p 804.
13. Ghosh, G. *Opt. Commun.* **1999,** *163,* 95–102. doi:10.1016/S0030-4018(99)00091-7
14. Barnes, W. L.; Dereux, A.; Ebbesen, T. W. *Nature* **2003,** *424,* 824–830. doi:10.1038/nature01937
15. Xi, P. *Optical Nanoscopy and Novel Microscopy Techniques;* CRC Press, 2014. doi:10.1201/b17421
16. Koberling, F.; Kolb, U.; Philipp, G.; Potapova, I.; Basché, T.; Mews, A. *J. Phys. Chem. B* **2003,** *107,* 7463–7471. doi:10.1021/jp027800b
17. Gryczynski, I.; Malicka, J.; Jiang, W.; Fischer, H.; Chan, W. C. W.; Gryczynski, Z.; Grudzinski, W.; Lakowicz, J. R. *J. Phys. Chem. B* **2005,** *109,* 1088–1093. doi:10.1021/jp046173i
18. Liu, J.; Jiang, X.; Ishii, S.; Shalaev, V.; Irudayaraj, J. *New J. Phys.* **2014,** *16,* 063069. doi:10.1088/1367-2630/16/6/063069

License and Terms

Chapter 5: Mapping a bound plasmon propagating on a nanoscale stripe waveguide using quantum dots: Effect of spacer layer thickness

The authors listed below have certified* that:

21. they meet the criteria for authorship in that they have participated in the conception, execution, or interpretation, of at least that part of the publication in their field of expertise;
22. they take public responsibility for their part of the publication, except for the responsible author who accepts overall responsibility for the publication;
23. there are no other authors of the publication according to these criteria;
24. potential conflicts of interest have been disclosed to (a) granting bodies, (b) the editor or publisher of journals or other publications, and (c) the head of the responsible academic unit, and
25. they agree to the use of the publication in the student's thesis and its publication on the QUT ePrints database consistent with any limitations set by publisher requirements.

In the case of this chapter:

Mapping bound plasmon propagating on a nanoscale stripe waveguide using quantum dots: Effect of spacer layer thickness

Chamanei S. Perera, K. C. Vernon, A. M. Funston, and H. Cheng, submitted to BJ nano

Contributor	Statement of contribution*
C. S. Perera Signature Date	wrote the manuscript, conducted experiment and analysis
K.C. Vernon	Originally suggested the idea, aided in simulations, data analysis, interpretation of results and paper writing
Alison Funston	Aided in experiment
H. Cheng	Aided in experiment

Principal Supervisor Confirmation

I have sighted email or other correspondence from all Co-authors confirming their certifying authorship.

Kristy Vernon		17 July 2015
Name	Signature	Date

BEILSTEIN JOURNAL OF NANOTECHNOLOGY

Mapping bound plasmon propagation on a nanoscale stripe waveguide using quantum dots: influence of spacer layer thickness

Chamanei S. Perera[1], Alison M. Funston[2], Han-Hao Cheng[3] and Kristy C. Vernon[*1]

Full Research Paper

Open Access

Address:
[1]Queensland University of Technology, Brisbane 4001, QLD, Australia, [2]School of Chemistry, Monash University, Clayton 3800, VIC, Australia and [3]Australian National Fabrication Facility-QLD Node, AIBN, University of Queensland, St. Lucia 4072, QLD, Australia

Email:
Kristy C. Vernon[*] - k.vernon@qut.edu.au

* Corresponding author

Keywords:
photoluminescence; plasmonics; quantum dot; spacer layer; stripe waveguide

Beilstein J. Nanotechnol. **2015,** *6,* 2046–2051.
doi:10.3762/bjnano.6.208

Received: 21 July 2015
Accepted: 24 September 2015
Published: 19 October 2015

Associate Editor: A. J. Meixner

Abstract

In this paper we image the highly confined long range plasmons of a nanoscale metal stripe waveguide using quantum emitters. Plasmons were excited using a highly focused 633 nm laser beam and a specially designed grating structure to provide stronger incoupling to the desired mode. A homogeneous thin layer of quantum dots was used to image the near field intensity of the propagating plasmons on the waveguide. We observed that the photoluminescence is quenched when the QD to metal surface distance is less than 10 nm. The optimised spacer layer thickness for the stripe waveguides was found to be around 20 nm. Authors believe that the findings of this paper prove beneficial for the development of plasmonic devices utilising stripe waveguides.

Introduction

Plasmons are a coherent oscillation of electrons in a metal [1]. Loosely bound electrons can combine with incoming photons and propagate along the metal/dielectric interface. These charge density waves create a strong near-field [1]. There is increasing demand for high speed data communication as well as miniaturised devices, and plasmonics is a possible solution that can provide both the high speed and miniaturisation [2,3]. Plasmonics enables the squeezing of optical waves into miniscule structures and manipulating these waves to achieve all-optical circuits. Metal waveguides are a popular method to route light in nanoscale all-optical circuitry. Of all the waveguides, stripe waveguides are popular due to their ease of fabrication as well as the ability to support plasmon modes having relatively high propagation lengths [4,5]. These special modes are called long range surface plasmon polaritons (LRSPPs). LRSPPs have been shown to have large propagation lengths in the visible light range, greater than 10 μm [6].

When quantum dots (QDs) are placed in the vicinity of propagating plasmons, QDs can be locally excited by the plasmon if

the plasmon frequency lies within the absorption spectral range of the QDs [1,7]. Photoluminescence of the QD occurs due to excitation of the QD by the incident field of the propagating SPP on the stripe.

Intensity of the QD photoluminescence (PL) arising from the propagating plasmons is proportional to the intensity of the local electric field at the given position [7,8]. Therefore, QDs can be used to map the propagating plasmons on a waveguide [9,10]. It is well known that QD PL can be quenched via non-radiative transition of energy from QD to the metal if the QDs are placed too close to the metal surface [7,11]. Therefore, optimisation of the distance between the QD and metal surface is vital to enhance the PL intensity.

In this paper we present the mapping of the above bound plasmon mode using quantum dot photoluminescence. For a plasmonic stripe waveguide, we demonstrate that QD to waveguide surface distance is a critical factor on the QD PL [11]. We use degree of polarisation (DoP) measurements to prove that QD PL in the vicinity of the metal waveguide is arising from the local excitation of QDs by the propagating plasmon. Our experimental findings are supported by finite element modelling using COMSOL Multiphysics. Authors believe that findings of this work will prove beneficial in studying light matter interaction in nanoscale devices and all-optical circuitry.

Theory

COMSOL Multiphysics was used to run simulations on silver stripe waveguides supported on an indium tin oxide (ITO)-coated glass substrate with poly(methyl methacrylate) (PMMA) cladding. The width of the waveguide was chosen to be 750 nm to visualise easily under an optical microscope. Silver stripe waveguides were designed to be excited using a 633 nm laser. Permittivities of the materials used in modelling were, Silver as $-16.4 + 1.13i$ [12], ITO as $3.42 + 0.22i$ from Sopra database, glass 2.3, and SiO_2 as 2.4 [13]. The thickness of the ITO was 15 nm. Geometrical parameters of the stripe waveguide were theoretically determined to ensure the waveguide was single mode (ss_b^0). This required the thickness of the waveguide to be around 30 nm. The propagation length of this mode within a waveguide of these parameters has been previously reported experimentally to be 18 ± 6 μm [6]. The electric field profile of this mode is shown in Figure 1 below.

The grating periodicity (a) was calculated to provide stronger incoupling to the desired mode using [14]:

$$\beta = k \sin\theta + \frac{2\pi m}{a}, \quad (1)$$

where β is the wavenumber of the plasmon mode, k is the wavenumber of the incident light, θ is the angle of incidence and m is the order of the grating. For a 1st order grating at normal incidence of light θ = 0 and m = 1. The calculated grating periodicity was 416 nm. The groove-to-pitch ratio was chosen as 1/2 [7].

Experimental

We fabricated stripes 30 nm thick, 750 nm wide with grating using electron beam lithography (EBL). Bilayer PMMA (950k A4 and 495k A4 PMMA from Microchem GmbH) was patterned using EBL and then developed for 30 seconds in MIBK:IPA developer solution. A silver film with 30 nm thick-

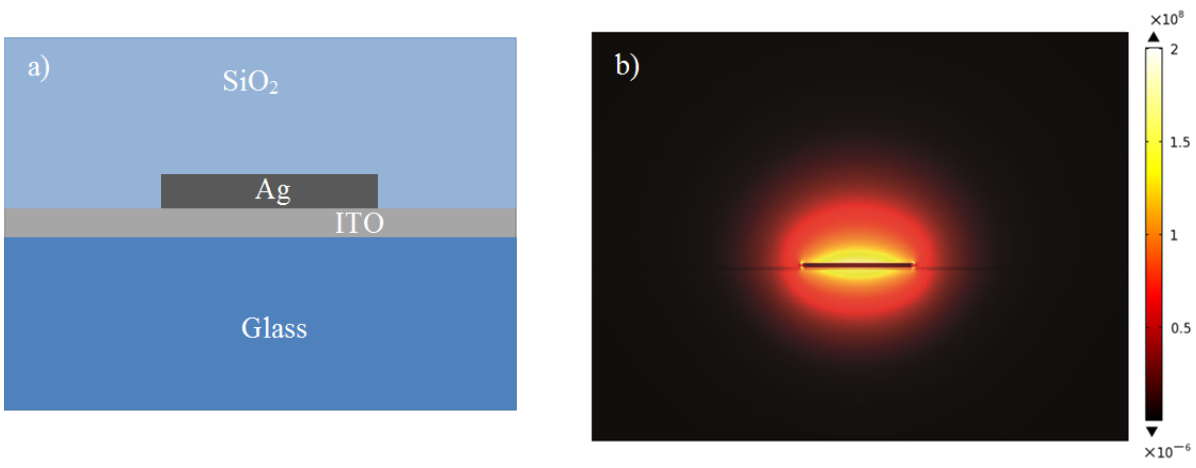

Figure 1: (a) The schematic diagram of the stripe waveguide covered with SiO_2 on an ITO-coated glass substrate, and (b) The magnitude of the electric field of the bound LRSPP mode supported by a 750 nm wide, 30 nm thick silver stripe waveguide on an ITO coated glass substrate at an excitation wavelength of 633 nm.

ness was evaporated onto the resist using PVD 75 electron beam evaporator under 0.1 Å/s. Lift-off of the resist was achieved in an acetone bath. Stripes with length 20 µm were fabricated (Figure 2). When using bilayer PMMA in EBL, the substrate must be relatively conductive. We used ITO-coated glass substrate as a conductive substrate. The presence of the ITO layer affects the plasmonic mode propagation, and thus the ITO layer is included in the FEM simulation. The ITO layer affects the propagation length and loss of the wavenumber of the guided mode and any cut-off thicknesses for particular modes. For more information see [6].

Fabricated structures were then optically tested for plasmon propagation. The sample was mounted on an inverted microscope stage. A laser beam was focused onto the input grating through the high numerical aperture (NA 1.3) 100× oil objective in contact with the backside of the sample through index matching oil (Figure 3). The outcoupled light from the opposite end of the waveguide was observed. CCD image of the outcoupling at the stripe end is shown in Figure 6b.

Finally, the samples were covered with SiO_2 spacer layers of thicknesses 5, 10, 15, 20, 25, 30, 40, and 50 nm using a PVD 75 electron beam evaporator. Quantum dots with an emission wavelength of 655 nm were obtained from invitrogen (Cat. No: Q21321MP). These carboxyl QDs are made from CdSe nanocrystals shelled with a ZnS layer. The core–shell material is further coated with a polymer layer to allow for better dispersion of the QDs in aqueous solution. These QDs have a narrow symmetric emission band with a maximum at 655 nm and are about 10 nm in size. Above QDs were diluted 50× in deionised water and spin coated onto the SiO_2 surface. Under these conditions the QD layer is highly dense. A schematic diagram of the sample cross-section is depicted in Figure 4 (image is not to scale).

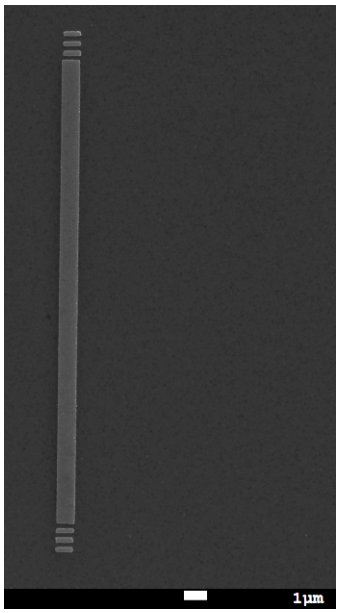

Figure 2: SEM image of 20 µm stripe with grating periodicity of 408 nm.

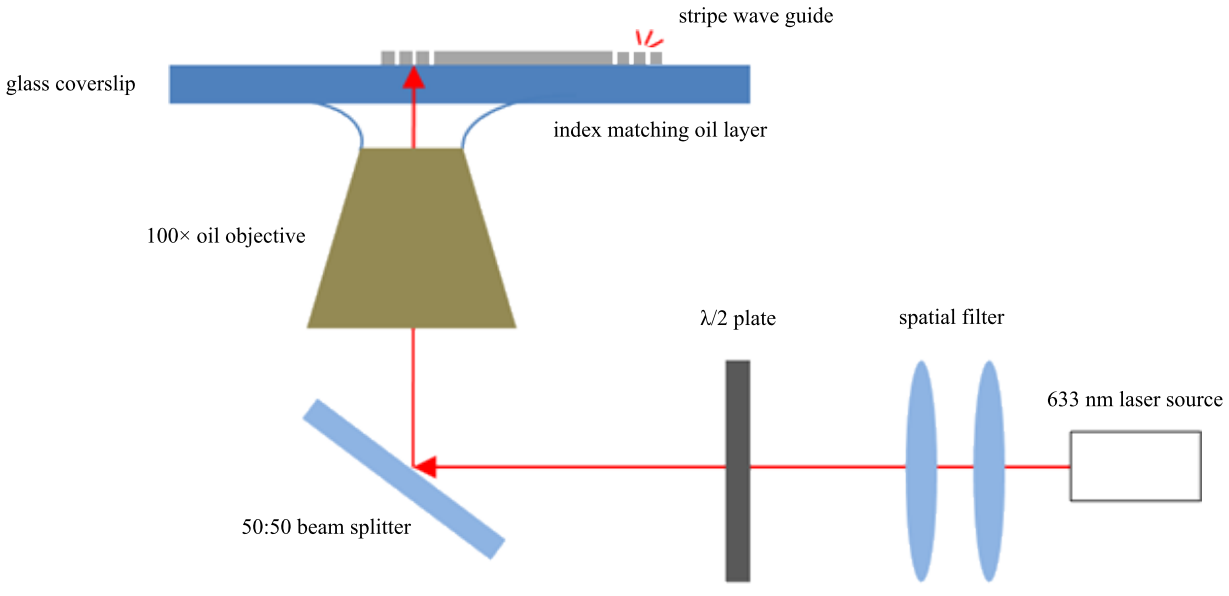

Figure 3: Conceptual representation of the excitation setup. The stripe waveguide is excited using the input gratings and light outcoupling is observed at the opposite end.

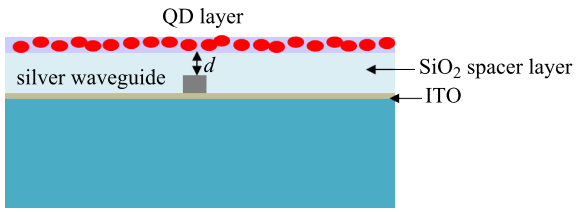

Figure 4: Schematic diagram of the cross section of the sample. Silver stripe waveguide on ITO-coated glass slide. Structures are covered with SiO_2 spacer layer with thickness *d*. QDs were spin coated on top of SiO_2.

The above experimental arrangement was modified to include a filter setup (632.8 nm excitor/649 nm single-edge dichroic beam splitter/655 nm single band bandpass filter) in the microscope for the QD emission line of 655 nm. Plasmon excited QD PL was observed at 655 nm following excitation of the stripe waveguide at 633 nm. Incident intensity of the laser was 2.52 mW/mm^2.

Results and Discussion

The polarisation dependence of the outcoupled light from the stripe waveguides (LRSPP mode) in the absence of a QD layer was investigated by varying the polarisation of the incoming excitation light (refer Figure 5). For each angle outcoupling intensity in the captured CCD image was analysed. Measured intensity values were normalised w.r.t. the incident laser intensity at the waveguide input.

Degree of Polarisation, DoP = $(I_{max} - I_{min})/(I_{max} + I_{min})$, analysis [10] shows that the outcoupled light is 78.9% TM polarised, which is in good agreement with other works and indicates the presence of plasmons [10]. This verifies that the far-field outcoupling observed at the end of the waveguides is a direct result of the propagating plasmons on the stripe.

CCD images of the plasmon outcoupling without QD and with QD are shown in Figure 6. When the LRSPP mode on the stripe waveguide was excited, the excited plasmon propagated along the stripe and scattered into the far field at the end of the waveguide or at a surface defect as shown in Figure 6a. When the waveguides were coated with a homogeneous QD layer (with a spacer layer of thickness 20 nm), we observed the bright luminescence around the waveguide rapidly decaying along the waveguide length (Figure 6b). If the frequency of the plasmons propagating on the stripe lies within the broad absorption band of the QDs, QDs in the immediate vicinity of the waveguide can be excited via propagating plasmons resulting in PL around the waveguide. We interpret the brighter QD PL along the waveguide edges is arising due to scattering of the propagating plasmons due to surface defects present along the edges. Intensity of the QD PL should be propotional to the intensity of the local field at the position of the QD. Therefore, the QDs placed in the evanescent tail of propagating plasmons provide a convenient method to probe plasmon propagation.

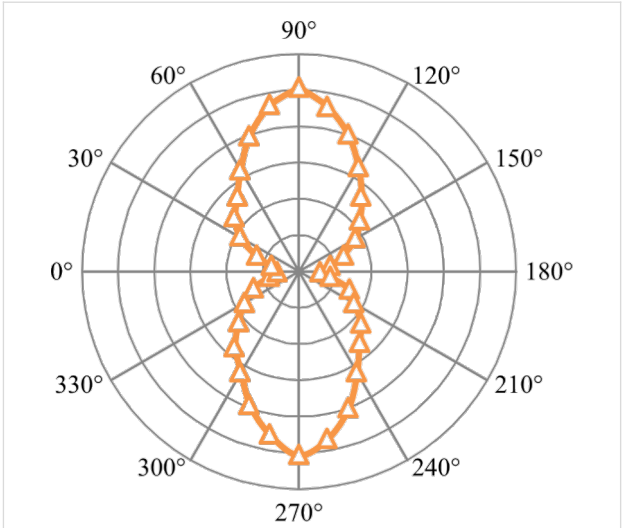

Figure 5: Polar plot for plasmons on 20 µm long stripe waveguide excited via grating coupling. Radial scale goes from 0 to 1.

Photoluminescence from the QDs where there with no waveguides in the vicinity (bulk QDs) was analysed for polarisation dependancy of the excitation laser (refer Figure 7, curve represented by the squares). DoP analysis showed that bulk QDs show a very little degree of polarisation (~8% TM polarised).

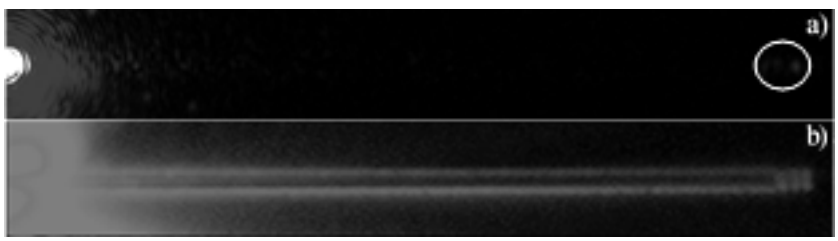

Figure 6: 20 µm stripes a) plasmon outcoupling when excited via grating coupling, b) QD coupling. Spacer layer 20 nm.

These QDs are slightly elongated in the direction of its crystal axis. The light emission of these QDs is preferentially polarised along the crystal axis [15]. The random orientation of this crystal axis in QDs in the film may result in nearly unpolarised behaviour in bulk QDs [16,17]. Then the stripe waveguides were excited using 633 nm laser light. The polarisation of this laser beam was varied and the QD PL near the waveguide surface was observed (refer Figure 7, curve represented by the circles).

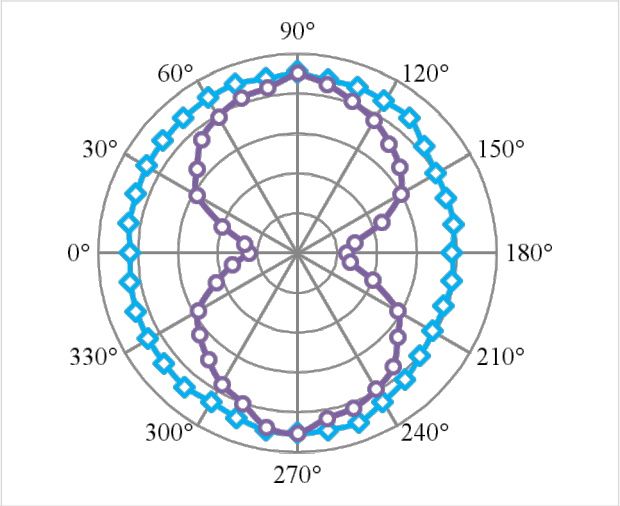

Figure 7: Polar plot for plasmon excited (circles) and b) bulk QDs (squares). The radial scale goes from 0 to 1.

As observed earlier, plasmons on the supported waveguides were 78.9% TM polarised. DoP analysis showed that the QD PL near the stripe waveguide showed 57.5% TM polarisation. In simple terms, the QD PL has an increased PL intensity when excited using a TM polarised laser. This increase in the DoP is an evidence that plasmons are causing the near-waveguide luminescence and QDs near the waveguide are excited by the propagating surface plasmons on the waveguide.

PL of the QDs can be quenched due to non-radiative decay into ohmic losses in the metal if placed too close to the metal surface of the waveguide [11]. This can be eliminated by inserting a dielectric spacer layer between QDs and the waveguide. In this experiment we used SiO_2 as the dielectric spacer layer. The SiO_2 layer acts as a spacer layer as well as helps to keep the excited LRSPP mode bound. The PL of QDs at the 20 µm long stripe end was measured as a function of spacer layer thickness (Figure 8). Intensities are normalised with respect to the incident light intensity. For each spacer layer, outcoupling intensity from five different stripes were obtained and averaged values are used in the graph below.

We observed that a spacer layer with a thickness of ca. 20 nm gives the highest outcoupling intensity. This is expected from theoretical calculations of single QD coupling to stripe waveguides [11]. When the QD to waveguide surface distance is less than 10 nm, non-radiative decay into metallic losses is prominent. Hence, the outcoupling intensity at the end is decreased and our observation is consistent with previously reported values [10,18]. After 30 nm, the distance between QD and waveguide surface increases and the QD is positioned far from the evanescent surface plasmon mode tail. Therefore, QD coupling in to plasmon-mediated free charge carriers is lower at larger distances.

Conclusion

We demonstrated that the QD PL can be used to image LRSPP propagating on a stripe waveguide. The optimised PL can be

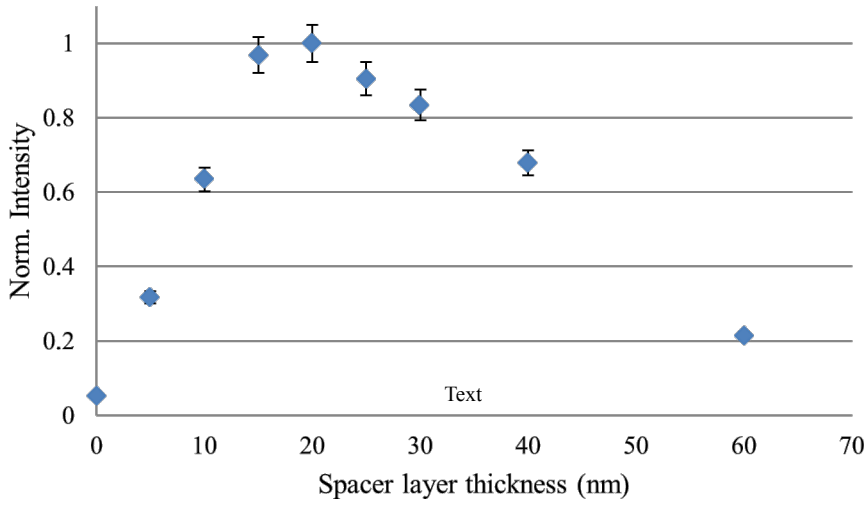

Figure 8: Normalised intensity at the outcoupling end of 20 µm stripe against spacer layer thickness.

obtained at a spacer layer thickness of approx. 18 nm. QD photoluminescence is quenched due to ohmic losses when the spacer layer thickness is less than 10 nm. Polar plots proved that the QDs in proximity to the waveguide surface were excited by the evanescent filed of the propagating plasmons.

Acknowledgements

This work was performed in parts at the Queensland node of the Australian National Fabrication Facility (ANFF), a company established under the National Collaborative Research Infrastructure Strategy to provide nano and micro-fabrication facilities for Australia's researchers. CP acknowledges valuable support from the UQ AIBN, UQ CMM, and QUT CARF team. CP and KV acknowledge the Australian Research Council (ARC) grant DP110101454 and the Asian Office of Aerospace Research and Development grant FA2386-14-1-4056. AMF acknowledges the Australian Research Council (ARC) fellowship FT110100545.

References

1. Maier, S. A. *Plasmonics: Fundamentals and Applications;* Springer, 2007. doi:10.1007/0-387-37825-1
2. Atwater, H. A. *Sci. Am.* **2007,** *296,* 56–62. doi:10.1038/scientificamerican0407-56
3. Bozhevolnyi, S. *Plasmonic nano-guides and circuits;* Pan Stanford: Singapore, 2008; p 441.
4. Berini, P. *Opt. Lett.* **1999,** *24,* 1011–1013. doi:10.1364/OL.24.001011
5. Berini, P. *Adv. Opt. Photonics* **2009,** *1,* 484–588. doi:10.1364/AOP.1.000484
6. Perera, C. S.; Vernon, K. C.; Funston, A. M.; Cheng, H.; Eftekhari, F.; Davis, T. J. *Opt. Express* **2015,** *23,* 10188–10197. doi:10.1364/OE.23.010188
7. Ditlbacher, H.; Krenn, J. R.; Felidj, N.; Lamprecht, B.; Schider, G.; Salerno, M.; Leitner, A.; Aussenegg, F. R. *Appl. Phys. Lett.* **2002,** *80,* 404–406. doi:10.1063/1.1435410
8. Wei, H.; Li, Z.; Tian, X.; Wang, Z.; Cong, F.; Liu, N.; Zhang, S.; Nordlander, P.; Halas, N. J.; Xu, H. *Nano Lett.* **2010,** *11,* 471–475. doi:10.1021/nl103228b
9. Ropp, C.; Cummins, Z.; Nah, S.; Fourkas, J. T.; Shapiro, B.; Waks, E. *Nat. Commun.* **2013,** *4,* 1447. doi:10.1038/ncomms2477
10. Bracher, G.; Schraml, K.; Blauth, M.; Wierzbowski, J.; López, N. C.; Bichler, M.; Müller, K.; Finley, J. J.; Kaniber, M. *J. Appl. Phys.* **2014,** *116,* 033101. doi:10.1063/1.4889859
11. Vernon, K. C.; Gomez, D. E.; Davis, T. J.; Tischler, N. *J. Appl. Phys.* **2011,** *110,* 074315. doi:10.1063/1.3650900
12. Palik, E. D. *Handbook of Optical Constants of Solids;* Elsevier Science and Tech, 1985; p 804.
13. Ghosh, G. *Opt. Commun.* **1999,** *163,* 95–102. doi:10.1016/S0030-4018(99)00091-7
14. Barnes, W. L.; Dereux, A.; Ebbesen, T. W. *Nature* **2003,** *424,* 824–830. doi:10.1038/nature01937
15. Xi, P. *Optical Nanoscopy and Novel Microscopy Techniques;* CRC Press, 2014. doi:10.1201/b17421
16. Koberling, F.; Kolb, U.; Philipp, G.; Potapova, I.; Basché, T.; Mews, A. *J. Phys. Chem. B* **2003,** *107,* 7463–7471. doi:10.1021/jp027800b
17. Gryczynski, I.; Malicka, J.; Jiang, W.; Fischer, H.; Chan, W. C. W.; Gryczynski, Z.; Grudzinski, W.; Lakowicz, J. R. *J. Phys. Chem. B* **2005,** *109,* 1088–1093. doi:10.1021/jp046173i
18. Liu, J.; Jiang, X.; Ishii, S.; Shalaev, V.; Irudayaraj, J. *New J. Phys.* **2014,** *16,* 063069. doi:10.1088/1367-2630/16/6/063069

License and Terms

Chapter 6: Highly compact refractive index sensor based on stripe waveguides for Lab-on-a-chip sensing applications

The authors listed below have certified* that:

26. they meet the criteria for authorship in that they have participated in the conception, execution, or interpretation, of at least that part of the publication in their field of expertise;
27. they take public responsibility for their part of the publication, except for the responsible author who accepts overall responsibility for the publication;
28. there are no other authors of the publication according to these criteria;
29. potential conflicts of interest have been disclosed to (a) granting bodies, (b) the editor or publisher of journals or other publications, and (c) the head of the responsible academic unit, and
30. they agree to the use of the publication in the student's thesis and its publication on the QUT ePrints database consistent with any limitations set by publisher requirements.

In the case of this chapter:

Highly compact refractive index sensor based on stripe waveguides for Lab-on-a-chip sensing applications.

C. S. Perera, K. C. Vernon, H. Cheng, J. Sathian, E. Jaatinen, and T. J. Davis, submitted to Journal of the Optical Society of America B

Contributor	Statement of contribution*
C. S. Perera	wrote the manuscript, conducted experiment and analysis
Signature	
Date	
K.C. Vernon	Originally suggested the idea, aided in simulations, data analysis, interpretation of results and paper writing
H. Cheng	Aided in experiment
Juna Sathian	Aided in experiment

Principal Supervisor Confirmation

I have sighted email or other correspondence from all Co-authors confirming their certifying authorship.

Kristy Vernon		10 December 2015
Name	Signature	Date

Highly Compact Refractive index sensor based on stripe waveguides for Lab-on-a-chip sensing applications

C.S. PERERA,[1] K.C. VERNON,[1,*] H. CHENG[2], J. SATHIAN[3], E.A. JAATINEN[1], T.J. DAVIS[4]

[1] Queensland University of Technology (QUT), Science and Engineering Faculty, Brisbane 4001, QLD, Australia
[2] Australian National Fabrication Facility QLD Node, AIBN, University Queensland, St. Lucia 4072, QLD, Australia
[3] Department of Materials, Imperial College, London SW7 2AZ, UK
[4] School of Physics, University of Melbourne, Parkville 3010, VIC, Australia

*Corresponding author: k.vernon@qut.edu.au

Received XX Month XXXX; revised XX Month, XXXX; accepted XX Month XXXX; posted XX Month XXXX (Doc. ID XXXXX); published XX Month XXXX

In this paper we report the design and experimental realisation of a novel refractive index sensor based on coupling between three nanoscale stripe waveguides. The sensor is highly compact and designed to operate at a single wavelength. We demonstrate that the sensor exhibits linear response with a resolution of 6×10^{-4} RIU (refractive index unit) for a change in relative output intensity of 1%. Authors expect that the outcome of this paper will prove beneficial in highly compact, label-free and highly sensitive refractive index analysis.

OCIS codes: (240.6608) Surface plasmons; (230.3120) Integrated optics devices.

http://dx.doi.org/10.1364/AO.99.099999

1. Introduction

Plasmons are coherent oscillations of free electrons existing on metal dielectric interfaces and are highly sensitive to the surrounding dielectric environment. This unique property is incredibly useful in sensing applications. Mach-Zehnder (MZ) interferometry (Ref. [1-5]), surface enhanced Raman spectroscopy (SERS) (Ref. [6-9]), ring resonators (Ref. [10]) and surface plasmon resonance (SPR) (Ref. [11-13]) are widely used techniques utilising plasmons to measure refractive index changes.

SPR is the most widely used sensing technique. It provides high sensitivity with label-free detection. Most commercially available SPR sensors employ a prism configuration to excite SPs on a metal surface which makes the device bulky and requires precise alignments (Ref. [12, 14]).

Nano-plasmonic sensors utilising metallic nanostructures can be used to overcome these limitations. In addition, they allow miniaturisation of the overall device size as well as improving the ease of excitation. The plasmonic Mach-Zehnder interferometer (MZI) is one such alternative passive nano-optical device used in refractive index sensing applications (Ref. [3, 5, 15, 16]). In physics, a MZI is a device used to determine the relative phase shift variations between two collimated beams derived from splitting light from the same single source (Ref. [17]).

Batoli et al. have designed a MZI integrated on a microfluidic platform consisting of two parallel nanoslits in a metal film coated on a glass substrate (Ref. [3, 18]). One slit was used to scatter white light into SP modes on a metal/fluidic interface (sample) on top and a metal/glass interface (reference) at the bottom. Launched SPs on the top and bottom surfaces travelled along the interfaces toward the other slit. These two SP modes interfered with each other and modulated the far-field scattering at this slit. Far-field intensity depends on the phase shift between two SP modes. The resolution of this MZI was 1.5×10^{-4} RIU while the minimum size of the device had a lateral dimension of 23 μm.

Pacifici at el. also developed an MZI consisting of two grooves separated by a slit (Ref. [5]). White light was directed onto the grooves and excited multiple SPs with different frequencies. Counter propagating SP waves interfered with the incident light at the slit location causing modification of the light intensity transmitting through the slit. The intensity of the transmitted light carries information about the near-field interaction of the plasmon with the dielectric environment. The resolution of this sensor was 3×10^{-7} RIU.

All of the interferometric designs described require exciting a SP on a metal slab with a surface defect (such as a groove or slit) and then analysing the resulting interference pattern transmitted through a slit. These sensors enable excitation using white light beams and generate interference patterns from multi-frequency SPs. Most of the presented MZI designs are quite bulky and it is difficult to analyse two analytes at once. As an example, the sensor proposed by Pacifi et al. needs to run separately for reference and sample solutions to allow analysis (Ref. [5]).

MZIs can be designed to be wavelength specific and more compact using waveguide structures. Vernon et al. proposed a compact interferometer design using stripe waveguide coupling to measure the change in the refractive index of a sample using the change in the output intensity (Ref. [19]). The stripe waveguides in the proposed design were supporting Long-Range Surface Plasmon Polaritons (LRSPPs). The design consisted of four stripes in total. Light coupled into the sensor using the input arm with the generated LRSPP

travelling along the input arm before coupling into the two outer reference and sample arms. Waves propagating along the two outer arms then evanescently coupled into the output arm. The presence of a sample in the sample arm caused a phase change in the wave travelling in the sample arm. This phase shift was then detected by the change in the output intensity at the output arm.

In this paper, we report the realisation of a refractive index sensor based on stripe waveguide coupling. The structure is similar to the structure proposed by Vernon et al (Ref. [19]) but without the output coupling arm, thus reducing the overall size of the device. The sample window was etched on top of the sample arm via a second ebeam lithography (EBL) process, and was used to place sample solution on top of the sample arm. The presence of the sample changes the wavenumber of the propagating plasmon mode hence changes the output intensity at the end of the sample arm. This design can be modified such that each outer arm can confine two different solutions at once and get the intensity change in the output with respect to each solution. The sample arm and reference arms must be separated from the input arm sufficiently so that the propagating modes do not couple between the sample and reference arm, only between the input arm and the outer arms. The length of the waveguides must also be chosen to ensure there is full transfer of energy between the input and outer arms (i.e. the lengths of the arms are determined by the coupling length of the system). A schematic of the interferometer design is given in Figure 1.

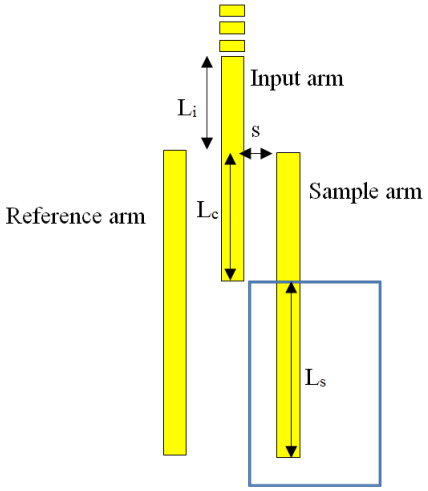

Fig. 1. Schematic diagram of the proposed sensor. The sample window is shown as the blue rectangle. L_i is the length of the input waveguide before coupling with the outer arms, L_c is the coupling length, L_s is the sample length and s is the separation between inner arm and outer arms

2. Theory

For the MZI based on stripe waveguides, the waveguide is required to support a single LRSPP mode (ss_b^0) at 633 nm excitation wavelength. Previously it has been reported (Ref. [20]) that this can be achieved with a silver stripe waveguide of width 750 nm and thickness 30 nm. The overall sensor design consists of three identical stripe waveguides labelled as input arm, reference arm and sample arm (Figure 1). The ss_b^0 mode of the input arm can be excited via end-fire excitation or grating coupling. This mode propagates along the input arm until its evanescent field starts to interact with the two outer arms.

Li is the length of the input waveguide before coupling with the outer arms, Lc is the coupling length and Ls is the sample length. The sample arm and reference arm are separated from the input arm by a separation distance s, and are uncoupled to each other. This situation can produce only three eigenmodes as shown in Fig. 2 below.

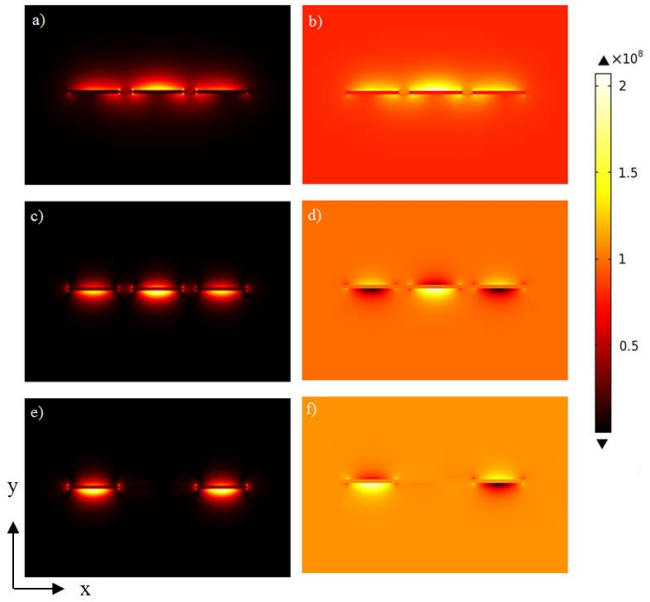

Fig. 2. [(a), (c) and (e)] Magnitude of the electric field distribution of the eigenmodes 1, 2 and 3. [(b), (d) and (f)] The *y*-component of the electric filed for eigenmodes 1, 2 and 3. Stripes are made from silver, 750 nm wide, 30 nm thick, and separated by 200 nm on ITO coated glass substrate with PMMA cladding for an excitation wavelength of 633 nm. These simulations were done using COMSOL Multiphysics.

The total field of the coupled system is a linear combination of these three eigenmodes and can be derived using the Haus and Fonstad approach (Ref. [21]). Refer to the Appendix for more details. The parameters of the proposed design are separation distance (s) 200 nm, L_i = 5μm, L_c = 29 μm and L_s = 20μm.

A. Intensity Analysis

We are interested in the output intensity difference at the sample arm and the reference arm. The corresponding *z* at this point is,

$$z = L_i + L_c + L_s \quad \textbf{(1)}$$

Electric field of the reference arm at this point

$$E_r = a_r e^{ik_r(z - L_i - L_c)} \quad \textbf{(2)}$$

where, k_r is the wavenumber of the mode travelling along the reference arm. Intensity from the reference arm (i.e. at $z = L_i + L_c + L_s$) can be determined using

$$I_r = |E_r|^2 \quad \textbf{(3)}$$

The wavenumber of the propagating mode on the stripe waveguide changes due to presence of a sample. Electric field of the sample arm at $z = L_i + L_c + L_s$ is given by

$$E_s = a_s e^{ik_s(z - L_i - L_c)} \quad \textbf{(4)}$$

and corresponding intensity can be found using

$$I_s = |E_s|^2 \quad \textbf{(5)}$$

To determine the sensitivity, we analyse the intensity difference between the reference arm and sample arm due to a small change in the sample refractive index.

3. Fabrication

The refractive index sensor (RI sensor) with a sample window on top of the sample arm was fabricated using a multi-step e-beam lithography (EBL) technique. First, the RI sensor designs and alignment marks were patterned on a 300 nm bilayer PMMA resist (950k A4 / 495 k A4 PMMA resist from Microchem GmbH) using electron beam lithography (JEOL-7800 FE- SEM with Raith Quantum Elphy) with a beam current of ~75 pA and 20 kV acceleration voltage under optimal dose of 280 μC/cm^2. The patterned PMMA bilayer was then developed for 30 seconds in MIBK:IPA 1:3 solution. 30 nm Ag was evaporated on the developed sample using the PVD 75 e-beam evaporator under a slow rate of 0.1 angstrom per second. A scanning electron microscope image was obtained (Fig. 3) which shows the successfully survived sensor designs after lift-off in acetone bath. Second, a 300 nm bilayer PMMA resist was spincoated on top of the structures to pattern the sample window on top of the sample arm. Then, the sample windows were patterned in the second EBL step. Finally, the patterned bilayer was developed in the developer solution for 30 seconds.

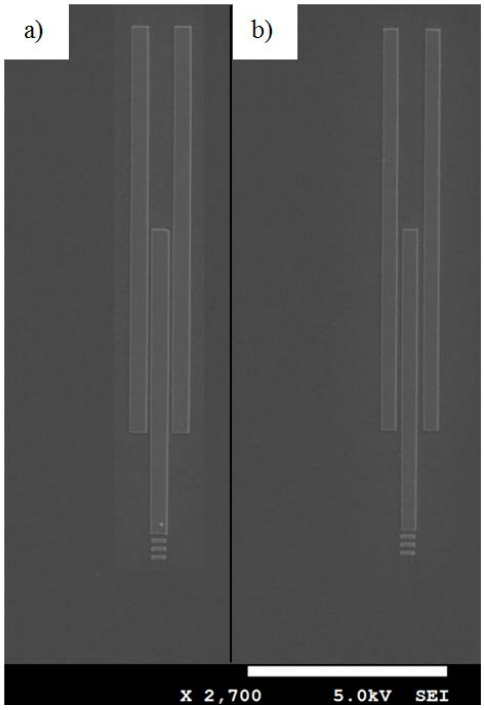

Fig. 3. SEM images of interferometers with gap separation a) 200 nm and b) 300 nm. Scale bar in the figure represents 10 μm.

Lengths of the input guide, reference arm and sample arm were 15 μm, 25 μm and 25 μm respectively. The design was tested for two separation distances of 200 nm and 300 nm as shown in Fig. 3.

4. Results and Discussion

A grating structure was placed at the input end to increase the energy transfer of incoming light into the input waveguide (Ref. [22]). The gratings were excited through an inverted microscope set-up using a 633 nm wavelength laser. The plasmon propagation and coupling in the RI sensor was imaged using CdSe quantum dots (QDs) with emission wavelength at 655 nm (From Invitrogen Cat. No. Q21321MP). An optimum QD spacer layer thickness of 18 nm SiO2 was selected (Ref. [23]). The sensor designs with separations between two outer arms of 300 nm [Fig.4(a)] and 200 nm [Fig. 4(b)] were observed under QD luminescence.

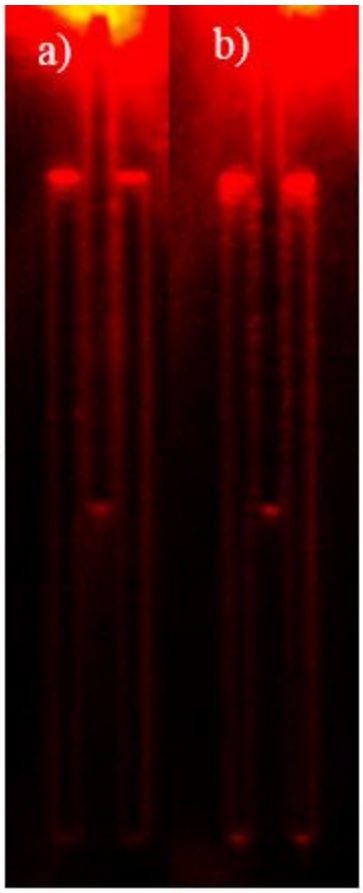

Fig. 4. QD luminescence images of interferometers with 300 nm gap and 200 nm gap when excited via input arm with a 633 nm laser.

We observed that plasmon outcoupling intensity was higher when the outer waveguide separation is lower. Based on the experimental results obtained from the QD images we chose to proceed with the sensor with 200 nm outer arm separation.

An input laser of wavelength 633 nm and power level of 4.0 mW was used to excite the LRSPP mode in the input arm. The excitation setup is described in detail in Ref. [22]. A series of CCD images of the RI sensor in operation for different solutions with different refractive indices are shown in Fig. 5. Refractive index of the sample in the sample arm was varied by varying the glucose concentration in deionized (DI) water.

Maximum incoupling was ensured by adjusting the beam position on the input grating such that it obtains maximum intensity. Incoupling and outcoupling intensities of the sensor were analysed using CCD images. For a laser power of 4.0 mW, input intensity had an averaged value of 65370 ± 90 Gray value. The outcoupling intensity of the reference and sample arm were measured for each sucrose solution. Fig. 6 depicts the relative intensity change ΔI/I0 between the sample and reference arm versus sucrose weight percentage in each sucrose solution, where I0 is the intensity on the reference arm, Ir (Eq. (3)).

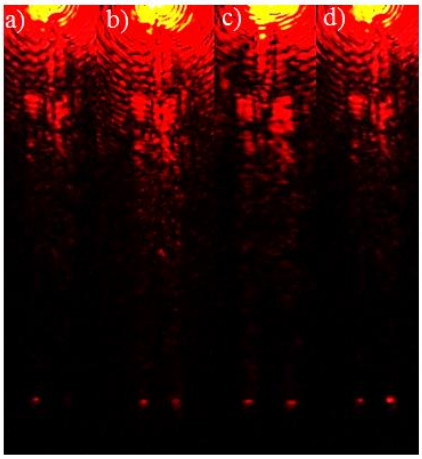

Fig. 5. Plasmonic RI sensor. Right outer arm (reference arm –covered with PMMA), left outer arm (sample arm – covered with 0.5% sucrose in DI water) Rightmost to lest are series of CCD images obtained for 0%, 10%, 80% sucrose in DI water and index matching oil.

$$\frac{\Delta I}{I_0} = \frac{I_r - I_s}{I_r} \times 100\% \qquad (6)$$

I_s is the sample arm output intensity at a specific glucose concentration (Eq. (5)). $I_0 = I_r$ is the reference arm output intensity and the reference arm was covered by PMMA of refractive index 1.4888 (at 633 nm, 20°C) (Ref. [24]). Five RI sensors are used to calculate the relative intensity change for each sucrose measurements, and the results averaged. The error bars in Fig. 6 are for the standard error in this averaging.

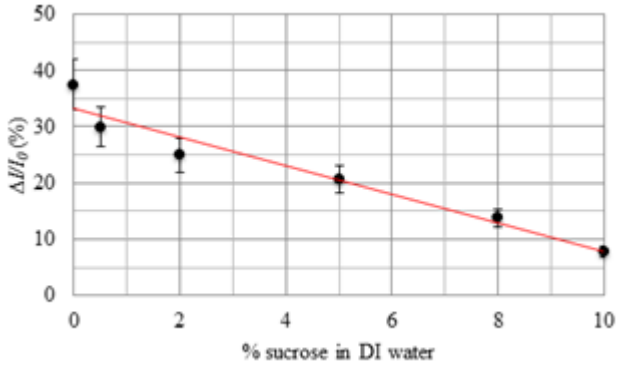

Fig. 6. Relative intensity difference between the sample arm and reference arm versus weight percentage of sucrose in DI water. The error bars are for the standard error.

The relative intensity difference was highest for DI water (with no sucrose) and lowest for 10% sucrose in DI water. For further clarification, a graph was plotted against relative intensity change as a function of refractive index change with respect to PMMA (Fig. 7). All the refractive indices of all sucrose solutions were measured at 20°C at a wavelength of 633 nm relative to air (Ref. [24]).

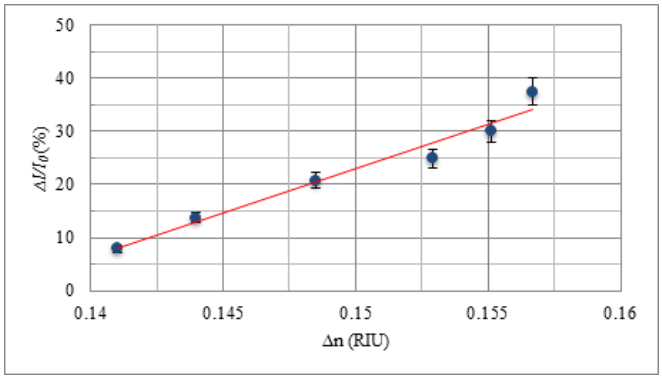

Fig. 7. Relative intensity difference between sample arm and reference arm vs refractive index difference (between PMMA and sucrose solutions) in refractive index units (RIU).

We observed that the intensity difference between arms changes linearly with the change in the refractive index of the solution (w.r.t. PMMA). Figure of Merit (FOM) relative to the intensity change was calculated by dividing the difference in the relative intensity change $\Delta I/I_0$ by Δn.

$$FOM = \lim_{\Delta n \to 0} \frac{\Delta I / I_0}{\Delta n} \qquad (7)$$

Calculated FOM for relative intensity change of the device was ~10^3 %/RIU. The gradient of the graph $\Delta I/I_0$ vs. Δn depicts the relative intensity difference for a refractive index change of 1 RIU in the sample arm. The device has a resolution of 6×10^{-4} RIU for a change in relative output intensity of 1%.

The sensor was further tested for 80% Sucrose (R.I. 1.4906) and an index matching oil of RI 1.5150. For 80% sucrose solution and for index matching oil, the sample arm intensity was higher than the reference arm [refer to CCD images on Fig. 5(c) and Fig. 5(d)]. These intensity differences when plotted on the above graph were consistent with the linear behaviour (these points are not shown on the graph).

5. Conclusion

We experimentally realised a three arm refractive index sensor design with a resolution of ~6×10^{-4} RIU for a 1% relative intensity change between output arms. The device is highly compact and authors believe it's the first attempt to fabricate an RI sensor with stripe waveguide coupling system.

6. Appendix

A. Additional Theory information

Here we assume that propagating modes in all three stripes are identical and the amplitudes of each wave is represented by $a_i(z)$ (input), $a_r(z)$ (reference) and $a_s(z)$ (sample) with direction of the propagating waves along z. Due to coupling between the stripes, the amplitudes of the propagating modes decrease along the waveguides.

Changes in the amplitude of each wave on each arm as a function of z can be given by

$$\frac{da_i}{dz} = i\kappa(a_r + a_s) \qquad (A.1)$$

$$\frac{da_r}{dz} = i\kappa a_i \qquad \textbf{(A.2)}$$

$$\frac{da_s}{dz} = i\kappa a_i \qquad \textbf{(A.3)}$$

where κ is the coupling strength. The solution to the above equations is in the form of $e^{-i\gamma z}$ with γ satisfying

$$\gamma^3 - 2\kappa^2\gamma = 0 \qquad \textbf{(A.4)}$$

The solutions γ of the above equation (0, $\sqrt{2}\kappa$, $-\sqrt{2}\kappa$) are the wavenumbers of the amplitudes of each eigenmode in the coupled system. When γ =0, the input arm has zero amplitude and the two outer arms have equal amplitudes but a π phase difference. This mode is depicted in Fig. 2(e) and Fig. 2(f). When $\gamma = \sqrt{2}\kappa$, the mode exists in all three arms but the input arm is out of phase by π radians with the reference and sample arms. This mode is called the anti-symmetric mode and is shown in Fig. 2(c) and Fig. 2(d) The wave in the input guide starts interacting with the outer arms at $z = L_i$. a_r and a_s are zero at this point. During the coupling process the reference and sample arms are in phase with each other due to their identical parameters. The input LRSPP mode excites symmetric and anti-symmetric eigenmodes in the two outer arms [Fig. 2 (a), Fig. 2(b) and Fig.2(c), Fig. 2(d)] leading to an energy transfer from the input waveguide to the outer waveguides. Then the change in the amplitudes at $z = L_i$ are given by,

$$a_i(z) = A_i\left(e^{-i\gamma(z-L_i)} + e^{i\gamma(z-L_i)}\right) \qquad \textbf{(A.5)}$$

$$a_r(z) = \frac{1}{\sqrt{2}}A_i\left(-e^{-i\gamma(z-L_i)} + e^{i\gamma(z-L_i)}\right) \qquad \textbf{(A.6)}$$

$$a_s(z) = \frac{1}{\sqrt{2}}A_i\left(-e^{-i\gamma(z-L_i)} + e^{i\gamma(z-L_i)}\right) \qquad \textbf{(A.7)}$$

where A_i is the amplitude of the first (all arms are in phase) and second modes (reference and samples are π out of phase with the input arm) of the Fig. 2(a), Fig. 2(b) and Fig. 2(c), Fig. 2(d) respectively.

B. Choosing structural parameters

The chosen isolated stripes should support bound single modes. The coupling length L_c is defined as the distance the plasmon must travel before the full energy transfer occurs from the input waveguide to the two outer arms. This is dependent on the separation distance of outer the arms from the input waveguide (s) and the wavenumbers of the symmetric and anti-symmetric modes k_s and k_a (Ref. [19]).

$$L_c = \frac{\pi}{k_s - k_a} \qquad \textbf{(A.8)}$$

For the chosen s, L_c must be lower than the propagation distance of the plasmon mode and large enough to keep the reference and sample arms uncoupled to each other.

Funding Information. Australian Research Council (ARC) (DP110101454); Asian Office of Aerospace Research and Development (FA2386-14-1-4056).

Acknowledgment. This work was performed in part at the Queensland node of the Australian National Fabrication Facility (ANFF), a company established under the National Collaborative Research Infrastructure Strategy to provide nano and micro-fabrication facilities for Australia's researchers. CP acknowledges valuable support from the UQ AIBN, UQ CMM, and QUT CARF team. CP and KV also acknowledge the QUT High Performance Computer facility.

References

1. K. Zetie, S. Adams, and R. Tocknell, "How does a Mach-Zehnder interferometer work?," Physics Education **35**, 46 (2000).
2. G. Jacek, M. Laurent, D. Alain, and I. B. Sergey, "Thermo-optic control of dielectric-loaded plasmonic Mach–Zehnder interferometers and directional coupler switches," Nanotechnology **23**, 444008 (2012).
3. Y. Gao, Q. Gan, Z. Xin, X. Cheng, and F. J. Bartoli, "Plasmonic Mach–Zehnder interferometer for ultrasensitive on-chip biosensing," ACS nano **5**, 9836-9844 (2011).
4. X. Zeng, Y. Gao, H. Hu, D. Ji, Q. Gan, and F. Bartoli, "A metal-insulator-metal plasmonic Mach-Zehnder interferometer array for multiplexed sensing," J. Appl. Phys. **113**, 133102 (2013).
5. J. Feng, V. S. Siu, A. Roelke, V. Mehta, S. Y. Rhieu, G. T. R. Palmore, and D. Pacifici, "Nanoscale plasmonic interferometers for multispectral, high-throughput biochemical sensing," Nano letters **12**, 602-609 (2012).
6. S. Lal, N. K. Grady, J. Kundu, C. S. Levin, J. B. Lassiter, and N. J. Halas, "Tailoring plasmonic substrates for surface enhanced spectroscopies," Chemical Society Reviews **37**, 898-911 (2008).
7. J. B. Jackson and N. J. Halas, "Surface-enhanced Raman scattering on tunable plasmonic nanoparticle substrates," Proceedings of the National Academy of Sciences **101**, 17930-17935 (2004).
8. S. Nie and S. R. Emory, "Probing single molecules and single nanoparticles by surface-enhanced Raman scattering," Science **275**, 1102-1106 (1997).
9. F. Scholes, T. Davis, K. Vernon, D. Lau, S. Furman, and A. Glenn, "A hybrid substrate for surface-enhanced Raman scattering spectroscopy: coupling metal nanoparticles to strong localised fields on a micro-structured surface," Journal of Raman Spectroscopy **43**, 196-201 (2012).
10. S. I. Bozhevolnyi, V. S. Volkov, E. Devaux, J.-Y. Laluet, and T. W. Ebbesen, "Channel plasmon subwavelength waveguide components including interferometers and ring resonators," Nature **440**, 508-511 (2006).
11. B. Liedberg, C. Nylander, and I. Lunström, "Surface plasmon resonance for gas detection and biosensing," Sensors and actuators **4**, 299-304 (1983).
12. J. Homola, S. S. Yee, and G. Gauglitz, "Surface plasmon resonance sensors: review," Sensors and Actuators B: Chemical **54**, 3-15 (1999).
13. N. Mehan, V. Gupta, K. Sreenivas, and A. Mansingh, "Surface plasmon resonance based refractive index sensor for

liquids," Indian Journal of Pure and Applied Physics **43**, 854 (2005).
14. B. Feltis, B. Sexton, F. Glenn, M. Best, M. Wilkins, and T. Davis, "A hand-held surface plasmon resonance biosensor for the detection of ricin and other biological agents," Biosensors and Bioelectronics **23**, 1131-1136 (2008).
15. X. Wu, J. Zhang, J. Chen, C. Zhao, and Q. Gong, "Refractive index sensor based on surface-plasmon interference," Opt. Lett. **34**, 392-394 (2009).
16. H. Fan, R. Charbonneau, and P. Berini, "Long-range surface plasmon triple-output Mach-Zehnder interferometers," Opt. Express **22**, 4006-4020 (2014).
17. L. Pezzé and A. Smerzi, "Phase sensitivity of a Mach-Zehnder interferometer," Phys. Rev. A **73**, 011801 (2006).
18. Q. Gan, Y. Gao, and F. J. Bartoli, "Vertical plasmonic Mach-Zehnder interferometer for sensitive optical sensing," Opt. Express **17**, 20747-20755 (2009).
19. K. Vernon, D. Gómez, and T. Davis, "A compact interferometric sensor design using three waveguide coupling," J. Appl. Phys. **106**, 104306-104306-104307 (2009).
20. K. C. Vernon, D. E. Gomez, T. J. Davis, and N. Tischler, "Simulations of the effect of waveguide cross-section on quantum dot–plasmon coupling," J. Appl. Phys. **110**, 074315 (2011).
21. P. Berini, N. Lahoud, and R. Charbonneau, "Fabrication of surface plasmon waveguides and integrated components on ultrathin freestanding membranes," Journal of Vacuum Science & Technology A **26**, 1383-1391 (2008).
22. C. Perera, K. Vernon, A. Funston, H. Cheng, F. Eftekhari, and T. Davis, "Excitation of bound plasmons along nanoscale stripe waveguides: a comparison of end and grating coupling techniques," Opt. Express **23**, 10188-10197 (2015).
23. C. S. Perera, A. M. Funston, H. Cheng, and K. C. Vernon, "Mapping bound plasmon propagation on a nanoscale stripe waveguide using quantum dots: influence of spacer layer thickness," Beilstein J. Nanotechnol. **6**, 2046-2051 (2015).
24. D. R. Lide, *CRC handbook of chemistry and physics,* 85 ed. (CRC press, 2004).

Chapter 7: Conclusions

In this thesis we concentrated on developing plasmon waveguides for nano-optical applications, and studied various methods of excitation and control of plasmon propagation. It is hoped that the results of this work will contribute to the future development of nano-optical circuitry.

The main contributions of this thesis are summarized as follows.

Chapter 3: This chapter focussed on numerical and experimental analysis of the QD-plasmon interaction when an optically excited QD is placed in proximity to a plasmon waveguide. Chapter 3 consisted of three sections.

Section 3.1: A numerical analysis of active control of gap plasmon propagation using Quantum dots was presented. The effect of gap width and waveguide-to-quantum dot distance were analysed extensively. *The probability of a QD spontaneous emission decaying into gap plasmon mode in a symmetric gap waveguide was observed to increase up to 50% when the gap width was reduced to 25 nm.*

Section 3.2: The effect of gap height, emitter-waveguide separation, and sharpness of the edge of the gap were studied to establish the effect on the efficiency of a dipole emitter coupling into gap plasmon modes when the emitter is placed in the vicinity of a symmetric nano gap waveguide. *Up to 5-fold increase in dipole emission into a guided plasmon mode was produced by varying gap height and this could be further increased by placing the emitter of optimal distance of 10 nm from the waveguide surface.*

Section 3.3: This paper describes a detailed analysis of the effect of Local Density of States (LDOS) of an optically excited Quantum dot at near-proximity of a single mode gap plasmon waveguide. We analysed the effect of gap parameters as well as the

symmetry of the surrounding dielectric media on QD-plasmon coupling efficiencies and *found that the symmetric environment provides better coupling efficiency of spontaneous emission of QD into plasmon mode of the gap waveguide.* To make the paper more realistic we studied the effect of the edge sharpness on the QD-plasmon interaction.

Chapter 4: This chapter discusses experimental realisation of excitement of bound plasmon modes on a stripe waveguide in the visible region using a highly focused laser beam. Two excitation methods were considered; endcoupling –where a highly focused laser beam was directed onto the waveguide's end and grating coupling- where a highly focused laser beam was directed onto a grating. The grating coupling provided better coupling of incoming light into the desired plasmon mode propagating on the stripe. The outcoupling intensity was increased by a factor of 2 when excited by grating coupling hence we were able to visually observe plasmon outcoupling from a 50μm long stripe. ***This is the first experimental realisation of an excited highly confined long-range plasmon mode on a stripe waveguide, using visible light excitation.***

Chapter 5: In this section QDs were used to image the bound plasmon propagating on a nanoscale stripe. It was known from **Chapter 3** that QD-waveguide separation needs to be optimised to enhance the QD-plasmon coupling. The spacer layer thickness was changed from 5 nm to 50 nm in increments of 5 nm. *It was found that the optimum coupling between QDs and highly confined plasmons propagating along the nanoscale waveguide occur when the QDs were placed 18 nm on top of the waveguide.* This agreed well with the existing literature on stripe-QD coupling. QD photoluminescence was quenched when the spacer layer thickness was less than 10 nm.

Chapter 6: *A novel plasmonic refractive index sensor based on stripe waveguides was fabricated and analysed in this Chapter*. The sensor design consisted of three stripe

waveguides; input waveguide and two identical outer arms named as sample arm and reference arm. Grating coupling excitation was used to excite Long-range plasmon mode on the input stripe waveguide. The excited plasmon travelled along the input guide until the evanescent field of the mode interacted with the two closely placed outer arms. This resulted in three-waveguide coupling. Coupled modes in the outer arms propagated along the waveguides with the same wavenumber. A sample solution was placed on top of sample arm. When the propagating mode on the sample arm encountered the sample, the wavenumber of the mode changed, due to the change in the refractive index. This resulted in an intensity change at the output end of the sample waveguide. The intensity difference between the reference and sample arms behaved linearly with the refractive index change. *The sensitivity of this refractive index (RI) sensor was found to be* $\sim 4 \times 10^5$ *per one intensity change.*

In conclusion, this thesis has presented both theoretical and experimental investigation of plasmonic nanostructures to use in applications. In particular, nanoscale plasmon waveguides supporting bound plasmon modes propagating micron distances have been experimentally realised and implemented to create a passive nano-optical device. The interaction of quantum dots with plasmon modes has also been studied experimentally and theoretically. It is hoped that the QD-plasmon study and the realisation of this nanoscale plasmon waveguide will benefit future developments in the nano-optics area. In particular, future avenues of future works are: all-optical logic gates and the use of plasmonic effects to increase solar cell and sensing efficiencies.

Recently, nanoscale all-optical logic gates have attracted enormous attention due to their important applications in optical computing and tetra-hertz speed information processing. We believe it is possible to develop nanoscale all-optical logic gates using the stripe waveguides discussed in this thesis. By placing a single emitter in the vicinity

of the output waveguide the emitter can be used to control the propagation of the light hence controlling the output digital state.

Plasmonics is mainly used to focus and localise light in the nanoscale using minuscule structures. This can be effectively used to increase the light harvesting inside a solar cell. Findings in this thesis could prove beneficial in increasing the efficiency of certain types of Solar cells. For instance, a Plasmonic QD-solar cell incorporating grating assisted light incoupling could be designed to excite propagating plasmon modes on a thin metal stripe waveguide with sunlight. QDs placed on the stripe waveguide will be excited by the plasmonic evanescent field propagating on the stripe and could be used to enhance the light absorption inside the solar cell.

By studying the interaction of light with the conduction electron of a metal, scientists have found new possibilities in many areas, such as data transmission in integrated circuits, chemical and biological sensing, spectroscopy, and photovoltaics. We believe further investigation into these fascinating phenomena will open up even more exciting discoveries in the future.

Bibliography

1. G. Moore, "Cramming more components onto integrated circuits," Electronics **38**, 56 (2000).
2. W. L. Barnes, A. Dereux, and T. W. Ebbesen, "Surface plasmon subwavelength optics," Nature **424**, 824-830 (2003).
3. A. V. Zayats and Smolyaninov, II, "Near-field photonics: surface plasmon polaritons and localized surface plasmons," J. Opt. a-Pure Appl. Op. **5**, S16-S50 (2003).
4. D. Tian, "Editorial (Moore's Law)," Potentials, IEEE **27**, 3-3 (2008).
5. B. Lamprecht, J. R. Krenn, G. Schider, H. Ditlbacher, M. Salerno, N. Felidj, A. Leitner, F. R. Aussenegg, and J. C. Weeber, "Surface plasmon propagation in microscale metal stripes," Appl. Phys. Lett. **79**, 51 (2001).
6. S. A. Maier, *Plasmonics: Fundamentals and Applications* (Springer, 2007).
7. H. A. Atwater, "The promise of plasmonics," Scientific American **296**, 56-63 (2007).
8. S. I. Bozhevolnyi, "Plasmonic nano-guides and circuits," in *Plasmonics and Metamaterials*, (Optical Society of America, 2008),
9. J. Feng, V. S. Siu, A. Roelke, V. Mehta, S. Y. Rhieu, G. T. R. Palmore, and D. Pacifici, "Nanoscale plasmonic interferometers for multispectral, high-throughput biochemical sensing," Nano letters **12**, 602-609 (2012).
10. H. Masuhara and S. Kawata, *Nanoplasmonics: From Fundamentals to Applications* (Elsevier Science, 2006), Vol. 2.
11. M. I. Stockman, "Nanoplasmonics: The physics behind the applications," Physics Today **64**, 39 (2011).
12. D. E. Chang, A. S. Sørensen, E. A. Demler, and M. D. Lukin, "A single-photon transistor using nanoscale surface plasmons," Nature Physics **3**, 807-812 (2007).
13. S. Lal, S. Link, and N. J. Halas, "Nano-optics from sensing to waveguiding," Nat. Photonics **1**, 641-648 (2007).
14. C. J. Min, J. Li, G. Veronis, J. Y. Lee, S. H. Fan, and P. Peumans, "Enhancement of optical absorption in thin-film organic solar cells through the excitation of plasmonic modes in metallic gratings," Appl. Phys. Lett. **96**(2010).
15. H. A. Atwater and A. Polman, "Plasmonics for improved photovoltaic devices," Nat. Mater. **9**, 205-213 (2010).
16. A. V. Akimov, A. Mukherjee, C. L. Yu, D. E. Chang, A. S. Zibrov, P. R. Hemmer, H. Park, and M. D. Lukin, "Generation of single optical plasmons in metallic nanowires coupled to quantum dots," Nature **450**, 402-406 (2007).
17. Y. C. Jun, R. D. Kekatpure, J. S. White, and M. L. Brongersma, "Nonresonant enhancement of spontaneous emission in metal-dielectric-metal plasmon waveguide structures," Phys. Rev. B **78**, 153111 (2008).
18. Y. C. Jun, R. Pala, and M. L. Brongersma, "Strong Modification of Quantum Dot Spontaneous Emission via Gap Plasmon Coupling in Metal Nanoslits," Journal of Physical Chemistry C **114**, 7269-7273 (2010).
19. C. Ropp, Z. Cummins, S. Nah, J. T. Fourkas, B. Shapiro, and E. Waks, "Nanoscale imaging and spontaneous emission control with a single nano-positioned quantum dot," Nat. Commun. **4**, 1447 (2013).

20. J. A. Dionne, H. J. Lezec, and H. A. Atwater, "Highly confined photon transport in subwavelength metallic slot waveguides," Nano Letters **6**, 1928-1932 (2006).
21. K. Tanaka and M. Tanaka, "Simulations of nanometric optical circuits based on surface plasmon polariton gap waveguide," Appl. Phys. Lett. **82**, 1158-1160 (2003).
22. H. Ditlbacher, A. Hohenau, D. Wagner, U. Kreibig, M. Rogers, F. Hofer, F. R. Aussenegg, and J. R. Krenn, "Silver nanowires as surface plasmon resonators," Phys. Rev. Lett. **95**, 257403 (2005).
23. S. A. Maier, P. G. Kik, H. A. Atwater, S. Meltzer, E. Harel, B. E. Koel, and A. A. Requicha, "Local detection of electromagnetic energy transport below the diffraction limit in metal nanoparticle plasmon waveguides," Nat. Mater. **2**, 229-232 (2003).
24. A. Bouhelier and G. P. Wiederrecht, "Surface plasmon rainbow jets," Opt. Lett. **30**, 884-886 (2005).
25. A. Hohenau, J. Krenn, A. Drezet, O. Mollet, S. Huant, C. Genet, B. Stein, and T. Ebbesen, "Surface plasmon leakage radiation microscopy at the diffraction limit," Opt. Express **19**, 25749-25762 (2011).
26. A. Bouhelier, T. Huser, H. Tamaru, H.-J. Güntherodt, D. Pohl, F. I. Baida, and D. Van Labeke, "Plasmon optics of structured silver films," Phys. Rev. B **63**, 155404 (2001).
27. T. Wang, E. Boer-Duchemin, Y. Zhang, G. Comtet, and G. Dujardin, "Excitation of propagating surface plasmons with a scanning tunnelling microscope," Nanotechnology **22**, 175201 (2011).
28. J. Jose, F. Segerink, J. Korterik, J. Herek, and H. Offerhaus, "Imaging of surface plasmon polariton interference using phase-sensitive photon scanning tunneling microscope," Applied Physics A **103**, 673-676 (2011).
29. A. Passian, A. Wig, A. Lereu, P. Evans, F. Meriaudeau, T. Thundat, and T. Ferrell, "Probing large area surface plasmon interference in thin metal films using photon scanning tunneling microscopy," Ultramicroscopy **100**, 429-436 (2004).
30. R. Reddick, R. Warmack, and T. Ferrell, "New form of scanning optical microscopy," Phys. Rev. B **39**, 767 (1989).
31. S. I. Bozhevolnyi, V. S. Volkov, E. Devaux, and T. W. Ebbesen, "Channel plasmon-polariton guiding by subwavelength metal grooves," Phys. Rev. Lett. **95**, 046802 (2005).
32. S. I. Bozhevolnyi, V. S. Volkov, E. Devaux, J.-Y. Laluet, and T. W. Ebbesen, "Channel plasmon subwavelength waveguide components including interferometers and ring resonators," Nature **440**, 508-511 (2006).
33. H. Ditlbacher, J. Krenn, N. Felidj, B. Lamprecht, G. Schider, M. Salerno, A. Leitner, and F. Aussenegg, "Fluorescence imaging of surface plasmon fields," Appl. Phys. Lett. **80**, 404-406 (2002).
34. H. Wei, Z. Li, X. Tian, Z. Wang, F. Cong, N. Liu, S. Zhang, P. Nordlander, N. J. Halas, and H. Xu, "Quantum dot-based local field imaging reveals plasmon-based interferometric logic in silver nanowire networks," Nano letters **11**, 471-475 (2010).
35. G. Zoriniants and W. L. Barnes, "Fluorescence enhancement through modified dye molecule absorption associated with the localized surface plasmon resonances of metallic dimers," New Journal of Physics **10**, 105002 (2008).

36. C. Gruber, A. Trügler, A. Hohenau, U. Hohenester, and J. R. Krenn, "Spectral modifications and polarization dependent coupling in tailored assemblies of quantum dots and plasmonic nanowires," Nano letters **13**, 4257-4262 (2013).
37. R. Chance, A. Prock, and R. Silbey, "Molecular fluorescence and energy transfer near interfaces," Adv. Chem. Phys **37**, 65 (1978).
38. G. Bracher, K. Schraml, M. Blauth, J. Wierzbowski, N. C. Lopez, M. Bichler, K. Müller, J. J. Finley, and M. Kaniber, "Imaging surface plasmon polaritons using proximal self-assembled InGaAs quantum dots," J. Appl. Phys. **116**, 033101 (2014).
39. D. Solis Jr, W.-S. Chang, B. P. Khanal, K. Bao, P. Nordlander, E. R. Zubarev, and S. Link, "Bleach-imaged plasmon propagation (BlIPP) in single gold nanowires," Nano letters **10**, 3482-3485 (2010).
40. D. Solis Jr, B. Willingham, S. L. Nauert, L. S. Slaughter, J. Olson, P. Swanglap, A. Paul, W.-S. Chang, and S. Link, "Electromagnetic energy transport in nanoparticle chains via dark plasmon modes," Nano letters **12**, 1349-1353 (2012).
41. R. Zia, J. A. Schuller, A. Chandran, and M. L. Brongersma, "Plasmonics: the next chip-scale technology," Materials Today **9**, 20-27 (2006).
42. D. K. Gramotnev and S. I. Bozhevolnyi, "Plasmonics beyond the diffraction limit," Nat. Photonics **4**, 83-91 (2010).
43. S. Bozhevolnyi, ed., *Plasmonic nano-guides and circuits* (Pan Stanford, Singapore, 2008), p. 441.
44. M. L. Brongersma and V. M. Shalaev, "Applied physics the case for plasmonics," (2010).
45. K. C. Vernon, in *Nanotechnology in Australia* (Pan Stanford, 2011).
46. P. Berini, "Long-range surface plasmon polaritons," Adv. Opt. Photonics **1**, 484-588 (2009).
47. D. Sarid, "Long-range surface-plasma waves on very thin metal films," Phys. Rev. Lett. **47**, 1927 (1981).
48. S. I. Bozhevolnyi, "Effective-index modeling of channel plasmon polaritons," Optics Express Online **14**, 9467-9476 (2006).
49. S. I. Bozhevolnyi and J. Jung, "Scaling for gap plasmon based waveguides," Opt. Express **16**, 2676-2684 (2008).
50. K. C. Vernon, *Strongly localised plasmons in metallic nanostructures* (Queensland Uni. of Tech., 2008), Vol. Dissertation/Thesis.
51. G. Veronis and S. Fan, "Subwavelength plasmonic waveguide structures based on slots in thin metal films," in *Integrated Optics: Devices, Materials, and Technologies X*, (SPIE, 2006), 12308-12308.
52. G. Veronis and S. H. Fan, "Guided subwavelength plasmonic mode supported by a slot in a thin metal film," Opt. Lett. **30**, 3359-3361 (2005).
53. G. Veronis and S. H. Fan, "Modes of subwavelength plasmonic slot waveguides," J. Lightwave Technol. **25**, 2511-2521 (2007).
54. G. Veronis, Z. F. Yu, S. E. Kocabas, D. A. B. Miller, M. L. Brongersma, and S. H. Fang, "Metal-dielectric-metal plasmonic waveguide devices for manipulating light at the nanoscale," Chin Opt Lett **7**, 302-308 (2009).
55. G. Veronis and S. H. Fan, "Plasmonic Slot Waveguides," in *Plasmonic Nanoguides and Circuits*, S. Bozhevolnyi, ed. (Pan Stanford publishing Pte Ltd, Singapore, 2009), pp. 159-187.

56. L. Chen, B. Wang, and G. P. Wang, "High efficiency 90° bending metal heterowaveguides for nanophotonic integration," Appl. Phys. Lett. **89**, 243120-243120 (2006).
57. R. A. Flynn, I. Vurgaftman, K. Bussmann, B. S. Simpkins, C. S. Kim, and J. P. Long, "Transmission efficiency of surface plasmon polaritons across gaps in gold waveguides," Appl. Phys. Lett. **96**(2010).
58. C. J. Min and G. Veronis, "Theoretical investigation of fabrication-related disorders on the properties of subwavelength metal-dielectric-metal plasmonic waveguides," Opt. Express **18**, 20939-20948 (2010).
59. P. Berini, "Plasmon-polariton waves guided by thin lossy metal films of finite width: Bound modes of asymmetric structures," Phys. Rev. B **63**, 125417 (2001).
60. P. Berini, "Plasmon-polariton waves guided by thin lossy metal films of finite width: Bound modes of symmetric structures," Phys. Rev. B **61**, 10484-10503 (2000).
61. P. Berini, "Plasmon polariton modes guided by a metal film of finite width," Opt. Lett. **24**, 1011-1013 (1999).
62. G. Bracher, K. Schraml, C. Jakubeit, M. Kaniber, and J. Finley, "Direct measurement of plasmon propagation lengths on lithographically defined metallic waveguides on GaAs," J. Appl. Phys. **110**, 123106 (2011).
63. H. Ditlbacher, J. R. Krenn, G. Schider, A. Leitner, and F. R. Aussenegg, "Two-dimensional optics with surface plasmon polaritons," Appl. Phys. Lett. **81**, 1762-1764 (2002).
64. M. U. González, J. C. Weeber, A. L. Baudrion, A. Dereux, A. L. Stepanov, J. R. Krenn, E. Devaux, and T. W. Ebbesen, "Design, near-field characterization, and modeling of 45° surface-plasmon Bragg mirrors," Phys. Rev. B **73**, 155416 (2006).
65. B. Wang and G. P. Wang, "Simulations of nanoscale interferometer and array focusing by metal heterowaveguides," Opt. Express **13**, 10558-10563 (2005).
66. R. Charbonneau, C. Scales, I. Breukelaar, S. Fafard, N. Lahoud, G. Mattiussi, and P. Berini, "Passive integrated optics elements based on long-range surface plasmon polaritons," J. Lightwave Technol. **24**, 477-494 (2006).
67. A. Boltasseva, T. Nikolajsen, K. Leosson, K. Kjaer, M. S. Larsen, and S. I. Bozhevolnyi, "Integrated optical components utilizing long-range surface plasmon polaritons," J. Lightwave Technol. **23**, 413-422 (2005).
68. B. Wild, L. Cao, Y. Sun, B. P. Khanal, E. R. Zubarev, S. K. Gray, N. F. Scherer, and M. Pelton, "Propagation lengths and group velocities of plasmons in chemically synthesized gold and silver nanowires," ACS nano **6**, 472-482 (2012).
69. W. Wang, Q. Yang, F. Fan, H. Xu, and Z. L. Wang, "Light propagation in curved silver nanowire plasmonic waveguides," Nano letters **11**, 1603-1608 (2011).
70. H. Wei, Z. Wang, X. Tian, M. Käll, and H. Xu, "Cascaded logic gates in nanophotonic plasmon networks," Nat. Commun. **2**, 387 (2011).
71. B. Wang and G. P. Wang, "Metal heterowaveguides for nanometric focusing of light," Appl. Phys. Lett. **85**, 3599-3601 (2004).
72. Y. Matsuzaki, T. Okamoto, M. Haraguchi, M. Fukui, and M. Nakagaki, "Characteristics of gap plasmon waveguide with stub structures," Opt. Express **16**, 16314-16325 (2008).

73. D. K. Gramotnev, M. G. Nielsen, S. J. Tan, M. L. Kurth, and S. I. Bozhevolnyi, "Gap surface plasmon waveguides with enhanced integration and functionality," Nano letters **12**, 359-363 (2011).
74. D. F. P. Pile, T. Ogawa, D. K. Gramotnev, Y. Matsuzaki, K. C. Vernon, K. Yamaguchi, T. Okamoto, M. Haraguchi, and M. Fukui, "Two-dimensionally localized modes of a nanoscale gap plasmon waveguide," Appl. Phys. Lett. **87**, 261114 (2005).
75. Y. Fu, X. Hu, C. Lu, S. Yue, H. Yang, and Q. Gong, "All-optical logic gates based on nanoscale plasmonic slot waveguides," Nano letters **12**, 5784-5790 (2012).
76. L. Dobrzynski and A. Maradudin, "Electrostatic edge modes in a dielectric wedge," Phys. Rev. B **6**, 3810 (1972).
77. J. Q. Lu and A. Maradudin, "Channel plasmons," Phys. Rev. B **42**, 11159 (1990).
78. I. Novikov and A. Maradudin, "Channel polaritons," Phys. Rev. B **66**, 035403 (2002).
79. D. F. P. Pile and D. K. Gramotnev, "Channel plasmon-polariton in atriangular groove on a metal surface," Opt. Lett. **29**, 1069-1071 (2004).
80. D. K. Gramotnev and D. F. P. Pile, "Single-mode subwavelength waveguide with channel plasmon-polaritons in triangular grooves on a metal surface," Appl. Phys. Lett. **85**, 6323-6325 (2004).
81. E. Moreno, S. G. Rodrigo, S. I. Bozhevolnyi, L. Martín-Moreno, and F. García-Vidal, "Guiding and focusing of electromagnetic fields with wedge plasmon polaritons," Phys. Rev. Lett. **100**, 023901 (2008).
82. S. A. Maier, P. G. Kik, and H. A. Atwater, "Observation of coupled plasmon-polariton modes in Au nanoparticle chain waveguides of different lengths: Estimation of waveguide loss," Appl. Phys. Lett. **81**, 1714-1716 (2002).
83. S. A. Maier, P. G. Kik, L. A. Sweatlock, H. A. Atwater, J. Penninkhof, A. Polman, S. Meltzer, E. Harel, A. A. Requicha, and B. E. Koel, "Energy transport in metal nanoparticle plasmon waveguides," in *MRS Proceedings*, (Cambridge Univ Press, 2003), T7. 1.
84. Y. Cui, M. T. Björk, J. A. Liddle, C. Sönnichsen, B. Boussert, and A. P. Alivisatos, "Integration of colloidal nanocrystals into lithographically patterned devices," Nano Letters **4**, 1093-1098 (2004).
85. H.-Y. Chen, C.-L. He, C.-Y. Wang, M.-H. Lin, D. Mitsui, M. Eguchi, T. Teranishi, and S. Gwo, "Far-field optical imaging of a linear array of coupled gold nanocubes: Direct visualization of dark plasmon propagating modes," ACS nano **5**, 8223-8229 (2011).
86. B. Willingham and S. Link, "Energy transport in metal nanoparticle chains via sub-radiant plasmon modes," Opt. Express **19**, 6450-6461 (2011).
87. K. Zetie, S. Adams, and R. Tocknell, "How does a Mach-Zehnder interferometer work?," Physics Education **35**, 46 (2000).
88. B. Wang and G. P. Wang, "Surface plasmon polariton propagation in nanoscale metalgap waveguides," Opt. Lett. **29**, 1992-1994 (2004).
89. R. G. Hunsperger, *Integrated optics: theory and technology* (Springer, 1984), Vol. 2.
90. L. Pezzé and A. Smerzi, "Phase sensitivity of a Mach-Zehnder interferometer," Phys. Rev. A **73**, 011801 (2006).

91. Q. Gan, Y. Gao, and F. J. Bartoli, "Vertical Plasmonic Mach-Zehnder interferometer for sensitive optical sensing," Opt. Express **17**, 20747-20755 (2009).
92. K. Vernon, D. Gómez, and T. Davis, "A compact interferometric sensor design using three waveguide coupling," J. Appl. Phys. **106**, 104306 (2009).
93. E. Purcell, "Spontaneous emission probabilities at radio frequencies," in *Confined Electrons and Photons* (Springer US, 1995), pp. 839-839.
94. K. C. Vernon, D. E. Gomez, T. J. Davis, and N. Tischler, "Simulations of the effect of waveguide cross-section on quantum dot–plasmon coupling," J. Appl. Phys. **110**, 074315 (2011).
95. D. E. Chang, A. S. Sorensen, P. R. Hemmer, and M. D. Lukin, "Quantum optics with surface plasmons," Phys. Rev. Lett. **97**, 053002 (2006).
96. D. E. Chang, A. S. Sorensen, P. R. Hemmer, and M. D. Lukin, "Strong coupling of single emitters to surface plasmons," Phys. Rev. B **76**, 035420 (2007).
97. Y. Chen, T. R. Nielsen, N. Gregersen, P. Lodahl, and J. Mørk, "Finite-element modeling of spontaneous emission of a quantum emitter at nanoscale proximity to plasmonic waveguides," Phys. Rev. B **81**, 125431 (2010).
98. K. S. Harsha, *Principles of vapor deposition of thin films* (Elsevier, 2005).
99. C. A. Volkert and A. M. Minor, "Focused ion beam microscopy and micromachining," MRS bulletin **32**, 389-399 (2007).
100. R. Pease, "Electron beam lithography," Contemporary Physics **22**, 265-290 (1981).
101. C. Vieu, F. Carcenac, A. Pepin, Y. Chen, M. Mejias, A. Lebib, L. Manin-Ferlazzo, L. Couraud, and H. Launois, "Electron beam lithography: resolution limits and applications," Applied Surface Science **164**, 111-117 (2000).
102. M. A. Mohammad, M. Muhammad, S. K. Dew, and M. Stepanova, *Fundamentals of electron beam exposure and development* (Springer, 2012).
103. V. R. Manfrinato, L. Zhang, D. Su, H. Duan, R. G. Hobbs, E. A. Stach, and K. K. Berggren, "Resolution limits of electron-beam lithography toward the atomic scale," Nano letters **13**, 1555-1558 (2013).
104. H. Yang, A. Jin, Q. Luo, J. Li, C. Gu, and Z. Cui, "Electron beam lithography of HSQ/PMMA bilayer resists for negative tone lift-off process," Microelectronic Engineering **85**, 814-817 (2008).
105. K. Suzuki, S. Matsui, and Y. Ochiai, *Sub-half-micron Lithography for ULSIs* (Cambridge University Press, 2000).
106. L. Novotny and B. Hecht, *Principles of nano-optics* (Cambridge university press, 2012).
107. A. W. Snyder and J. Love, *Optical waveguide theory* (Springer Science & Business Media, 2012).

Appendices

Appendix A: Modelling f QD-plasmon interactions

This section repeats the numerical modelling of SE emission of an excited quantum emitter in the vicinity of a waveguide decays into the plasmonic mode travelling along the waveguide by *Chen et al* [97].

When a quantum emitter is placed in the vicinity of a metallic plasmonic waveguide, there are three possible decay channels for the quantum emitter to decay into. (i) Radiatively decay into free space (γ_{rad}), (ii) nonradiatively decay into ohmic losses in the metal (γ_{nonrad}), and (iii) decay into guided plasmon mode of the waveguide (γ_{pl}).

The spontaneous emission β factor defined by $\beta = \frac{\gamma_{pl}}{\gamma_{tot}}$ where γ_{tot} is the sum of all three decay channels. β factor gives the probability of SE of the quantum emitter decaying into guided plasmon mode on the waveguide. In order to find spontaneous emission β factor, first we need to find γ_{pl}.

A1. Modelling spontaneous emission decay rate into the plasmonic mode (γ_{pl})

Maxwell's wave equation for the electric field is given by,

$$\nabla \times \left(\frac{\nabla \times \bar{E}(\bar{r})}{\mu_r} \right) - k_0^2 \varepsilon(\bar{r}) \bar{E}(\bar{r}) = 0 \qquad (1)$$

where, $k_0 = \omega\sqrt{\varepsilon_0 \mu_0}$ is the vacuum wavenumber, $\bar{\varepsilon}(r)$ is the dielectric function relative to vacuum, $\mu(r)$ denotes the relative permeability constant assumed to be equal to 1.

$$\bar{E}(x,y,z) = \bar{E}_{\alpha}(x,y)e^{-j(\omega t-\beta z)} \tag{2}$$

where, $\alpha = \{p, \beta\}$ denotes the complete orthogonal modes for the guided plasmonic mode with β as the component of the wavevector along the z axis (propagation constant) and p as the polarisation of the mode. The symmetric waveguide structure consists of a dielectric gap in a metal film and the structure is surrounded by the same dielectric material (refer **Figure A1**).

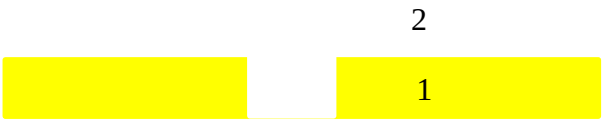

Figure A1 Symmetric waveguide structure. 1 represents the metal region and 2 represents the dielectric region.

The transverse component of the wavevector ($k_{i\perp} = j\kappa_{i\perp}$) fulfils $k_{i\perp} = \sqrt{\frac{\omega^2}{c^2}\varepsilon_i - \beta^2}$ with $i \in (1,2)$, where ε_i is the relative permittivity.

GPW parameters we chosen such that the waveguide only supports fundamental plasmonic mode with a strong E_y component. Electric field dyadic Green's function of the guided mode can be constructed using eigenmode analysis and normalised plasmonic decay rate can be extracted.

The electric dyadic Green's function $\bar{\bar{G}}(\bar{r}, \bar{r}', \omega)$ is given by,

$$\hat{L}\bar{\bar{G}}(\bar{r}, \bar{r}', \omega) = \bar{\bar{I}}\delta(\bar{r} - \bar{r}') \tag{3}$$

where $\bar{\bar{I}}$ is the unit dyad. The operator $\hat{L} = [\nabla \times \nabla \times -k_0^2 \varepsilon(\bar{r})]$ doesn't have a set of complete orthogonal eigenmodes if the $\varepsilon(\bar{r})$ is complex. Suppose $\bar{E}_n$ is a set of eigensolutions defined by $\hat{L}$, the eigensolutions of the adjoint operator $\hat{L}^\dagger$ are defined as the biorthogonal modes $\bar{E}_m^\dagger$. $\hat{L}^\dagger$ is obtained from the operator $\hat{L}$ by replacing the complex conjugate of $\varepsilon(\bar{r})$. The biorthogonality condition is given by,

$$\int \varepsilon(\bar{r}) \bar{E}_n(r) \cdot [\bar{E}_m^\dagger(\bar{r})]^* d^3 r = \delta_{nm} N_n$$

with the completeness relation $\sum \frac{\varepsilon(\bar{r}) \bar{E}_n(\bar{r}) [\bar{E}_n^\dagger(\bar{r}')]^*}{N_n} = \bar{\bar{I}} \delta(\bar{r} - \bar{r}')$.

From the biorthogonality completeness relation, the dyadic Green's function $\bar{\bar{G}}(\bar{r}, \bar{r}', \omega)$ constructed using the eigen expansion is given by,

$$\bar{\bar{G}}(\bar{r}, \bar{r}', \omega) = \bar{\bar{G}}_{GT}(\bar{r}, \bar{r}', \omega) + \bar{\bar{G}}_{GL}(\bar{r}, \bar{r}', \omega) = \sum_n \frac{\bar{E}_n(\bar{r}) [\bar{E}_n^\dagger(\bar{r}')]^*}{N_n \lambda_n} + \sum_n \frac{\nabla \phi_n(\bar{r}) [\nabla \phi_n^\dagger(\bar{r}')]^*}{M_n k_0^2} \quad (4)$$

where, $\bar{\bar{G}}_{GT}(\bar{r}, \bar{r}', \omega)$ is the generalized transverse part of the dyadic Green's function. It is constructed using the complete set of transverse eigenfunction $\bar{E}_n(\bar{r})$ defined by,

$$-\nabla \times \nabla \times \bar{E}_n(\bar{r}) + k_0^2 \varepsilon(\bar{r}) \bar{E}_n(\bar{r}) = \lambda_n \varepsilon(\bar{r}) \bar{E}_n(\bar{r})$$

and $\nabla \cdot [\varepsilon(\bar{r}) \bar{E}_n(\bar{r})] = 0$ with eigenvalue λ_n.

The generalised longitudinal part of the dyadic Green's function is constructed from longitudinal eigenfunctions that can be found from a complete set of scalar eigenmodes $\phi_n(\bar{r})$ satisfying $\nabla \cdot [\varepsilon(\bar{r}) \nabla \phi_n(\bar{r})] = \sigma_n \phi_n(\bar{r})$ with the biorthogonality relation $\int \varepsilon(\bar{r}) \nabla \phi_n(r) \cdot [\nabla \phi_n^\dagger(\bar{r})]^* d^3 r = \delta_{nm} M_n$. Since the guided plasmonic mode is the field

solution in the absence of electric charge ($\nabla \cdot [\varepsilon(\bar{r})\bar{E}_n(\bar{r})] = 0$), the longitudinal component will vanish in the following calculations.

It is found the contribution to the dyadic Green's function from the plasmonic mode as,

$$\bar{\bar{G}}_{pl}(\bar{r}, \bar{r}', \omega) = \sum_p \int_{-\infty}^{+\infty} \frac{\varepsilon_2 \bar{E}_\alpha(x,y)[\bar{E}_\alpha^\dagger(x',y')]^* e^{j\beta(z-z')}}{[k_0^2\varepsilon_2 - (\beta^2 - \kappa_{2\perp}^2)]N} d\beta \tag{5}$$

where, the simplified normalization factor *N* is given by,

$N = 2\pi \int \varepsilon(x,y)\bar{E}_\alpha(x,y)[\bar{E}_\alpha^\dagger(x,y)]^* dxdy$.

Equation (5) is evaluated for one plasmon mode using contour integration method because the intergrand decays to zero at infinity in the upper and the lower β planes,

$\bar{\bar{G}}_{pl}(\bar{r}, \bar{r}', \omega) = \dfrac{j\pi c^2 \bar{E}_\alpha(x,y)[\bar{E}_\alpha^\dagger(x',y')]^*}{\omega N v_g}$ where, v_g is the group velocity defined by the $v_g = d\omega/d\beta$.

According to *Novotny et al* [106], The dyadic Green's function can be used to calculated the projected LDOS for one plasmonic mode,

$\rho_\mu(r_0, \omega_0) = 6\omega[\bar{n}_\mu \cdot \mathrm{Im}\{\bar{\bar{G}}(r_0, r_0, \omega_0)\} \cdot \bar{n}_\mu] / (\pi c^2)$ where $\bar{n}_\mu$ is the unit vector of the dipole moment of the quantum emitter. If the emitter is oriented along *Y* axis, the projected LDOS for the plasmonic mode is given by, $\rho_{pl}(\bar{r}, \omega) = 6 \,|\, E_{\alpha,y}(x,y) \,|^2 / (N v_g)$

The decay rate of the spontaneous emission into plasmonic mode (γ_{pl}) is given by,

$\gamma_{pl} = \dfrac{\pi\omega_0}{3\hbar\varepsilon_0} |\, \mu \,|^2 \, \rho_{pl}(\bar{r}, \omega)$ and γ_{pl} can be normalised w.r.t the spontaneous emission decay rate in the vacuum (γ_0). The normalised spontaneous emission decay rate into plasmonic mode is given by,

$$\frac{\gamma_{pl}}{\gamma_0} = \frac{6\pi^2 c^3 \bar{\bar{E}}_{\alpha_0,y}(x,y)[\bar{\bar{E}}^{\dagger}_{\alpha_0,y}(x',y')]^*}{\omega_0^2 N v_g} \tag{7}$$

According to *Snyder et al* [107], the group velocity v_g can be calculated using, $v_g = \int_{A_\infty} (\bar{E} \times \bar{H}^*) \cdot \bar{z} dA / \int_{A_\infty} \varepsilon_0 \varepsilon(x,y) |\bar{E}(x,y)|^2 \, dA$, where A_∞ denotes integration over the transverse plane. By applying the power orthogonal approximation along with the group velocity equation used by *Snyder et al* [107] into equation (7), spontaneous emission decay to the fundamental plasmonic mode is given by,

$$\frac{\gamma_{pl}}{\gamma_0} = \frac{3\pi c \varepsilon_0 \bar{\bar{E}}_{\alpha_0,y}(x,y)[\bar{\bar{E}}^{\dagger}_{\alpha_0,y}(x',y')]^*}{k_0^2 \int_{A_\infty} (\bar{E} \times \bar{H}^*) \cdot \bar{z} dA} \tag{8}$$

In order to find spontaneous emission β factor, the next step is to find the sum of all three decay channels γ_{tot}.

A2. Modelling total decay rate (γ_{tot})

Well defined field components in the transverse plane of the waveguide enable the numerical construction of plasmonic mode of the quantum emitter spontaneous emission using dyadic Green's function. When the model domain is reasonably large, the concentrated fields near the metallic edge of the waveguide tends to decay to zero on the borders. Therefore, the scattering boundary condition ensuring absorption of plane waves is used in the truncated 2D modelling domain. The field components of the radiation modes in transverse plane does not vanish even at large domain size. To determine the total decay rate of the spontaneous emission of the emitter, a full 3D numerical solution is needed to include the radiation modes.

Electric field is generated by the quantum emitter and is constructed as a linear current source. In the model used in Chapter 3, we looked into the fundamental mode of the

GPW which has a dominant E_y field component with field maximal along the waveguide edge. The quantum emitter is oriented along the *y* axis in the vicinity of the waveguide with strong dipole emission along the same axis. The total decay rate of the, γ_{tot}, can be extracted from the total power dissipation of the current source coupled to the nearby metallic waveguide, $\gamma_{tot}/\gamma_0 = P_{tot}/P_0$ with $P_{tot} = 1/2\int_V \mathrm{Re}(\bar{J}^* \cdot \bar{E}_{tot})dV$ is the total power dissipation of the current source coupled to the metallic waveguide and $P_0 = 1/2\int_V \mathrm{Re}(\bar{J}^* \cdot \bar{E}_0)dV$ is the total power dissipated by the same current source in the vacuum. P_0 is used as the normalizing quantity. For an electric current source with finite size of l ($l \ll \lambda_0$), and linear distribution of current (I_0), the dipole moment of the source is given by, $\mu = jI_0 l/\omega$. The size of the linear current source must be restricted below 2 nm to avoid higher order multiple moments. Therefore, in our model we constructed QD as a linear current source carrying 1A current. The size of the emitter restricted to 1 nm to consider it as a dipole emitter. Therefore, the simplified equation for the normalised total decay rate of the spontaneous emission of the quantum emitter is given by,

$$\frac{\gamma_{tot}}{\gamma_0} = \frac{\int(\bar{E}_y)dI}{\int(\bar{E}_{0y})dI} \tag{9}$$

dI implies the integration over the length of the emitter. To solve the above equation, the electric field strength at the emitter position needs to be calculated. The waveguide should be sufficiently long enough to avoid the reflected plasmon modes interfere with the QD. Therefore the chosen waveguides are longer than 4 times the propagation length of the fundamental mode.

Appendix B: Supplementary materials

B1. Gap waveguide fabrication

Gap waveguides were fabricated using the FIB technique. 250 nm Au was thermally (or e beam) evaporated on to a glass substrate of thickness 1 mm. Then 300 nm wide 250 nm deep, 10 µm long gaps were milled using focused ion beam (**Figure B1**).

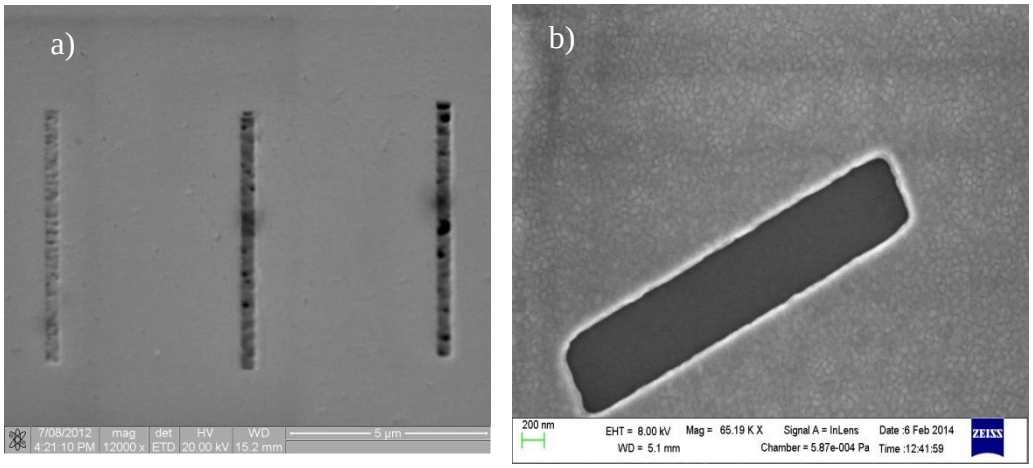

Figure B1 (a) FIB milled gaps with left most gap with low number of passes, middle to right increased number of passes in raster scan and (b) a successful 300 nm wide 250 nm deep 3 µm long slot

After familiarising myself with the FIB operation the next target was to fabricate a stripe waveguide using FIB. The first method was to mill a PMMA layer, deposit gold and lift off. 100 µm x 100 µm x 100 nm square waveguide survived after lift-off but smaller structures survived poorly due to poor adhesion of gold to glass surface (**Figure B2**)

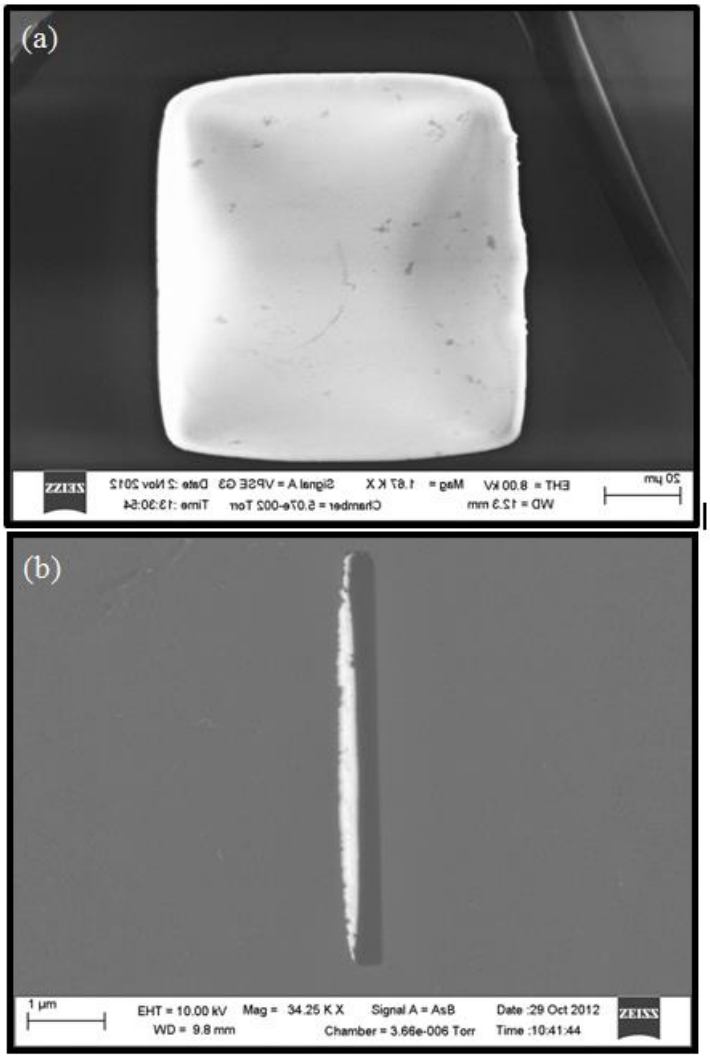

Figure B2 Attempt to make stripe waveguides using FIB milling into PMMA followed by lift-off. a) Survived 100 µm x 100 µm x 100 nm square waveguide. Polymer layer in the background is left after liftoff process probably the PMMA layer exposed to e beam while imaging using SEM. b) unsuccessful 200 nm wide 250 nm deep 10 µm long stripes.

Next attempt was to mill stripe waveguide on the metal coated sample by milling away a large area leaving the stripe in the middle. We could obtain stripes successfully using this method. We incorporated grating structures to provide better incoupling into plasmons when excited using highly focused laser beam (**Figure B3**)

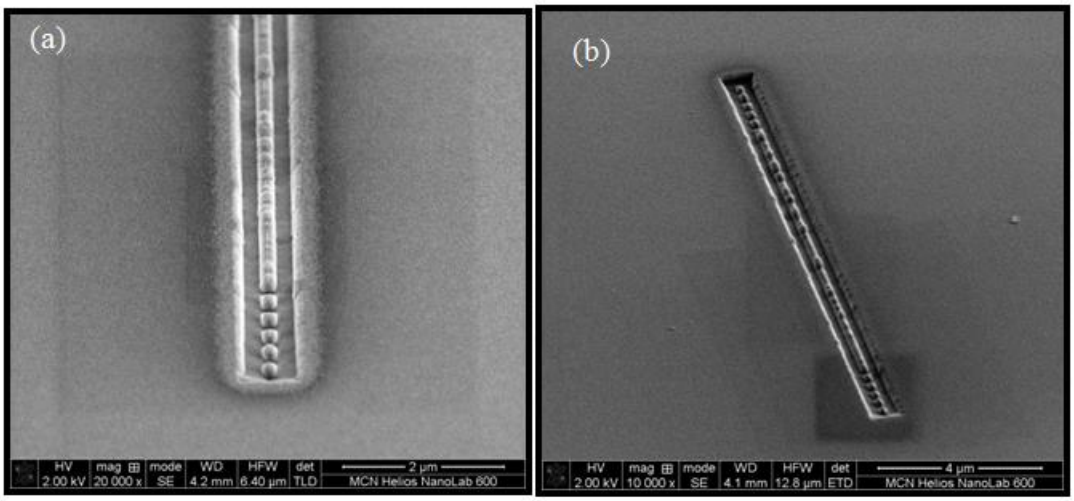

Figure B3 (a) 200 nm wide, 100 nm thick, 10 µm long stripe with grating structures (grating periodicity 383 nm with groove to pitch ratio 1/2), and (b) tilted view of the same stripe waveguide. The structure was produced at Melbourne Centre for Nanofabrication, Melbourne.

Since the fabrication difficulties and excitation difficulties, wider stripes were milled using FIB technique. Fabricated structures were checked for plasmon propagation using highly focused laser beam focused on to the input grating using x100 times oil objective with 1.3 numerical aperture. CCD images were obtained of propagated plasmons outcoupled from the other end into the far-field (refer **Figure B4**).

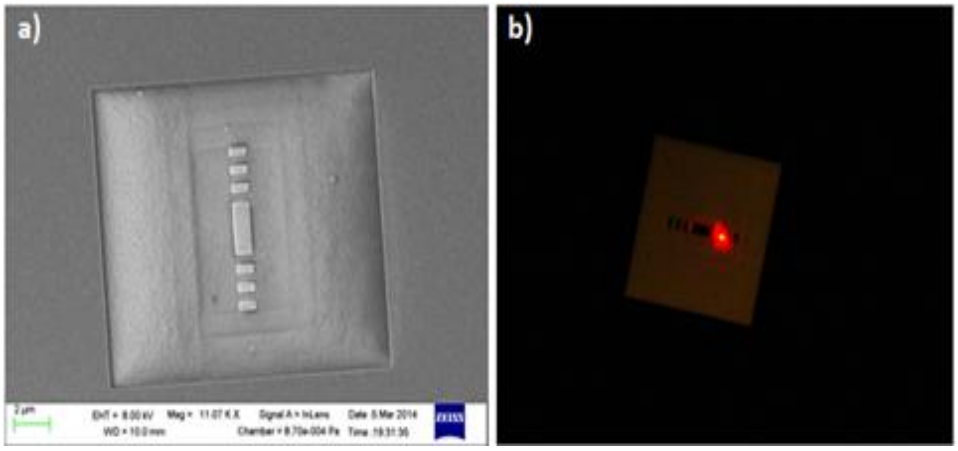

Figure B4 (a) 1 µm wide, 5 µm long 100 nm thick Au waveguides fabricated using FIB, and (b) plasmon propagating on a FIB milled stripe when excited using highly focused laser beam of wavelength 633 nm. Structures produced by the author at QUT using CARF facilities and dark field image obtained by the author using inhouse excitation setup.

Very low propagation length was observed in these structures which was discouraging. Therefore, stripes were fabricated using e beam lithography. First, 300 nm thick bilayer PMMA resist (using 950k A4 / 495 k A4 PMMA resist from Microchem GmbH) was prepared on a cleaned ITO coated coverslip. Then the 750 nm wide stripes (length 5 µm and 10-50 µm) with and without grating section were patterned onto the PMMA layer using electron beam lithography (JEOL-7800 FE-SEM with Raith Quantum Elphy). Patterned PMMA layer was then developed for 30 seconds in MIBK:IPA 1:3 solution. 30 nm Ag was evaporated on the developed sample using the PVD 75 e-beam evaporator. SEM image below shows the 750 nm wide stripes survived successfully after lift- off in acetone bath (refer **Figure B5**). A 200 nm SiO_2 layer was then evaporated on top of the waveguides to preserve the symmetry of the system for the desired mode. The grating periodicity was 416 nm with a groove to pitch ratio of ½.

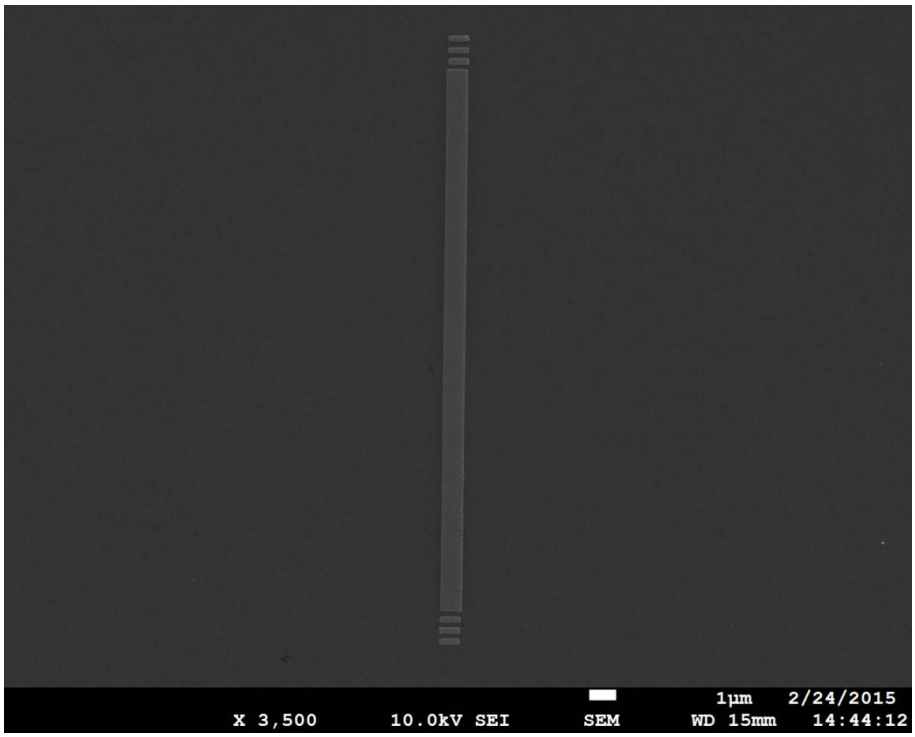

Figure B5 30 nm height, 750 nm wide, 20 µm long stripe with gratings at both ends survived successfully after lift-off process. Image was produced by author at QUT CARF.

Plasmonic refractive index sensor was fabricated using the same lithographical technique. SEM image of the sensor structure is shown in **Figure B6** below. For more information refer to **Chapter 5**.

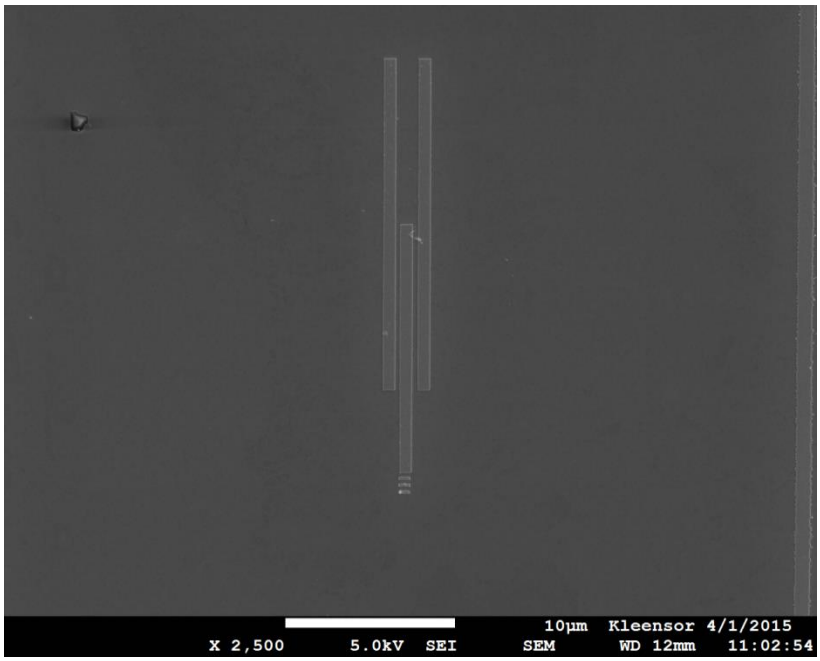

Figure B6 SEM image of a plasmonic refractive index sensor consisting of three 750 nm wide, 30 nm thick Ag stripes. Outer arms are 25 µm long and central arm is 15 µm long.

B2. Excitation technique

There are several methods to generate SPP in stripe waveguides. As mentioned in **Section 2.2**, our inhouse experimental setup uses a high numerical aperture 100x oil-immersion microscope objective to focus laser light on to the sample and collect the outcoupling light using the same objective. Schematic diagram of the excitation set up used is shown in **Figure B7**.

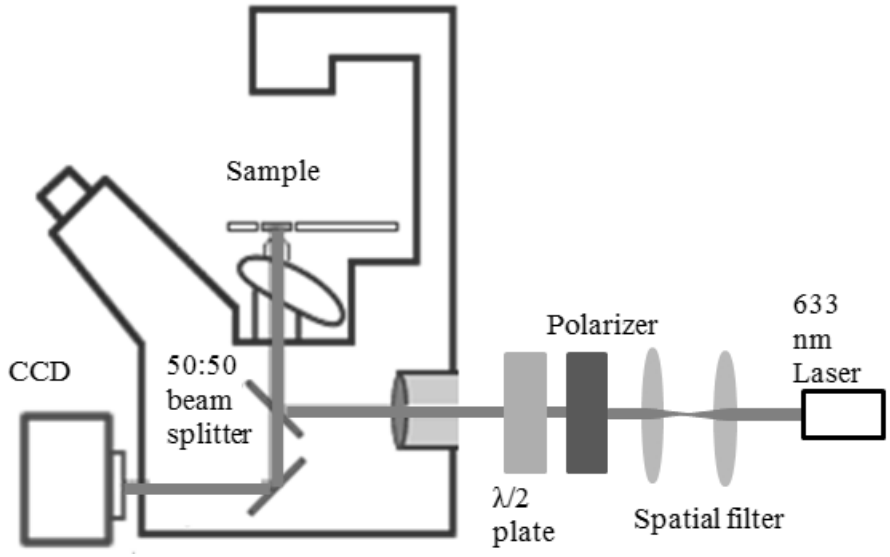

Figure B7 Plasmon excitation set up. A highly focused laser beam focused onto the sample using high numerical aperture objective.

The inverted microscope consists of a light source and a condenser on top of the stage and objectives and turret are below the stage facing upward. In this set up, waveguides can be viewed clearly under dark field. A spatial filter system is used to provide a diffraction limited beam and to transform the laser beam into a clean Gaussian beam. He-Ne continuous wavelength laser (532 – 633 nm) is used in this set up. Half-wave plate is used to change the polarisation of the incoming light. Light enters into the inverted microscope from the backport and is partially reflected upward towards the sample by a 50:50 beam splitter. Light goes through a high numerical aperture of 1.3 achieved using 100x oil immersion objective and is focused onto the sample. Light coming out of the high numerical aperture has a large angular spread including angles greater than the critical angle of metal/superstrate interface. Glass side of the sample is brought into contact with the objective via a layer of index matching immersion oil (refractive index 1.51). For successful use of the inverted microscope, structures must be fabricated on a glass substrate with thickness less than 0.17 mm as the working

distance of the x100 oil objective is around 0.17 mm. If the structures are on a thicker glass, sample must be inverted onto a coverslip (thickness $\geq$ 0.17 mm) and glass side of the coverslip brought into contact with the objective.

Coupling can be further enhanced if the highly focused beam is directed in to an optimised grating structure at the incoupling end. Light gets scattered when it is incident normally to the grating structure. Momentum of the scattered light can be manipulated easily by altering the grating periodicity. The reverse process is also possible by placing grating structures at the outcoupling end. Plasmons traveling to the end of the waveguide modulate with grating and couple to light and radiate.